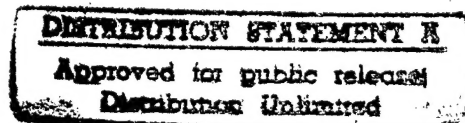


DOT/FAA/AR-95/43

Office of Aviation Research
Washington, D.C. 20591

Axial Crack Propagation and Arrest in a Pressurized Fuselage



September 1996

Final Report

19961127 050

This document is available to the U.S. public
through the National Technical Information
Service, Springfield, Virginia 22161.



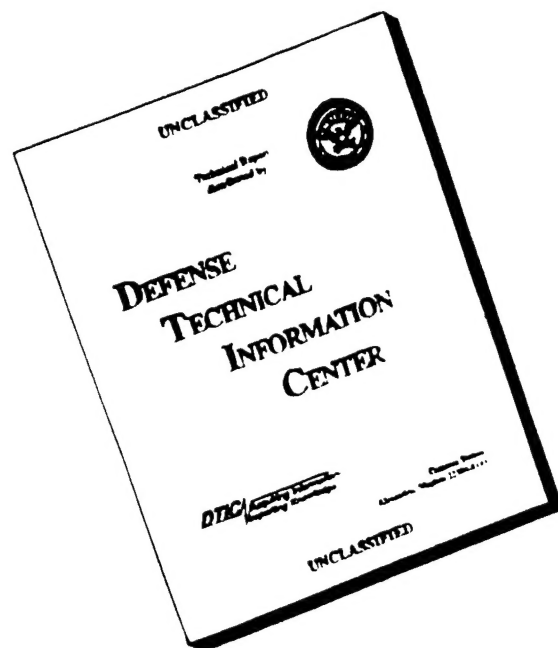
U.S. Department of Transportation
Federal Aviation Administration

DTIC QUALITY INSPECTED 3

NOTICE

This document is disseminated under the sponsorship of the U.S. Department of Transportation in the interest of information exchange. The United States Government assumes no liability for the contents or use thereof. The United States Government does not endorse products or manufacturers. Trade or manufacturer's names appear herein solely because they are considered essential to the objective of this report.

DISCLAIMER NOTICE



**THIS DOCUMENT IS BEST
QUALITY AVAILABLE. THE
COPY FURNISHED TO DTIC
CONTAINED A SIGNIFICANT
NUMBER OF PAGES WHICH DO
NOT REPRODUCE LEGIBLY.**

1. Report No. DOT/FAA/AR-95/43	2. Government Accession No.	3. Recipient's Catalog No.	
4. Title and Subtitle AXIAL CRACK PROPAGATION AND ARREST IN A PRESSURIZED FUSELAGE		5. Report Date September 1996	
		6. Performing Organization Code	
7. Author(s) M. Kosai, A. Shimamoto*, and A.S. Kobayashi		8. Performing Organization Report No. UW/DME/TR-95/2	
9. Performing Organization Name and Address University of Washington Department of Mechanical Engineering Seattle, WA 98195		10. Work Unit No. (TRAIS)	
		11. Contract or Grant No.	
12. Sponsoring Agency Name and Address U.S. Department of Transportation Federal Aviation Administration Office of Aviation Research Washington, DC 20591		13. Type of Report and Period Covered Final Report	
		14. Sponsoring Agency Code AAR-430	
15. Supplementary Notes FAA William J. Hughes Technical Center COTR: Dr. Paul Tan *On leave from Saitama Institute of Technology, Japan, at the time of this research.			
16. Abstract <p>A hybrid experimental-numerical investigation was undertaken to establish a practical crack kinking criterion in the presence or absence of multiple site damage (MSD) in a pressurized airplane fuselage. Ramulu-Kobayashi crack kinking criteria was modified to predict self-similar crack propagation along a line of MSD and subsequent kinking near a tear strap. Instrumented biaxial test specimens and small-scale fuselage rupture experiments were conducted to generate the crack kinking and crack velocity data which was then input to a large deformation, elasto-dynamic, finite element model of the fracture specimen. The computed Mixed-Modes I and II stress intensity factors and a large axial stress preceding the propagating crack were used to evaluate the self-similar crack extension and the crack kinking criterion along the crack trajectory. Excellent agreement was obtained between the predicted and measured crack kinking angles and locations. Additional verification was made through the match between the computed and measured strain gage data.</p> <p>The biaxial specimen tests showed that in spite of the presence of plane strain Mode II stress intensity factor (K_{II}) and the large axial stress ahead of the propagating crack, axial crack extension would continue in the axial direction of the skin is weakened by MSD. The crack propagated through the tear strap in the presence of a continuous MSD and kinked when the MSD terminated at the tear strap. However, if there is a short secondary crack under the tear strap, the lead crack kinked at the long groove end but reconnected to the secondary crack.</p> <p>The small-scale fuselage rupture tests showed that the pre-existing axial through crack along the stringer immediately kinked upon propagation due to the Mixed-Modes I and II state caused by the one-sided opening of the crack flap. The diagonally running crack subsequently turned circumferentially along the tear straps or the two cylinder ends. Again the experimental results were used to execute an elasto-dynamic finite element analysis to verify crack kinking and self-similar crack extension in the presence of the mixed-mode state along the stringer and final crack curving at the tear strap.</p>			
17. Key Words Widespread fatigue damage, Aging aircraft, Mixed mode, Tear strap, Multiple site damage (MSD)		18. Distribution Statement This document is available to the public through the National Technical Information Service (NTIS), Springfield, Virginia 22161.	
19. Security Classif. (of this report) Unclassified	20. Security Classif. (of this page) Unclassified	21. No. of Pages 180	22. Price

TABLE OF CONTENTS

	Page
EXECUTIVE SUMMARY	xiii
INTRODUCTION	1
Aging Airplane Accident	1
Airplane Fuselage Structure	1
Structural Concepts of the Airplane Fuselage	1
Design Philosophy	2
Design Details	3
Scope	4
LITERATURE REVIEW	4
Axial Crack Propagation in a Pressurized Cylinder	4
Crack Arrest and Kinking Criterion	6
Crack Kinking Criterion Under Mixed-Mode Loading	6
Crack Kinking Criterion Under Mode I	6
Axial Crack Propagation With MSD	9
Experimental Analysis	9
Numerical Analysis	11
Future Research on MSD	11
OBJECTIVES	12
METHOD OF APPROACH	12
THEORETICAL ANALYSIS	13
Mixed-Mode Loading Condition	13
Assumptions	14
Static Analysis	14
Geometric Nonlinear, Material Linear (Elastic) Analysis	14
Thin Shell Membrane Analysis	14
Crack Kinking Criterion	14
Mixed-Mode Crack Kinking Criterion	15
Mode I Crack Kinking Criterion	16

EXPERIMENTAL ANALYSIS	17
Biaxial Experiment	17
Specimen	17
Instrumentation	18
Experimental Procedure	18
Small-Scale Fuselage Rupture Experiment	18
Specimen	19
Instrumentation	19
Experimental Procedure	19
NUMERICAL ANALYSIS	20
Finite Element Method	20
Finite Element Model	20
Biaxial Specimen	20
Small-Scale Fuselage Specimen	20
Loading Conditions	21
Biaxial Test	21
Small-Scale Fuselage Rupture Test	21
Data Reduction	21
RESULTS AND DISCUSSION	22
Biaxial Test	22
Phase I (Type MV Series)	22
Phase II (Type MA, MB, MC, and MD Series)	23
Phase III (Type MG Series)	24
Small-Scale Fuselage Rupture Test	25
Mode I Test Specimen (Types a-1 and e-1)	25
Specimens With a Stringer (Types b-1, b-2, and d-1)	26
Fully Reinforced Specimens (Types c-1, c-2, and c-3)	26
Summary of Results	27
Biaxial Test	27
Small-Scale Fuselage Rupture Test	27
Discussion	28
Crack Kinking	28
Stress Intensity Factors	28
Nonlinear Effect	29

CONCLUDING REMARKS	29
--------------------	----

REFERENCES	30
------------	----

APPENDICES

- A — Mixed-Mode Crack Kinking Criterion
- B — Small-Scale Fuselage Specimen Preparation
- C — Material Properties of 2024-T3 and 7075-T6 Alloys

LIST OF ILLUSTRATIONS

Figure	Page
1 Aloha Incident [1]	37
2 Fuselage Damage Tolerance Sizes for Structural Design [9]	38
3 Schematic Drawing of Typical Skin Lap Splice	39
4 Comparison of Failures of Cylinders Pressurized With Air and Oil [12]	40
5 Maximum Principal and Circumferential Stress Criteria [25]	41
6 Fuselage Fatigue and Fail-Safe Development Tests [43]	42
7 Flow Chart of Method of Approach	43
8 Flow Chart of Hybrid Experimental-Numerical Analysis	44
9 Polar Coordinates	45
10 Crack Kinking Under Mixed-Mode Loading	46
11 σ_{ox} Dependence of Kinking Angle θ_c	47
12 Aluminum Cruciform Specimen (Type MV)	48
13 Aluminum Cruciform Specimen (Type MA)	49
14 Aluminum Cruciform Specimen (Types MB, MC, and MD)	50
15 Aluminum Cruciform Specimen (Types MC-6 and MD-7)	51
16 Aluminum Cruciform Specimen (Type MG)	52
17 Schematics of Biaxial Test Facility With Instrumentation	53
18 Biaxial Testing Machine	54
19 Small-Scale Model Fuselage Specimen (Type c-3)	55
20 Outside View of Specimen (Type c-3)	56
21 Inside View of Specimen (Type c-3)	57
22 Schematic of Instrumentation Setup for Small-Scale Cylinder Tests	58
23 Schematic of Instrumentation Setup for Imacon 790	59
24 Small-Scale Fuselage Rupture Test Setup	60

25	Small-Scale Fuselage Rupture Test Stand	61
26	Typical Finite Element Mesh of Biaxial Test Specimen (Type MV)	62
27	Typical Finite Element Mesh of Biaxial Test Specimen (Types MB and MC)	63
28	Typical Finite Element Mesh of Small-Scale Specimen	64
29	Axial Rupture of a Fuselage [91]	65
30	Photograph of Specimen MV-1	66
31	Variations in P_y . Specimen MV-1	67
32	Variations in K_I , K_{II} , and σ_{ox} . Specimen MV-1.	68
33	Photograph of Specimen MV-3	69
34	Variations in P_x and P_y . Specimen MV-3.	70
35	Strain Gage Responses. Specimen MV-3.	71
36	Variations in K_I , K_{II} , and σ_{ox} . Specimen MV-3.	72
37	Photograph of Specimen MV-7 and MV-9. 2024-T3 Cruciform Specimen With Large Flapping.	73
38	Variations in P_x and P_y . Specimen MV-7.	74
39	Variations in P_x and P_y . Specimen MV-9.	75
40	Strain Gage Responses. Specimen MV-7.	76
41	Strain Gage Responses. Specimen MV-9.	77
42	Variations in K_I , K_{II} , and σ_{ox} . Specimen MV-7.	78
43	Variations in K_I , K_{II} , and σ_{ox} . Specimen MV-9.	79
44	Photograph of Specimen 7MV-7	80
45	Variations in P_x and P_y . Specimen 7MV-7.	81
46	Strain Gage Responses. Specimen 7MV-7.	82
47	Variations in K_I , K_{II} , and σ_{ox} . Specimen 7MV-7.	83
48	Photograph of Specimen MA-2	84
49	Photograph of Specimen MB-3	85
50	Photograph of Specimen MC-2	86

51	Photograph of Specimen MC-5	87
52	Photograph of Specimen MC-6	88
53	Variations in P_x and P_y . Specimen MB-3.	89
54	Variations in P_x and P_y . Specimen MC-2.	90
55	Variations in P_x and P_y . Specimen MC-6.	91
56	Strain Gage Responses. Specimen MB-3.	92
57	Strain Gage Responses. Specimen MC-2.	93
58	Strain Gage Responses. Specimen MC-6.	94
59	Variations in K_I , K_{II} , and σ_{ox} . Specimen MB-3.	95
60	Variations in K_I , K_{II} , and σ_{ox} . Specimen MC-2.	96
61	Variations in K_I , K_{II} , and σ_{ox} . Specimen MC-6.	97
62	Photograph of Specimen MD-6	98
63	Photograph of Specimen MD-7	99
64	Variations in P_x and P_y . Specimen MD-6.	100
65	Variations in P_x and P_y . Specimen MD-7.	101
66	Strain Gage Responses. Specimen MD-6.	102
67	Strain Gage Responses. Specimen MD-7.	103
68	Variations in K_I , K_{II} , and σ_{ox} . Specimen MD-6.	104
69	Variations in K_I , K_{II} , and σ_{ox} . Specimen MD-7.	105
70	Variations in P_x and P_y . Specimen MG-6.	106
71	Strain Gage Responses. Specimen MG-6.	107
72	Variations in K_I , K_{II} , and σ_{ox} . Specimen MG-6.	108
73	Direction of Principal Strains. Specimen MG-6.	109
74	Photograph of Specimen 1 (Type a-1) After Rupture	110
75	Photograph of Specimen 13 (Type c-1) After Rupture	111
76	Pressure-Time Relation in Specimen 13 (Type e-1)	112
77	Strain Gage Response in Specimen 13 (Type e-1)	113

78	Variations in K_I , K_{II} , and σ_{ox} With Crack Extension. Specimen 13 (Type e-1).	114
79	Variations in r_0 With Crack Extension. Specimen 13 (Type e-1).	115
80	Schematic Drawing of One-Sided Crack Opening	116
81	Photograph of Specimen 4 (Type b-1) Before Rupture	117
82	Photograph of Specimen 4 (Type b-1) After Rupture	118
83	Pressure-Time Relation in Specimen 4 (Type b-1)	119
84	Variations in K_I , K_{II} , and σ_{ox} With Crack Extension. Specimen 4 (Type b-1).	120
85	Photograph of Specimen 14 (Type b-2) Before Rupture	121
86	Photograph of Specimen 14 (Type b-2) After Rupture	122
87	Pressure-Time Relation in Specimen 14 (Type b-2)	123
88	Strain Gage Response in Specimen 14 (Type b-2)	124
89	Variations in K_I , K_{II} , and σ_{ox} With Crack Extension. Specimen 14 (Type b-2).	125
90	Photograph of Specimen 12 (Type d-1) Before Rupture	126
91	Photograph of Specimen 12 (Type d-1) After Rupture	127
92	Photograph of Specimen 7 (Type c-1) Before Rupture	128
93	Photograph of Specimen 7 (Type c-1) After Rupture	129
94	Photograph of Specimen 8 (Type c-2) Before Rupture	130
95	Photograph of Specimen 8 (Type c-2) After Rupture	131
96	Pressure-Time Relation in Specimen 8 (Type c-2)	132
97	Strain Gage Response in Specimen 8 (Type c-2)	133
98	Variations in K_I , K_{II} , and σ_{ox} With Crack Extension. Specimen 8 (Type c-2).	134
99	Photograph of Specimen 11 (Type c-3) Before Rupture	135
100	Photograph of Specimen 11 (Type c-3) After Rupture	136

101	High-Speed Photographs of a Rupturing Small-Scale Fuselage (Type c-3)	137
102	High-Speed Photographs of a Rupturing Small-Scale Fuselage (Type c-3)	138
103	Pressure-Time Relation in Specimen 11 (Type c-3)	139
104	Strain Gage Response in Specimen 11 (Type c-3)	140
105	Variations in K_I , K_{II} , and σ_{ox} With Crack Extension. Specimen 11 (Type c-3).	141
106	Variation in Crack Velocity With Crack Extension	142
107	Variation in Crack Kinking Angle With Stringer Area	143
108	Finite Element Model of an Idealized Fuselage With an Axial Crack [90]	144
109	Effect of Bulging Due to Pressure and Curvature [9]	145
110	Variations in K_I , K_{II} , k_1 , and k_2 With Crack Extension. Specimen 11 (Type c-3).	146
111	Radial Displacement Along the Crack Path. Small-Scale Fuselage Model.	147
112	Radial Displacement Along the Crack Path. Idealized Fuselage Model [90].	148

LIST OF TABLES

Table	Page
1 Comparison of the Old and New FAR Requirement [4, 8]	149
2 Small-Scale Fuselage Specimens	150
3 Small-Scale Fuselage Specimens	151
4 Small-Scale Fuselage Specimens	152
5 Test Results. Material: 2024-T3, Thickness=0.81 mm (0.032 in)	153
6 Test Results. Material: 2024-T3, Thickness=0.81 mm (0.032 in)	154
7 Test Results. Material: 7075-T6, Thickness=0.81 mm (0.032 in)	155
8 Test Results. Material: 7075-T6, Thickness=0.81 mm (0.032 in)	156
9 Comparison of Experimental and FEM Analysis. Material: 2024-T3 Cruciform Specimen	157
10 Comparison of Experimental and FEM Analysis. Material: 2024-T3 Cruciform Specimen	158
11 Comparison of Experimental and FEM Analysis. Material: 7075-T6 Cruciform Specimen	159
12 Test Results (Type MA)	160
13 Test Results (Type MB)	161
14 Test Results (Type MC)	162
15 Test Results (Type MC)	163
16 Test Results (Type MD)	164
17 Test Results (Type MG)	165
18 Summary of Bursting Pressure	166
19 Summary of K_I , K_{II} , and Apparent K_{III} at the Onset of the Rupture	167
20 Summary of Measured and Computed Crack Kinking Angle	168

EXECUTIVE SUMMARY

A hybrid experimental-numerical investigation was undertaken to establish a practical crack kinking criterion in the presence or absence of multiple site damage (MSD) in a pressurized airplane fuselage. Ramulu-Kobayashi crack kinking criteria were modified to predict self-similar crack propagation along a line of MSD and subsequent kinking near a tear strap. Instrumented biaxial test specimens and small-scale fuselage rupture experiments were conducted to generate the crack kinking and crack velocity data which were then input to a large deformation, elasto-dynamic, finite element model of the fracture specimen. The computed Mixed-Modes I and II stress intensity factors and a large axial stress preceding the propagating crack were used to evaluate the self-similar crack extension and the crack kinking criterion along the crack trajectory. Excellent agreement was obtained between the predicted and measured crack kinking angles and locations. Additional verification was made through the match between the computed and measured strain gage data.

The biaxial specimen tests showed that in spite of the presence of K_{II} and the large axial stress ahead of the propagating crack, axial crack extension would continue in the axial direction if the skin is weakened by MSD. The crack propagated through the tear strap in the presence of a continuous MSD and kinked when the MSD terminated at the tear strap. However, if there is a short secondary crack under the tear strap, the lead crack kinked at the long groove end but reconnected to the secondary crack.

The small-scale fuselage rupture tests showed that the pre-existing axial through crack along the stringer immediately kinked upon propagation due to the Mixed-Modes I and II state caused by the one-sided opening of the crack flap. The diagonally running crack subsequently turned circumferentially along the tear straps or the two cylinder ends. Again the experimental results were used to execute an elasto-dynamic finite element analysis to verify crack kinking and self-similar crack extension in the presence of the mixed-mode state along the stringer and final crack curving at the tear strap.

INTRODUCTION

AGING AIRPLANE ACCIDENT.

On April 28, 1988, the fuselage of a Boeing 737 on Aloha Airlines Flight 243 came apart where overlapping skin panels had been joined (figure 1) [1]. The accident on the Aloha aircraft, which had been subject to a severe operating environment over its 19-year life, made aging airplanes a national issue. Despite this and other isolated incidents, commercial airplanes are extremely safe. U.S. statistics show that the risk of a fatal accident is one in one million flights. A combination of factors caused the catastrophic failure of Aloha Flight 243: tear strap debonding due to corrosion and multiple site damage (MSD) along the skin lap splice due to fatigue. Economics and market conditions have resulted in the use of commercial airplanes beyond their original economic design life of 15 to 20 years; the average age of the 4,100 U.S. commercial transports is 10.5 years [2]. As more airplanes exceed their economic design life and as the length of time by which they exceed this life becomes greater, fatigue cracks and corrosion may become more widespread.

Swift [3] postulated that widespread fatigue damage (WFD) is of great concern because the residual strength of a structure with a lead crack might be significantly reduced by the presence of adjacent smaller cracks. According to Boeing reports [2, 4, 5], there are two distinct types of WFD. One is called MSD, meaning the simultaneous presence of fatigue cracks in the same structural elements. The other is called multiple element damage (MED), the simultaneous presence of fatigue cracks in adjacent structural elements. Because it is difficult to detect such cracks when they are small before they link together, coalescence of WFD is a potential cause of catastrophic failure. Goranson [5] has noted that the emphasis on residual strength verification has gradually shifted in recent years from wing structures to fuselage pressure shells. A fuselage structure is typically more susceptible to WFD because it has numerous similar components subjected to pressure load cycles together with flight loads [5].

AIRPLANE FUSELAGE STRUCTURE.

The modern airplane structure must satisfy demanding safety requirements. The following is a description of the basic structure of the airplane fuselage and the evolution of pertinent safety standards.

STRUCTURAL CONCEPTS OF THE AIRPLANE FUSELAGE. The fuselage of a modern airplane is commonly referred to as semimonocoque structure and consists of a thin-skinned shell stiffened by reinforcements. These reinforcements are longitudinal elements (longerons and stringers) and transverse elements (frames and bulkheads). The fuselage skin carries the in-plane shear and tension loads caused by the cabin pressure and the applied external transverse and torsional loads. The skin must be stiffened by surrounding reinforcements to withstand compression loads, out-of-plane transverse shear loads, and bending moment loads. In addition to stabilizing the external skin, stringers also carry axial loads induced by the bending moment. The main purposes of frames are to maintain the shape of the fuselage and to reduce the effective column length of the stringers in order to prevent general instability of the structure. A semimonocoque structure is very efficient and has a high strength-to-weight ratio and design flexibility. Furthermore, it is one of the structures best able to withstand local failure through load redistribution, thereby preventing total catastrophic failure [6].

Loads affecting fuselage design can result from flight maneuvers, landing, or ground handling conditions. Of these, fuselage pressurization is one of the important structural loading conditions. It induces hoop and axial stresses in the fuselage that are combined with flight and ground loading conditions.

DESIGN PHILOSOPHY. It has been known since the 1930s that aluminum, which is used in more than 80 percent of the structure of commercial airplanes, is susceptible to fatigue problems. Damage caused by fatigue is difficult to detect and reduces the strength of critical members. In the 1950s, airplane structures were required to demonstrate a satisfactory fatigue strength in addition to the static ultimate design strength. The original fatigue design philosophy was the safe-life concept, in which components must remain crack free during service life. Safe life must include a margin for the scatter of fatigue results and for other unknown factors.

Current fatigue design methods have increased the fatigue life of airplanes through accurate stress analysis based on the finite element method, through life predictions based on fracture mechanics and fatigue crack propagation analysis, and through computer-controlled testing methods. In spite of these improvements in design, testing, and inspection methods, fatigue failures still occur. As a result of the possible existence of minor production deficiencies and severe operating environment, it must be assumed that cracks will occur long before the service life of the airplane is expended. Thus, safety demands a structural design that can withstand an appreciable load even in the presence of cracks or failed parts [7]. However, safe-life design philosophy does not take into consideration initial and accidental defects in the fatigue life estimation analysis. Fatigue analyses which include consideration of inherent material scatter characteristics often result in overly conservative and uneconomical designs [5]. Since safety requirements based only on fatigue strength were inadequate, more advanced safety requirements have been developed to design a structure which has a high degree of structural reliability and safety during the intended service life of the structure.

Fail-Safe Design Philosophy. By the late 1950s, a fail-safe design philosophy was added to the safe-life design philosophy. The basic requirements of the fail-safe philosophy is that a failure or obvious partial failure of any single main structural element shall not cause the loss of the airplane while in flight.

The fail-safe design criterion for most commercial airplanes requires that the fuselage be able to withstand a two-frame bay crack (40 inches for the B-737) without suffering catastrophic failure. This criterion was derived from an estimate of the maximum external damage expected to occur to the fuselage as a result of external damage that might occur from the penetration of projectiles produced by an uncontained engine disintegration [1, 5]. It must be shown that a flight can be safely completed after such damage has occurred. Initially, however, there was no consideration given to the joining of adjacent cracks that might develop during extended service.

Damage Tolerant Design Philosophy. Since 1956, it has been common practice for civil aviation authorities to demand that a designer show that his design will meet the fail-safe requirements when cracks arise during the operational life of the airplane. Later, by incorporating inspection, a more effective design philosophy of damage tolerance was developed. This involves the discovery and repair of damage before the crack reaches a catastrophic length. In December 1978, U.S. federal regulations for the design of commercial transport aircraft structures were revised to incorporate damage tolerant design. Table 1 shows a comparison of the old and new Federal Aviation Regulations (FAR) requirements [4, 8].

One of the significant differences between the old and new regulations is that under the new regulations initial damage has to be assumed to be already at multiple sites. These cracks are assumed to propagate independently during the operational use of the aircraft [4, 8].

Damage tolerance philosophy is a refinement of fail-safe design. As shown in table 1, the damage tolerance philosophy is made up of three fundamental elements: a residual strength analysis, a crack propagation analysis, and the establishment of an inspection and maintenance program. To insure that fatigue or corrosion cracks are detected before they reach the fail-safe damage limits, inspection intervals based on previous service experience, crack growth histories

obtained from analysis or tests, or a combination of these must be established. Aircraft structures must now be designed to be damage tolerant unless it can be shown that such design is impractical [4].

DESIGN DETAILS. The stiffened skin is the most critical structure because it carries all primary loads resulting from fuselage bending, shear, torsion, and cabin pressure. Although the skin panels are as large as possible to reduce the number of splices, which are one of the most critical parts, the size of skin panels is limited by manufacturing realities. For example, the forward fuselage of Boeing 737 has nine axial skin splices. Typically, single lap splices, which is the lightest design, are used for the axial skin splices.

The minimum gage of the fuselage shell is determined primarily by the fatigue strength of a skin lap splice. Much of the fuselage is at a minimum gage in the forward section. The upper crown of a fuselage structure is primarily designed for nosedown bending tension loads with internal pressure. The lower lobe is designed for smaller negative bending compression loads. Therefore, the upper lobe is fatigue critical in tension loading and the lower lobe becomes critical under ultimate compression loading. If a fatigue crack developed in one of these members and the crack is not easily inspectable externally because of an obstructed view, it could rapidly propagate to failure.

Swift [9] indicated that a fuselage structure should be designed to sustain the damage shown in figure 2 for the limit load condition. From the standpoint of damage tolerant design, there are two types of damage to be considered related to crack propagation and residual strength of a pressurized fuselage structure. These are longitudinal cracks subjected to high hoop stresses caused by internal pressurization and circumferential cracks due to vertical bending of the fuselage. The possibility of circumferential crack propagation at the top on the crown is fairly low since the butt splice—which is less susceptible to WFD than the lap splice—is normally used for circumferential skin splices.

In aircraft structures, fatigue cracking is primarily found in the upper row of rivet holes in the outer skin panel lap joint (figure 3). This is due to the higher transfer load through the rivets in this area where the highest tension load occurs at the knifed edge of the countersunk fastener holes. For the inner skin of the lap joint, the area of the highest stress is along the lower row of lap joint rivet holes. However, since the rivet holes in this skin panel are not countersunk, fatigue cracking is not as likely to initiate here [1].

Tear straps are located at or between each frame station. Early in the Boeing 737 program (up to line No. 291), cold bonding, in which surfaces are mated with adhesive at room temperature, was used to bond skin to skin and tear strap to skin. Later, bonds formed by cold bonding were found to weaken in a moist environment. This process was subsequently replaced by hot bonding using autoclaves, which eliminated the moisture and distributed the adhesive more uniformly [1].

The role of a tear strap in an airplane is to arrest a crack that is propagating axially either subcritically under fatigue loading or dynamically after reaching criticality. Such crack arrest can result from lower stresses due to the reinforcing effect of the tear strap or by crack kinking due to the complex crack-tip stress field generated by the crack flap and the tear strap. This flapping and crack kinking provide controlled damage and decompression and improve the damage tolerance of the pressurized fuselage. Thus, it is very important to ensure crack diversion by redirecting the crack into the hoop direction from the longitudinal direction that gives rise to skin flapping and contained decompression of the fuselage.

According to Aviation Week (July 25, 1988), there were at least two cases before the Aloha accident in which the flapping theory did not hold true: the Far Eastern Air Transport (FEAT) Boeing 737 accident in 1981 and the Japan Air Lines Boeing 747 accident in 1985. The FEAT

airplane had been weakened by extreme corrosion while the cause of the JAL accident was the collapse of the aft pressure bulkhead, which resulted from a series of human errors.

The Aloha Airlines incident shows that the fail-safe concept is not always effective in preventing a catastrophic failure due to unexpected conditions, such as widespread corrosion fatigue cracks at rivet holes in the fuselage skin (figure 3) and debonded tear straps. As mentioned before, this incident revealed that the crack arrest capability of the tear strap can be compromised by the presence of the MSD and which is especially dangerous because MSD is difficult to detect under real-life conditions. Therefore, Goranson [5] suggested that a special failure criterion and detection parameters are necessary for estimating the residual strength and crack propagation rate of a damaged structure with short secondary cracks near a larger primary crack.

Although the tear strap is the last defense of an axially rupturing fuselage, little is known about its effectiveness in arresting a rapidly propagating axial crack. Much of its design is based on rules derived from sub- and full-scale testing of pressurized fuselages. Research on dynamic crack propagation is also important to prevent catastrophic failure, a fundamental safety requirement in the fail-safe design philosophy, when the principle of damage tolerance is violated due to unexpected human errors in design, manufacturing, maintenance, or inspection.

SCOPE.

The purpose of this research was to develop a practical crack kinking and arrest criteria for a pressurized airplane fuselage using a hybrid experimental-numerical technique. A literature survey on previous fracture mechanics studies related to this subject is presented in the Literature Review section. Specific objectives of this research are documented in the Objectives section and the research method is described in the Method of Approach section. The Theoretical Analysis section explains the theoretical basis of a crack kinking criteria. The Experimental Analysis and Numerical Analysis sections describe the experimental procedures and numerical methods used, respectively. The Results and Discussion section contains the results and discussion of a biaxial test and a small-scale fuselage rupture test, respectively. The Concluding Remarks section offers conclusions from these findings.

LITERATURE REVIEW

As mentioned previously, the main purpose of a crack arrester (tear strap) in a pressurized fuselage is not only to limit a rapidly propagating axial crack to one or two bays of the fuselage but also to deflect it in the circumferential direction. The design of such crack arresters requires knowledge of crack driving force(s) and crack arrest and kinking conditions in addition to an understanding of the fuselage structure and its loading conditions. Existing literature related to this subject deals primarily with axial crack propagation in pressurized cylinders and dynamic crack curving and branching. The following is a review of the available papers on these subjects as well as on crack arrest in the airplane fuselage.

AXIAL CRACK PROPAGATION IN A PRESSURIZED CYLINDER.

As mentioned previously, longitudinal cracks along the skin lap splice are more dangerous than circumferential cracks due to the possibility of WFD along the longitudinal lap splice. Furthermore, in curved shells subjected to internal pressure, longitudinal crack tips are more affected by bulging than circumferential crack tips [10]. This bulging causes local bending at the crack tip, which increases the effective crack-tip stress intensity factor [11].

The fracture strength of cracked pressurized cylinders is substantially less than that of corresponding flat tension specimens. This strength reduction is due to the increase in the crack-tip stress intensity caused by bulging near the crack. Peters and Kuhn [12] investigated the

bursting strength of 2024-T3 and 7075-T6 aluminum alloy, unstiffened cylinders which contained slits simulating cracks. They concluded that the bursting strength was substantially reduced by increasing the slit length and increasing the curvature. Although cylinders pressurized with air failed at approximately the same hoop tensile stress as those pressurized with oil, the failure modes between air and oil tests were quite different. The cylinder tested with air split open from one end dome to another, and the sheet was torn away from the end domes for a considerable distance around the perimeter. The fracture mode in cylinders tested with oil was simply a self-similar extension of the original slit at each end (figure 4).

Anderson and Sullivan [13] derived the stress intensity factor and related the circumferential stress at fracture to the crack length, cylinder radius, material fracture toughness, yield strength, and an empirical bulge coefficient. The good agreement between the derived equation for fracture strength and the experimental data [12] suggested that the strength of a cylindrical pressure vessel with a longitudinal through crack is related to the geometry of the cylinder, the crack length, the material yield strength, and the fracture toughness.

Linear elastic fracture mechanics (LEFM) has been used to predict the stress intensity factor of an axial crack in a pressurized cylinder [14, 15]. The stress intensity factor for a through-the-thickness axial crack of length $2a$ in a cylindrical vessel was derived theoretically by Folias [10, 14] as

$$K_I = M_F \frac{pR}{t} \sqrt{\pi a} = \frac{pR}{t} \left[\left(1 + 1.61 \frac{a^2}{Rt} \pi a \right) \right]^{\frac{1}{2}} \quad (1)$$

where R is the radius of the vessel or pipe, t is the wall thickness, and p is the internal pressure. M_F is a stress intensity magnification factor which accounts for the outward bulging of the crack edges due to the internal pressure.

Hahn et al. [16] obtained the following empirical hyperbolic-tangent modification of the Folias' equation. Hahn's modified equation contains a plasticity correction factor, which was derived from the Dugdale crack model:

$$K_I = \frac{pR}{t} \left[\left\{ 1 + 1.61 \frac{a^2}{R^2} \left(50 \tanh \frac{R}{50t} \right) (\pi a \phi_3) \right\} \right]^{\frac{1}{2}} \quad (2)$$

where ϕ_3 is the plastic correction factor.

Equation 2, which does not involve any additional unknown parameters, is appropriate to predict the bursting pressure for a vessel in which the wall radius-to-thickness ratio is more than 50. Hahn's empirical adjustment to Folias' correction factor provided a good approximation for short axial cracks in a pressurized cylinder.

The mechanisms and parameters that control the direction of crack growth in thin pressurized cylinders under different loading conditions, such as quasi-static pressure conditions, explosive loading, and fatigue loading were determined by Fyfe and Sethi [17]. In their fatigue crack growth study using an idealized model of a stringer-reinforced fuselage, the axial stretching due to the resultant one-sided crack flap generated axial tensile stresses along the cracked upper skin and imposed a Mode II stress intensity factor, K_{II} . Their study showed that the bulging configuration gave rise to conditions in which a crack growth could be unstable.

CRACK ARREST AND KINKING CRITERION.

Sampath and Broek [18] indicate that fractures occur in the upper skin with the lower skin attached to the stringer. Under this condition, axial stretching due to the resultant one-sided crack flap generates axial tensile stresses along the cracked upper skin and imposes a Mode II state at the crack tip.

CRACK KINKING CRITERION UNDER MIXED-MODE LOADING. According to current theory on elasto-static fracture under mixed-mode loading, crack extension and fracture criteria under combined tension and shear loading are based on either the maximum energy released or the maximum circumferential stress criterion. The mixed-mode crack extension criterion developed by Erdogan and Sih [19] is commonly referred to as the maximum principal stress criterion ($\tau_{r\theta} = 0$).

Cotterell and Rice [20] modified the maximum circumferential stress theory by incorporating a second-order term, σ_{ox} , to predict the curving direction of a slightly curved crack. Depending on the test conditions and the shape of the fractured specimens, the theoretically predicted angle could deviate from the experimentally measured fracture angle when the second-order term was neglected [21, 22].

Ramulu and Kobayashi [23, 24] incorporated a second-order term of σ_{ox} in the dynamic crack-tip stress field and then derived the dynamic counterpart of the crack stability model. This derivation was based on the maximum circumferential stress criterion as well as the minimum strain energy density criterion. The factor σ_{ox} was found to influence significantly the kinking angle of a running crack.

Although these two concepts, the maximum principal stress ($\tau_{r\theta} = 0$) and the maximum circumferential stress theories ($\partial\sigma_{\theta\theta}/\partial\theta = 0$), may be physically similar, they represent two different ideas. In the maximum circumferential stress model, $\sigma_{\theta\theta}$ may not be the principal stress because the condition $\tau_{r\theta}$ is not always satisfied. That is, the maximum values of $\sigma_{\theta\theta}$ and σ_{11} (larger principal stress) are different in the presence of the second-order term as shown in figure 5 [25]. Without the second-order term, however, they yield identical results.

As for the energy approach, Hussain et al. [26], Palaniswamy and Knauss [27], Gupta [28], Wu [29], and Nemat-Nasser et al. [30, 31] predicted the direction of a kinked crack based on the rate of energy release at maximum strain. Sih [32], on the other hand, proposed a fracture theory for the problem of mixed-mode crack extension based on the local strain energy density. The basic assumption of this minimum strain density criterion is that the crack will propagate in the direction where the strain energy density, S , is at a minimum. Later, Theocaris and Andrianopoulos [33] modified the S -theory by designating its mean value, S_m , as the critical quantity for crack initiation under the mixed-mode loading condition.

Swenson and Ingraffea [34] computed the crack path in a centrally cracked Homalite-100 plate under the biaxial loading condition by using the maximum circumferential stress for the crack propagation direction. They compared these calculated results with experimental results obtained by Dadkhah [35]. Good correlation was obtained with the available data for crack path and observed stress intensities.

CRACK KINKING CRITERION UNDER MODE I.

The Maximum Circumferential Stress Criterion. The maximum circumferential stress theory ($\partial\sigma_{\theta\theta}/\partial\theta = 0$) was first derived by Yoffe [36] in 1951 to explain crack branching of a rapidly propagating Mode I crack. Later, Williams and Ewing [37] extended this theory by incorporating a second-order term, σ_{ox} , which is applied parallel to the crack plane. Finnie and

Saith [38] improved the Williams and Ewing model by correcting an oversight. Streit and Finnie [39] applied this theory to a static crack curving criterion and predicted the directional stability of Mode I crack propagation. This stability criterion introduced another critical material parameter, r_c , which is the radial distance from the crack tip. As such r_c is a material constant that specifies the characteristic crack-tip region in which the off-axis microcracks are triggered and connected to the main crack tip. The assumption of the maximum circumferential stress criterion, as modified by Ramulu and Kobayashi [23], is that the crack will extend towards the circumferential stress, which reaches its maximum value at a critical distance, r_o , away from the crack tip. The characteristic distance, r_o , is derived from the crack stability criterion, which involves a second-order term σ_{ox} in a dynamic crack-tip stress field.

This maximum circumferential stress condition based on LEFM results in a characteristic crack-tip distance, r_o , in which the propagating crack will deviate from its axis by an angle of θ_c . For a dynamic crack, these values under pure Mode I are

$$r_o = \frac{I}{128\pi} \left[\left(\frac{K_I}{\sigma_{ox}} \right) V_o(c, c_1, c_2) \right]^2 \quad (3)$$

where

$$V_o(c, c_1, c_2) = B_I(c) \left\{ -(1 + S_2^2)(2 - 3S_1^2) - \frac{4S_1S_2}{1 + S_2^2} (14 + 3S_2^2) - 16S_1(S_1 - S_2) + 16(1 + S_1^2) \right\} \quad (4)$$

$$B_I(c) = \frac{1 + S_2^2}{4S_1S_2 - (1 + S_2^2)^2} \quad S_1^2 = 1 - \frac{c^2}{c_1^2} \quad S_2^2 = 1 - \frac{c^2}{c_2^2}$$

where c_1 is the dilatational wave velocity and c_2 is the shear wave velocity.

The crack kinking angle θ_c can be obtained from the following transcendental equation:

$$r_o = \frac{I}{4\pi} \left[\left(\frac{K_I}{\sigma_{ox}} \right) \frac{B_I(c)}{\sin 2\theta_c} \left\{ \begin{aligned} & \left((S_1^2 - S_2^2) - (1 + S_1^2) \cos 2\theta_c \right) \frac{\partial f_{11}}{\partial \theta} + 2(1 + S_1^2) \sin 2\theta_c f_{11} \\ & + \frac{4S_1S_2}{1 + S_2^2} \cos 2\theta_c \frac{\partial f_{22}}{\partial \theta} - 2 \frac{4S_1S_2}{1 + S_2^2} \sin 2\theta_c f_{22} \\ & - (2S_1 \sin 2\theta_c) \left(\frac{\partial g_{11}}{\partial \theta} - \frac{\partial g_{22}}{\partial \theta} \right) - (4S_1 \cos 2\theta_c) (g_{11} - g_{22}) \end{aligned} \right\} \right]^2 \quad (5)$$

where

$$\begin{aligned}
 f_{11} &= [f(c_1) + g(c_1)]^{\frac{1}{2}} \\
 g_{11} &= [f(c_1) - g(c_1)]^{\frac{1}{2}} \\
 f_{22} &= [f(c_2) + g(c_2)]^{\frac{1}{2}} \\
 g_{11} &= [f(c_2) - g(c_2)]^{\frac{1}{2}}
 \end{aligned}
 \quad \text{for } 0 < \theta \leq \pi
 \quad (6)$$

$$\begin{aligned}
 f(c_1) &= \frac{1}{\sqrt{\left(1 - \frac{c^2}{c_1^2} \sin^2 \theta\right)}} & g(c_1) &= \frac{\cos \theta}{\left(1 - \frac{c^2}{c_1^2} \sin^2 \theta\right)} \\
 f(c_2) &= \frac{1}{\sqrt{\left(1 - \frac{c^2}{c_2^2} \sin^2 \theta\right)}} & g(c_2) &= \frac{\cos \theta}{\left(1 - \frac{c^2}{c_2^2} \sin^2 \theta\right)}
 \end{aligned}
 \quad (7)$$

where K_I and σ_{ox} are the Mode I stress intensity factor and either the remote stress component or the first nonsingular term in the elastic crack-tip stress field, respectively.

The elastic crack kinking criterion requires that $r_0 < r_c$ for the crack to curve an angle, θ_c , away from its axis.

The Minimum Strain Energy Density Criterion. The minimum strain energy density criterion, as modified by Ramulu et al. [23], also incorporates the characteristic distance of r_0 and thus the second-order term of σ_{ox} in the strain energy density factor, S , of Sih [32]. The extended minimum strain energy density criterion with the σ_{ox} term can be used to predict crack kinking of a Mode I static crack or of a crack propagating at a low crack velocity.

The crack kinking angles predicted by using either the maximum circumferential stress or the minimum strain energy density fracture criterion are almost the same for smaller values of the Mode II stress intensity factor, K_{II} . The fracture angle for negative σ_{ox} is much smaller than those with positive σ_{ox} . Furthermore, the difference in dynamic crack kinking angles predicted by either theory is almost equal for the Poisson's ratio $\nu = 0.33$ to those of static analysis when $c/c_1 < 0.25$ [23].

The Maximum Energy Release Rate Criterion. Achenbach [40] proposed an approximation method based on the assumption that the near-tip field for a kinked crack can be assumed from the field for a crack propagating in its own plane, provided the new crack faces are subjected to tractions corresponding to the kinking crack. This approximate method was used for both Mode III and Mixed-Modes I-II crack kinking under stress-wave loading.

Ma [41] considered the maximum energy release rate criterion for a kinked crack and obtained the dynamic stress intensity factor at the kinked crack tip by using a perturbation method. This criteria suggested that the kinked crack would choose to propagate in the direction and at a velocity for which the energy flux into the crack tip was a maximum.

The $K_{II} = 0$ Criterion. Sumi [42] predicted curved crack growth paths under proportional loading conditions by using a fracture criterion that states that the crack will kink in the direction along which the stress intensity factor of the in-plane shear mode, K_{II} , vanishes for an infinitesimally small crack extension. The stress analysis was performed by the method of superposition of analytical and finite element solutions. Two examples (a DCB-type specimen and an edge crack approaching a hole) were solved by this method, which predicted a path that agreed well with the experimentally measured path.

AXIAL CRACK PROPAGATION WITH MSD.

The following section describes the results of the experimental and numerical analyses of the crack behavior with MSD in a typical aluminum fuselage. These findings are being analyzed and assessed by researchers, manufacturers, and airworthiness authorities.

EXPERIMENTAL ANALYSIS. To accurately analyze crack growth rate and the residual strength in a damaged structure, it is necessary to conduct a program of damage tolerance tests that examine materials ranging from small laboratory specimens to full-scale airframes. Because it is impossible to test all members of the structure, verification of the damage tolerance criterion for most of the structure must be performed numerically. However, the numerical analysis must be verified by a minimum number of effective experiments [4].

For example, Swift [43] used damage tolerance analyses in the design of the DC-10 in the early 1970s. Various configurations were studied to produce an optimum structure, which not only provided the fail-safe capability but also improved the service life of the fuselage. Numerical techniques were verified and the fail-safe strength of the fuselage shell was substantiated by flat and curved panel tests under uniaxial and biaxial loading, respectively. Typical test panels used by Swift are shown in figure 6.

Flat Panel Tests. Uniaxially loaded, unstiffened flat panels with multiple open holes and lap splice specimens with MSD were tested by Dawicke et al. [44]. They found that the prediction of MSD fatigue crack growth behavior was strongly dependent upon an accurate description of the stress intensity factor of the specific cracking pattern. Fatigue crack closure analysis, based on Elber's crack closure phenomenon [45, 46], was used to predict fatigue life. Elber [45, 46] observed that fatigue cracks closed at loads above the minimum load, reducing the stress intensity factor range over which damage occurred. Dawicke et al. concluded that the current crack closure analysis could describe the behavior for MSD with equal spaced cracks but could not describe MSD with unequal spaced cracks or crack linkup.

Mayville et al. [47], Jones et al. [48], Schijve [49], and Molent and Jones [50] conducted fatigue tests on riveted lap joints to determine a fracture criterion for linkup of MSD. These studies indicated that the linking of two adjacent cracks was due to net section failure of the remaining ligament, a hypothesis first proposed by Swift [51]. Also, Schijve [49] concluded in his study that the crack growth might be sufficiently slow to allow a timely detection in service, but this should be confirmed by full-scale fatigue tests for aging airplanes.

Moukawsher et al. [52] tested a 2024-T3 flat panel with a relatively large central lead crack along a series of 10 or 11 holes. The test results showed that the residual strength was significantly reduced due to MSD ahead of the lead crack and was also affected by the holes themselves. The importance of MSD, which reduced the residual strength, ahead of the lead crack was discussed.

Curved Panel Tests. A curved panel pressure test was conducted by Samavedam and Hoadley at Foster-Miller [53]. Panel loading was achieved by pulling on the curved ends and pressure loading the panel on its concave side by pressurized water. They observed that the

initial 914-mm (36-in.) skin crack extended over two frame bays and then turned at the frames, as one would expect in the ideal situation, causing decompression. They also tested panels with a 315-mm (12.4-in.) lead crack and found that the reduction in residual strength was about 20 percent under typical MSD conditions.

Full-Scale Tests. Airplane manufacturers such as Boeing, Douglas, and Airbus have conducted their own damage tolerance tests using full-scale models. Hoggard [54] used DC-9 fleet data to analyze the effectiveness of full-scale tests for maintaining safety of an aging fleet of airplanes against structural degradation due to widespread fatigue damage. He concluded that full-scale tests provided significant insight into future fatigue related behavior of airplane design including modes of failure and probable locations in spite of the tremendous investment in resources and time. There are no available papers on the full-scale tests conducted by Douglas. The following is a summary of full-scale tests conducted by Airbus and Boeing and their findings.

Airbus A-320 Full-Scale Tests. Brandecker and Hilgert [55] reported on the full-scale structural testing of the Airbus Industry A-320 airplane with regard to the damage tolerance requirements as specified by FAR 25 Amendment 45 and JAR 25.571. The primary purpose of these damage tolerance tests was to verify theoretical investigations such as the stress distributions, assumed failure modes, the damage tolerance analytical results, and finally, the defined inspection intervals using fracture mechanics. The longitudinal lap splice joint of the fuselage was known to be one of the significant structural components where fatigue damage was more likely to occur. Crack turning was verified and the crack propagation was slightly slower than predicted. No information was reported about the residual strength of the lap joint [55].

Boeing Full-Scale Tests. Maclin [56] summarized the 35 years of testing conducted by Boeing on the fuselage pressure structure. The test structure employed for design development and verification was made of large pressurized panels configured in the shape of a Quonset hut. Various combinations of skin gages and types of tear straps and shear ties were subjected to saw cuts and punctures by guillotine blades. Test sections were modeled using finite element analysis, and the results were compared with a comprehensive set of strain gage and crack opening displacement measurements. The structural modeling of crack behavior was refined, as necessary, to provide a validated tool for future airplane design.

The B-707 full-scale fatigue tests and the B-737 aft fuselage fatigue tests showed that safe decompression occurred by flapping and that naturally generated MSD did not prevent flapping. For a worst-case MSD due to normal fatigue scatter in a heavier skin gage of 1.5 mm (0.063 inch), flapping may not occur and hence the residual strength would be reduced.

Boeing [5, 57] has constructed two large pressure test fixtures. One fixture has a radius of curvature of a 1,800 mm (74 inches), representing a narrow body, while the other has a radius of curvature of a 3,200 mm (127 inches), representing a wide body. These fixtures were designed for fatigue crack growth and residual strength tests. Residual strength tests conducted in these fixtures indicate that MSD may influence safe decompression. The findings showed that small cracks under approximately 0.5 mm in length at the rivet holes can significantly reduce the residual strength of a large crack in the same row of holes. Cracks in skins of gages 1 mm (0.036 inch) or less and reinforced with tear straps and/or shear ties show a strong tendency to form flaps and provide safe decompression except when the cracks appear in a row of fasteners that contains a large (and perhaps unrealistic) amount of MSD. Cracks in skins of gages 1.5 mm (0.063 inch) and greater have not demonstrated safe decompression by flapping because the shear-tied frame reduced the effects of out-of-plane displacement, or bulging, and held the crack closed [5, 57].

NUMERICAL ANALYSIS. The stress intensity factor of a crack in a flat stiffened panel can be calculated by both analytical and finite element methods. An advantage of analytical method over the finite element method is its effectiveness in conducting parametric studies for optimizing the design of stiffened panels. On the other hand, the finite element analysis can easily incorporate structural complexities, such as stringer eccentricity and fastener hole and fastener deformations. For a cracked, curved stiffened panel, finite element or boundary element methods are indispensable in solving 3D models of fuselage structures.

Displacement Compatibility Method. The displacement compatibility method has been used by many researchers (Poe [58, 59], Vlieger [60]) to solve LEFM problems associated with a fastener hole in a reinforced panel. This method can be classified as a general flexibility matrix approach in structural mechanics. The stiffened panel is split up into its composite parts of skin and stringer, and load transmission takes place through the fasteners. Compatibility requires equal displacements at the corresponding fastener locations in the skin and the stringer. In this approach, fasteners are represented by a series of concentrated forces on the sheet. Various improvements to the analytical procedure for stiffened panels such as shear deformation of the fasteners, hole deformation, and also plastic deformation of the stringers have been incorporated by Swift [61]. Shear displacement characteristics of the adhesive were also considered by Swift [62] and the effects of adhesive delamination are accounted for together with stiffener yielding. After the Aloha incident, Nishimura [63, 64] combined this method with a Fredholm integral method to solve the stress intensity factors of multiple cracks in a sheet stiffened by riveted stiffeners. Although these methods were used for a parametric study in the design phase, their use is limited to 2D finite panels.

Displacement Finite Element Method (FEM). The stress intensity factor for crack problems is strongly influenced by the nonlinear geometric response of the stiffened fuselage shell structure. During the last decade, several displacement FEM methods for computing stress intensity factor solutions to complex crack configurations have been developed [65]. The finite element method with the nodal-force method [66], the virtual-crack-closure technique [67], and empirical stress intensity factor equations [68] have been used to obtain solutions for 3D crack problems. The equivalent domain integral method [69], which is appropriate for 2D and 3D crack problems with mixed-mode loadings and material nonlinearity, has also been used in recent years.

The finite element analyses used to predict the results of the Boeing full-scale test [5, 57], mentioned before, were conducted by Miller et al. [57, 70]. The predicted crack growth trajectory, calculated using the maximum strain energy release rate approach, and the measured one were in good agreement at all crack lengths for a narrow-body panel with floating frames. It should be noted that, although K_{III} of unknown accuracy was obtained from the analysis, only membrane stress intensity factors, K_I and K_{II} , were used for this prediction.

FEM/BEM Alternating Methods. Atluri and Tong [71] developed effective computational strategies to analyze structure integrity in the presence of MSD. Their strategy combines the displacement compatibility method with the finite element method. In the alternating technique [71, 72], the stresses in the uncracked body are first analyzed by using a FEM/boundary element method (BEM), then the stress intensity factors are determined from the analytical solution for a crack subjected to arbitrary tractions in an infinite body. Park and Atluri [73] also applied this method to analyze the fatigue crack growth of multiple cracks and obtained good agreement with the previously mentioned lap joint coupon tests conducted by Monent and Jones [50].

FURTHER RESEARCH ON MSD. Although the MSD problem is a critical issue, there is still little experimental information on crack growth and residual strength in riveted lap splices in the

presence of MSD. Such experimental data are necessary to validate the numerical MSD analyses.

Schijve [49] summarized an experimental approach to the MSD problem. As a start, the experiments can be carried out on flat uniaxially loaded specimens and then extended to biaxial loading. These tests should include the use of curved panels under biaxial loading to determine the crack-driving mechanism. Observations from these experiments are most fundamental for the study of failure criteria. Failure criteria can be justified by hybrid experimental-numerical analysis [74].

In order to use the hybrid experimental-numerical analysis to develop a failure criterion for curving cracks in thin shell, one needs to experimentally obtain enough information to prescribe the boundary conditions of a numerical analysis such as load, strain, crack velocity, and crack trajectory. After testing, experimental data can be used to drive a finite element code to compute fracture parameters such as K_I , K_{II} , and σ_{ox} .

There is no agreement on a crack kinking and arrest criteria for a pressurized fuselage. Therefore, these criteria will have to be established to develop the design methodology for tear straps to ensure skin flapping and controlled decompression.

OBJECTIVES

The Introduction and Literature Review sections provided an overview of axial crack propagation in a pressurized fuselage and its importance for safety. The purpose of the present research was to develop a practical crack kinking and arrest criteria in a pressurized airplane fuselage by using a hybrid experimental-numerical technique.

The specific aims of this study were

- to study the mechanics of axial crack propagation and arrest and to establish practical crack kinking and arrest criteria through analytical modeling,
- to establish the experimental and data reduction procedures for two-dimensional biaxial tests and small-scale fuselage rupture tests,
- to conduct elasto-dynamic finite element analyses using the above experimental data in order to verify of the proposed crack kinking criteria,
- and to investigate the effectiveness of a tear strap and crack trajectory in the absence and presence of MSD.

METHOD OF APPROACH

A hybrid experimental-numerical analysis was used where instrumented biaxial test specimens and small-scale fuselage rupture experiments were analyzed using finite element analysis. First, the biaxial test was used to verify the proposed plane crack extension and kinking criteria as applied to flat panels. Then, small-scale fuselage rupture tests were conducted to apply these criteria to curved panels. Figures 7 and 8, respectively, show the flow diagrams of the method of approach and the hybrid experimental-numerical analysis used in this study.

The sequence of steps followed in this method of approach are as follows:

1. Theoretical crack extension and kinking criteria were developed.

2. Two-dimensional biaxial experiments were conducted to obtain strain data and to determine crack trajectory. These strain data were used to compute the average crack velocity between two strain gages. Elasto-dynamic finite element analysis was then used to determine the crack-tip stress state associated with the measured crack trajectory.
3. The experimental findings—such as strain data and crack kinking angle—were compared with the computed finite element strains at the strain gage locations and the stress intensity factors derived from the finite element analysis.
4. After verifying the application of the proposed crack extension and kinking criteria to flat panels, several different configurations of biaxial specimens were tested to investigate the crack trajectory in the presence or absence of MSD.
5. Small-scale fuselage rupture experiments were conducted to verify the proposed criteria for a three-dimensional thin shell structure. The verification procedures were exactly the same as that used in the biaxial experiments.
6. Several different types of small-scale fuselage specimens were tested to investigate the crack trajectory and the effectiveness of a tear strap under mixed-mode and Mode I only loading β conditions.
7. Finally, the flapping phenomenon was investigated through small-scale fuselage rupture experiments using a high-speed camera.

THEORETICAL ANALYSIS

As mentioned previously, the function of a tear strap is not only to arrest a propagating axial crack by reducing the hoop stress but also to turn the crack from the axial to the hoop direction. Such crack deflections are induced by the Mode II stress intensity factor, K_{II} , which is generated by the outward deflection of the upper skin. In addition to K_{II} , a large axial stress generated by the outward deflection ahead of the propagating crack tip (Kobayashi, et al. [75, 76]) and reduced hoop stress due to the presence of the tear strap and frame lead to crack kinking under mixed-mode crack-tip loading. Without K_{II} —that is, for a K_I only loading condition—crack kinking can also be triggered by the reduced ratio of K_I/σ_{ox} , which is caused by the large axial stress, σ_{ox} , and also by the reduced K_I of the crack tip in vicinity of a tear strap.

Modified crack extension and kinking criteria under mixed-mode and Mode I loading will be proposed in this chapter.

MIXED-MODE LOADING CONDITION.

The asymmetrical skin separation caused by the constraint of the stringer on the lower skin, as shown in figure 3, generates a large differential tension or shear stress. Thus, the crack-tip stress field is under combined Modes I and II loading. The large axial stress ahead of the propagating crack tip on the upper skin, which is related to the second-order term of the linear elastic fracture mechanics, σ_{ox} , and the reduced hoop stress caused by the tear strap and frame, will induce the crack to kink under mixed-mode crack-tip loading. A criterion for such crack kinking can be derived by following the procedure used in [23] or [24] with the addition of only K_{II} since the second-order term vanishes in the asymptotic stress field for Mode II crack-tip deformation. The elastic crack kinking criterion of [23, 24] assumes that when the circumferential stress within a prescribed crack-tip region attains a maximum value off the axis of a self-similar crack extension, then crack kinking will occur.

If, however, the apparent Mode I stress intensity factor, K_I , is elevated by the presence of a row of MSD cracks along the axis of the main crack, then the fuselage rupture of Aloha Airlines Flight 243 suggests that the crack will continue to propagate in the axial direction. This occurs despite the presence of asymmetric crack-tip flapping, which generates the inevitable K_{II} in a pressurized fuselage. The physical evidence of such self-similar crack extension along a row of MSD cracks in the presence of K_{II} thus requires new crack propagation and kinking criteria.

ASSUMPTIONS.

Three fundamental assumptions were made to simplify the analysis:

STATIC ANALYSIS. Previous experimental results obtained by Arakawa [77] showed that the maximum crack velocity in fracturing aluminum specimens is approximately 40 meters per second for the brittle 7075-T6 aluminum alloy. For the more ductile 2024-T3 alloy, it is estimated to be less than 20 meters per second. It was assumed that at this low crack velocity the state of stress of the crack tip can be approximated by its static counterpart, even though the entire structural deformation must be treated dynamically. If the crack velocity is less than $c/c_1 = 0.1$, the difference between the static and dynamic kinking angles is less than 0.5 percent [23].

GEOMETRIC NONLINEAR, MATERIAL LINEAR (ELASTIC) ANALYSIS. Significant out-of-plane (radial) deformation occurs in the crack-tip region due to internal pressure in the fuselage. Consequently, a large deformation analysis based on geometric nonlinearity is required. Such geometric nonlinear analysis has been used to solve the crack problem in pressurized fuselages since the 1970s [78-81].

Although material nonlinearity is appropriate for the ductile aluminum alloys used for most of the airplane fuselage, it will be ignored in the present analysis since the kinking angle depends on the ratio of K_{II}/K_I and σ_{ox}/K_I and not on the absolute value of each. LEFM analysis is also justified for high-strain rate loading [82]. Furthermore, evidence from experiments to be discussed later has shown that the plastic strain is the same order as the elastic strain. Thus, geometric nonlinear but materially linear analysis (an elastic analysis) will be used to predict kinking angle.

THIN SHELL MEMBRANE ANALYSIS. A through crack in the skin of a pressurized fuselage undergoes out-of-plane bending as well as in-plane membrane loading. This out-of-plane bending complicates the fracture analysis. Hui and Zehnder [83] proposed a set of four stress intensity factors based on Kirchhoff plate theory that can be used to account for both types of loading experienced by a crack in a fuselage structure. Since the thin shell deforms more radially, like a balloon, to carry the applied membrane stresses, the transverse shear stress along the hoop direction is small. Furthermore, at the skin midsurface, $z = 0$, the two bending stress intensity factors do not affect propagation angle, because the bending stresses on the inside and outside surfaces negate one another. Therefore, the out-of-plane stress intensity factors, k_1 and k_2 , as defined in [83], will be neglected in this crack kinking study, although they were computed for reference purposes. This means that the crack problem will be treated as a plane stress problem, which is a justifiable simplification of the actual state of stress at the crack tip. However, the bending stresses which were caused by joint eccentricity must be taken into consideration in the lap joint study in the future.

CRACK KINKING CRITERION.

For the thin-gage skin used in a B-737 fuselage, i.e., 0.9 mm (0.036 in.), the following plane crack kinking criterion, which is governed by the state of stress at the crack tip, should be applicable.

MIXED-MODE CRACK KINKING CRITERION.

Mixed-Mode Stress Field. Elastic stress fields in the vicinity of a crack tip are related to the mode of crack-tip displacements. Because the effects of Mode I and II loadings are of primary concern and the true Mode III crack-tip deformation does not exist in the thin shell considered here, the following discussion is limited to Modes I and II. The stress field of the mixed-mode elastic crack tip, presented in the polar coordinate system as shown in figure 9, is given by

$$\begin{aligned}\sigma_{rr} &= \frac{1}{\sqrt{2\pi r}} \cos \frac{\theta}{2} \left[K_I \left(1 + \sin^2 \frac{\theta}{2} \right) + \frac{3}{2} K_{II} \sin \theta - 2 K_{II} \tan \frac{\theta}{2} \right] + \frac{\sigma_{ox}}{2} (1 + \cos 2\theta) \\ \sigma_{\theta\theta} &= \frac{1}{\sqrt{2\pi r}} \cos \frac{\theta}{2} \left[K_I \cos^2 \frac{\theta}{2} - \frac{3}{2} K_{II} \sin \theta \right] + \frac{\sigma_{ox}}{2} (1 - \cos 2\theta) \\ \tau_{r\theta} &= \frac{1}{\sqrt{2\pi r}} \cos \frac{\theta}{2} \left[K_I \sin \theta + K_{II} (3 \cos \theta - 1) \right] - \frac{\sigma_{ox}}{2} \sin 2\theta\end{aligned}\quad (8)$$

where σ_{ox} is the second-order term commonly referred to as the remote stress component.

The Maximum Principal Stress Criterion. In section 2, several elasto-static kinking criteria under mixed-mode loading were discussed. Erdogan and Sih [19] derived the angle of crack kinking, θ_c , in the presence of K_{II} by applying the maximum principal stress criterion, which is identical to the maximum circumferential stress criterion without the second-order term, σ_{ox} , and considering the crack-tip stress field:

$$K_I \sin \theta_c + K_{II} (3 \cos \theta_c - 1) = 0 \quad (9)$$

where K_I and K_{II} are the stress intensity factors for Modes I and II, respectively. This equation can be derived from the condition that the third equation of 8 is equal to zero, that is $\tau_{r\theta} = 0$.

This crack kinking criterion predicts a positive θ_c for a negative K_{II} , since K_I is always positive as shown in figure 10. Likewise, a negative θ_c is predicted for a positive K_{II} . In the absence of K_{II} , equation 9 predicts a self-similar crack propagation, or $\theta_c = 0$, and fails to explain the physically observed crack instability where crack kinking occurs under pure Mode I. Also, this theory does not account for the influence of material properties around the crack tip on the stress distribution nor does it account for the influence of the nonsingular term σ_{ox} on the direction of crack propagation.

The Maximum Circumference Stress Criterion. The static-elastic kinking criterion of Streit and Finnie [39], which incorporates either the second-order term in the crack-tip stress field or the dynamic counterpart of Ramulu and Kobayashi [23], predicts crack kinking under pure Mode I and was found to agree well with available experimental data. A mixed-mode crack kinking criterion based on the maximum circumferential stress criterion can be derived by this crack kinking criterion with the addition of K_{II} .

The mixed-mode crack extension criterion based on the maximum circumferential stress criterion is derived by assuming that fracture will occur when the maximum circumferential stress is equal to the equivalent circumferential stress in a Mode I fracture. From the second equation of 8, the mixed-mode crack extension criterion is

$$K_{Ic} = K_I \cos^3 \frac{\theta_c}{2} - 3K_{II} \cos^2 \frac{\theta_c}{2} \sin \frac{\theta_c}{2} + \frac{\sqrt{2\pi r_c}}{2} \sigma_{ox} (1 - \cos 2\theta_c) \quad (10)$$

Equation 10 can be satisfied by a proper combination of a nonvanishing K_I , K_{II} , σ_{ox} , and θ_c , or $K_I = K_{Ic}$ and $\theta_c = 0$. The latter satisfies a self-similar crack extension criterion, which will be used here. Otherwise, off-crack extension will occur when equation 10 is satisfied.

The kinking angle, θ_c , at which circumferential stress, $\sigma_{\theta\theta}$, is maximum, can be derived by setting the crack velocity to 0 in the mixed-mode elasto-dynamic equation of Ramulu [84], as shown in appendix A, and results in the following transcendental equation:

$$\frac{K_{II}}{K_I} = \frac{-\sin \frac{\theta_c}{2}}{(3 \cos \theta_c - 1)} \left[2 \cos \frac{\theta_c}{2} - \frac{16\sqrt{2}\pi}{3} A \cos \theta_c \right] \quad (11)$$

$$A = \sqrt{r_c} \frac{\sigma_{ox}}{K_I}$$

The crack kinking angle computed by equation 11 incorporates σ_{ox} the second-order term. Figure 11 shows the variations in crack kinking angle with changes in the K_{II}/K_I ratio and in r_c and σ_{ox} . The term, A , is related to the critical distance, r_c , from the crack tip and is proportional to the nonsingular stress, σ_{ox} ; r_c is an unknown quantity that must be determined experimentally [84]. As shown in figure 11, the crack kinking angle, θ_c , increases for an increasingly positive σ_{ox} , and a negative σ_{ox} tends to stabilize the crack path. Also, a larger r_c results in larger changes in the fracture angle.

MODE I CRACK KINKING CRITERION. After kinking in the presence of mixed-mode loading, i.e., K_I and K_{II} crack-tip loading, the crack could propagate under dominant Mode I crack-tip loading due to the lack of a constraining stringer. By setting $\theta = 0$ and $K_{II} = 0$ in equation 11, the distance r_0 , where the maximum stress deviates from the position of symmetry, can be derived.

$$r_0 J_{\theta=0} = \frac{9}{128\pi} \left(\frac{K_I}{\sigma_{ox}} \right)^2 < r_c \quad (12)$$

If distance r ahead of the crack tip is considered, then the maximum $\sigma_{\theta\theta}$ does not necessarily occur at $\theta = 0$. In fact, the maximum $\sigma_{\theta\theta}$ in the two-parameter representation does not have to be at $\theta = 0$ when $r_0 > r_c$. The kinking criterion is triggered only when $r_0 < r_c$.

The crack curving angle, θ_c , can be obtained by setting $K_{II} = 0$ in equation 11.

$$\theta_c = \cos^{-1} \left[\frac{1 \pm \sqrt{1 + \frac{1024\pi}{9} r_c \left(\frac{\sigma_{ox}}{K_I} \right)^2}}{\frac{512\pi}{9} r_c \left(\frac{\sigma_{ox}}{K_I} \right)^2} \right] \quad (13)$$

It was shown that the maximum circumferential stress theory can explain the crack kinking behavior under pure Mode I only if a critical distance from the crack tip, r_c , is defined. It was

also found that this critical r_c is dependent on the microstructure of the material. Rice and Johnson [85] and Richi et al. [86] showed that the kinking criterion must also be applied a few grain diameters ahead of the crack to insure that a flaw and/or a correctly oriented grain are within a zone of sufficient stress for failure. Therefore, it is supposed that a critical distance, r_c , ahead of the crack tip can describe the stability condition under both pure Mode I and combined Modes I and II loadings.

The Neuber constant, r , which is a material constant and is related to the grain size of material, can be considered the same material property as r_c . According to the Metals Handbook [87], an average value of r_c might be 1.5 mm for 2024-T3 aluminum alloy.

The proposed self-similar crack extension and crack kinking criteria under mixed mode, K_I and K_{II} , crack-tip loading is as follows:

- The crack will continue its self-similar crack propagation when $K_I > K_{Ic}$ unless large change in σ_{ox} trigger equation 12.
- When $K_I < K_{Ic}$, the crack will kink at a kinking angle predicted by equation 11.

EXPERIMENTAL ANALYSIS

This section describes the details of the experimental procedure including the specimen configuration, setup, and testing. First, specially configured, biaxially loaded 2024-T3 and 7075-T6 aluminum alloy specimens were tested to verify the proposed crack kinking criteria and to check the influence of MSD. Next, fully instrumented, axial-rupture experiments using small-scale models of an idealized fuselage were conducted to investigate the practical application of the proposed crack kinking criteria and the effectiveness of tear straps.

BIAXIAL EXPERIMENT.

Several types of biaxial specimens with MSD were tested with loads simulating the hoop stress and differential axial stress generated by an asymmetric flap opening.

SPECIMEN. The 2024-T3 aluminum alloy is used for the fuselage skins of commercial transports, which carry cyclic tension stress due to fluctuations in cabin pressure. The 2024-T3 alloy is also used for the lower wing skins, which must withstand mainly tension stresses as the wing flexes upwards during flight. Because of its toughness, however, it is used primarily in members where fatigue strength is critical. For the upper wing skins, which must bear mainly compression stresses, the 7075-T6 aluminum alloy is used. This alloy is also used for reinforcements such as stringers, longerons, and frames. Since 7075-T6 has greater static strength than 2024-T3, but less fracture toughness, 7075-T6 is used for members that require high ultimate strength. Because of this widespread use in airplane construction, these two alloys were chosen for this study. Material properties of 2024-T3 and 7075-T6 alloys are shown in appendix B.

Several configurations of cruciform-fracture test specimens with identical overall dimensions are shown in figures 12 through 16. The purpose of the machined slot in the four arms of the specimen was to create a uniform stress condition in the actual working zone [88, 89]. The configuration differences are in the location and attachment method of the tear strap and the MSD patterns. The presence of MSD was simulated by machined grooves of varying length about 0.41 mm deep (50 percent of thickness). The biaxial test specimens are identified as:

- Type MV: A tear strap is attached to the end of the specimen by cold bonding* only, and a v-groove lies in the middle in front of the tear strap (figure 12).
- Type MA: Same as Type MV except with a bonded and riveted tear strap (figure 13).
- Type MB: Tear strap located at approximately the middle of the specimen. A v-groove is just in front of the tear strap (figure 14).
- Type MC: Same as Type MB except another v-groove is located behind the tear strap (figure 14).
MC-6 has the same groove configuration, but different fastener patterns as shown in figure 15.
- Type MD: Same as Type MC except for a continuous v-groove under the tear strap (figure 14).
MD-7 has the same groove configuration but different fastener patterns as shown in figure 15.
- Type MG: Same as Type MB except for a short v-groove under the tear strap (figure 16).

INSTRUMENTATION. For each configuration, one or two preliminary tests were conducted to check the crack trajectory. Then, the cruciform specimen was instrumented with four to five strain gages along the crack trajectory. The gages were used to monitor the strain history during crack propagation as well as to estimate the crack velocity. These transient strains were recorded with digital storage scopes as shown schematically in figure 17. The two time-varying loads, P_x and P_y , which were measured by the two load cells were also recorded with the digital scopes.

EXPERIMENTAL PROCEDURE. The specimen was loaded rapidly (loading rate is about 1.5×10^6 N/sec) using a biaxial testing machine developed by Dadkhah [35] shown in figure 18. The y-direction load, P_y , simulates the hoop stress of the fuselage and the load parallel to the crack; the x-direction load, P_x , simulates the large axial stress. This axial stress was identified as the dominant force behind crack curving in pressurized pipes [75, 76] and fuselages [90]. The upper load, P_{x1} , which was twice the lower load, P_{x2} , simulated the differential axial load imposed by the flapping of the upper fuselage skin as the crack propagated axially along a fuselage lap joint. The asymmetric x-direction load, i.e., $P_{x1}/P_{x2} = 2$, at the left tab of the cruciform specimen was generated by a simple mechanical lever system at the bottom side of the cruciform specimen as shown in figure 18.

SMALL-SCALE FUSELAGE RUPTURE EXPERIMENT.

Thin cylinders of 2024-T3 aluminum alloy, with or without simulated stringers and tear straps, were tested to verify the plane stress crack kinking criteria in pressurized cylinders. They were also used to justify the biaxial specimen tests for detailed analysis of the effectiveness of tear straps.

* Epoxy bonding (Type VPAC - Measurement Group, Inc.) is used to bond a tear strap to a specimen.

The use of air as a pressurizing medium is necessary if the true dynamic conditions of crack growth in a representative fuselage structure are to be adequately assessed. However, the risks associated with this type of testing need to be properly understood and adequate safeguards taken [57].

SPECIMEN. The purpose of the small-scale model was to study the effect of total air volume on crack propagation. This was done in the hope of duplicating some aspects of the interaction between the rupturing fuselage and decompressing air. The model's dimensions were therefore intended to approximate the length-to-diameter ratio of the pressurized section of a Boeing 737 fuselage. In consideration of laboratory space limitations and to minimize the difficulty of manufacturing and handling the test specimens, a scaling factor equal to one-tenth of the dimensions of the Boeing 737 was used. As this scaling factor could not apply to the skin thickness, 2024-T3 aluminum alloy with a thickness of 0.3 mm (0.012 inches), which is the thinnest gage available, was used. The details of the fabrication procedure of this small-scale model specimen is given in appendix B.

Three types of fuselage specimens were tested. The three specimen configurations are shown in tables 2, 3, and 4 and can be classified as:

- Specimens without stringers, for Mode I tests (Types a-1 and e-1)
- Specimens with stringers, for mixed-mode tests (Types a-2, b-1, b-2, and d-1)
- Fully reinforced specimens (Types c-1, c-2, and c-3)

Each specimen had an axial through crack, 100 mm in length, which was machined as a starter crack and was sealed with cork gasket, duct tape, and silicon rubber sealant.

Figure 19 shows a schematic drawing of the Type c-3 specimen, and figures 20 and 21, respectively, show photographs of the outside and inside of the specimen.

INSTRUMENTATION. A schematic of the instrumentation setup is presented in figure 22. The specimen was instrumented with strain gages and a pressure transducer, and the test data were recorded on a magnetic tape recorder. Preliminary tests were conducted to establish the crack trajectory for a particular specimen configuration and loading conditions. Three to five strain gages were attached along the anticipated crack trajectory. One strain gage was used to measure the far-field, undisturbed hoop stress of the test cylinder for calibration purposes. The response time of the strain gage and the pressure transducer used in this study are shown in appendix D.

High-speed photographs of the rupturing event of specimen 17 were recorded using an IMACON 790 camera, which was triggered by a crack gage in the path of the crack. The gage, located about 50.8 mm (2 inches) from the tip of the starter crack, was triggered by the bulging effect prior to the passage of the crack. Since the minimum framing rate of the camera, about 10,000 frames/sec and four frames per film, was too fast to record the entire rupture event, high-speed photographs of five identical specimens were recorded at different start times. Figure 23 shows a schematic of the instrumentation setup for the IMACON 790 camera.

EXPERIMENTAL PROCEDURE. The specimen was mounted between two steel cylinders as shown schematically in figure 24. The steel cylinders, shown in figure 25, duplicated the diameter-to-length ratio of a typical passenger airplane. A 3/16-inch-thick rubber gasket provided a seal between the flanges of the end caps and the fixture. An air inlet was provided on the left-hand cylinder while the right-hand cylinder incorporated a 492 kPa (50 psi) relief valve as a safety feature. The right-hand cylinder, which supported the pressure transducer, was mounted on wheels to facilitate assembly.

The test fixture was shielded by three steel screens for retaining the fragments projected by the explosive rupture. Before the test, the model was pressurized at a low pressure to ensure that it was airtight. Any leaks found were repaired with silicon rubber. Then, the internal pressure in the scale-model fuselage was increased until a rapid fracture initiated from the pre-existing crack.

NUMERICAL ANALYSIS

This section describes the numerical analysis used in this study. The analysis was used to determine the fracture parameters K_I , K_{II} , and σ_{OX} using an elasto-dynamic analysis of the finite element model of the specimen. The crack velocity and the time-varying applied loads obtained from the biaxial and small-scale fuselage rupture experiments were prescribed.

FINITE ELEMENT METHOD.

It is essentially impossible to measure all of the quantities needed for crack kinking analyses during a single experiment. Therefore, a finite element model was used to obtain the complete crack-tip states of stress, strain, and displacement. The initial and transient data obtained from an experiment were prescribed on a finite element model of the specimen, and the numerical results generated during the analysis were compared with experimental results such as strains, kinking locations, and angles.

FINITE ELEMENT MODEL.

In this study, a commercial finite element code, ABAQUS*, was used for the analysis of the dynamic fracture of the biaxial specimens and the small-scale fuselage specimens.

BIAXIAL SPECIMEN. Four-node bilinear plane stress elements were used to model the biaxially loaded plate. The tear straps were modeled using beam elements with an arbitrary cross section. Figure 26 shows a finite element model of a Type MV specimen. Figure 27 shows a typical finite element mesh and the details of a refined mesh in the area of crack propagation used for Types MB and MC specimens. For Type MD, a different finite element model with a straight crack trajectory was used. After tests, actual crack path was modeled with double nodes. Then, dynamic crack propagation was simulated that double nodes along the prescribed crack trajectory were released at a time calculated from a crack velocity.

SMALL-SCALE FUSELAGE SPECIMEN. Experimental data such as crack kinking angle, crack velocity, and pressure decompression rate were input to the finite element model. Elasto-dynamic finite element analysis was used in this study to duplicate the conditions of the experimental data.

Doubly curved shell elements with 6 degrees of freedom per node were used for the skin of the small-scale fuselage specimen. Three- and four-noded shell elements were used. The longitudinal stringers and the tear straps were modeled by beam elements. Dynamic crack propagation was simulated by the same double nodal procedure used in the finite element models of the biaxial specimens.

The asymmetric crack-tip deformation along the stringer required that at least one-half of the scale-model fuselage be modeled. However, a finite element mesh of a quarter of the cylinder

*ABAQUS, HIBBITT, KARLSSON & SORESENSEN, INC. 100 Medway Street, Providence, Rhode Island 02906-4402.

was used to save computation time. According to Miller et al. [70], it is necessary to include approximately 60 to 90 degrees of the shell arc in the fuselage model to minimize interactions with an adjacent cracked fuselage structure. Planes of symmetry were assumed along the circumferential boundary crossing the centerline of the crack and along longitudinal boundaries. Implicit in modeling a one-quarter segment is the assumption that an identical axial crack is also propagating in the other symmetric quarters of the fuselage. This will not correctly model a very large crack-tip opening of a single crack in the scale-model fuselage, due to the inevitable coupling effect between the two symmetrically propagating cracks. As separate numerical analysis showed that the difference in predicting the kinking angle using a one-quarter scale model and a one-half scale model was less than 2 percent. Furthermore, the difference in the initial crack kinking angle between an irregular mesh (kinked model) and a regular mesh (straight crack model) was less than 1 percent. Therefore, the one-quarter kinked model was considered accurate enough to predict the kinking angle.

LOADING CONDITIONS.

BIAXIAL TEST. The measured time-varying load, P_x , was separated into the upper load, P_{x1} , and the lower load, P_{x2} , where the ratio was $P_{x1}/P_{x2} = 2$. The time-varying loads P_{x1} , P_{x2} , and P_y were then applied at each loading point. The initiation time of crack propagation was estimated from the data of strain gage 1, which was attached close to the edge of the machine notch.

SMALL-SCALE FUSELAGE RUPTURE TEST. The actual pressure distribution on the flap as the crack continues to open is unknown. A finite element analysis of an idealized fuselage with an axial crack along a lap joint as shown in figure 29 was conducted [91]. For the anticipated slow crack velocity of less than 500 meters/second from Kobayashi and Engstrom [92], Arakawa et al. [77] and the small-scale fuselage rupture test, the pressure-structure interaction effect was negligible [93]. Two hypothetical pressure distributions were prescribed on the crack flaps, one constant and the other a linearly decreasing pressure on the crack flap [91]. Since for these two cases the variation in the crack-tip stress intensity factor was less than 4 percent, details of the pressure distribution in the vicinity of the axial crack were considered unimportant for a crack propagating with constant cylinder pressure. These figures show that the cork gasket seal prevented depressurization during crack extension until the crack reached the gasket boundary. Thus, the measured full pressure was prescribed on the opening flap, and a constant pressure was applied to each element representing the skin of the model.

Static tests using four strain gages, which were located at 0, 90, 180, and 270 degrees on the circumference of the specimen, showed that the axial stress was about 60 percent of the hoop stress. Based on thin-shell theory, the axial stress should be 50 percent of the hoop stress. In this case, however, the inner diameter of the steel cylinder was about 1.1 times larger than that of the specimen (see figure 24). Consequently the axial force applied to the aluminum cylinder was slightly higher than that of a typical pressure vessel. The axial stress applied to the coarse nodes along the right edge of the FEM model was 60 percent of the hoop stress in order to simulate the effect of the internal pressure on the end caps.

DATA REDUCTION.

Before the fracture parameters are computed, each model had to be calibrated. These calibration factors were obtained by solving a known problem using the same finite element mesh as the specimens.

First, K_I and K_{II} were separated by assuming that the K_I/K_{II} ratio was equal to the ratio of the crack-opening versus crack-sliding displacements. These were calculated as the difference between the upper and lower nodal displacements one element behind the crack tip. Next, the

stress intensity factors were computed from the element stress using the linear-elastic crack-tip field equations. The remote stress component, σ_{ox} , was then computed by subtracting the singular stress component from the axial stress component ahead of the crack tip. Miller et al. [57] used the displacement at nodes on the crack near the crack tip to calculate stress intensity factors. Although displacement is more reliable than the element stresses, the element stress procedure is the only way to calculate σ_{ox} .

The true K_I and K_{II} for the crack propagating within the groove was obtained by multiplying the stress intensity factors from the finite element analysis by the square root of the ratio of the specimen thickness to the thickness at the notch root of the groove. This scaling factor was obtained by assuming that the strain energy released by the crack extension was dissipated within the section of reduced thickness at the groove.

The numerically determined K_I , K_{II} , and σ_{ox} were then used to assess the potential of self-similar crack propagation or crack kinking as described in earlier.

In addition to K_I and K_{II} , the apparent K_{III} was obtained from the transverse shear stress of the crack-tip element. The bending stress intensity factors based on Kirchhoff plate theory k_1 and k_2 were also obtained from the bending components of τ_{θ} and $\sigma_{\theta\theta}$ of the crack-tip element using the stress field equations in reference 83.

RESULTS AND DISCUSSION

This section presents the experimental and numerical results obtained by the procedures described previously. In particular, loading and strain histories; variation of K_I , K_{II} , and σ_{ox} ; and crack kinking angles are presented.

BIAXIAL TEST.

PHASE I (TYPE MV SERIES). A total of 16 specimens, nine 2024-T3 and seven 7075-T6 specimens, were loaded in the biaxial testing machine with uneven axial loadings on the upper and lower crack flaps. Tables 5 through 8 summarize the test results for each specimen. Of the 16 specimens, five were analyzed in detail using an elasto-dynamic finite element. All test results were divided into four groups based on material and crack growth differences as described later. Each of the four groups exhibited distinct crack growth behavior. One specimen per group was analyzed in detail. An additional specimen from the large flapping specimens group was studied due to load rate variability inherent of the test equipment. The effect of different loading rates on the crack trajectory were studied. These five test results together with the corresponding numerical results are summarized in tables 9, 10, and 11 and are discussed in the following paragraphs.

2024-T3 Specimens Mode I Loading Specimen. Two tests were conducted for baseline data by initiating rapid crack propagation with only the y-direction load, P_y , applied. The results for this loading condition are given in table 5. Although the x-direction load, P_x was not applied, there was small K_{II} due to the x-direction constraint from the mechanical lever system. As anticipated, the crack arrested after entering the ungrooved region without kinking since K_{II} was close to zero. Figure 30 shows the photograph of the fractured specimen MV-1 with an arrested crack. Figures 31 and 32 show the variations in P_y and in K_I , K_{II} , and σ_{ox} , respectively. No reliable strain gage measurements were obtained in these tests. Despite the negligible small K_{II} crack-tip deformation, equation 12 was satisfied and the crack kinked slightly in the vicinity of the tear strap as shown in table 9. The excellent agreement between the predicted and measured crack kinking location and angle is noted in table 9.

Crack Arrested Specimen. Under a lower maximum $P_y = 17,000\text{N}$ (3,820 lb.), the propagating crack in specimen MV-3 kinked after entering the ungrooved section as shown in tables 5 and 9 and figure 33. Figures 34 and 35 show the variations in loads and four strain gage responses, respectively. The data points in figure 35 represent the computed strains at the strain gage locations. The good agreement between the measured and computed strains indicates that the prescribed crack velocity in this FEM analysis was reasonable. Figure 36 shows the variation in K_I , K_{II} , and σ_{ox} . Table 9 compares the measured and predicted crack kinking and kinking angles at four locations. Note that at location 2, the crack kinked despite the fact that $K_I > K_{Ic}$, which according to the proposed crack kinking criteria would predict straight crack extension. One possible cause of this discrepancy is the slight local decrease in P_y indicated by the slight drop in the strain of gage 3 at approximately 15.5 msec as shown in figure 35, which was not accounted for in our modeling. Such a momentary drop in local loading could cause $K_I < K_{Ic}$ and the kinking angle would be computed by equation 11 as shown in table 9. The third kinking was triggered by equation 12 with a sudden increase in σ_{ox} . Then, the fourth kinking was triggered by equation 10 and the kinking angle was computed by equation 11 since $K_I < K_{Ic}$.

Large Flapping Specimens. The influence of crack flapping in the presence of a tear strap was investigated through four tests shown in table 6. Figure 37 shows two fractured specimens, MV-7 and MV-9, with large flapping, crack penetration through the tear strap, and final buckling of the specimens. Figures 38 and 39 show the variations in P_x and P_y loads of the two specimens. Figures 40 and 41 show the four strain gage responses from these two tests. While the load histories of the two tests varied considerably, as shown in figures 38 and 39, the trends of the measured strains at each strain location were similar. Also the measured and computed strain histories of strain gages 2 and 3, the latter of which is represented by the data points, are in good agreement. Figures 42 and 43 show the variations in K_I , K_{II} , and σ_{ox} with crack extension, Δ_a , which is measured along the curved crack. Despite the relatively large K_{II} , the crack propagated straight in the groove. Once in the ungrooved region, the crack kinked and both K_I and K_{II} dropped precipitously. The measured and computed locations of the first and subsequent crack kinking and kinking angles are given in table 10. Note that the second and third crack kinkings were actuated by the sudden rise in σ_{ox} which in turn triggered equation 12. As the crack approached the tear strap in specimen MV-7, K_I decreased below K_{Ic} at which time the crack kinked again following equation 11. On the other hand, the crack of MV-9 did not kink in front of the tear strap because K_I was still greater than K_{Ic} .

7075-T6 Specimen. The effect of low fracture toughness was investigated by testing the seven 7075-T6 specimens shown in tables 7 and 8. Figure 44 shows a photograph of the failed specimen where the crack curved after exiting the groove end but continued to propagate through the tear strap which eventually debonded. Figures 45 and 46 respectively show the variations in the P_x and P_y load histories and the four strain gage responses of 7MV-7. Figure 47 shows the K_I , K_{II} , and σ_{ox} variations with crack extension as well as the locations of crack kinking. The first kinking, which occurred after the crack entered the ungrooved region, was triggered by equation 10. The second crack kinking was triggered by equation 12 with the sudden rise in σ_{ox} . The third kinking was triggered by equation 10 when $K_I < K_{Ic}$ as the crack approached the tear strap. The predicted and measured crack kinking locations and the angles are shown in table 11.

PHASE II (TYPES MA, MB, MC, AND MD SERIES). A total of 14 specimens with bonded and riveted tear straps were loaded in the biaxial testing machine with uneven axial loading on the upper and lower crack flaps. Of the 14 specimens, only five were analyzed in detail. One specimen from each of the five different v-groove configurations and fastener patterns was analyzed.

Type MA Series. Table 12 shows the maximum loads and crack path of two MA specimens. The crack hit the closest rivet hole after entering the tear strap zone. Figure 48

shows the photograph of the failed MA-2 specimen. No numerical analysis was conducted for this specimen.

Type MB and MC Series. Tables 13 through 15 show the experimental results for two MB and four MC specimens with the tear straps located in the middle of the specimen. There was no simulated MSD under the tear strap. For specimens MB-2, MC-4, and MC-5, the crack curved after exiting the groove end, propagated to the closest rivet hole, and then crossed the specimen. After the crack passed through the first rivet hole of specimens MB-3, MC-2, and MC-6, the paths were different. The crack kinked into the next rivet hole, propagated to the third rivet hole, and then kinked to the right edge of the specimen. Figures 49 through 52 show photographs of the failed MB-3, MC-2, MC-5, and MC-6. Figures 53 through 55 show the variations in the P_x and P_y loads of specimens MB-3, MC-2, and MC-6. Also shown are the discontinuous crack velocities which were obtained from the four strain gage readings and were also used in the dynamic FEM analysis. The crack velocity, which is less than 30 m/sec before kinking, suddenly decreases to less than 10 m/sec after kinking.

Figures 56 through 58 show the measured and computed strain histories at the four strain gages of specimens MB-3, MC-2, and MC-6, respectively. The computed strain histories represented by the data points are in good agreement with the measured strains. The numerical results terminate after the first crack kinking point which is half way through the measured strain history. Figures 59 through 61 show the variations in K_I , K_{II} , and σ_{ox} with crack extension Δa , which was measured along the kinked crack. The crack propagated straight in the groove despite the relatively large K_{II} . Once in the ungrooved region, the crack kinked and both K_I and the absolute value of K_{II} dropped precipitously with K_{II} approaching zero. The measured and computed kinking angles, with and without the second-order term σ_{ox} , are also shown in figures 59 through 61. In all cases, the first crack kinking was actuated by K_I falling below K_{Ic} and triggering equation 10 when the crack exited the groove. During subsequent crack extension, the absolute value of K_{II} remained small and the crack propagated essentially in a K_I mode. While the numerical analysis was terminated shortly after the first kinking, the results suggest that the second kinking was caused by a sudden rise in σ_{ox} which in turn triggered equation 12.

Type MD Series. The experimental results of two MD specimens with a continuous simulating MSD under the tear strap are shown in table 16. MD-6 and MD-7 were exactly the same configurations except for the fastener patterns; in both specimens the crack penetrated through the tear strap. Figures 62 and 63 show photographs of specimens MD-6 and MD-7, respectively. Figures 64 and 65 show the variations in the P_x and P_y loads and the crack velocity histories of specimens MD-6 and MD-7. Figures 66 and 67 show the four strain gage responses in these two specimens. Figures 68 and 69 show the K_I , K_{II} , and σ_{ox} variations with crack extension. Despite the presence of K_{II} , the crack propagated along the groove as expected. Crack kinking, which occurred after the crack entered the ungrooved region, was triggered by equation 12 since $K_I > K_{Ic}$. The predicted Mode I kinking angle of specimen MD-6, which was calculated by equation 13, was 24 degrees and is much smaller than the measured kinking angle, θ_{1m} , of 60 degrees. The corresponding θ_{1m} of specimen MD-7 was only 19 degrees. The larger θ_{1m} of specimen MD-6 could be attributed to the rapid drop in P_x and P_y , as shown in figure 64, accompanied by a larger than computed drop in K_I , that is, K_I could be smaller than K_{Ic} . From this assumption, crack kinking was triggered by equation 10 and the predicted mixed-mode kinking angle, which was calculated by equation 11, was 52 degrees.

PHASE III (TYPE MG SERIES). For further validation of the crack kinking and self-similar extension criteria as well as further insight into the influence of MSD in channeling the crack in the axial direction, a total of six specimens were loaded in the biaxial testing machine with uneven axial loadings on the upper and lower crack flaps. The experimental results of two MG specimens, where the tear strap was located in the middle of the specimen and with a short v-groove under the tear strap, are shown in table 17. This specimen simulates discontinuous MSD

at the fastener hole of the tear strap. Table 17 shows two specimens with a v-groove terminating 22.9 mm before the tear strap and with a short and discontinuous v-groove in the crack path under the tear strap. As the figure in table 17 shows, the crack kinked at the long groove end but reconnected to the short v-groove under the tear strap. Figure 70 shows the variations in the P_x and P_y loads and the crack velocity histories of specimens MG-6. Figure 71 shows the computed and measured strain gage results. The match between the computed and measured strains of strain gage 4, located at the tip of the discontinuous v-groove, was obtained only by initiating a secondary crack propagation at the tip of the discontinuous groove at the fastener joint and propagating this secondary crack towards the oncoming main crack. Figure 72 shows the K_I , K_{II} , and σ_{ox} variations with crack extension. The predicted crack kinking angle, which was computed from fracture parameters in figure 72, was in good agreement with the measured value. FEM analysis also showed that the main crack and the secondary crack connected not by the crack kinking criterion but by plastic overload as indicated by the computed stress and the principal strain directions as shown in figure 73.

SMALL-SCALE FUSELAGE RUPTURE TEST.

Ten cylinders without simulated tear straps and 11 cylinders with tear straps of various configurations as shown in tables 2, 3, and 4 were tested. A total of 21 rupture tests were conducted. These tests were divided into three categories. The first category involves specimens without a stringer, the second involves specimens with one stringer only, and the last category involves specimens with one stringer and two tear straps. Of the 21 specimens, only five were analyzed in detail. The best specimen was selected from each category and two more specimens were added from fully reinforced specimens to check the effect of the stringer stiffness to the kinking angle.

The strain gage results were used to estimate the crack velocities. Crack velocities ranged from 15 to 120 meters per second in all cases. This low crack velocity justified the use of the static crack-tip equations described in the Theoretical Analysis section to extract the variation in the mixed-mode stress intensity factors, K_I and K_{II} , and the remote stress component, σ_{ox} , with crack extension.

As mentioned in the Numerical Analysis section, the prescribed pressure distribution on the flap might not be important as long as the cabin pressure was kept constant during crack propagation. The pressure data (shown in figures 76, 87, 96, and 103) were almost constant to the edge of the cork gasket during crack extension, because the gasket and overlying duct tape prevented pressure leakage. This will be discussed in detail later. Therefore, a constant pressure on the crack flap was used for numerical analysis in this study.

MODE I TEST SPECIMEN (TYPES a-1 AND e-1).

Type a-1. The specimen of Type a-1 (table 2), without the lap joint or stringer along the precrack, was tested to check for crack curving due to the axial tensile stress in the absence of K_{II} generated by large crack flaps. Figure 74 shows the photograph after rupture. The rapidly propagating crack did not bifurcate but turned abruptly and ran circumferentially along the two steel end cylinders.

Type e-1. The crack in the Type e-1 specimen (table 4) ran axially until it hit the tear straps and then ran circumferentially along the tear straps. Figure 75 shows a photograph after the rupture. Figure 76 shows the pressure data. The pressure is relatively constant until the crack reached strain gage 1, which was located 50.8 mm (2 inches) from the starter crack tip. Figure 77 shows the measured and computed strain histories at the four strain gage locations. Figure 78 shows the variations in K_I , K_{II} , and σ_{ox} with crack extension for specimen 13 (Type e-1). K_I is larger than K_{Ic} at the moment of rupture. Figure 79 shows the r_0 variation with crack

extension. The mode I crack kinking criterion in the Theoretical Analysis section did not predict crack kinking since the computed r_0 was larger than the r_c . This result indicates that the local circumferential stiffness reinforced by the tear strap was not large enough to reduce the ratio of K_I/σ_{ox} before the crack reached the tear strap.

SPECIMENS WITH A STRINGER (TYPES b-1, b-2, AND d-1). In the specimens with a stringer, the crack kinked immediately and ran diagonally but straight until it hit the steel end cylinder. In this case, the crack kinked due to the presence of K_{II} which was generated by the one-sided crack opening away from the lap joint and/or stringer as shown in figure 80.

Type b-1. A flat stringer was placed adjacent to the precrack in this specimen. Figures 81 and 82 show the photographs before and after rupture, respectively. Figure 83 shows the pressure-time relation. Since the locations of the strain gages were not close enough to measure the strain, no reliable strain data for this specimen was obtained. The crack velocity of specimen 14 (Type b-2) was used to drive the FEM. Since the measured crack velocity was less than 120 meters per second, which is less than 2 percent of the dilatational stress wave velocity of aluminum, it was assumed that the discrepancy of the crack velocity between two configurations did not affect the fracture parameters, K_I , K_{II} , and σ_{ox} . Figure 84 shows the variations in K_I , K_{II} , and σ_{ox} with crack extension. Crack kinking occurred at the onset of rapid crack propagation due to the presence of K_{II} and $K_I < K_{Ic}$.

Type b-2. An L-stringer was installed on this specimen to increase the kinking angle. Figures 85 and 86 show the photographs before and after rupture, respectively, for one Type b-2 specimen. Figure 87 shows the pressure with the relative time. To prevent leakage the precrack was sealed with a gasket attached to the inside surface with silicon rubber and duct tape was placed over the gasket to strengthen the seal. The end of the cork gasket coincided with the location of strain gage 4. The edge of the duct tape extended to gage 5. As expected, no air leaked until the crack reached the edge of the gasket. Therefore, for the analyses it is assumed that the internal pressure was almost constant. Figure 88 shows that the measured and computed strain histories at the four strain gages are in good agreement with each other. Figure 89 shows the variations in K_I , K_{II} , and σ_{ox} with crack extension. K_I is slightly lower than K_{Ic} , but there is a negative K_{II} at the moment of rupture and the crack ran under a mixed-mode condition. After the initial crack kinking, K_I becomes larger than K_{Ic} and K_{II} becomes positive.

Type d-1. Only field rivets were used in this specimen with no tear straps. Figures 90 and 91 show photographs before and after rupture, respectively. After the crack reached the rivet hole, the crack did not turn along the fastener line but propagated straight due to the lack of local circumferential reinforcement such as a tear strap. This test result will be compared with the cylinders with tear straps in order to delineate the effect of the tear straps.

FULLY REINFORCED SPECIMENS (TYPES c-1, c-2, AND c-3).

Type c-1. In these test specimens, tear straps were bonded but not riveted to the skin. Figures 92 and 93 show of the photographs before and after rupture. The crack kinked immediately upon extension but then propagated in an off-axis direction. The crack did not change direction due to debonding of the tear straps.

Type c-2. In these specimens, tear straps were bonded by the same epoxy bonding which was used for the biaxial specimen and riveted to the cylinder. The stringer thickness was 0.6 mm (0.025 inch). Figures 94 and 95 show photographs of the before and after rupture. As seen in figure 95, the crack kinked immediately upon extension but then propagated in an off-axis direction until it approached the tear straps where it turned circumferentially and propagated along the tear straps. Figure 96 shows the pressure-time relation. Figure 97 shows the measured and computed strain histories at the three strain gages are in good agreement with each other.

Figure 98 shows the variations in K_I , K_{II} , and σ_{ox} with crack extension. Crack kinking occurred at the onset of rapid crack propagation due to the presence of K_{II} and $K_I < K_{Ic}$.

Type c-3. The configuration of Type c-3 specimen was same as that of Type c-2 specimen except for the stringer thickness. The stringer thickness of Type c-3 specimen was 0.8 mm (0.032 inch). Figures 99 and 100 show the photographs before and after rupture, respectively. Figures 101 and 102 show a composite set of photographs, obtained during five different tests, of a rupturing Type c-3 specimen. These sequential photographs show the development of the crack flap after the crack kinked immediately upon extension. Figure 103 shows the pressure-time relation. Figure 104 shows the measured and computed strain histories at the three strain gages are in good agreement with each other. Figure 105 shows the variations in K_I , K_{II} , and σ_{ox} with crack extension. Crack kinking occurred at the onset of rapid crack propagation due to the presence of K_{II} and $K_I < K_{Ic}$.

SUMMARY OF RESULTS.

BIAXIAL TEST.

Loading Condition. The remote hoop stress, σ_y , in most of the tests was about 138 MPa (20 ksi). The average axial stress for the upper tab, σ_{x1} , was 152 MPa (22 ksi) and that of the lower tab, σ_{x2} , was 76 MPa (11 ksi). Therefore, the differential tension stress, that is, the shear stress τ_{xy} , was about 38 MPa (5.5 ksi). Consequently, τ_{xy}/σ_y was 0.28, which is very close to the value of K_{II}/K_I from the FEM analysis of about 0.30.

Crack Velocity. The average crack velocity along the v-groove was about 20 m/sec. This dropped to less than 10 m/sec when the crack entered the ungrooved area and kinked.

Stress Intensity Factors. Although the computed K_I at the initiation of crack propagation was lower than K_{Ic} , K_I rose to a value higher than K_{Ic} as the crack propagated along the v-groove. K_I dropped below K_{Ic} immediately after the crack exited the groove. Crack kinking then occurred due to the presence of K_{II} and the condition $K_I < K_{Ic}$.

Crack Kinking Angle. The computed kinking angle using σ_{ox} was always close to the measured angle. The computed kinking angle without σ_{ox} was 25 percent or more smaller than the measured angle.

Crack Trajectory. Crack kinking occurred immediately after the crack exited the v-groove if there was no MSD under the tear strap but never occurred in the continuous v-groove in spite of the tear strap. Furthermore, if there was a short v-groove under the tear strap, the crack kinked at the long groove end but reconnected to the short v-groove under the tear strap.

SMALL-SCALE FUSELAGE RUPTURE TEST.

Bursting Pressure. Table 18 shows the bursting pressure of each model. As expected, the bursting pressure of the specimens with a stringer was higher than that of the specimens without a stringer since the stringer constrained the out-of-plane deformation of the specimen. On the other hand, little difference in bursting pressure between the specimens with and without tear straps was noted.

Crack Velocity. The discontinuous crack velocities, which were obtained from the strain gage readings and used in the dynamic FEM analysis of typical specimens, are shown in figure 106. The crack velocity increased with crack propagation due to the relatively constant internal pressure where no sizable decompression occurred until the crack reached the edge of the cork gasket that sealed the starter crack. From the sequential photos taken by the IMACON 790 high-

speed camera, the average crack velocity over the range of crack extensions, which varied in length from 60 to 70 mm, was about 50 m/sec. This value agrees well with the velocity obtained with the strain gages shown in figure 106.

Stress Intensity Factors. Table 19 shows the stress intensity factors at the onset of the rupture for each specimen configuration. As expected, K_I is smaller than K_{Ic} for specimens subjected to mixed-mode loading, but K_I is slightly larger than K_{Ic} for specimen under mode I fracture. The absolute value of K_{II} is proportional to the stringer area, which also can be seen in figure 107. However, apparent K_{III} is very small and almost constant regardless of the configuration.

Crack Kinking Angle. Figure 107 shows the variation in crack kinking angle with the stringer area. As discussed earlier, the kinking angle increases in proportion to the stringer area. Table 20 shows a summary of the measured and computed kinking angle for each specimen. The good agreement between the predicted and the measured kinking angles and the subsequent self-similar crack extension demonstrated the effectiveness of the kinking criterion as applied to a rupturing fuselage. The σ_{ox} term is very important in predicting the kinking angle for the small-scale fuselage test, because the computed crack kinking angle without the σ_{ox} term is less than 1/2 of the measured one. The effect of the σ_{ox} term for the small-scale fuselage test is more significant than that for the biaxial test due to the larger ratio of σ_{ox}/K_I .

Crack Trajectory. Also shown in figure 91, the cylinder with only field rivets and no tear strap demonstrated no change in crack direction. If a tear strap was attached to the skin by cold bonding only, its effectiveness was negated due to debonding, as shown in figure 93. When a crack reached a tear strap attached to the skin by bonding and riveting, it continued along the circumferential row of tear strap rivets, as shown in figures 95 and 100. This shows that the high local circumferential stiffness of the tear strap, which increases the effective thickness of skin three times, induces flapping.

DISCUSSION.

CRACK KINKING. Tests conducted by Boeing [70] indicate that axial cracks in wide-body fuselage sections tend to grow with fatigue in a generally axial direction and do not result in controlled decompression. Similar cracks in narrow-body structures kink and grow circumferentially in about 50 percent of the cases. An exception is cracks located midway between stringers. In narrow-body panels, the tendency of the lead crack to kink often negates the effect of MSD on final failure [70].

The Boeing findings indicate that crack kinking results from a large, nonlinear deformation that causes an increase in the axial stress parallel to the crack as a result of one-sided skin flapping. If the skin is thick and attached to the frame by a shear tie, the difference in displacement between the upper and lower skins is small. This means that the differential tension in the longitudinal direction between the two skins is small. As a result, K_{II} and σ_{ox} are not large enough to cause the crack to kink. Crack kinking is primarily a function of the ratio of the radius to the thickness of the skin gage (R/t) and the initial crack location. Also, the circumferential stiffness such as tear strap dimensions, shear-tied frame or floating frame, and other designs control crack kinking on the real airplane fuselage.

Although the general trend obtained from the small-scale fuselage rupture test might represent a real case, the finite element analysis of an idealized fuselage model incorporating these details must be conducted to fully understand and predict crack kinking.

STRESS INTENSITY FACTORS. A complicating factor in the analysis used in this work is that the state of stress around the crack tip in a pressurized shell can never be a pure membrane

state, i.e., general bending components will be present. How these bending components influence the crack kinking response at present has not been resolved.

The bending stress in the axial direction is relatively large compared with that in the hoop direction due to the dimple caused by bulging, as shown in figure 109. This axial bending stress, however, does not affect the out-of-plane stress intensity factor, k_2 , until the crack propagates in the axial direction. As shown in figure 110, the out-of-plane stress intensity factor, k_2 , is relatively small before crack kinking. After the crack kinks, the component of this bending stress along the crack path will change the direction and increase the absolute value of k_2 . On the other hand, k_1 remains small throughout crack extension. Potyondy [94] concluded that this k_2 might increase the rate of fatigue crack propagation. The effect of k_1 and k_2 on crack growth rate is still under study but is expected to be a secondary effect [95].

NONLINEAR EFFECT. Figure 111 shows the effect of material and geometric nonlinearities for the small-scale monocoque cylinder used in the present study. The radial displacement at the center of crack obtained by linear analysis was seven times larger than that from geometric nonlinear analysis, while the difference of including the material nonlinearity was less than 15 percent. Figure 12 shows the nonlinear effect for the idealized model of a B-737 fuselage as shown in figure 108 [90].

Although the difference in geometric nonlinearity for this model was much larger than for the small-scale model, the difference in material nonlinearity was less than 2 percent. $R/a=3.6$ and $R/t=592$ for the small-scale fuselage model while $R/a=4.6$ and $R/t=2055$ for the idealized fuselage model. Therefore, the proposed kinking criterion, which neglects material nonlinearity, may be appropriate as a first-order estimation for a cylinder in which R/t is relatively large.

CONCLUDING REMARKS

This research project tested modified crack extension and crack kinking criteria in the presence or absence of Mode II loading, using a hybrid experimental-numerical technique.

The conclusions of this research are summarized as follows:

1. The modified crack kinking criterion of equation 11 will predict the crack kinking angle in the biaxial 2D specimens and the small-scale fuselage rupture specimens.
2. Self-similar crack extension in the presence of an elevated K_I can be accounted for by attaching a qualifier to the above crack kinking criterion. This qualifier is
 - a. the crack will continue in its self-similar propagation in the presence of K_{II} when $K_I > K_{Ic}$.
 - b. the crack kinking criterion will be activated when $K_I < K_{Ic}$.
3. The elasto-dynamic finite element model was successfully used to model the dynamic crack propagation in biaxial 2D specimens and small-scale fuselage rupture specimens. Fracture parameters, K_I , K_{II} , and σ_{ox} were determined.
4. The influence of MSD, which was simulated by a 50 percent v-groove, was observed through the biaxial test. MSD could not only channel the crack to propagate straight despite the presence of K_{II} but could also defeat the tear strap.
5. The effectiveness of tear straps in the biaxial tests and the small-scale fuselage rupture tests was confirmed by the final crack curving at the tear strap.

REFERENCES

1. National Transportation Safety Board Aircraft Accident Report, Aloha Airlines Flight 243, Boeing 737-200, N73711, Near Maui, Hawaii, April 28, 1988, NTSB/AAR-89/03, PB89-910404, 1989.
2. McGuire, J.F. and Goranson, U.G., Structural Integrity of Fracture Aging Airplanes. *Proceedings of the 1991 International Conference on Aging Aircraft and Structural Airworthiness*, C.E. Harris (Ed.), NASA Conference Publication 3160, 1992, pp. 33-47.
3. Swift, T., Damage Tolerance in Pressurized Fuselage. *Proceedings of the 14th Symposium of the International Committee on Aeronautical Fatigue (ICAF)*, D.L. Simpson (Ed.), Engineering Materials Advisory Services, 1987.
4. Goranson, U.G. and Rogers, J.T., Elements of Damage Tolerance Verification. *Proceedings of the 12th Symposium of the International Committee on Aeronautical Fatigue (ICAF)*, R. Labourdette and D. Deviller (Eds.), Centre d'Essais Aeronautique de Toulouse (CEAT), 1983.
5. Goranson, U.G., Damage Tolerance—Facts and Fiction. *Proceedings of the 17th Symposium of the International Committee on Aeronautical Fatigue (ICAF)*, A.F. Blom (Ed.), Engineering Materials Advisory Services, 1993.
6. Niu, M.C.Y., Airframe Structural Design. Conmilit Press Ltd., 1988.
7. Broek, D., Elementary Engineering Fracture Mechanics—Fourth Revised Edition, Martinus Nijhoff Publishers, 1987.
8. Vlieger, H., Damage Tolerance of Stiffened-Skin Structures: Prediction and Experimental Verification. *Fracture Mechanics, Nineteenth Symposium*, ASTM STP 969, American Society for Testing and Materials, 1988, pp. 169-219.
9. Swift, T., Design of Redundant Structure. AGARD-LS-97, North Atlantic Treaty Organization, 1978, pp. 9-1 through 9-22.
10. Folias, E.S., On the Theory of Fracture of Curved Sheets. *Engineering Fracture Mechanics*, Vol. 2, 1970, pp. 151-164.
11. Heath, W.G., Nicholls, L.F., and Kirby, W.T., Practical Applications of Fracture Mechanics Techniques to Aircraft Structural Problems. AGARD-CP-221, 1976, pp. 1-1 through 1-22.
12. Peters, R.W. and Kuhn, P., Bursting Strength of Unstiffened Pressure Cylinders with Slits. NACA TN 3993, 1957.
13. Anderson, R.B. and Sullivan, T.L., Fracture Mechanics of Through-Cracked Cylindrical Pressure Vessels. NASA TN D-3252, 1965.
14. Folias, E.S., Axial Crack in a Pressurized Cylindrical Shell. *International Journal of Fracture Mechanics*, Vol. 1, 1965, pp. 104-113.
15. Erdogan, F. and Kibler, J.J., Cylindrical and Spherical Shells with Cracks. *International Journal of Fracture Mechanics*, Vol. 5, 1969, pp. 229-236.

16. Hahn, G.T., Sarrate, M., and Rosenfield, A.R., Criteria for Crack Extension in Cylindrical Pressure Vessels. *International Journal of Fracture Mechanics*, Vol. 5, 1969, pp. 187-210.
17. Fyfe, I.M. and Sethi, V., The Role of Thin Cylinder Bulging on Crack Curvature. *AIAA Paper 914086*, 32nd Structures, Structural and Materials Conference, Baltimore, MD, April 1991.
18. Sampath, S. and Broek, D., Estimation of Requirements of Inspection Intervals for Panels Susceptible to Multiple Site Damage. Structural Integrity of Aging Airplanes, Proceedings of the International Workshop on Structural Integrity of Aging Airplanes, S.N. Atluri, S.G. Sampath, and P. Tong, (Eds.), Springer-Verlag, 1991, pp. 339-389.
19. Erdogan, F. and Sih, G.C., On the Crack Extension in Plates Under Plane Loading and Transverse Shear. *ASME Journal of Basic Engineering*, Vol. 85, 1963, pp. 519-527.
20. Cotterell, B. and Rice, J.R., Slightly Curved or Kinked Cracks. *International Journal of Fracture Mechanics*, Vol. 11, No. 2, 1981, pp. 155-164.
21. Charalambides, P.G., Lund, J., McMeeking, R.M., and Evans, A.G., A Test Specimen for Determining Fracture Resistance of Bimaterial Interfaces., *Journal of Applied Mechanics*, Vol. 56, 1989, pp. 77-82.
22. He, M-Y., Bartlett, A., and Evans, A.G., Kinking of a Crack out of an Interface: Role of In-Plane Stress. *Journal of American Ceramics Society*, Vol. 74, 1991, pp. 767-771.
23. Ramulu, M. and Kobayashi, A.S., Dynamic Crack Curving—A Photoelastic Evaluation. *Experimental Mechanics*, Vol. 23, 1983, pp. 1-9.
24. Ramulu, M., Kobayashi, A.S., and Kang, B.S.-J., Dynamic Crack Branching—A Photoelastic Evaluation. *Fracture Mechanics, Fifteenth Symposium*, ASTM STP 833, R.J. Sanford (Ed.), American Society for Testing and Materials, 1984, pp. 130-148.
25. Streit, R., Directional Stability of a Propagating Crack. Ph.D. Thesis, University of California, Berkeley, CA, 1979.
26. Hussain, M.A., Pu, S.L., and Underwood, J., Strain-Energy-Release Rate for a Crack under Combined Mode I and Mode II. *Fracture Analysis*, ASTM STP 560, American Society for Testing and Materials, 1974, pp. 2-28.
27. Palaniswamy, K. and Knauss, W.G., On the Problem of Crack Extension in Brittle Solids Under General Loading. Mechanics Today, 4, S. Nemat-Nasser (Ed.), Pergamon Press, 1978, pp. 87-148.
28. Gupta, G.D., Strain Energy Release Rate for Mixed-Mode Crack Problem. ASME Paper No. 76-WA/PVP-7, 1976.
29. Wu, C.H., Elasticity Problems of Slender Z-Crack. *Journal of Elasticity*, Vol. 8, 1978, pp. 183-205.
30. Hayashi, K. and Nemat-Nasser, S., Energy Release Rate and Crack Kinking. *International Journal of Solids and Structures*, Vol. 17, 1981, pp. 107-114.

31. Karihaloo, B.L., Keer, L.M., and Nemat-Nasser, S., Crack Kinking under Non-Symmetric Loading. Engineering Fracture Mechanics, Vol. 13, 1980, pp. 879-888.
32. Sih, G.C., A Special Theory of Crack Propagation. Methods of Analysis and Solutions of Crack Propagation, Vol. 1, G.C. Sih (Ed.), Noordhoff Inter. Publishing, 1973, Leyden, pp. 21-45.
33. Theocaris, P.S. and Andrianopoulos, N.P., A Modified Strain Energy Density Criterion Applied to Crack Propagation. *Journal of Applied Mechanics*, Vol. 49, 1982, pp. 81-86.
34. Swenson, D.V. and Ingraffea, A.R., Modeling Mixed-Mode Dynamic Propagation Using Finite Elements: Theory and Applications. *Computational Mechanics*, Vol. 3, 1988, pp. 381-397.
35. Dadkhah, M.S., Dynamic Fracture Under the Influence of Biaxial State of Stress. Master's Thesis, Mech. Eng., University of Washington, 1984.
36. Yoffe, E.H., The Moving Griffith Crack. *Philosophical Magazine*, Vol. 42, 1951, pp. 739-750.
37. Williams, J.G. and Ewing, P.D., Fracture under Complex Stress—The Angled Crack Problem. *International Journal of Fracture Mechanics*, Vol. 8, 1972, pp. 441-446.
38. Finnie, I. and Saith A., A Note on the Angled Crack Problem and the Directional Stability of Crack. *International Journal of Fracture Mechanics*, Vol. 9, 1973, pp. 484-486.
39. Streit, R. and Finnie, I., An Experimental Investigation of Crack-Path Directional Stability. *Experimental Mechanics*, Vol. 20, No. 1, 1980, pp. 17-23.
40. Achenbach, J.D. and Nuismer, R., Fracture Generated by a Dilatational Wave. *International Journal of Fracture*, Vol. 7, 1971, pp. 77-88.
41. Ma, C-C, Initiation, Propagation, and Kinking of an In-Plane Crack. *Journal of Applied Mechanics*, Vol. 55, 1988, pp. 587-595.
42. Sumi, Y., Computational Crack Path Prediction. *Theoretical and Applied Fracture Mechanics*, Vol. 4, 1985, pp. 149-156.
43. Swift, T., Development of the Fail-Safe Design Feature of the DC-10. *Damage Tolerance in Aircraft Structures*, ASTM STP 486, American Society for Testing and Materials, 1970, pp. 164-214.
44. Dawicke, D.S., Poe, C.C., Jr., Newman, J.C., Jr., and Harris, C.E., An Evaluation of The Pressure Proof Test Concept for Thin Sheet 2024-T3. *Theoretical and Applied Fracture Mechanics*, Vol. 4, 1990, pp. 101-116.
45. Elber, W., Fatigue Crack Closure under Cyclic Tension. *Engineering Fracture Mechanics*, Vol. 2, 1970, No. 1, pp. 37-45.
46. Elber, W., The Significance of Fatigue Crack Closure. *Damage Tolerance in Aircraft Structures*, ASTM STP 486, American Society for Testing and Materials, 1971, pp. 230-242.

47. Mayville, R.A. and Warren, T.J., A Laboratory Study of Fracture in the Presence of Lap Splice Multiple Site Damage. Structural Integrity of Aging Airplanes, Proceedings of International Workshop on Structural Integrity of Aging Airplanes, S.N. Atluri, S.G. Sampath, and P. Tong, (Eds.), Springer-Verlag, 1991, pp. 263-274.
48. Jones, R., Rees, D., and Kaye, R., Stress Analysis of Fuselage Lapjoint. Durability of Metal Aircraft Structures, Proceedings of the International Workshop on Structural Integrity of Aging Airplanes, S.N. Atluri, C.E. Harris, A. Hoggard, N. Miller, and S.G. Sampath, (Eds.), Atlanta Technological Publications, Atlanta, GA, 1992, pp. 118-131.
49. Schijve, J., Multiple-Site Damage Fatigue of Riveted Joints. Durability of Metal Aircraft Structures, Proceedings of the International Workshop on Structural Integrity of Aging Airplanes, S.N. Atluri, C.E. Harris, A. Hoggard, N. Miller, and S.G. Sampath, (Eds.), Atlanta Technological Publications, Atlanta, GA, 1992, pp. 118-131.
50. Molent, L., and Jones, R., Crack Growth and Repair of Multi-Site Damage of Fuselage Lap Joints. *Engineering Fracture Mechanics*, Vol. 44, No. 4, 1993, pp. 627-637.
51. Swift, T., Repairs to Damage Tolerant Aircraft. Structural Integrity of Aging Airplanes, Proceedings of International Workshop on Structural Integrity of Aging Airplanes, S.N. Atluri, S.G. Sampath, and P. Tong, (Eds.), Springer-Verlag, 1991, pp. 433-484.
52. Moukawsher E.J., Neussel, M.A., and Grant, A.F., Jr., Analysis of Panels with Multiple Site Damage. AIAA Paper No. 94-1459, 1994.
53. Samavedam, G. and Hoadley, D., Fracture and Fatigue Strength Evaluation of Multiple Site Damaged Aircraft Fuselage—Curved Panel Testing and Analysis. U.S. Department of Transportation, Federal Aviation Administration Technical Center, DTS-9024, 1991.
54. Hoggard, A.W., Maintaining the Safety of an Aging Fleet of Aircraft. Proceedings of the 1991 International Conference on Aging Aircraft and Structural Airworthiness, C.E. Harris (Ed.), NASA Conference Publication 3160, 1991, pp. 49-65.
55. Brandecker, B. and Hilgert, R., A-320 Full-Scale Structural Testing for Fatigue and Damage Tolerance Certification of Metallic and Composite Structure. ICAS-88-5.8, pp. 1244-1256.
56. Maclin, J.M., Performance of Fuselage Pressure Structure. *Proceedings of the 1991 International Conference on Aging Aircraft and Structural Airworthiness*, C.E. Harris (Ed.), NASA Conference Publication 3160, 1991, pp. 67-74.
57. Miller, M., Gruber, M.L., Wilkins, K.E., and Worden, R.E., Full-Scale Testing and Analysis of Fuselage Structures. Proceedings of FAA/NASA International Symposium on Advanced Structural Integrity Methods for Airframe Durability and Damage Tolerance, C.E. Harris (Ed.), NASA Conference Publication 3274, 1994, pp. 481-496.
58. Poe, C.C., Jr., Stress-Intensity Factor for a Cracked Sheet with Riveted and Uniformly Spaced Stringers. NASA TR R-358, 1971.
59. Poe, C.C., Jr., The Effect of Broken Stringers on the Stress Intensity Factor for a Uniformly Stiffened Sheet Containing a Crack, NASA TM X-71947, 1973.
60. Vlieger, H., The Residual Strength Characteristics of Stiffened Panels Containing Fracture Cracks. *Engineering Fracture Mechanics*, Vol. 5, 1974, pp. 447-477.

61. Swift, T., Damage Tolerance Analysis of Redundant Structures. Fracture Mechanics Design Methodology, AGARD-LS-97, 1979.
62. Swift, T., Important Considerations in Commercial Aircraft Damage Tolerance. *International Journal of Vehicle Design*, Vol. 7, 1986, pp. 264-287.
63. Nishimura, T., Stress Intensity Factors for a Cracked Stiffened Sheet with Cracked Stiffeners. *Journal of Engineering Materials and Technology*, Vol. 113, 1991, pp. 119-124.
64. Nishimura, T., Stress Intensity Factors of Multiple Cracked Sheet with Riveted Stiffeners. *Journal of Engineering Materials and Technology*, Vol. 113, 1991, pp. 280-284.
65. Harris, C.E., NASA Airframe Structure Integrity Program. Structural Integrity of Aging Airplanes, Proceedings of International Workshop on Structural Integrity of Aging Airplanes, S.N. Atluri, S.G. Sampath, and P. Tong, (Eds.), Springer-Verlag, 1991, pp. 141-152.
66. Raju, I.S. and Newman, J.C., Jr., Stress-Intensity Factors for a Wide Range of Semi-Elliptical Surface Cracks in Finite-Thickness Plates. *Engineering Fracture Mechanics*, Vol. 11, 1979, pp. 817-829.
67. Shivakumar, K.N., Tan, P.W., and Newman, J.C., Jr., A Virtual Crack-Closure Technique for Calculating Stress-Intensity Factors for Cracked Three-Dimensional Bodies. *International Journal of Fracture*, Vol. 36, 1988, pp. R43-R50.
68. Newman, J.C., Jr. and Raju, I.S., Stress-Intensity Factor Equations for Cracks in Three-Dimensional Finite Bodies. *Fracture Mechanics: Fourteenth Symposium, ASTM STP 791*, American Society of Testing and Materials, 1983, pp. 1238-1265.
69. Nikishkov, G.P. and Atluri, S.N., Calculation of Fracture Mechanics Parameters for Arbitrary Three-Dimensional Crack, by the "Equivalent Domain Integral" Method. *International Journal of Numerical Methods in Engineering*, Vol. 24, 1987, pp. 1801-1821.
70. Miller, M., Kaelber, K.N., and Worden, R.E., Finite Element Analysis of Pressure Vessel Panels. Durability of Metal Aircraft Structures, Proceedings of the International Workshop on Structural Integrity of Aging Airplanes, S.N. Atluri, C.E. Harris, A. Hoggard, N. Miller, and S.G. Sampath, (Eds.), Atlanta Technological Publications, Atlanta, GA, 1992, pp. 337-348.
71. Atluri, S.N. and Tong, P., Computational Schemes for Integrity Analyses of Fuselage Panels in Aging Airplanes. Durability of Metal Aircraft Structures, Proceedings of the International Workshop on Structural Integrity of Aging Airplanes, S.N. Atluri, C.E. Harris, A. Hoggard, N. Miller, and S.G. Sampath, (Eds.), Atlanta Technological Publications, Atlanta, GA, 1992, pp. 15-34.
72. O'Donoghue, P.E., Nishioka, T., and Atluri, S.N., Multiple Surface Flaws in Pressure Vessels. *Engineering Fracture Mechanics*, Vol. 20, 1984, pp. 545-560.
73. Park, J.H. and Atluri, S.N., Fatigue Growth of Multiple Cracks Near a Row of Fastener-Holes in a Fuselage Lap Joint. *Computational Mechanics*, 1993, 13, pp. 189-203.

74. Kobayashi, A.S., Hybrid Experimental-Numerical Stress Analysis. Handbook on Experimental Mechanics—Second Revised Edition, A.S. Kobayashi (Ed.), VCH Publishers, Inc., 1993, pp. 751-784.
75. Kobayashi, A.S., Emery, A.F., Love, W.J., Chao, Y.H., and Johansson, O., Ductile Crack Bifurcation and Arrest in Pressurized Pipe. *Fracture Mechanics, Nineteenth Symposium, ASTM STP 969*, American Society for Testing and Materials, 1988, pp. 441-465.
76. Kobayashi, A.S., Emery, A.F., Love, W.J., and Chao, Y.H., Subsize Experiments and Numerical Modeling of Axial Rupture of Gas Transmission Lines. *Journal of Pressure Vessel Technology*, Vol. 110, 1988, pp. 155-160.
77. Arakawa, K., Drinnon, R.H., Jr., Kosai, M., and Kobayashi, A.S., Dynamic Fracture Analysis by Moiré Interferometry. *Experimental Mechanics*, Vol. 31, 1991, pp. 306-309.
78. Lemaitre, J., Turbat, A., and Loubet, R., Fracture Mechanics Analysis of Pressurized Cracked Shallow Shells. *Engineering Fracture Mechanics*, Vol. 9, 1977, pp. 443-460.
79. Chen, D. and Schijve, J., Bulging of Fatigue Cracks in Pressurized Fuselage. *Proceedings of the 16th Symposium of the International Committee on Aeronautical Fatigue (ICAF)*, A. Kobayashi (Ed.), Ryojin and Engineering Materials Advisory Services, 1991.
80. Riks, E., Rankin, C.C., and Brogan, F.A., The Buckling Behavior of a Central Crack in a Plate under Tension. *Engineering Fracture Mechanics*, Vol. 43, No. 4, 1992, pp. 529-548.
81. Rankin, C.C., Brogan, F.A., and Riks, E., Some Computational Tools for the Analysis of Through Cracks in Stiffened Fuselage Shells. *Computational Mechanics*, Vol. 13, 1993, pp. 143-156.
82. Kanninen, M.F. and Popelar, C.H., Advanced Fracture Mechanics, Oxford University Press, 1985.
83. Hui, C.Y. and Zehnder, A.T., A Theory for the Fracture of Thin Plates Subjected to Bending and Twisting Moments. *International Journal of Fracture*, Vol. 61, 1993, pp. 211-229.
84. Ramulu, M., Dynamic Crack Curving and Branching. Ph.D. Thesis, University of Washington, 1982.
85. Rice, J.R. and Johnson, M.A., The Role of Large Crack Tip Geometry Change in Plane Strain Fracture. Inelastic Behavior of Solids, McGraw Hill, 1970, pp. 641-672.
86. Richi, R.O., Knott, J.F., and Rice, J.R., On the Relationship Between Critical Tensile Stress and Fracture Toughness in Mild Steel. *Journal of The Mechanics and Physics of Solids*, Vol. 21, 1973, pp. 395-410.
87. Metal Handbook—1954 Supplement, American Society for Metals, Cleveland, p. 101.
88. Eftis, J., Subramonian, N., and Liebowitz, H., Biaxial Load Effects on the Crack Border Elastic Strain Energy and Strain Energy Rate. *Engineering Fracture Mechanics*, Vol. 9, 1977, pp. 753-764.

89. Pisarenko, G.S., Naumenko, V.P., and Onishchenko, E.E., A Method of Investigating the Fracture of Sheet Materials. *Strength of Materials*, Vol. 14, No. 3, 1982, pp. 275-282.
90. Kosai, M. and Kobayashi, A.S., Axial Crack Propagation and Arrest in Pressurized Fuselage. Structural Integrity of Aging Airplanes, Proceedings of International Workshop on Structural Integrity of Aging Airplanes, S.N. Atluri, S.G. Sampath, and P. Tong, (Eds.), Springer-Verlag, 1991, pp. 225-239.
91. Kosai, M., Kobayashi, A.S., and Ramulu, M., Tear Straps in Airplane Fuselage. Durability of Metal Aircraft Structures, Proceedings of the International Workshop on Structural Integrity of Aging Airplanes, S.N. Atluri, C.E. Harris, A. Hoggard, N. Miller, and S.G. Sampath, (Eds.), Atlanta Technological Publications, Atlanta, GA, 1992, pp. 443-457.
92. Kobayashi, A.S. and Engstrom, W.L., Transient Analysis in Fracturing Aluminum Plate. *Proceedings of JSME 1967 Semi-International Symposium*, 1967, pp. 172-182.
93. Emery, A.F., Perl, M., Love, W.J., and Kobayashi, A.S., The Use of the Split Ring in Modeling of Ductile Axial Crack Extension in Pipes. *Journal of Pressure Vessel Technology*, Vol. 103, 1981, pp. 151-154.
94. Potyondy, D.O., A Software Framework for Simulating Curvilinear Crack Growth in Pressurized Thin Shells, Ph.D. Thesis, Cornell University, 1993.
95. Zehnder, A.T., Viz, M.J., and Ingraffea, A.R., Fatigue Fracture in Thin Plates Subjected to Tensile and Shearing Loads: Crack Tip Fields, J-Integral and Preliminary Experimental Results. *Proceedings of The VII Society for Experimental Mechanics International Congress on Experimental Mechanics*, Las Vegas, Nevada, 1992.

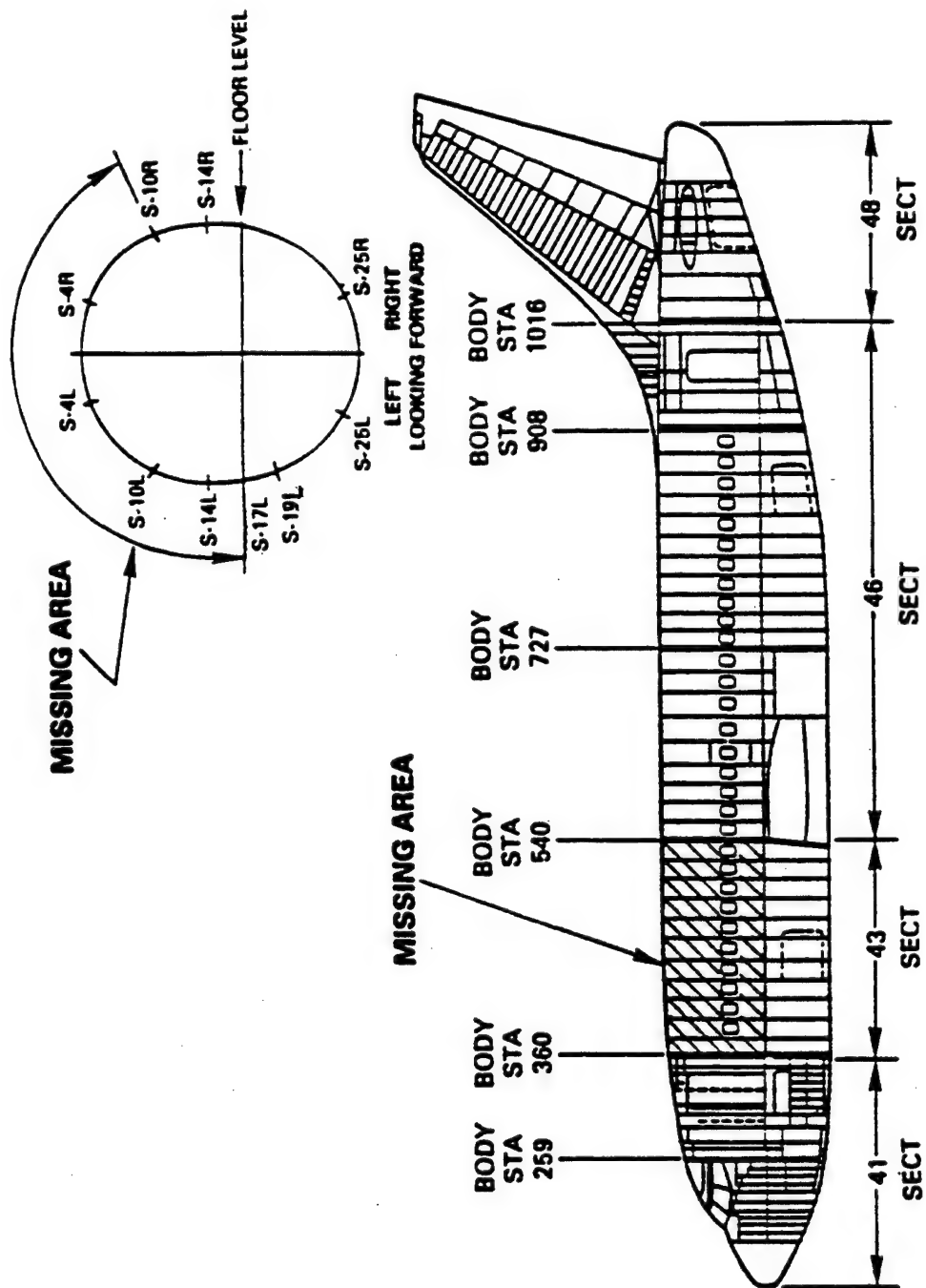


FIGURE 1. ALOHA INCIDENT [1]

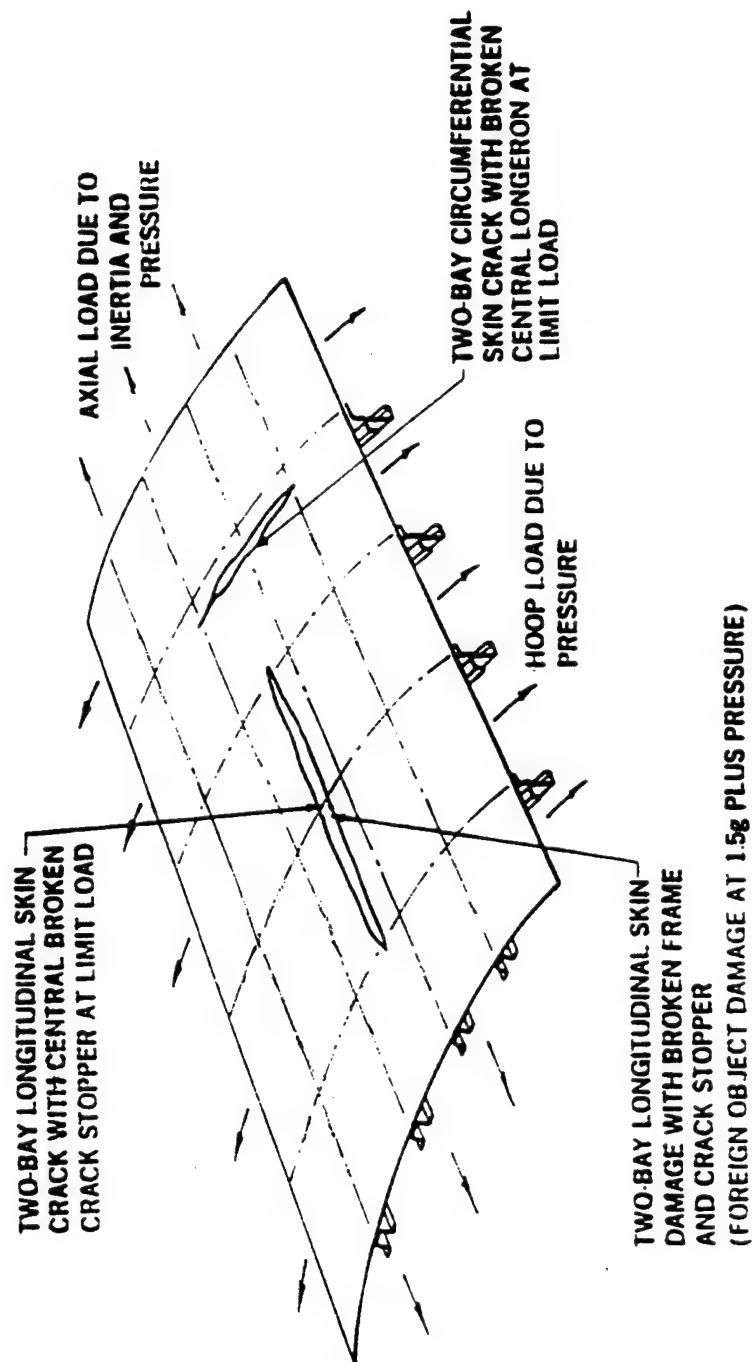


FIGURE 2. FUSELAGE DAMAGE TOLERANCE SIZES FOR STRUCTURAL DESIGN [9]

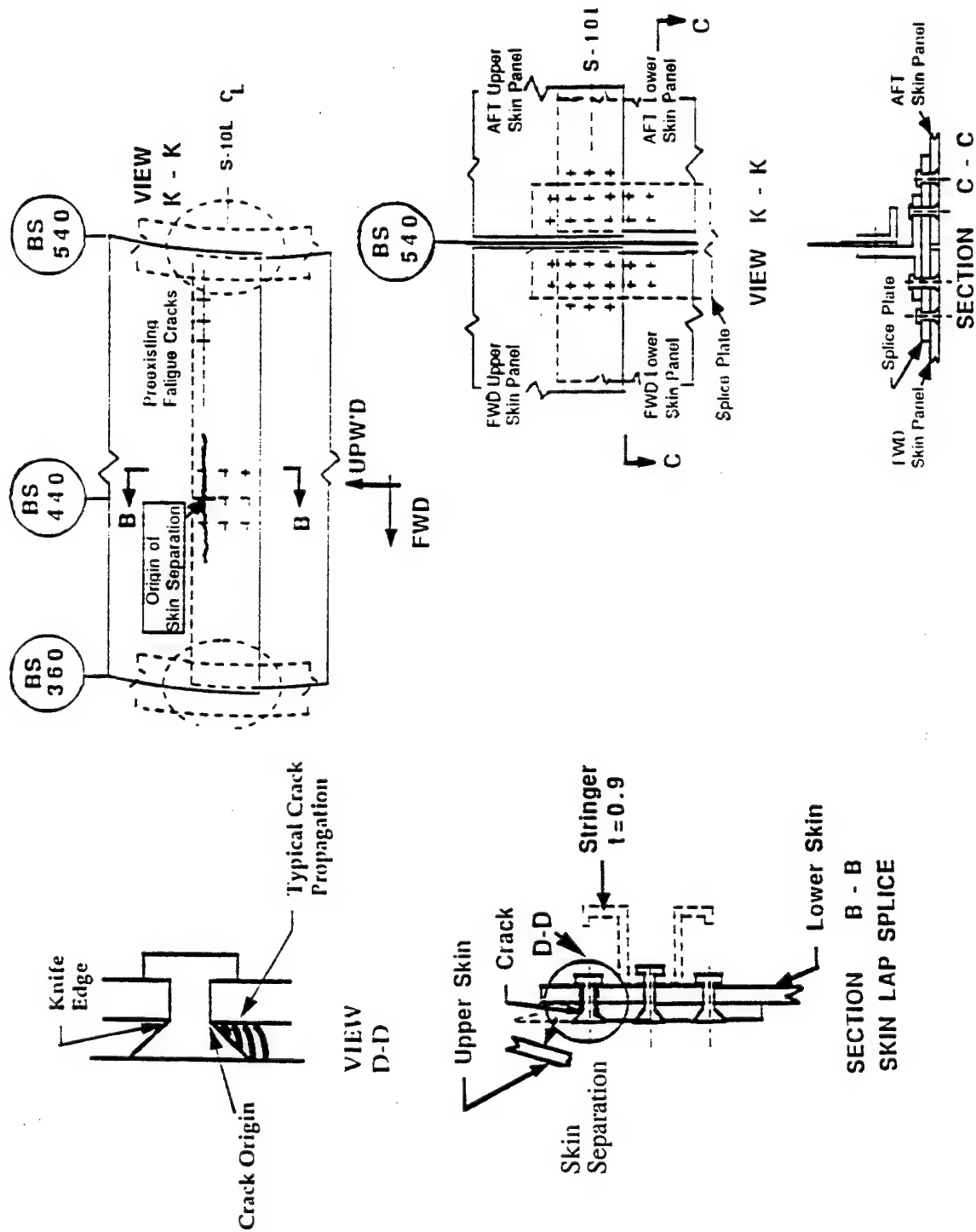
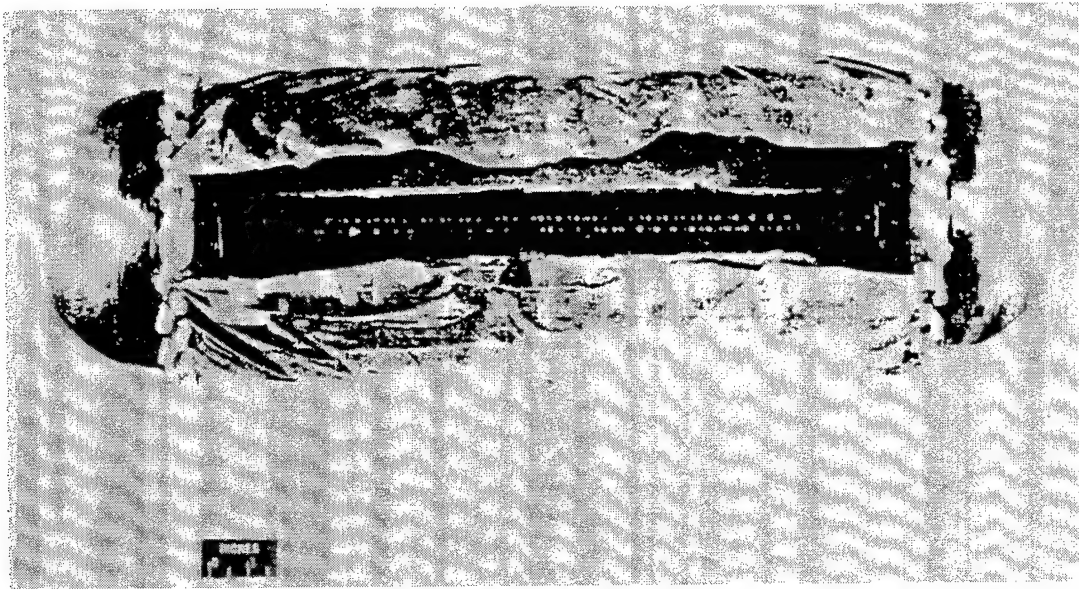
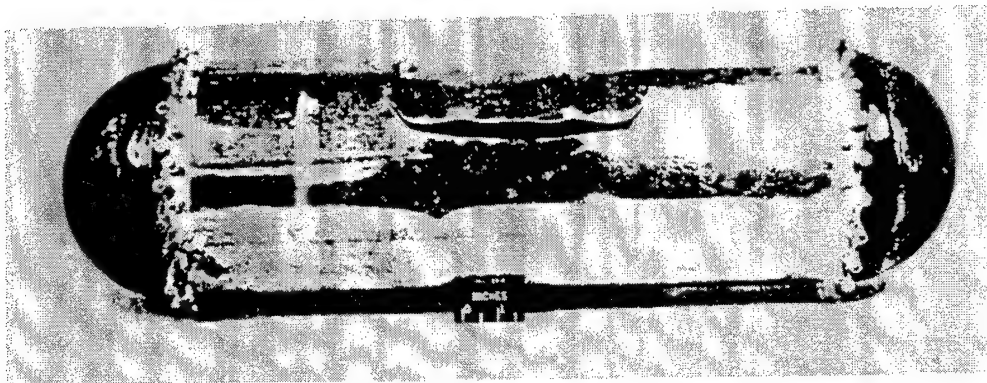


FIGURE 3. SCHEMATIC DRAWING OF TYPICAL SKIN LAP SPLICE



(a) AIR PRESSURIZATION



(b) OIL PRESSURIZATION

FIGURE 4. COMPARISON OF FAILURES OF CYLINDERS PRESSURIZED WITH AIR AND OIL [12]

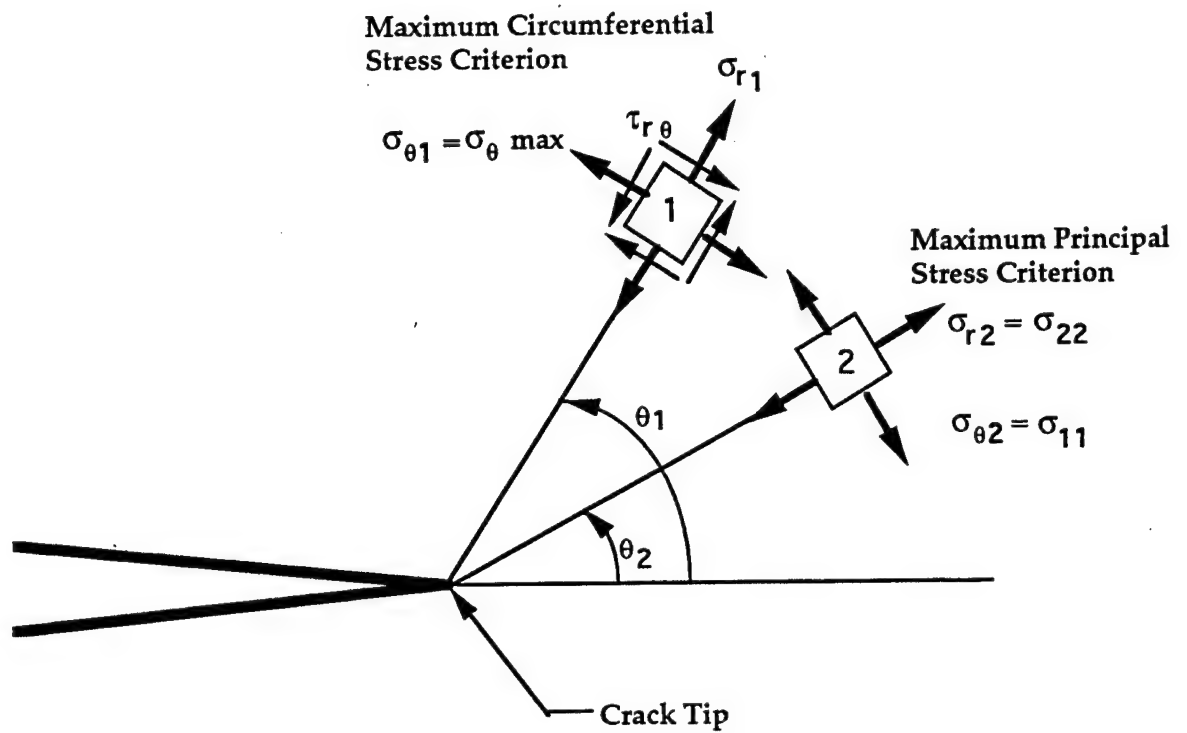


FIGURE 5. MAXIMUM PRINCIPAL AND CIRCUMFERENTIAL STRESS CRITERIA [25]

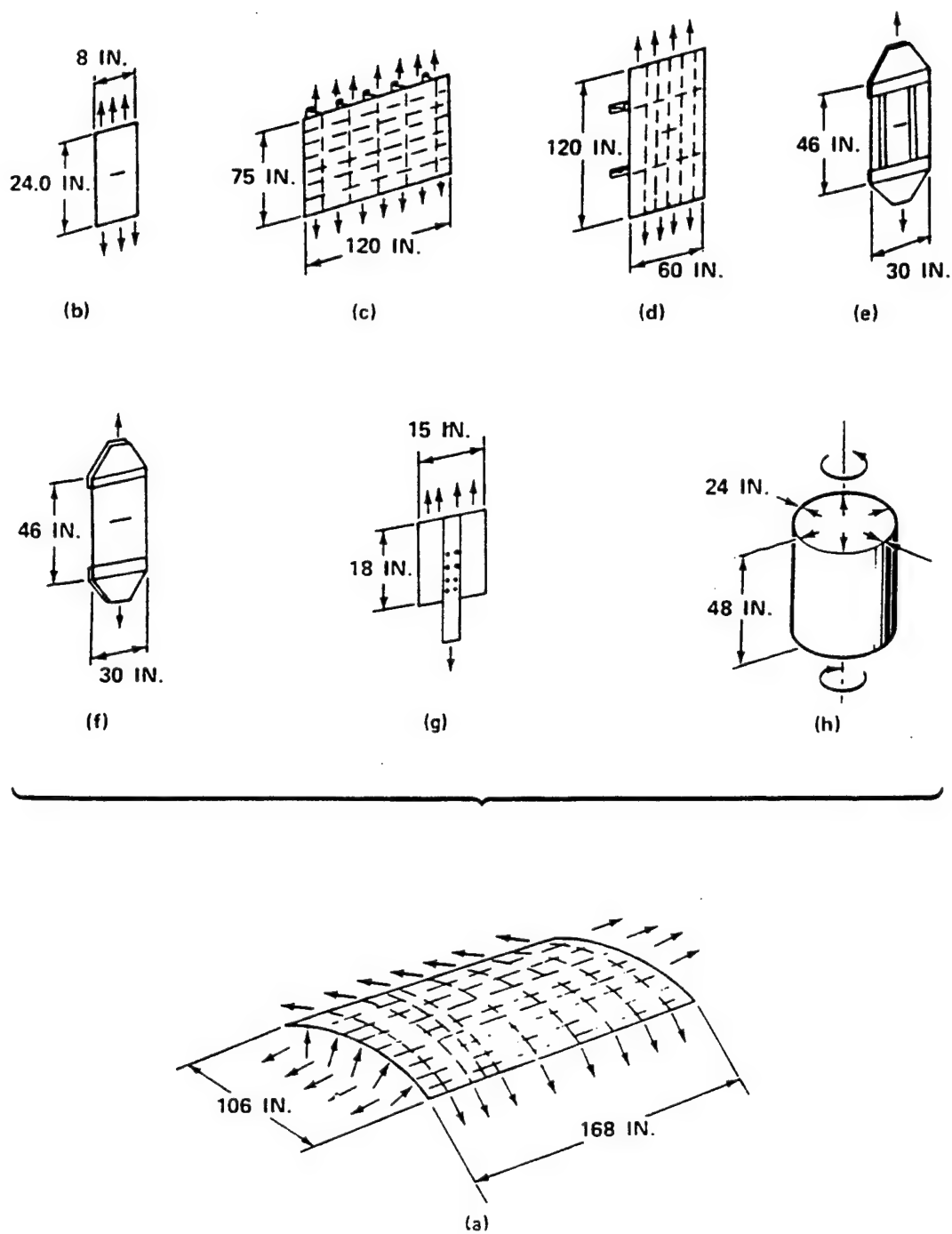


FIGURE 6. FUSELAGE FATIGUE AND FAIL-SAFE DEVELOPMENT TESTS [43]

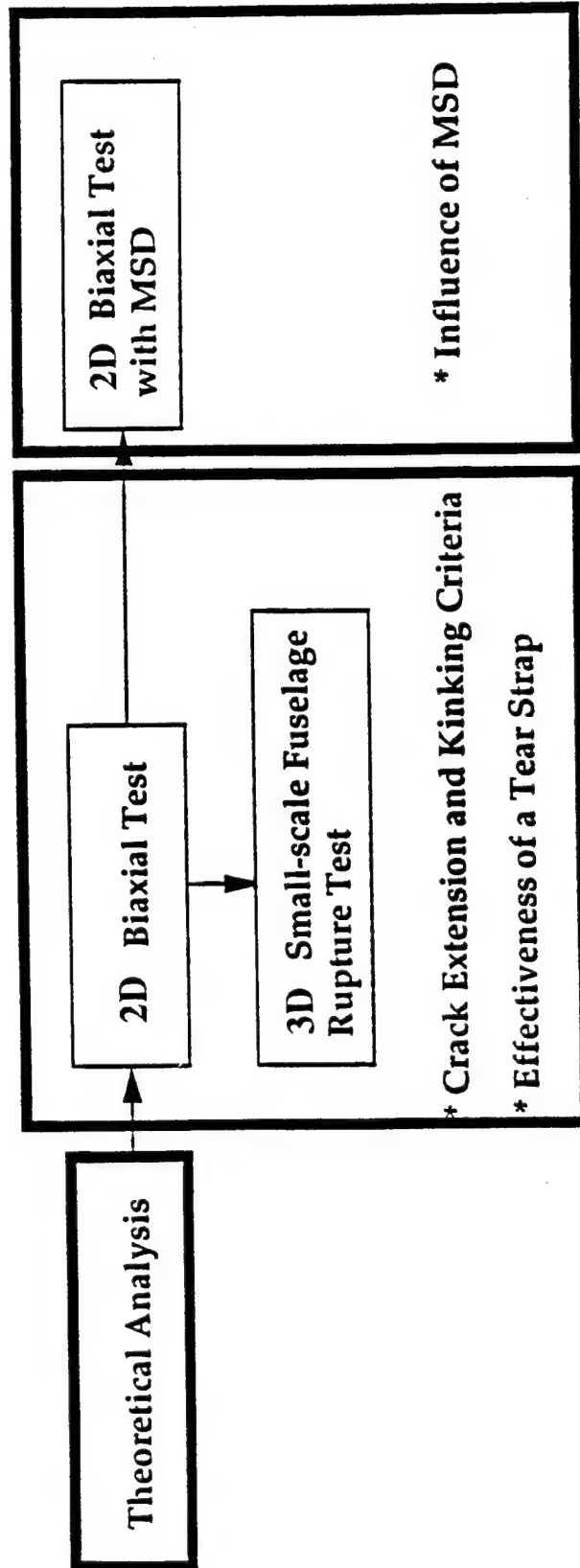


FIGURE 7. FLOW CHART OF METHOD OF APPROACH

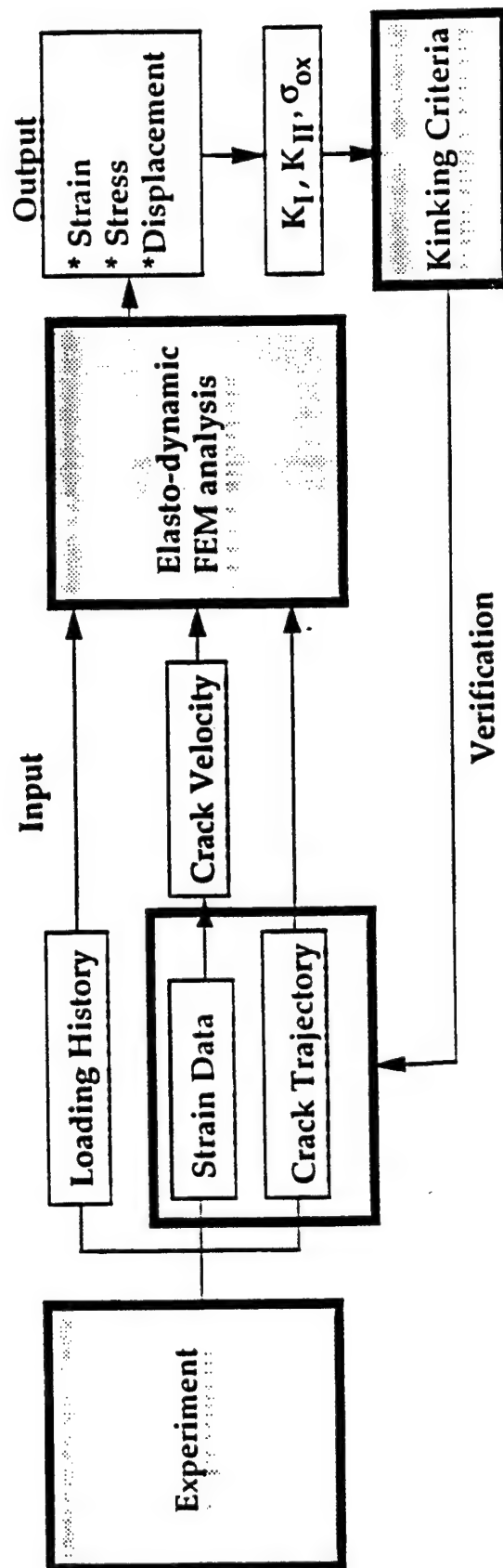


FIGURE 8. FLOW CHART OF HYBRID EXPERIMENTAL-NUMERICAL ANALYSIS

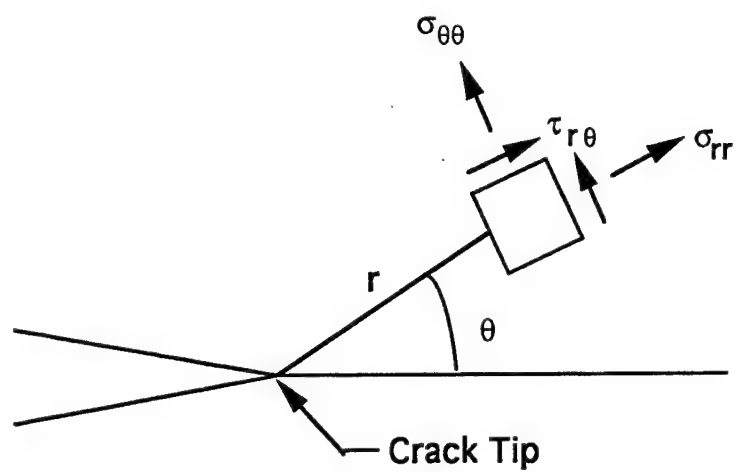


FIGURE 9. POLAR COORDINATES

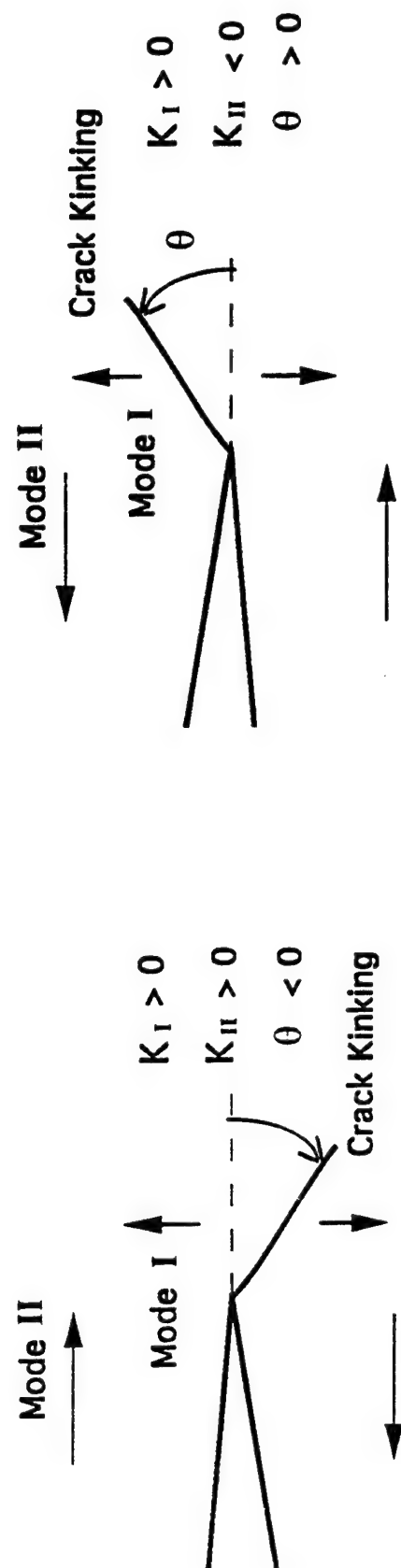


FIGURE 10. CRACK KINKING UNDER MIXED-MODE LOADING

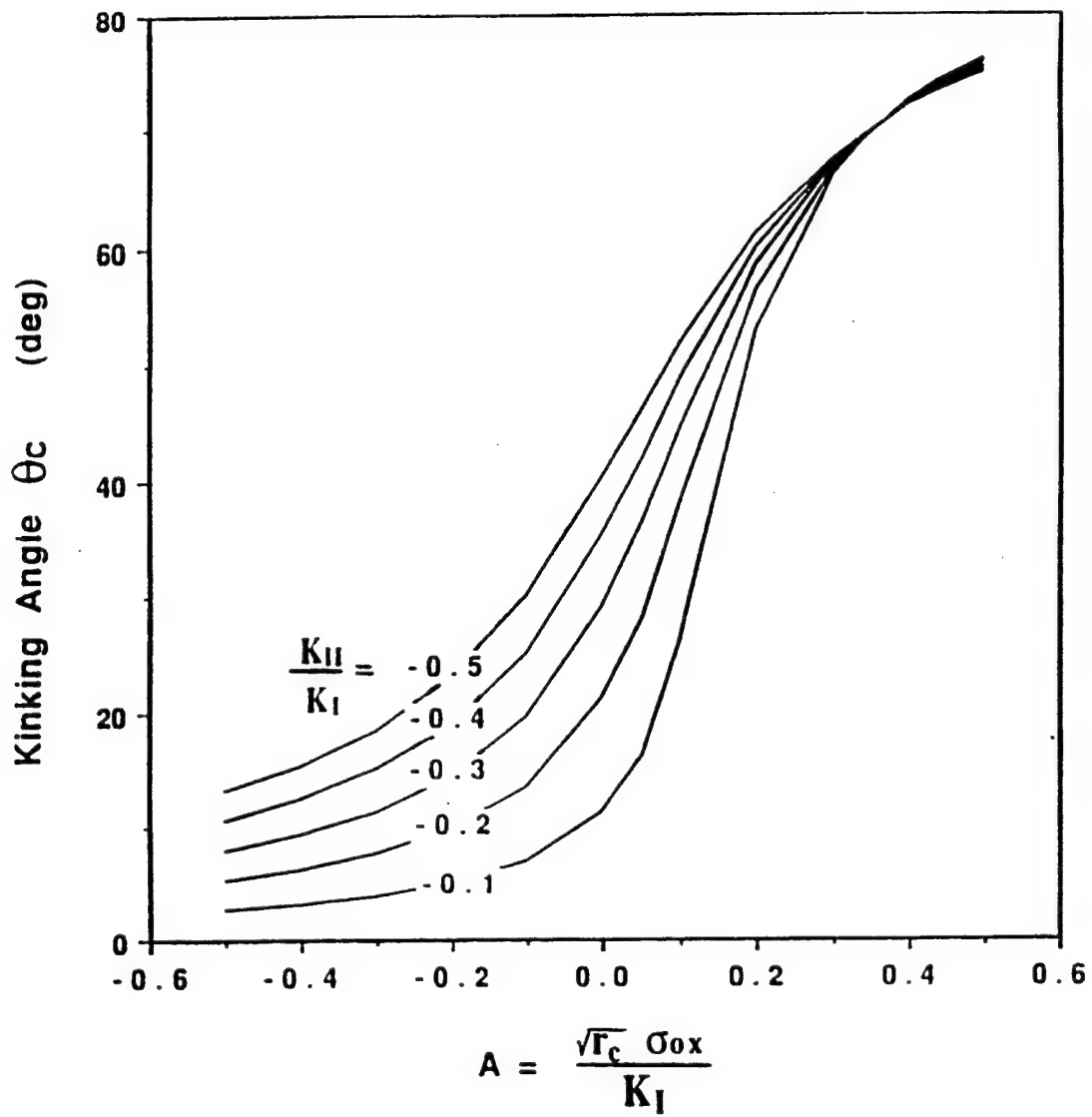


FIGURE 11. σ_{ox} DEPENDENCE OF KINKING ANGLE θ_c

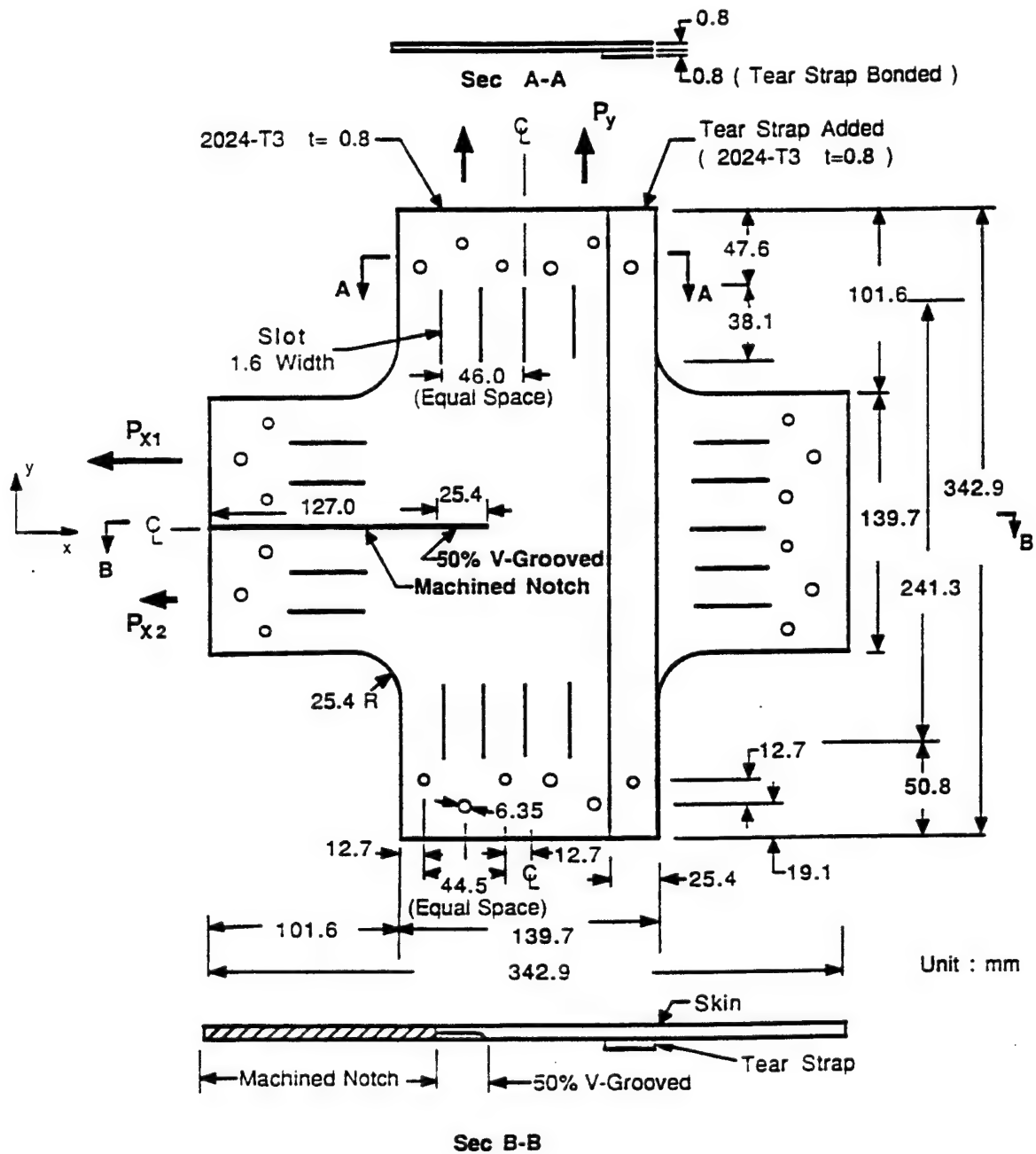


FIGURE 12. ALUMINUM CRUCIFORM SPECIMEN (TYPE MV)

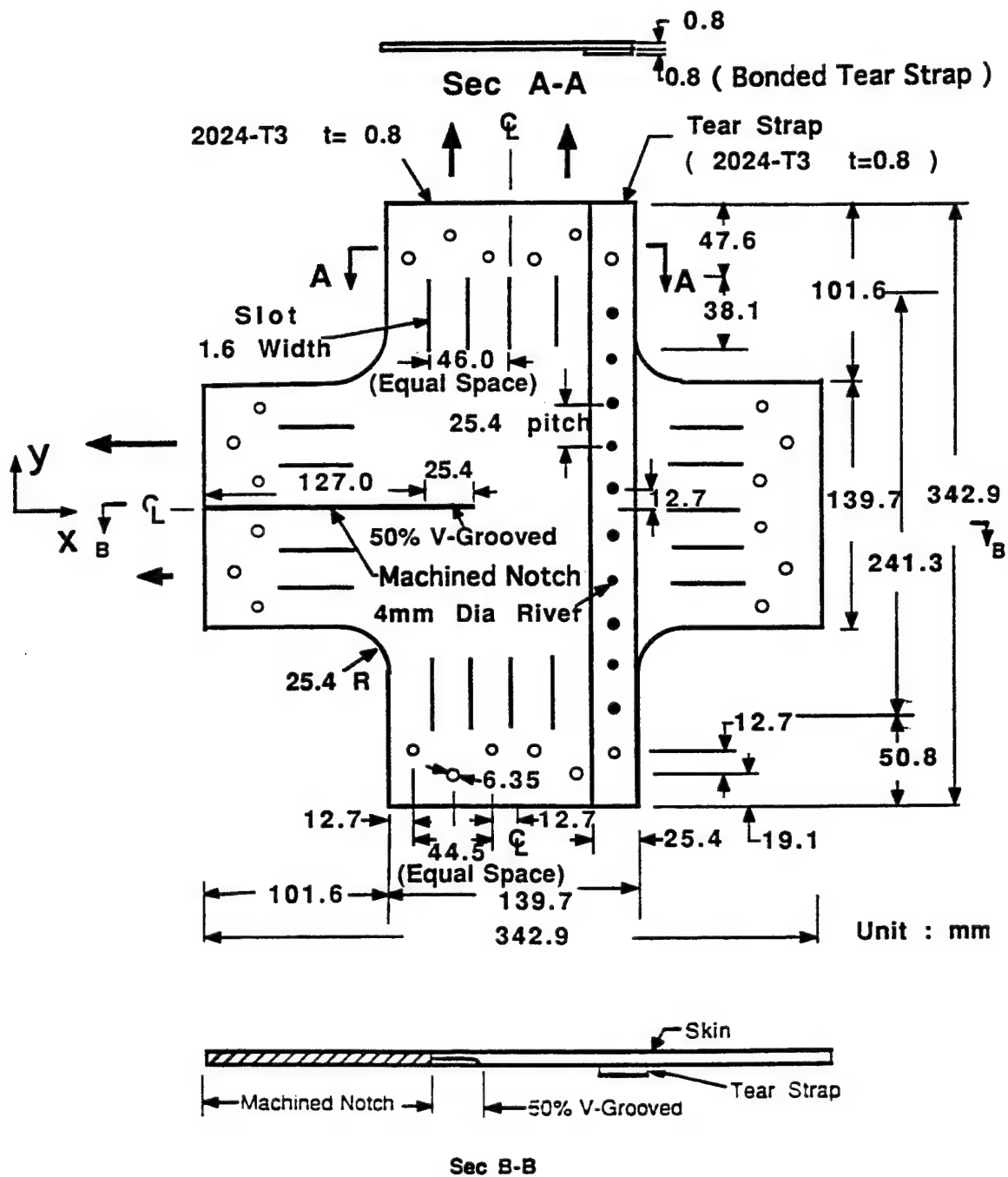


FIGURE 13. ALUMINUM CRUCIFORM SPECIMEN (TYPE MA)

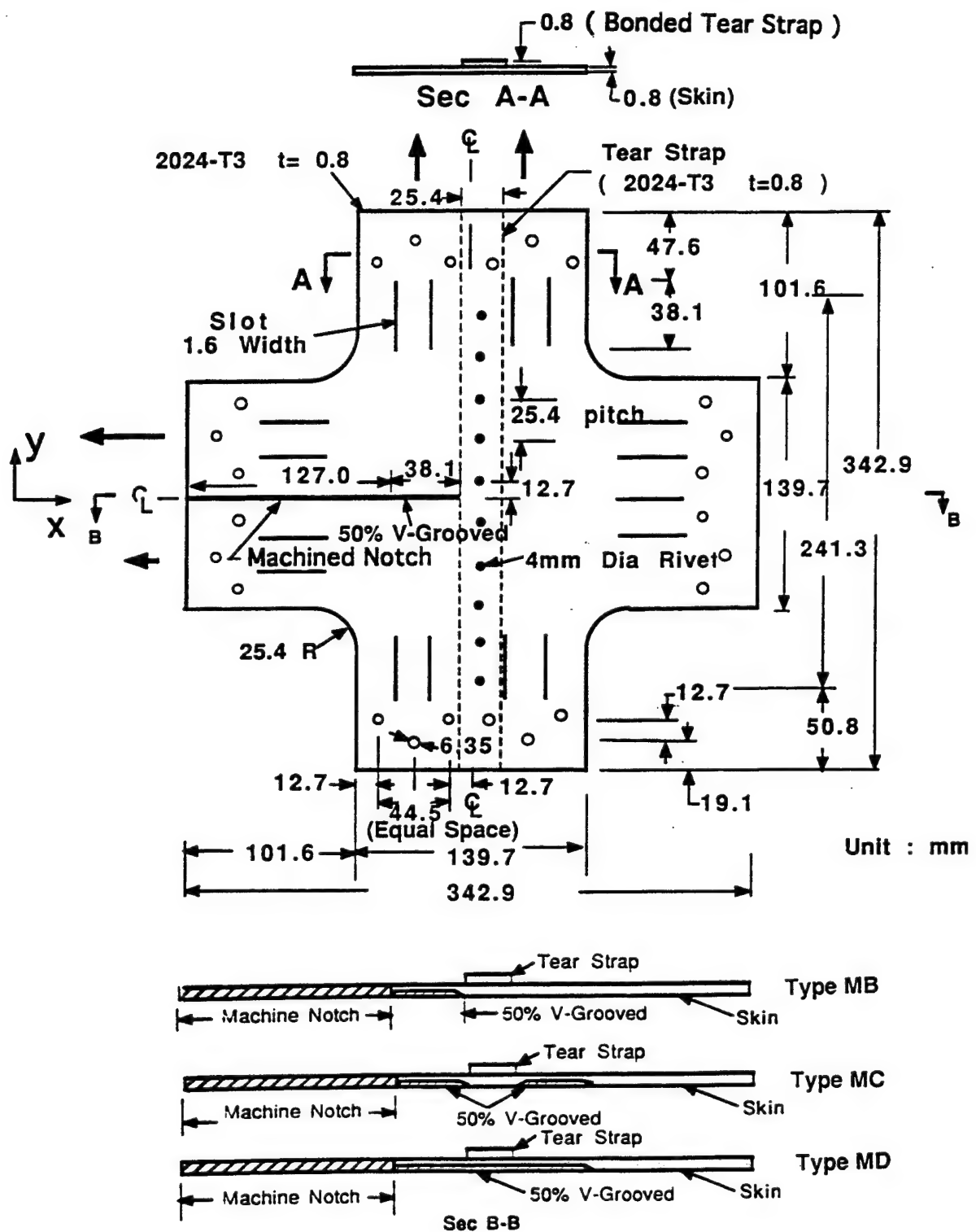


FIGURE 14. ALUMINUM CRUCIFORM SPECIMEN (TYPES MB, MC, AND MD)

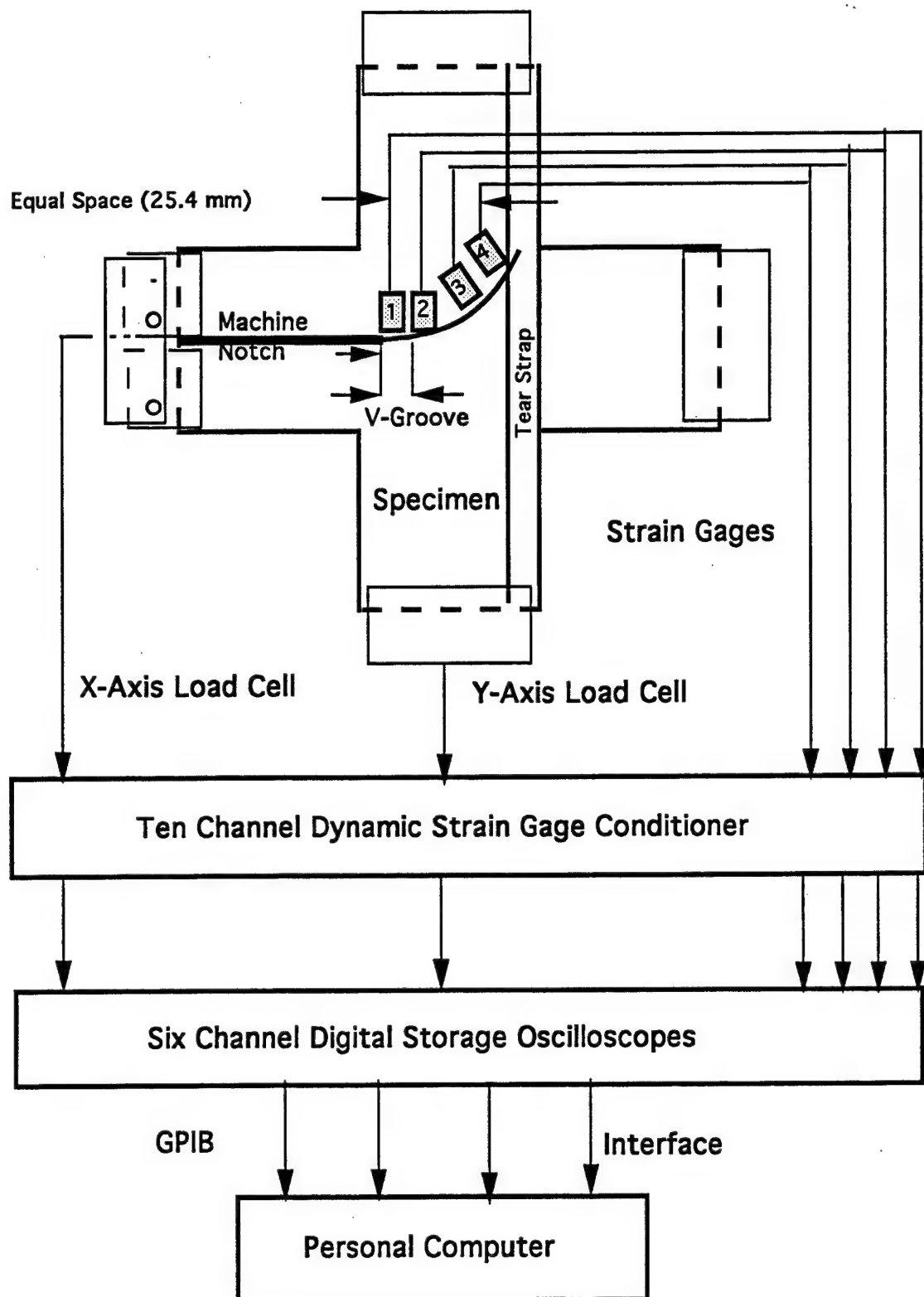


FIGURE 17. SCHEMATICS OF BIAXIAL TEST FACILITY WITH INSTRUMENTATION

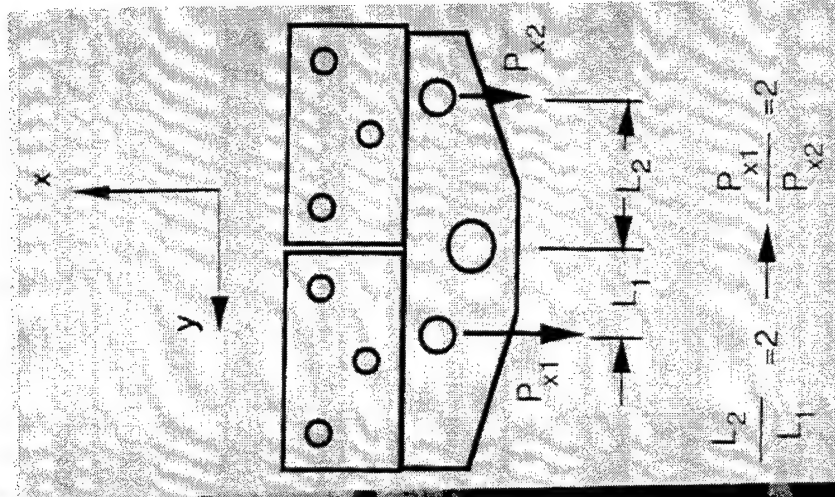
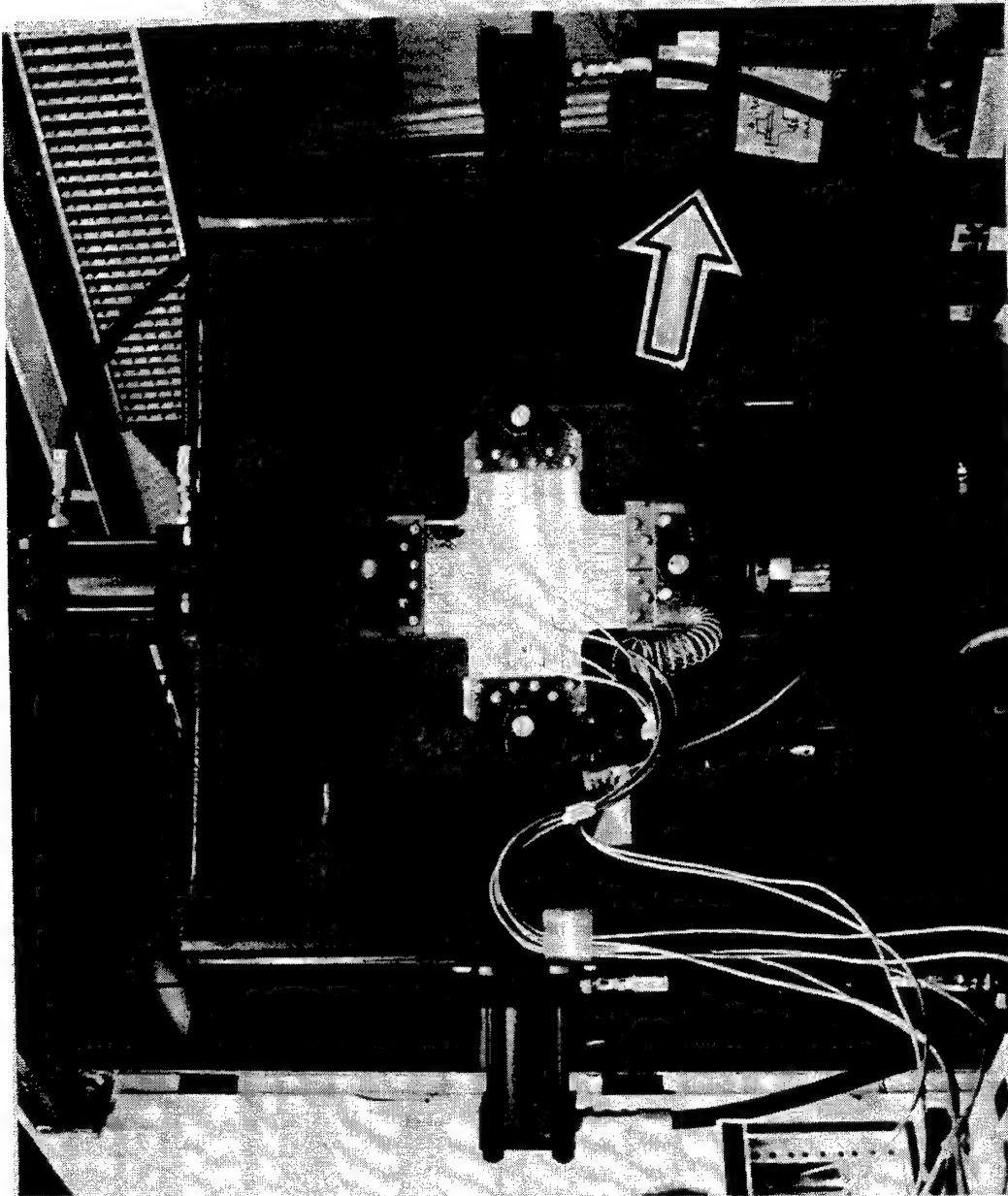


FIGURE 18. BIAXIAL TESTING MACHINE

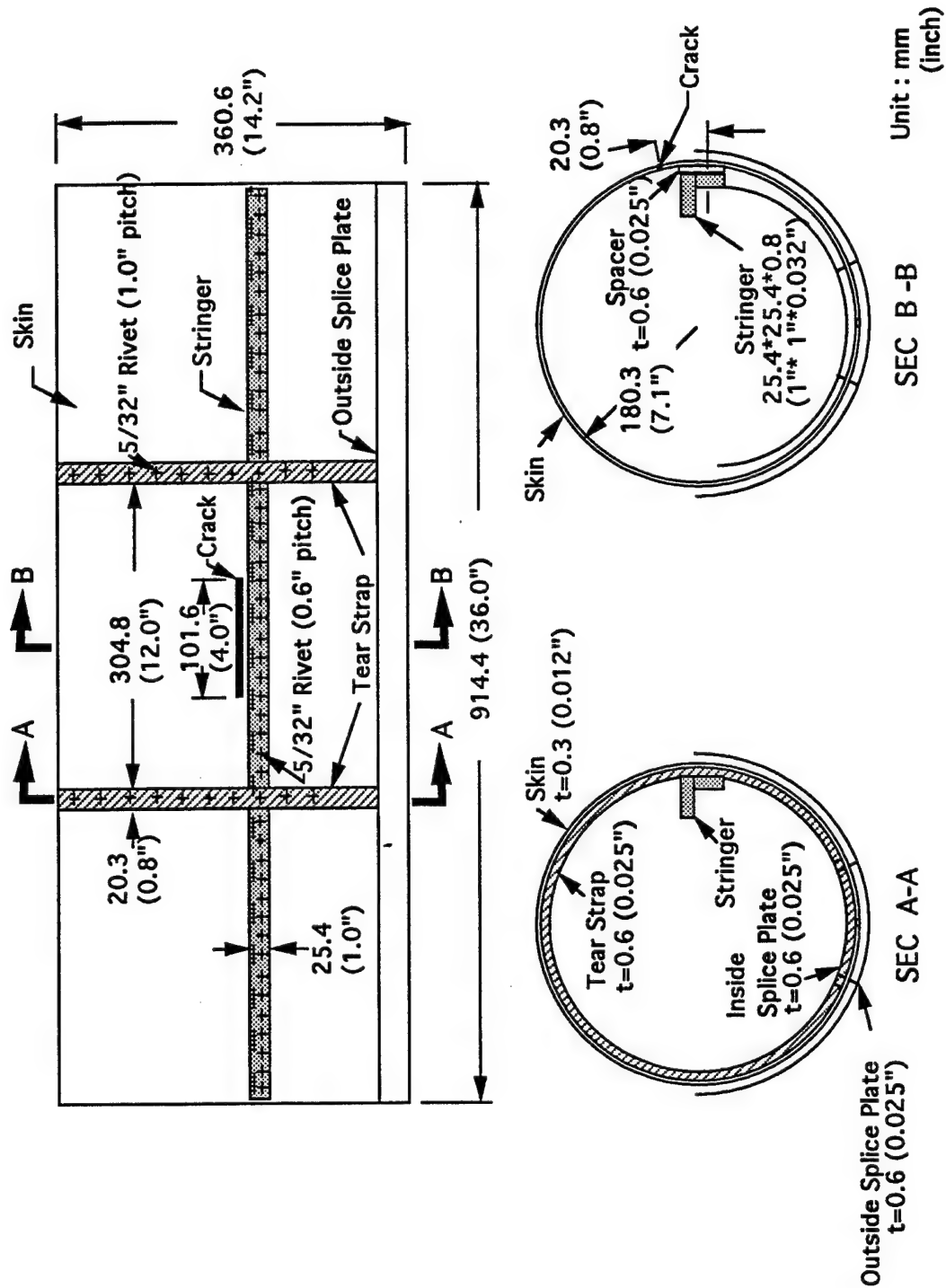


FIGURE 19. SMALL-SCALE MODEL FUSELAGE SPECIMEN (TYPE C-3)

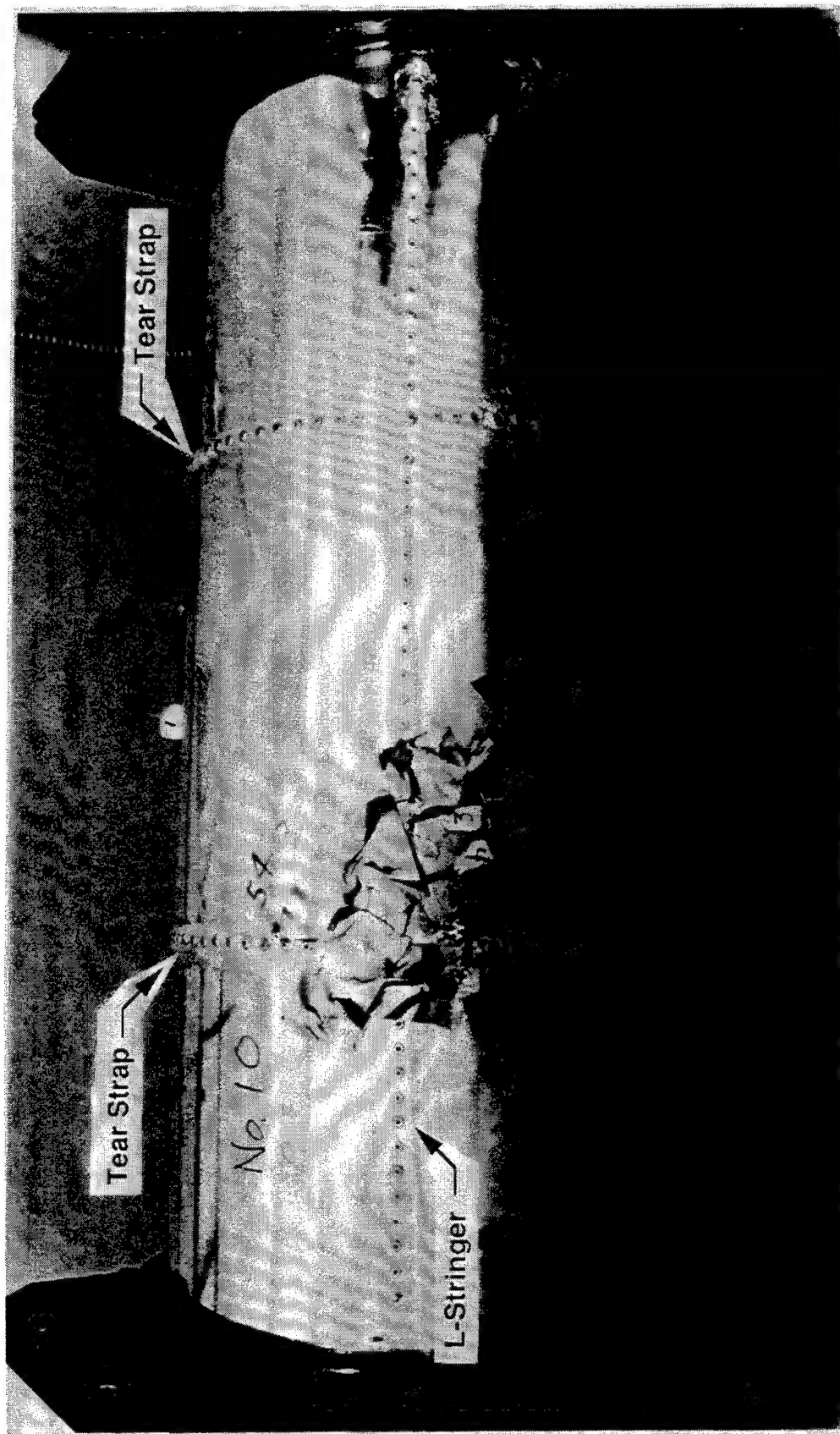


FIGURE 20. OUTSIDE VIEW OF SPECIMEN (TYPE C-3)

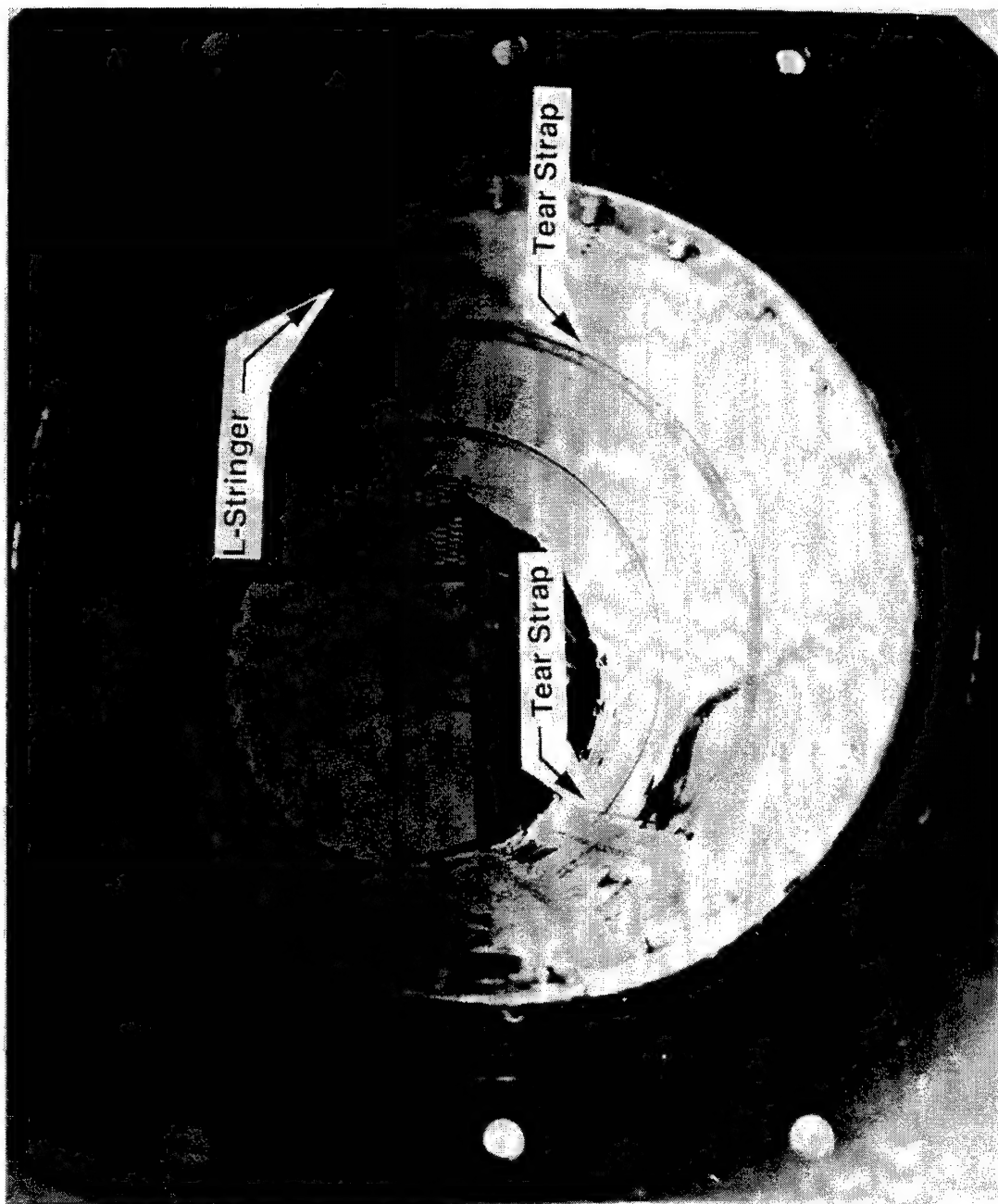


FIGURE 21. INSIDE VIEW OF SPECIMEN (TYPE C-3)

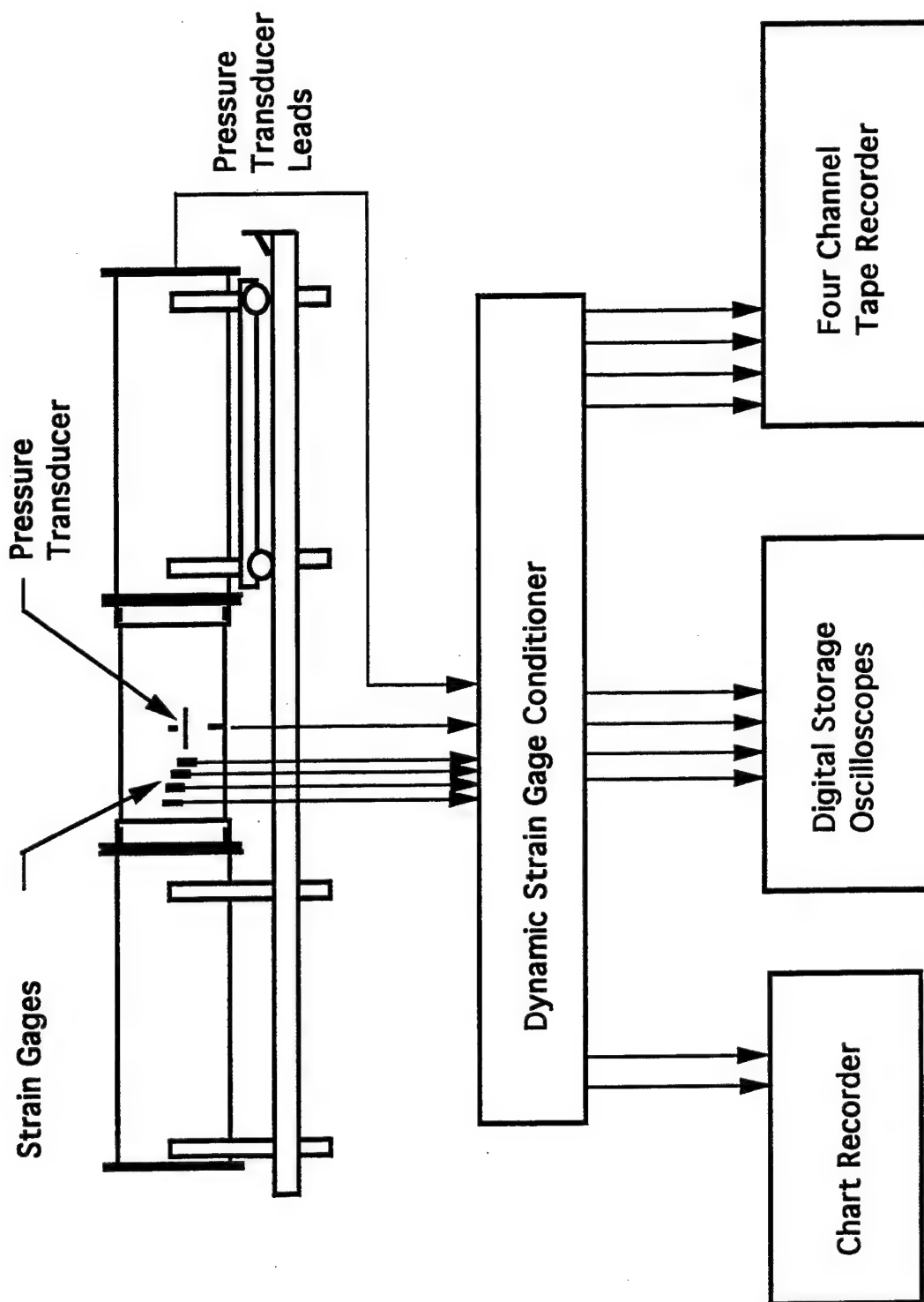


FIGURE 22. SCHEMATIC OF INSTRUMENTATION SETUP FOR SMALL-SCALE CYLINDER TESTS

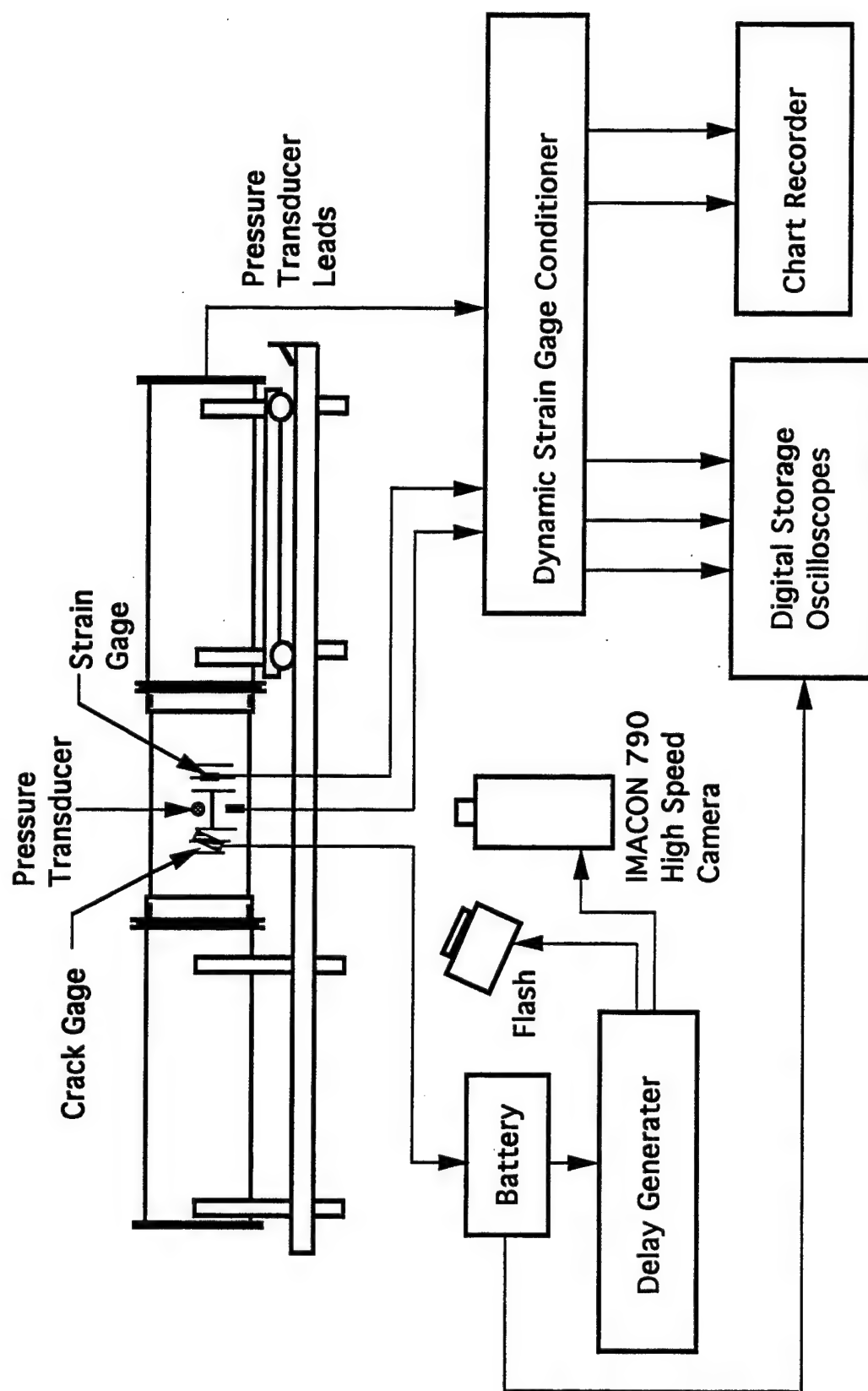


FIGURE 23. SCHEMATIC OF INSTRUMENTATION SETUP FOR IMACON 790

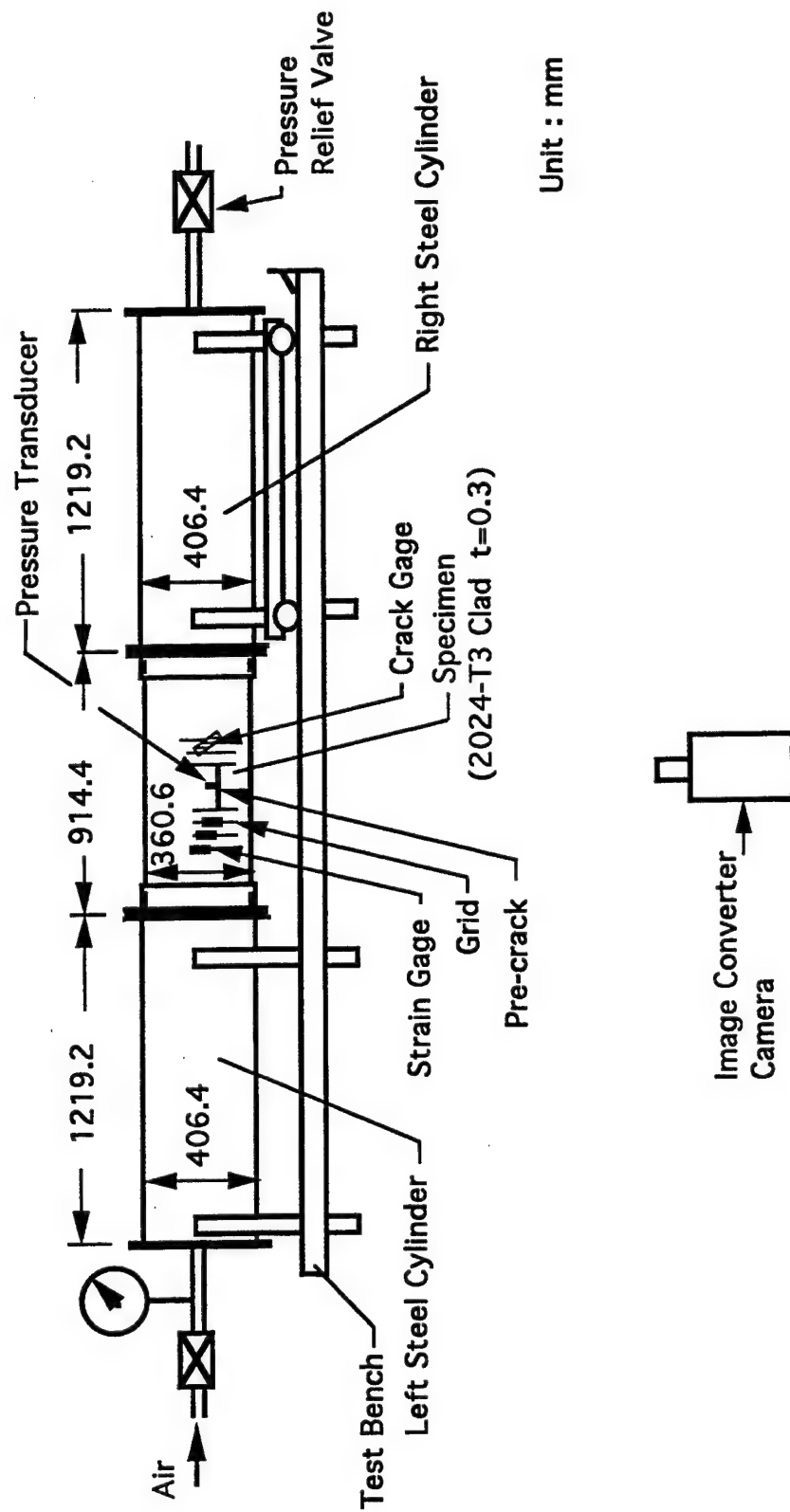


FIGURE 24. SMALL-SCALE FUSELAGE RUPTURE TEST SETUP

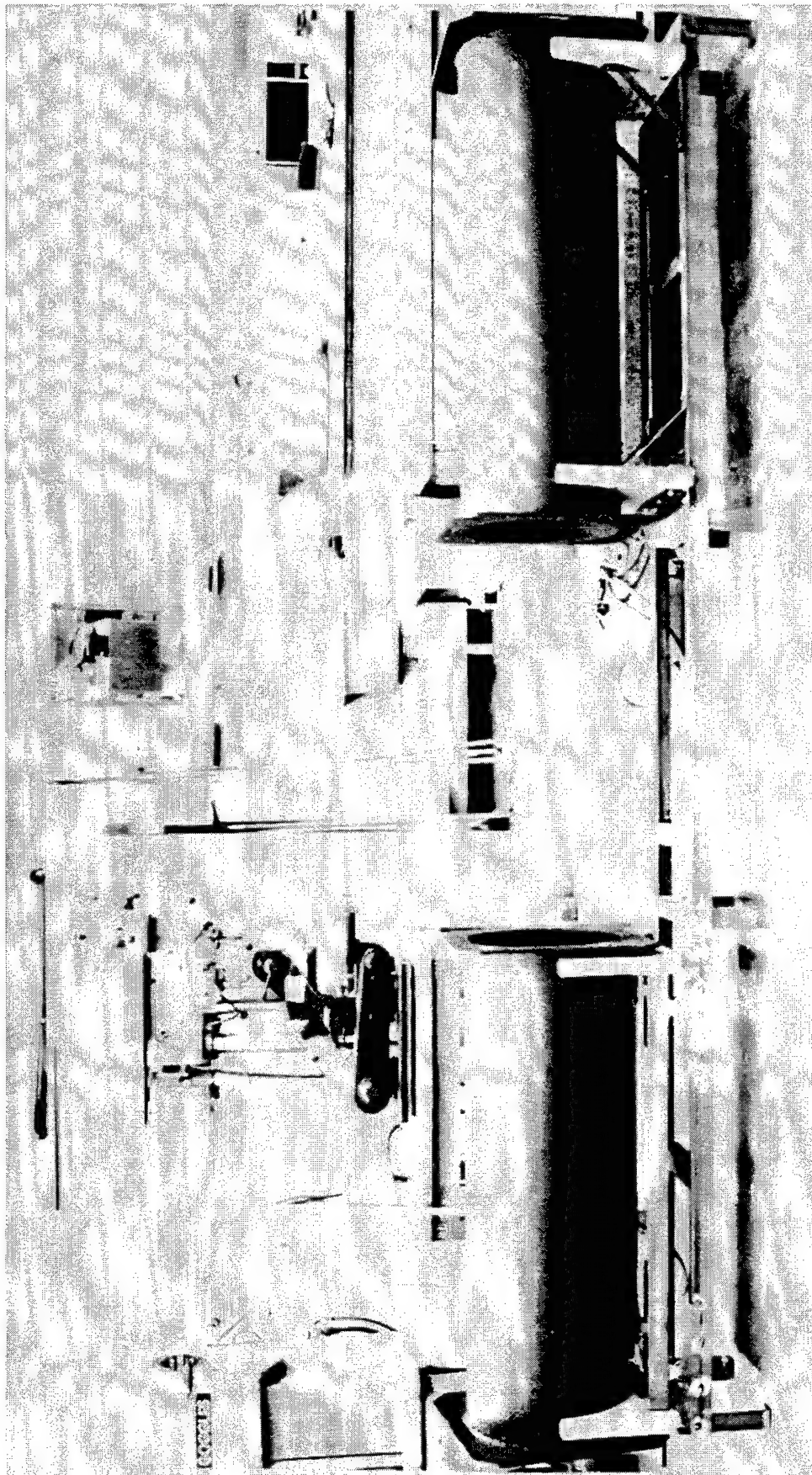


FIGURE 25. SMALL-SCALE FUSELAGE RUPTURE TEST STAND

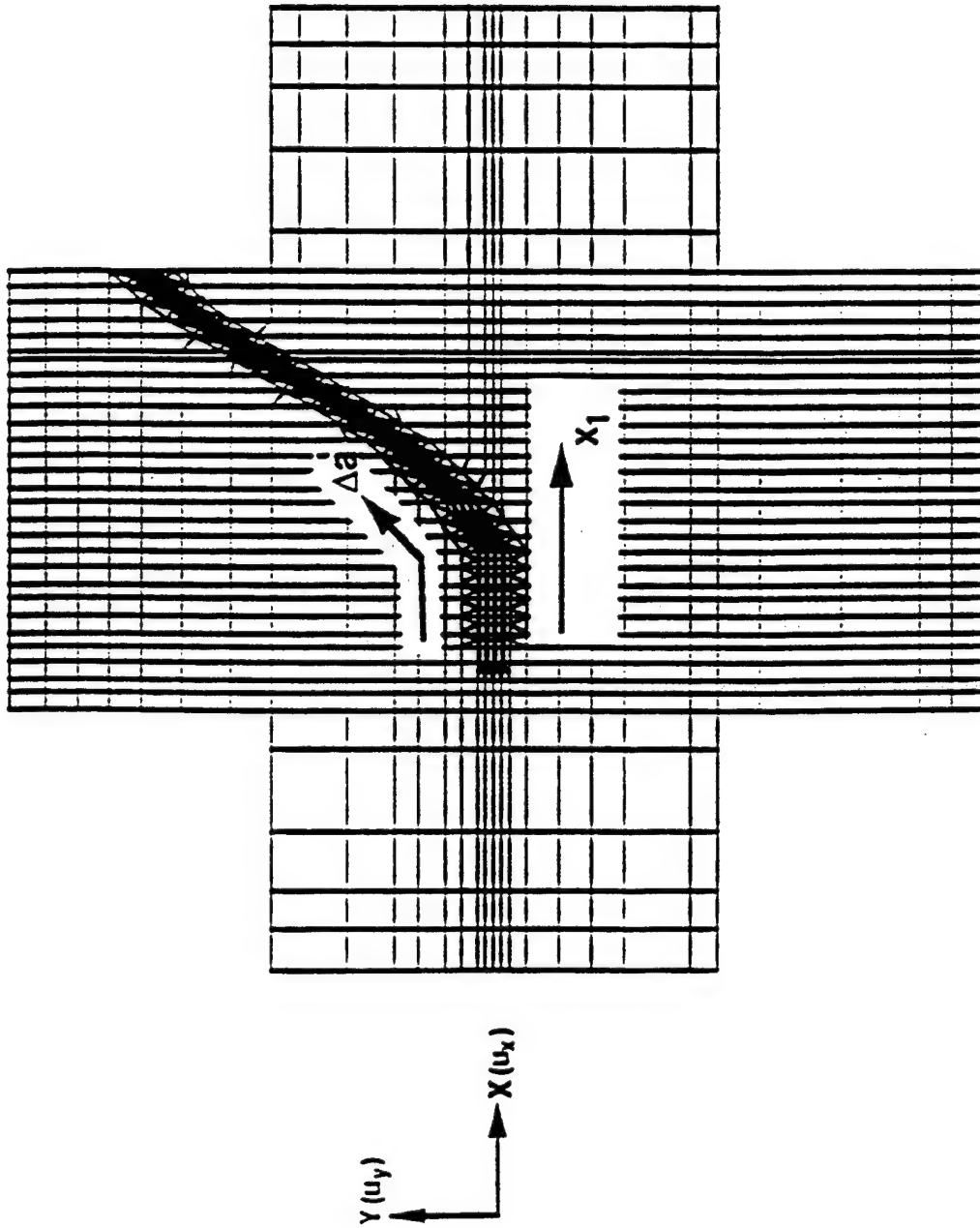


FIGURE 26. TYPICAL FINITE ELEMENT MESH OF BIAXIAL TEST SPECIMEN (TYPE MV)

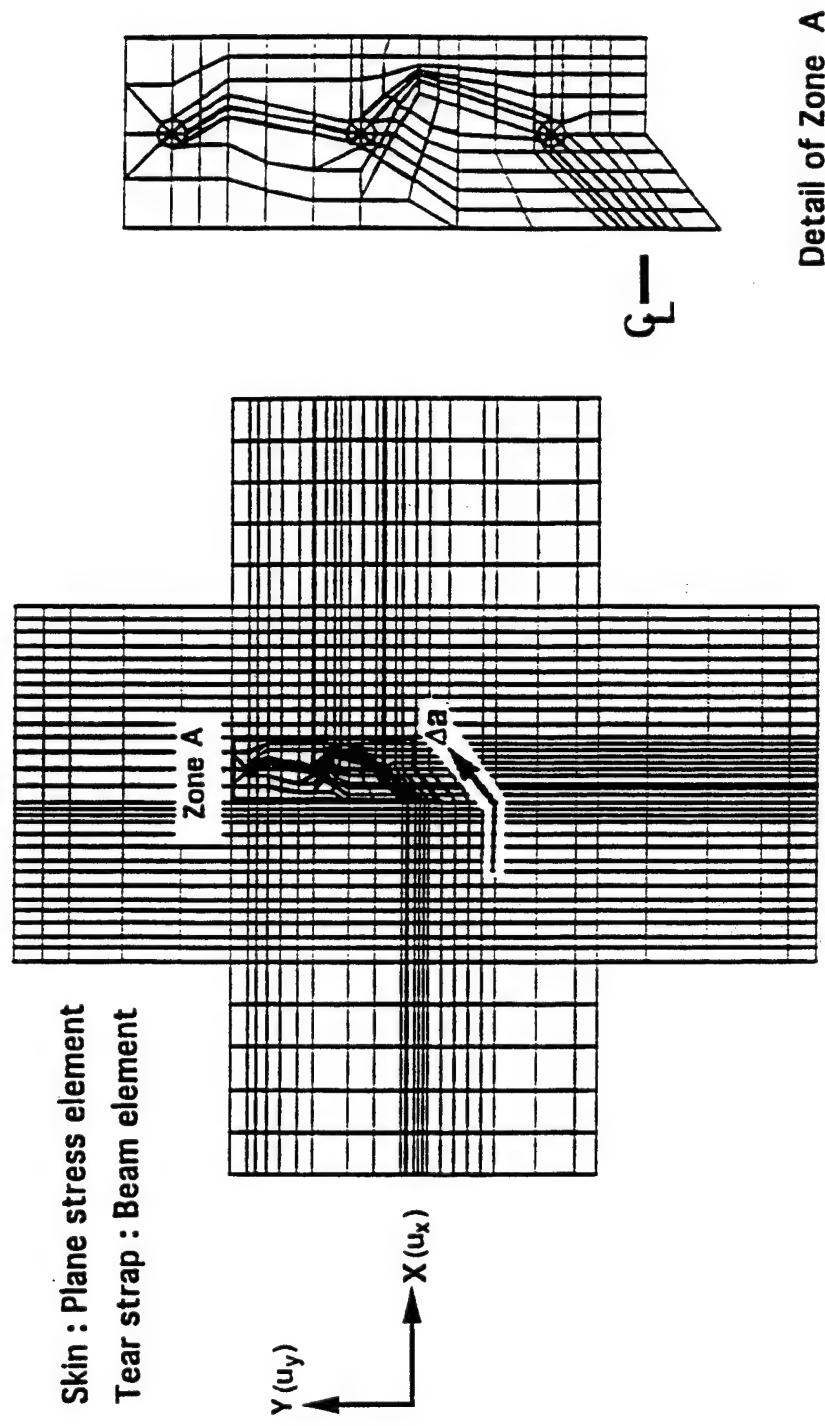


FIGURE 27. TYPICAL FINITE ELEMENT MESH OF BIAXIAL TEST SPECIMEN (TYPES MB AND MC)

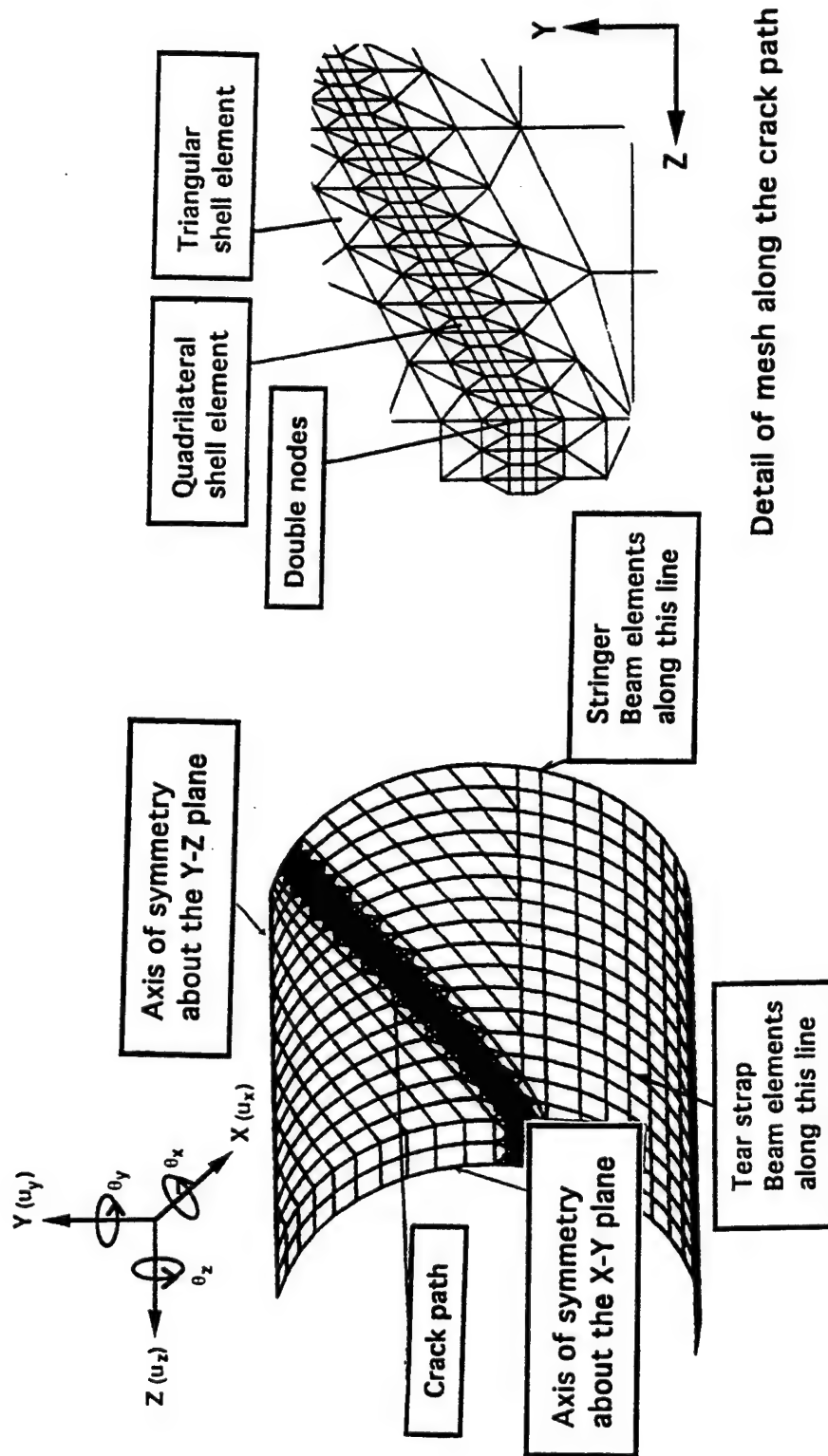


FIGURE 28. TYPICAL FINITE ELEMENT MESH OF SMALL-SCALE SPECIMEN

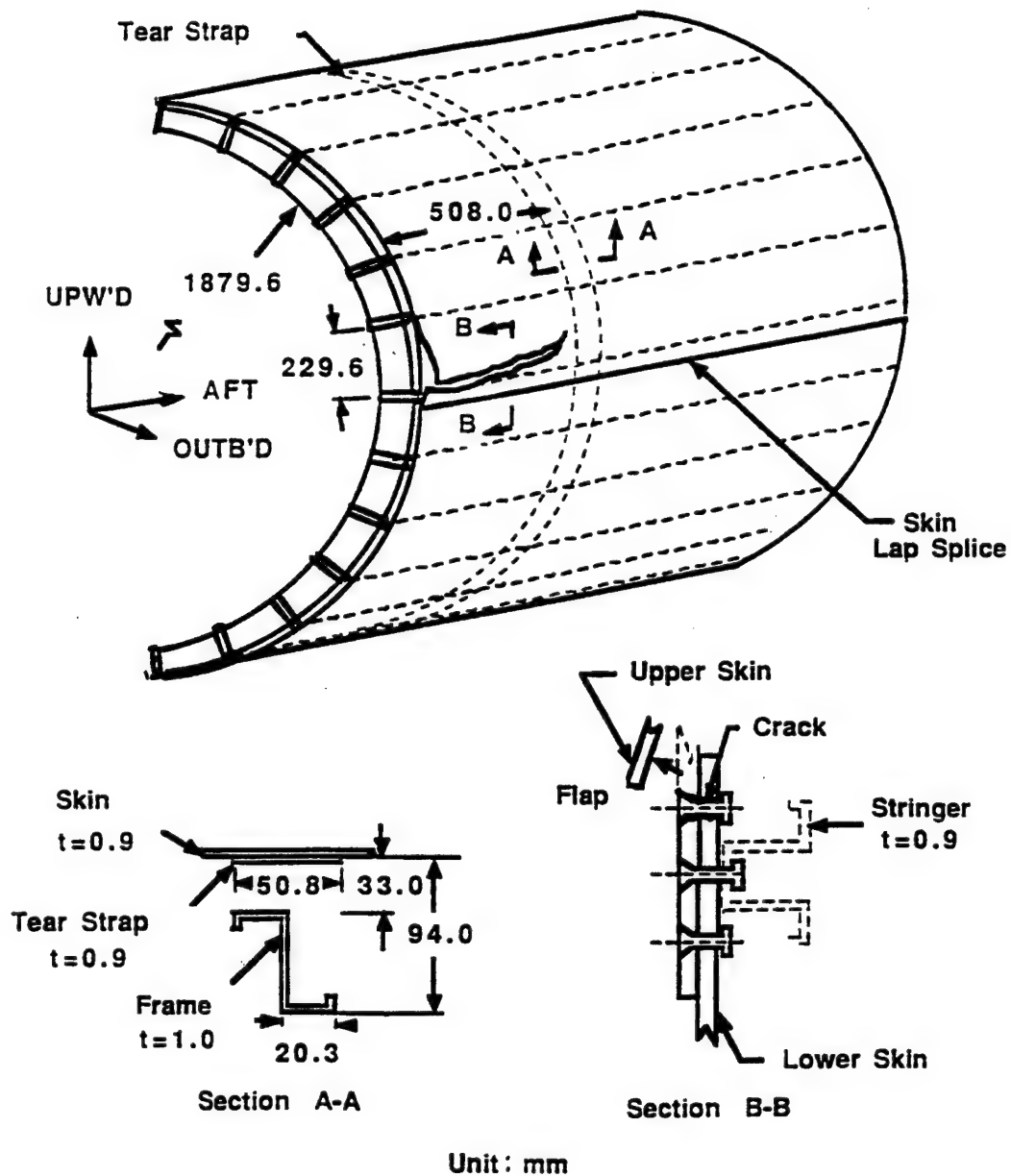


FIGURE 29. AXIAL RUPTURE OF A FUSELAGE [91]

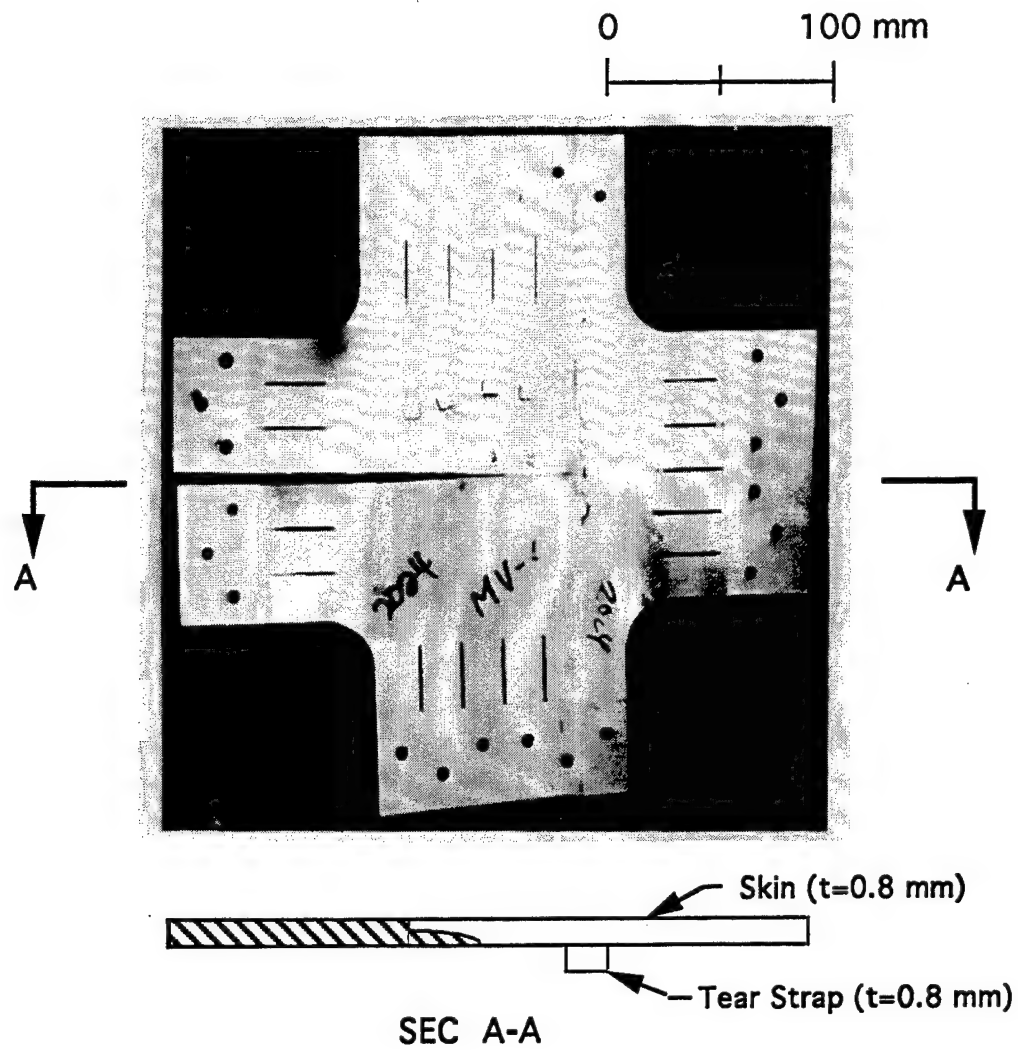


FIGURE 30. PHOTOGRAPH OF SPECIMEN MV-1

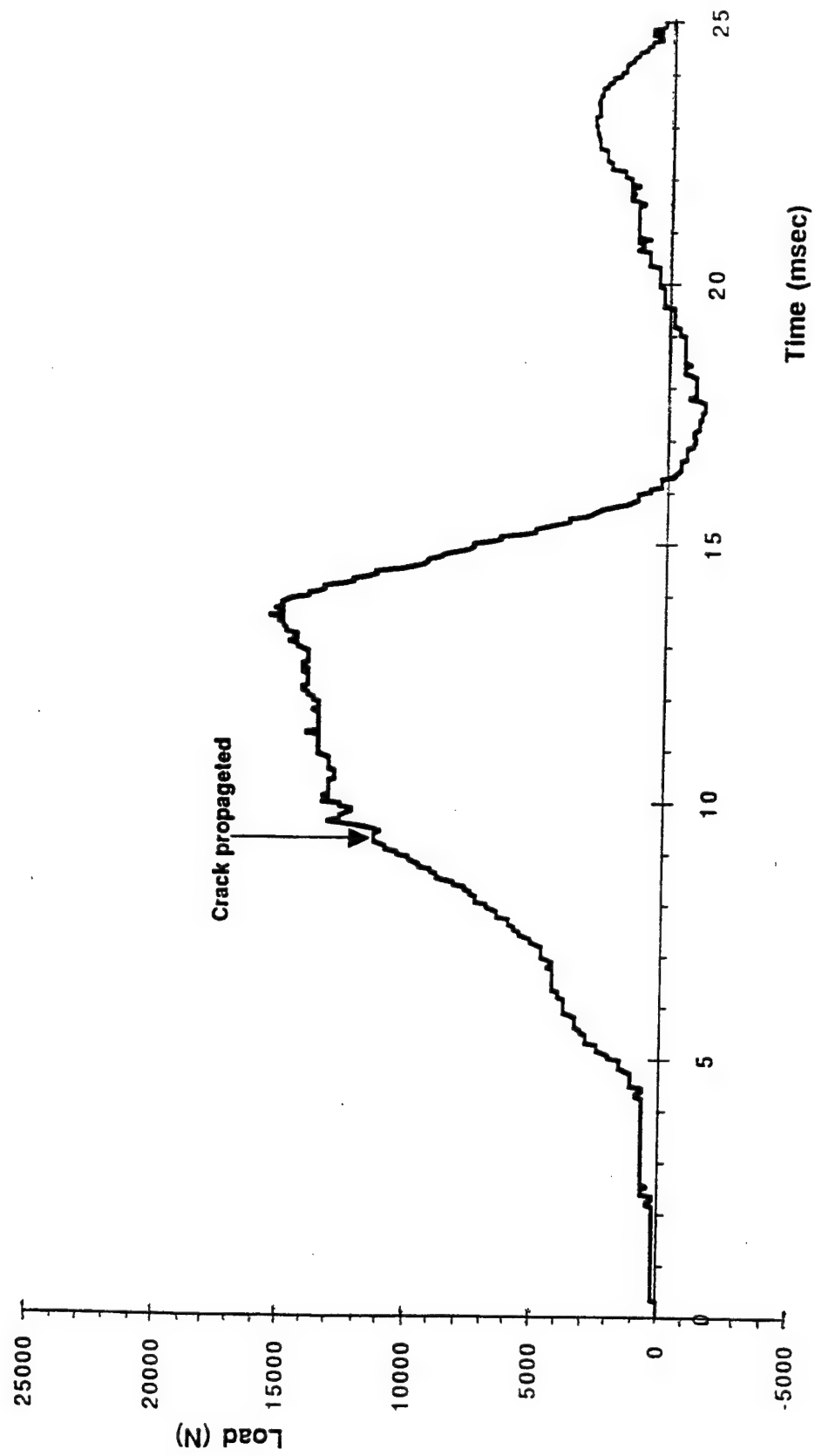


FIGURE 31. VARIATIONS IN P_y . SPECIMEN MV-1.

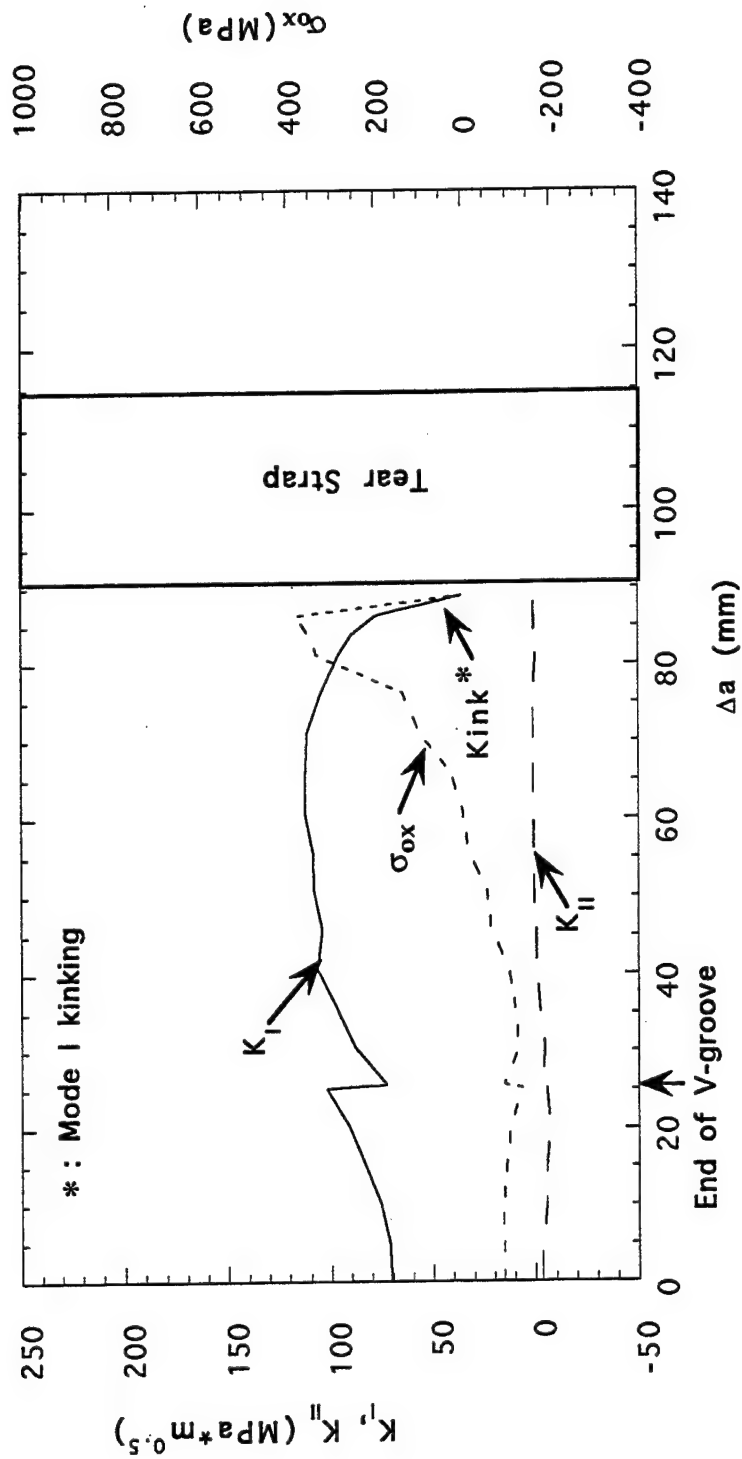


FIGURE 32. VARIATIONS IN K_I , K_{II} , AND σ_{ox} . SPECIMEN MV-1.

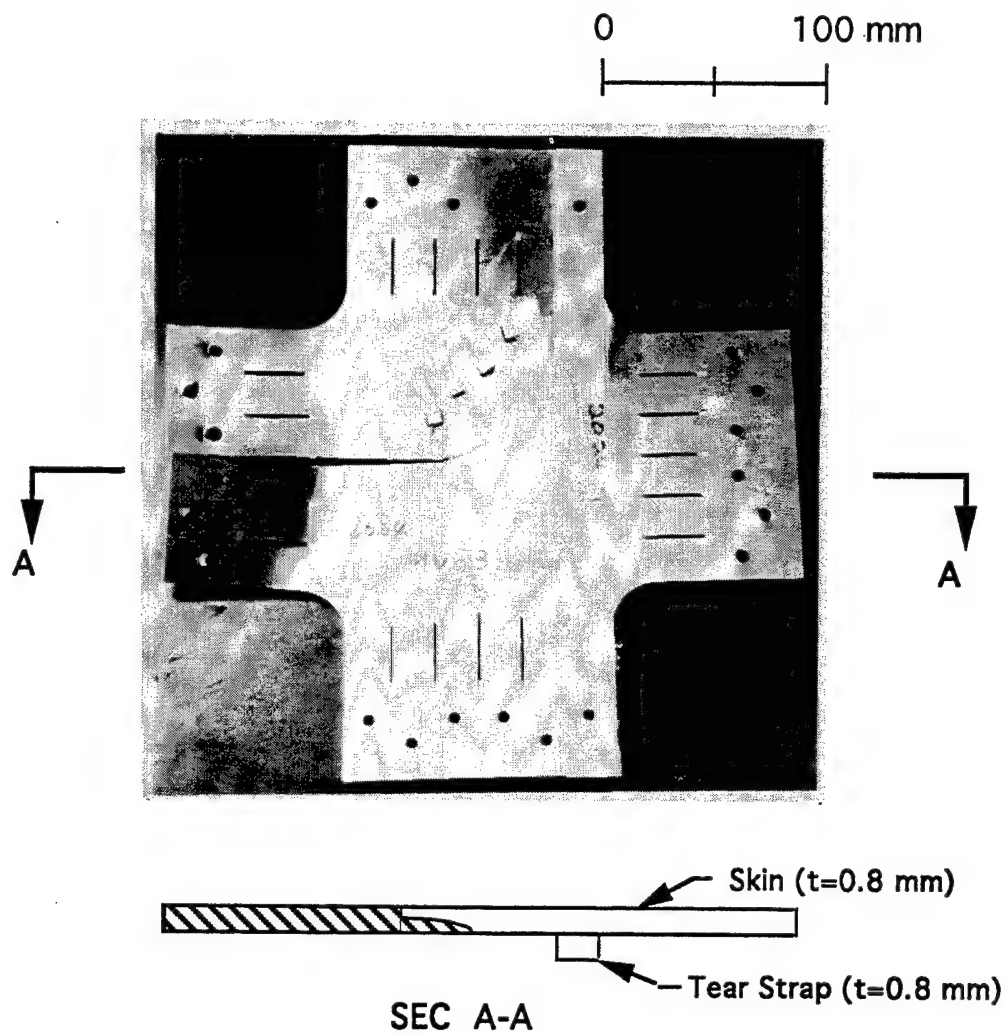


FIGURE 33. PHOTOGRAPH OF SPECIMEN MV-3

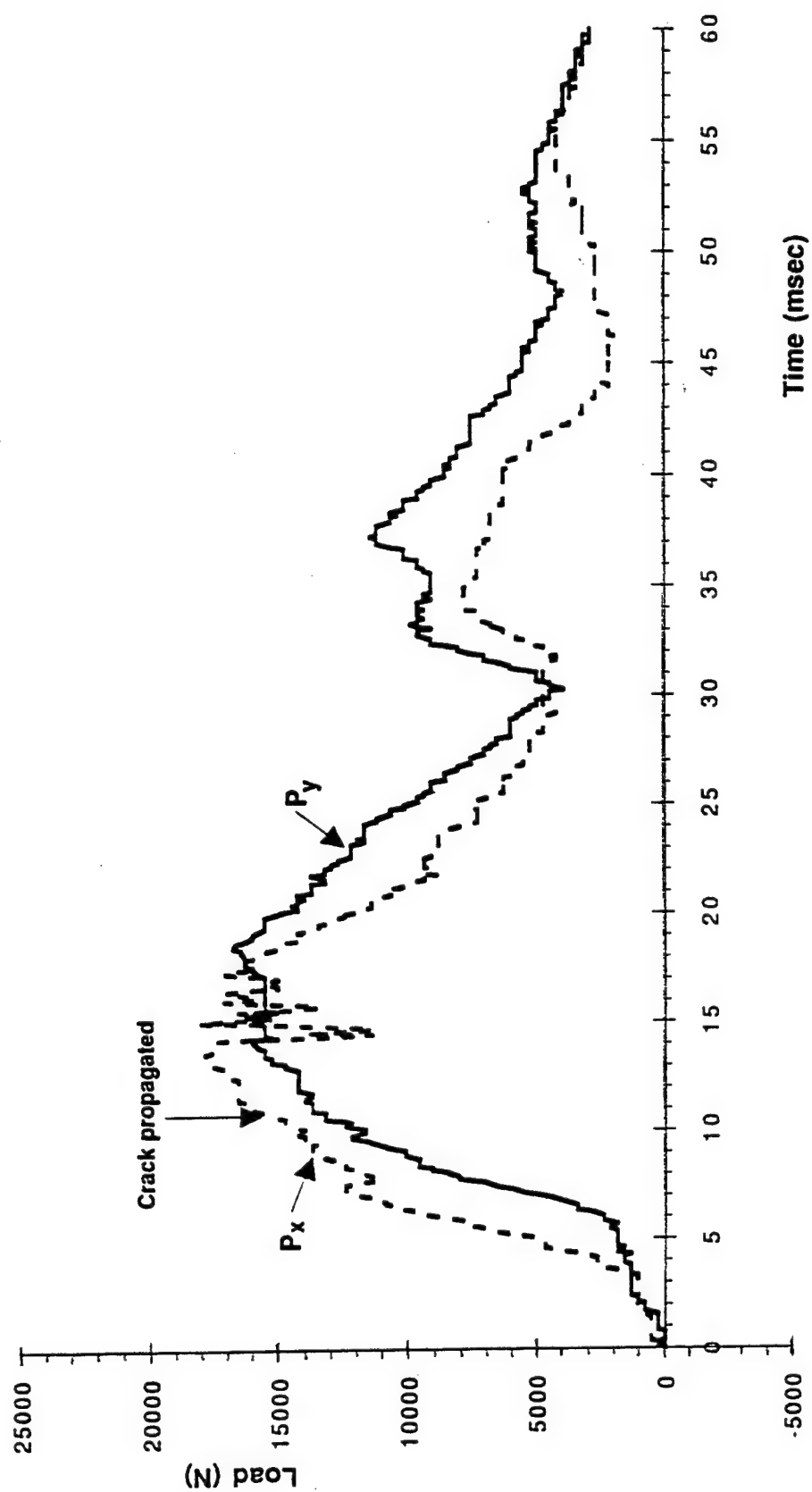


FIGURE 34. VARIATIONS IN P_x AND P_y SPECIMEN MV-3.

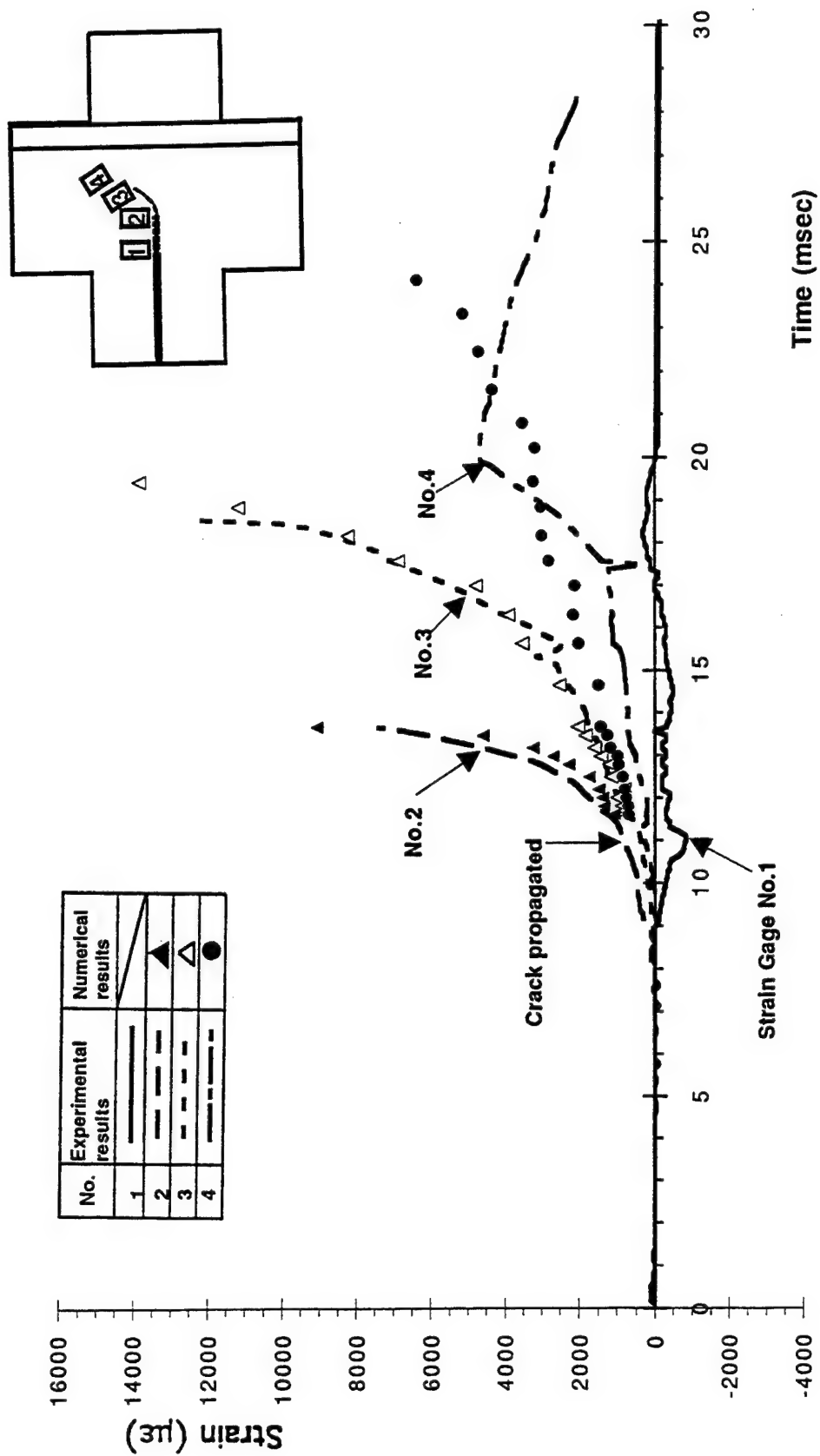


FIGURE 35. STRAIN GAGE RESPONSES. SPECIMEN MV-3.

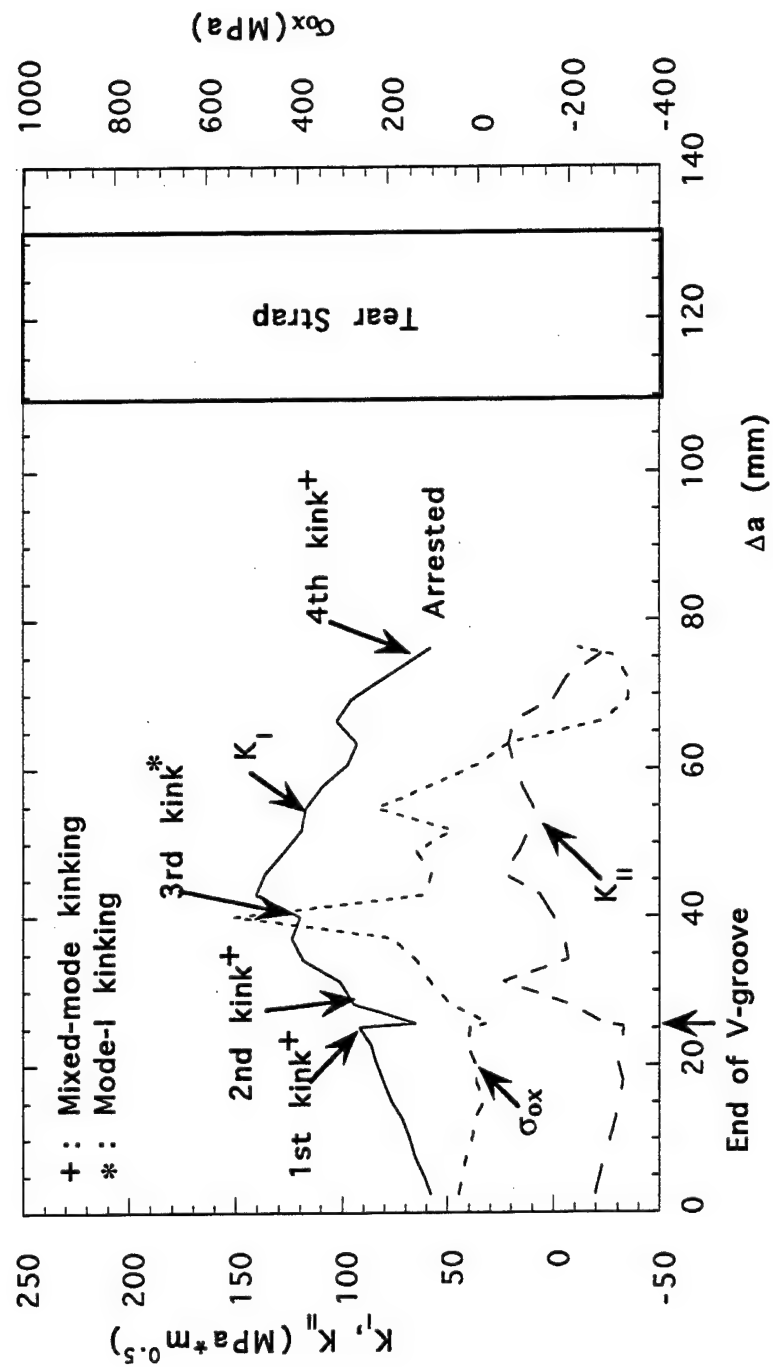


FIGURE 36. VARIATIONS IN K_I , K_{II} , AND σ_{ox} : SPECIMEN MV-3.

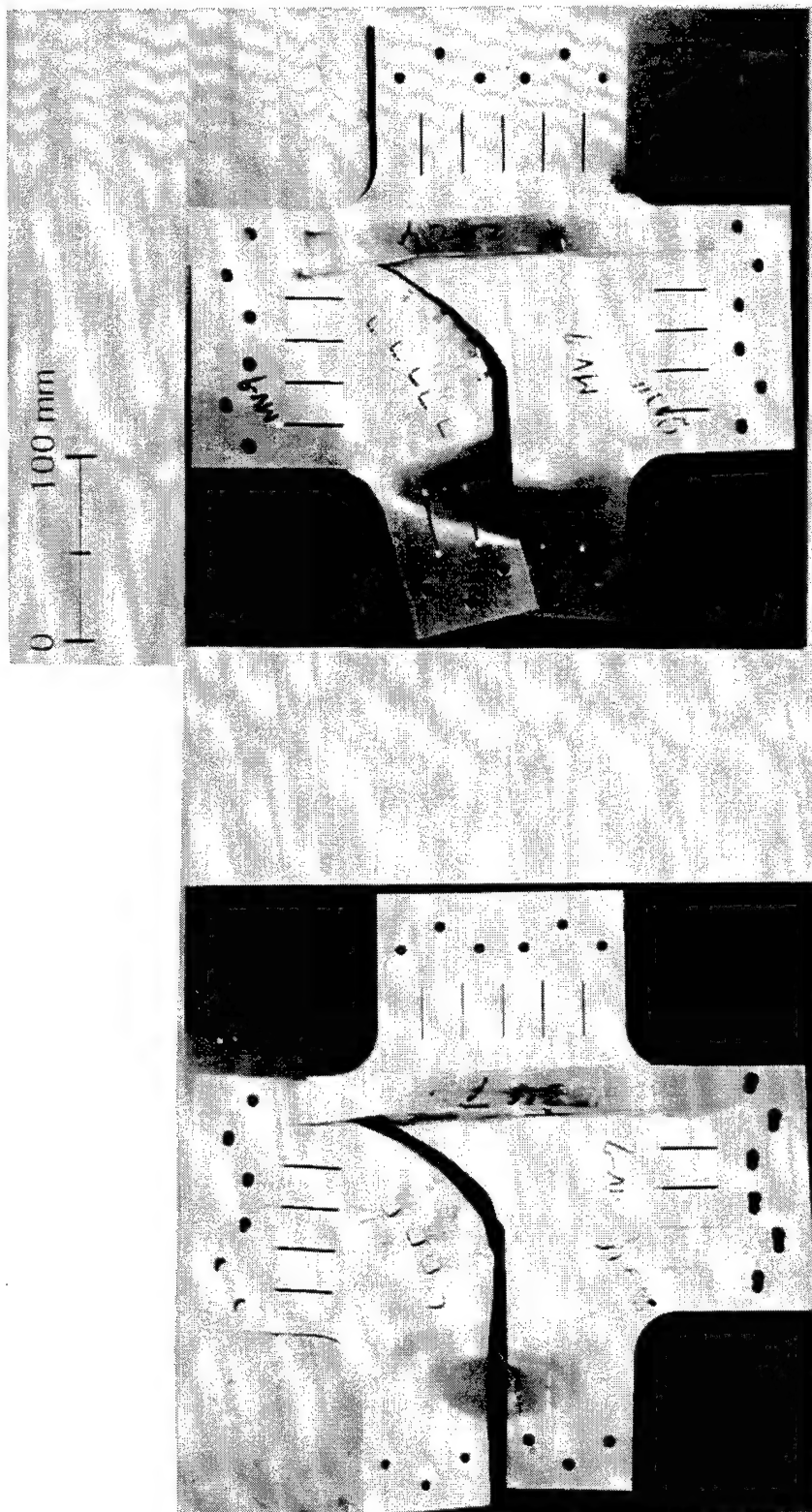


FIGURE 37. PHOTOGRAPH OF SPECIMEN MV-7 AND MV-9.
2024-T3 CRUCIFORM SPECIMEN WITH LARGE FLAPPING.

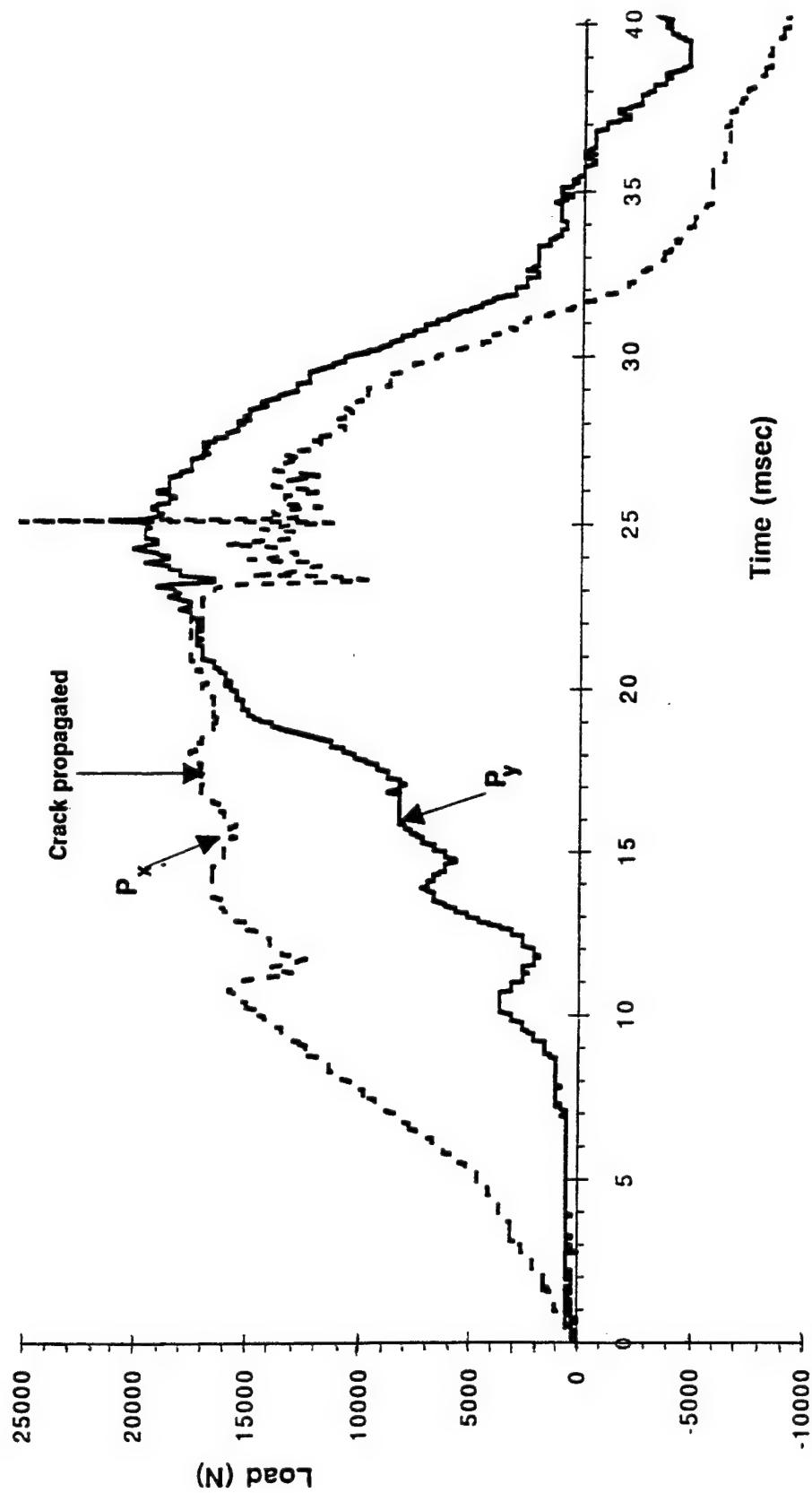


FIGURE 38. VARIATIONS IN P_x AND P_y . SPECIMEN MV-7.

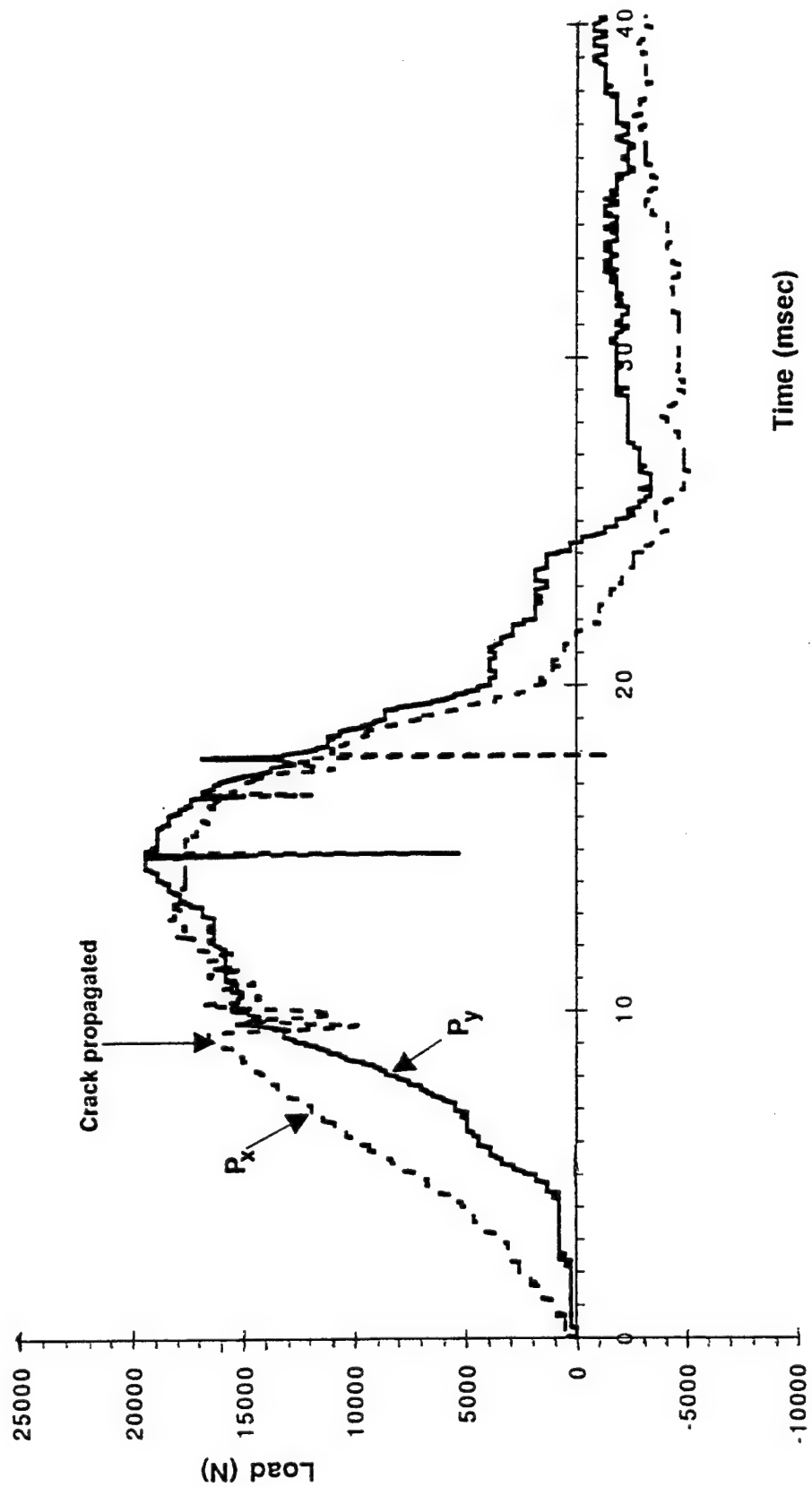


FIGURE 39. VARIATIONS IN P_x AND P_y . SPECIMEN MV-9.

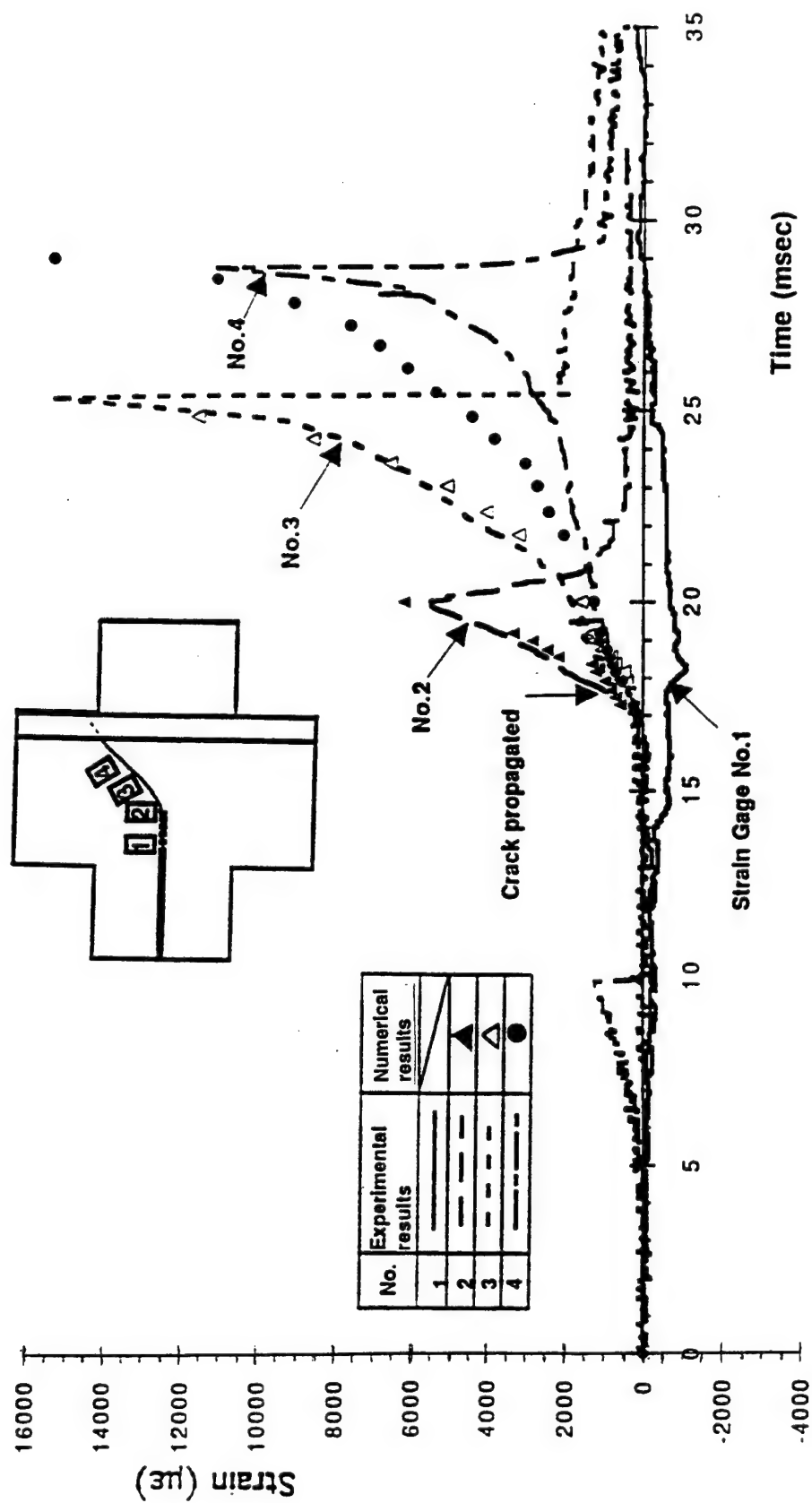


FIGURE 40. STRAIN GAGE RESPONSES. SPECIMEN MV-7.

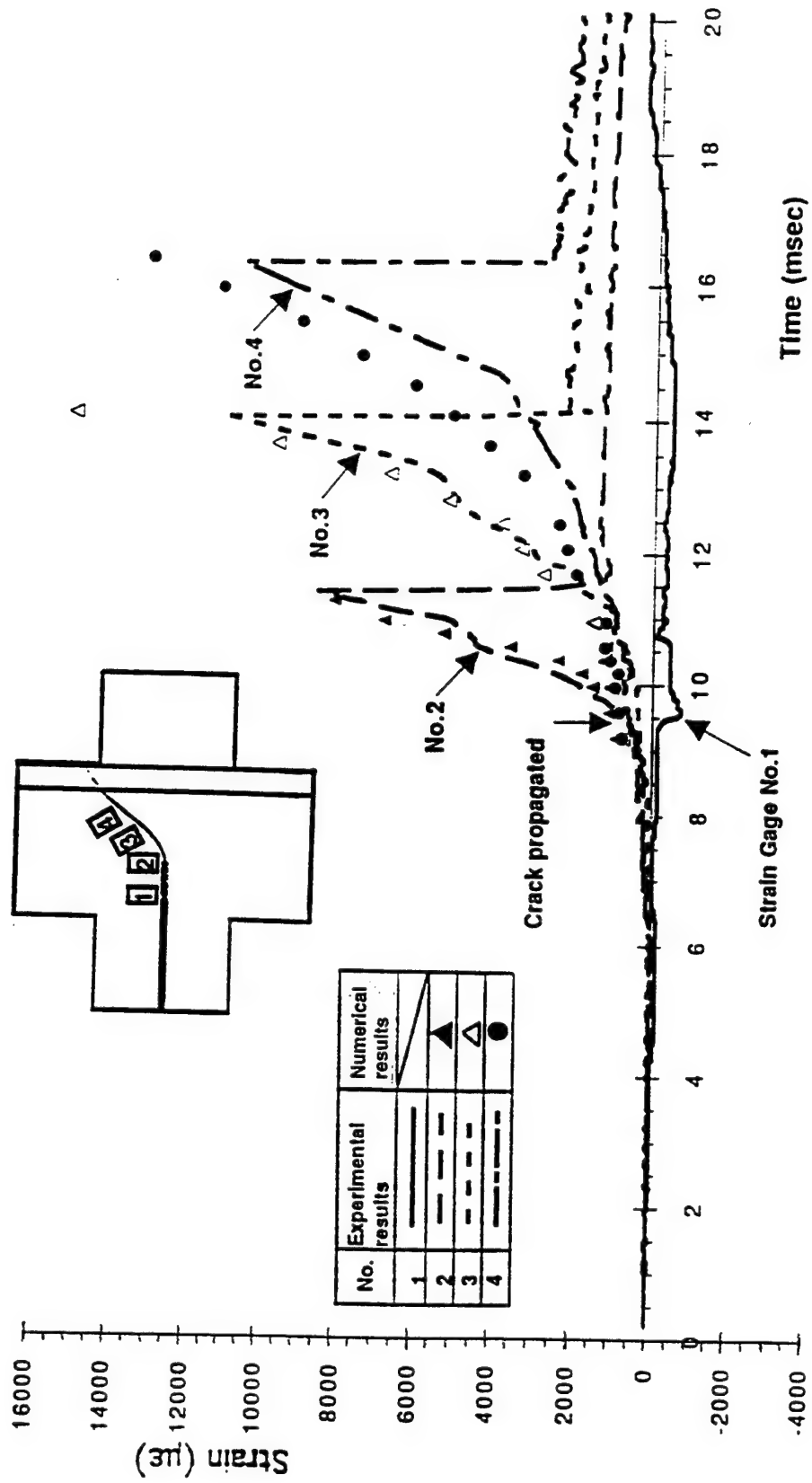


FIGURE 41. STRAIN GAGE RESPONSES. SPECIMEN MV-9.

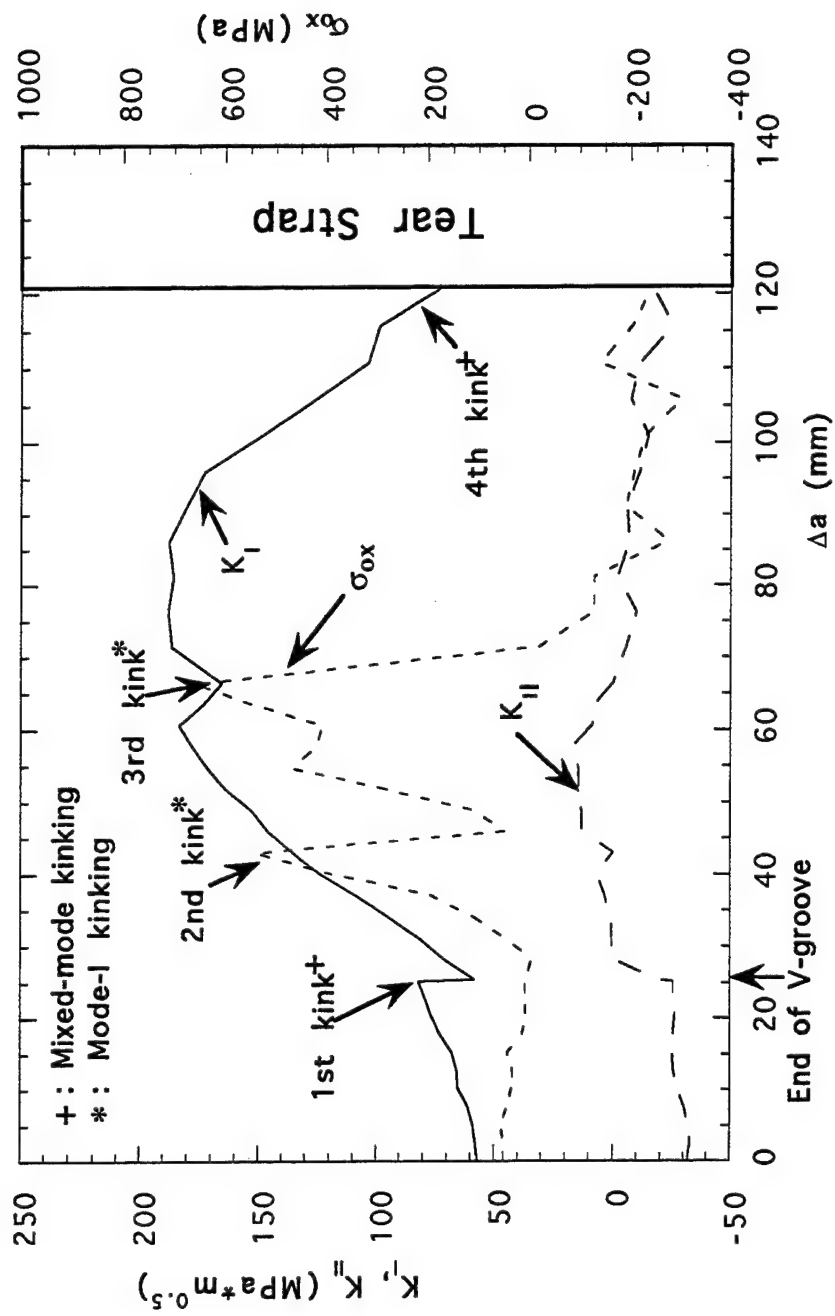


FIGURE 42. VARIATIONS IN K_I , K_{II} , AND σ_{ox} , SPECIMEN MV-7.

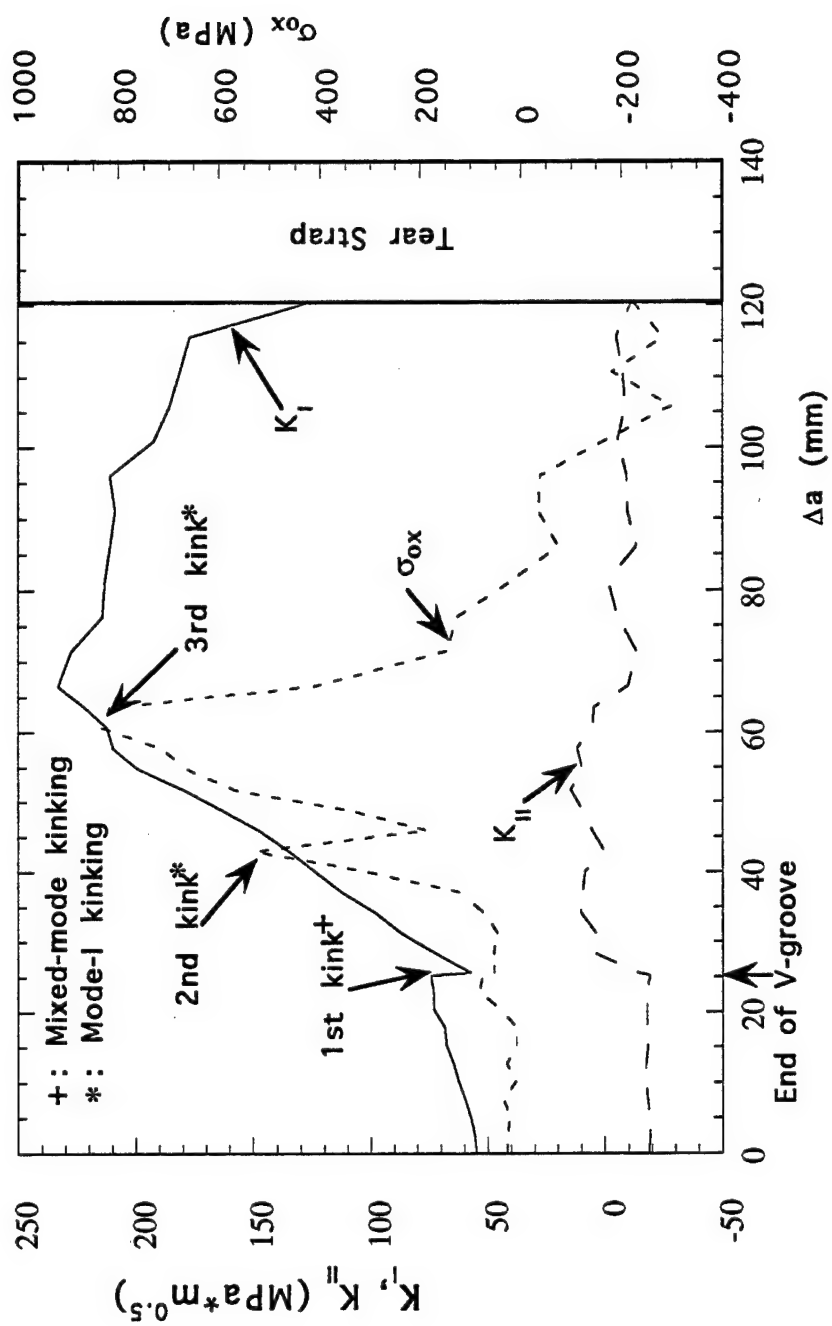


FIGURE 43. VARIATIONS IN K_I , K_{II} , AND σ_{ox} . SPECIMEN MV-9.

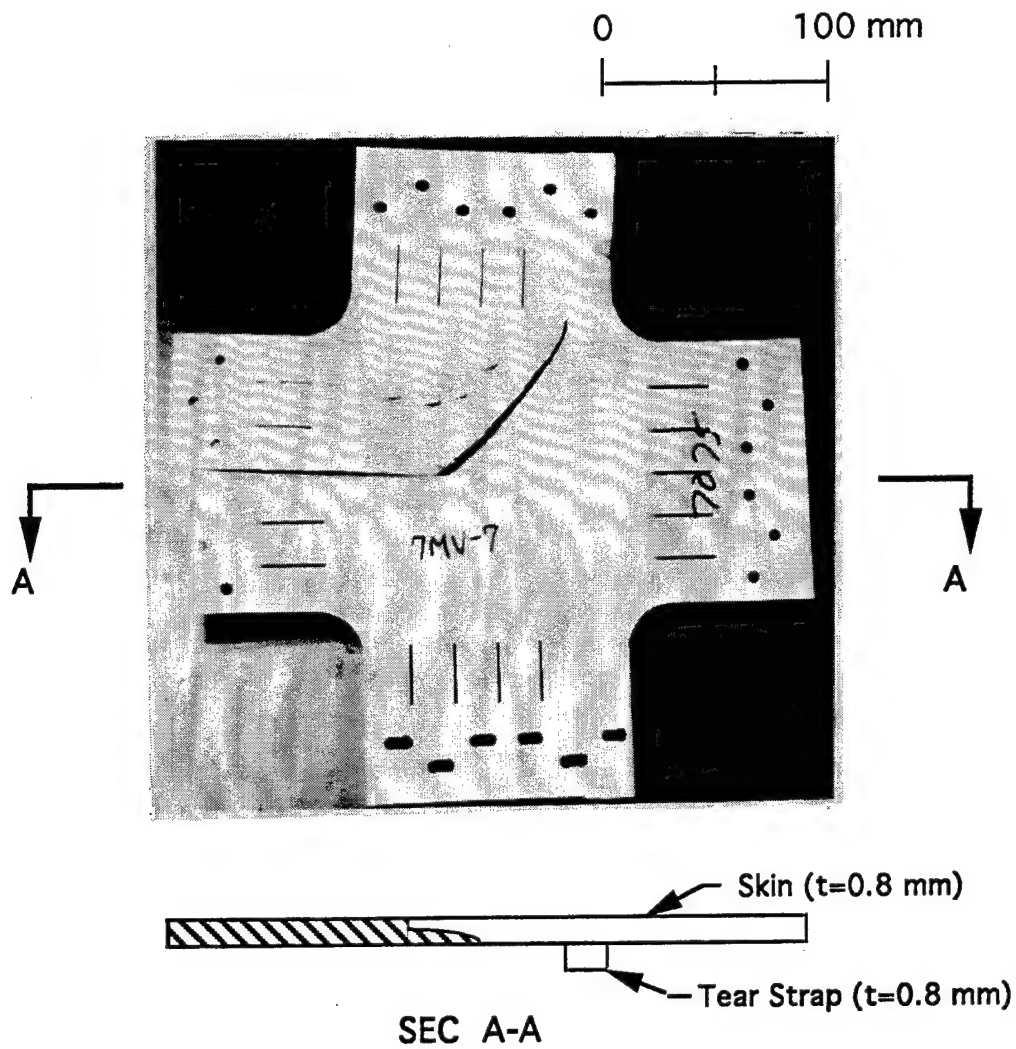


FIGURE 44. PHOTOGRAPH OF SPECIMEN 7MV-7

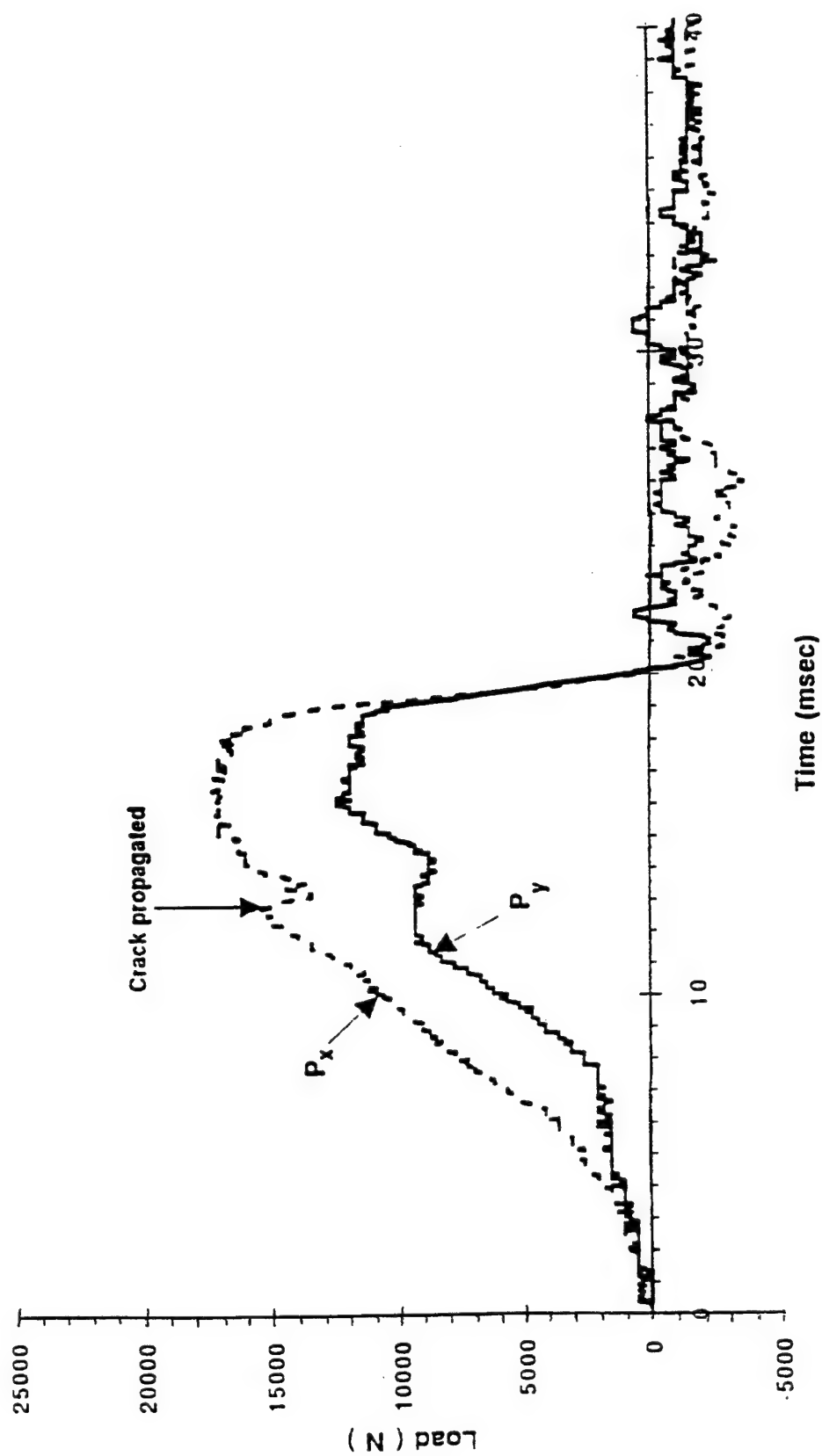


FIGURE 45. VARIATIONS IN P_x AND P_y . SPECIMEN 7MV-7.

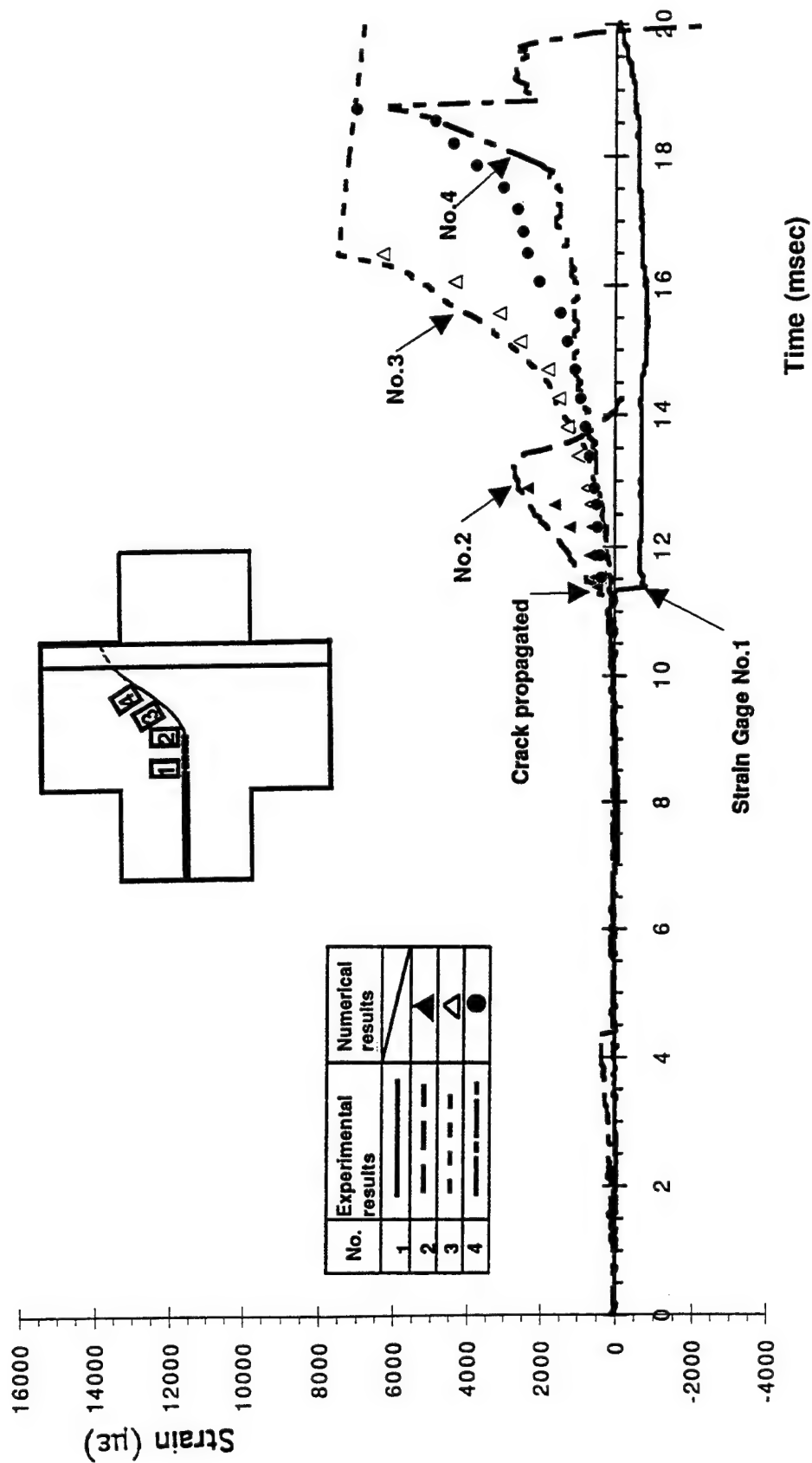


FIGURE 46. STRAIN GAGE RESPONSES. SPECIMEN 7MV-7.

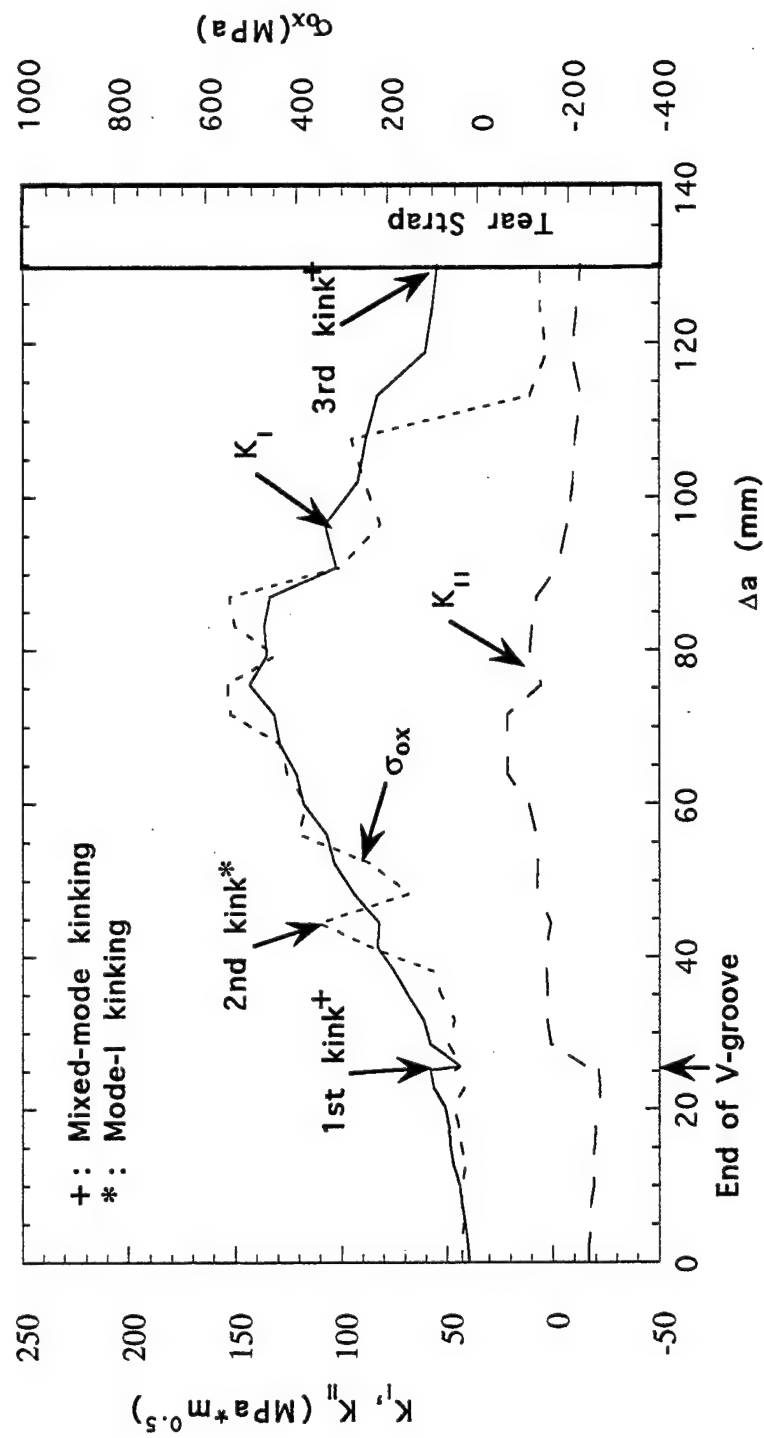


FIGURE 47. VARIATIONS IN K_I , K_{II} , AND σ_{ox} . SPECIMEN 7MV-7.

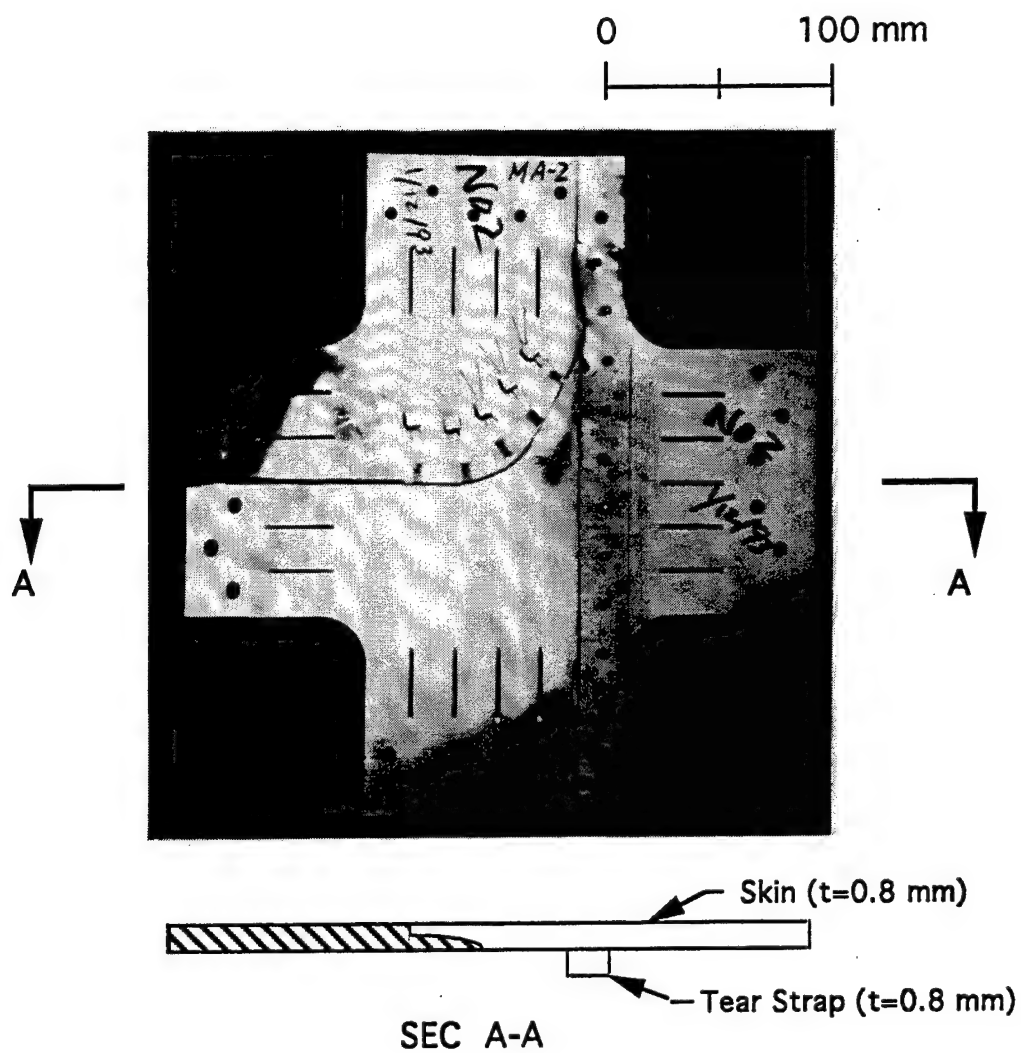


FIGURE 48. PHOTOGRAPH OF SPECIMEN MA-2

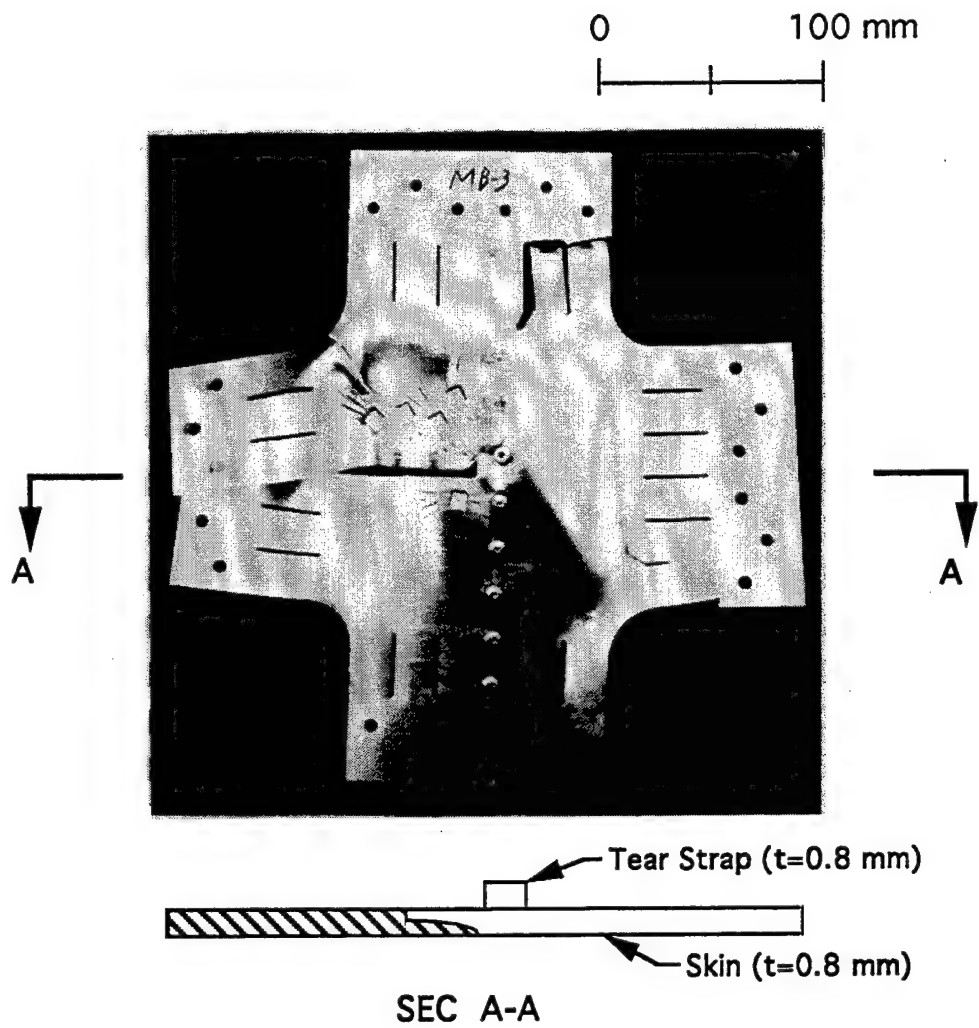


FIGURE 49. PHOTOGRAPH OF SPECIMEN MB-3

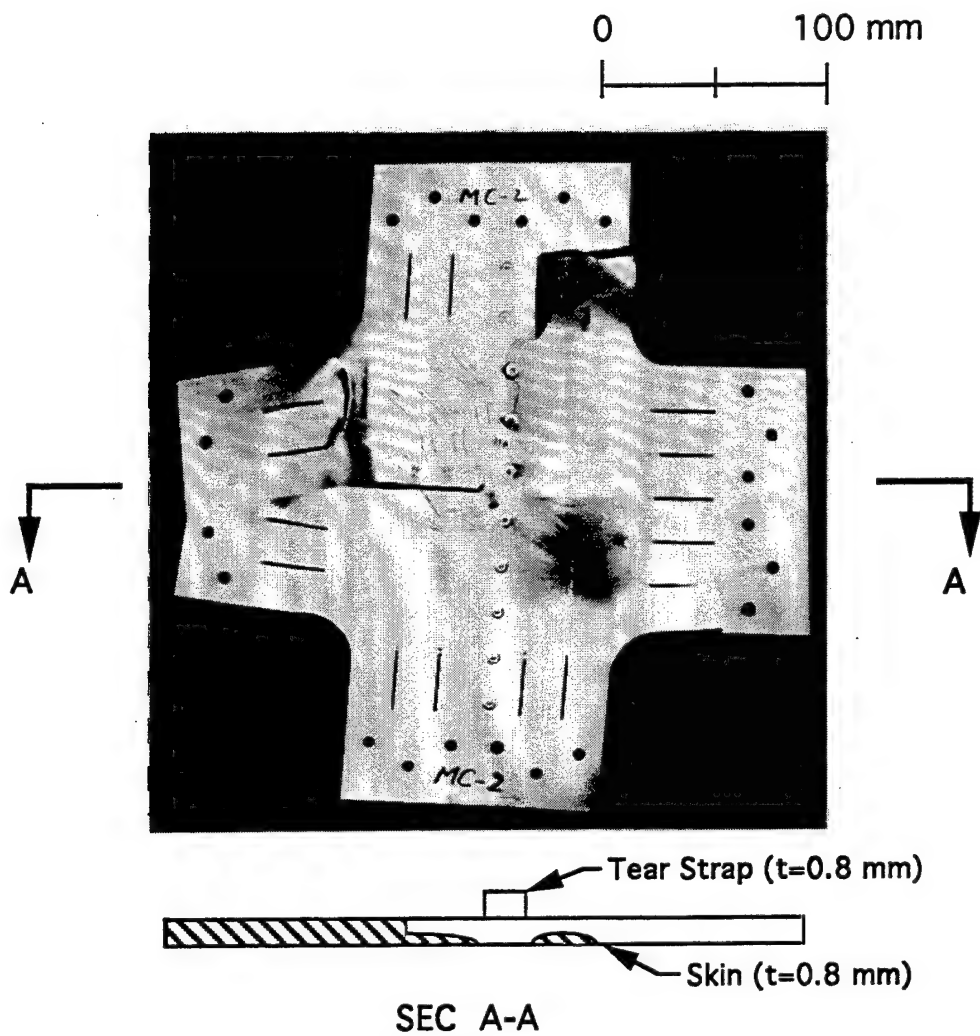


FIGURE 50. PHOTOGRAPH OF SPECIMEN MC-2

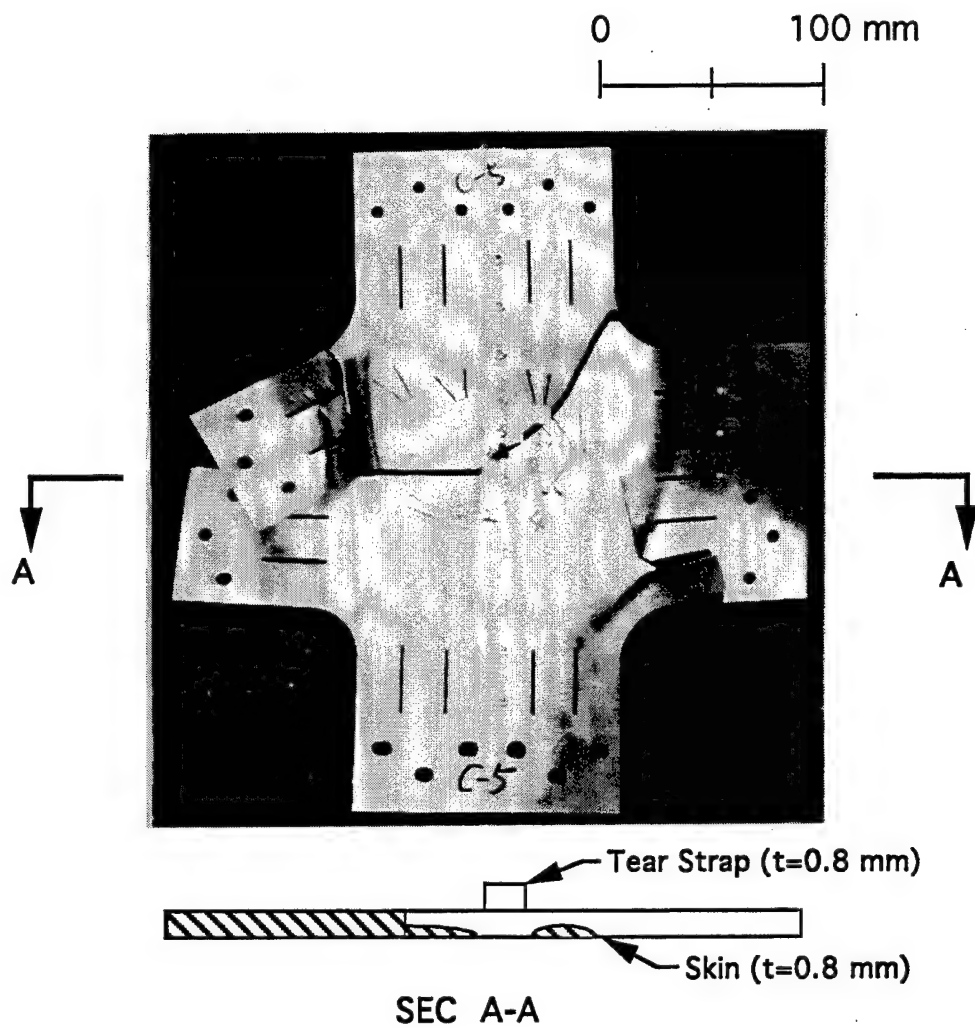


FIGURE 51. PHOTOGRAPH OF SPECIMEN MC-5

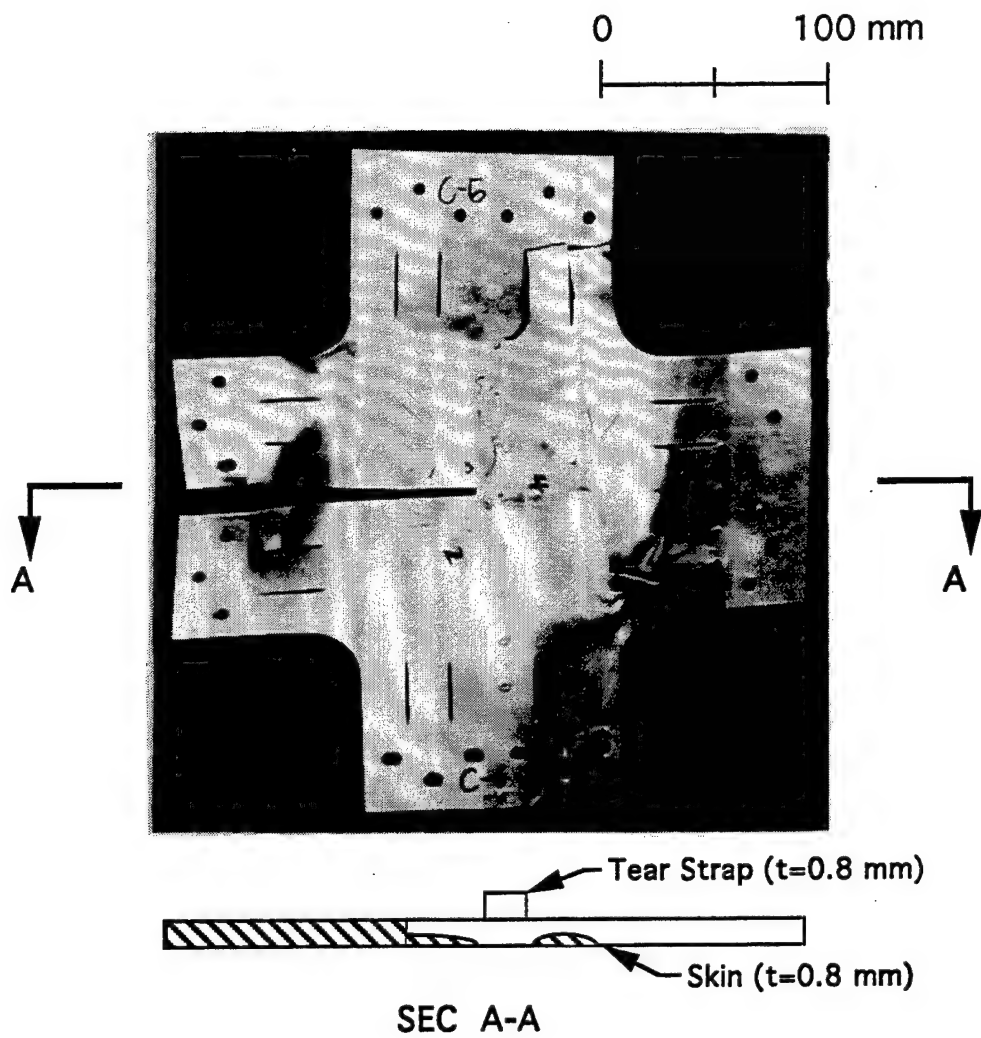


FIGURE 52. PHOTOGRAPH OF SPECIMEN MC-6

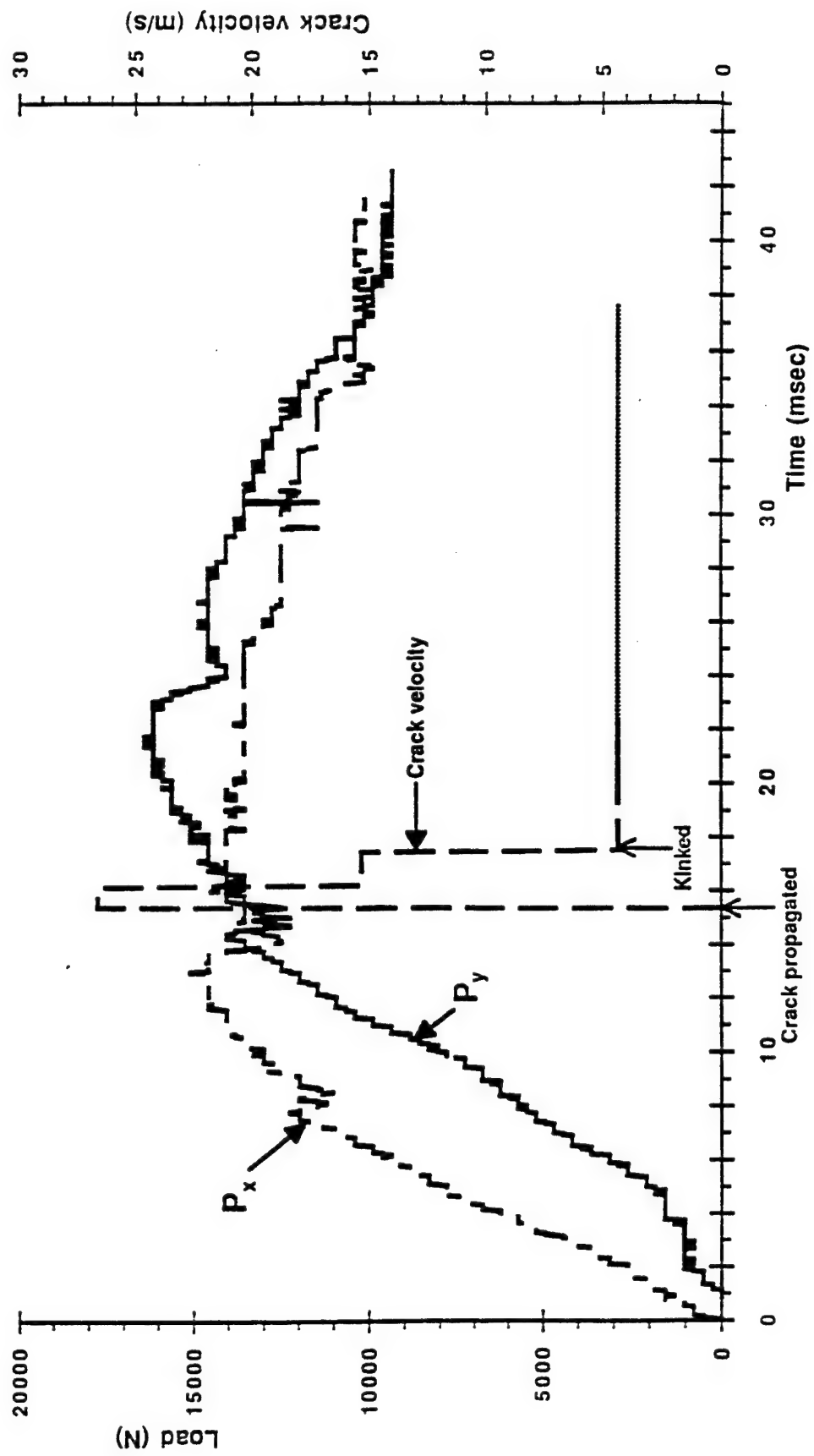


FIGURE 53. VARIATIONS IN P_x AND P_y . SPECIMEN MB-3.

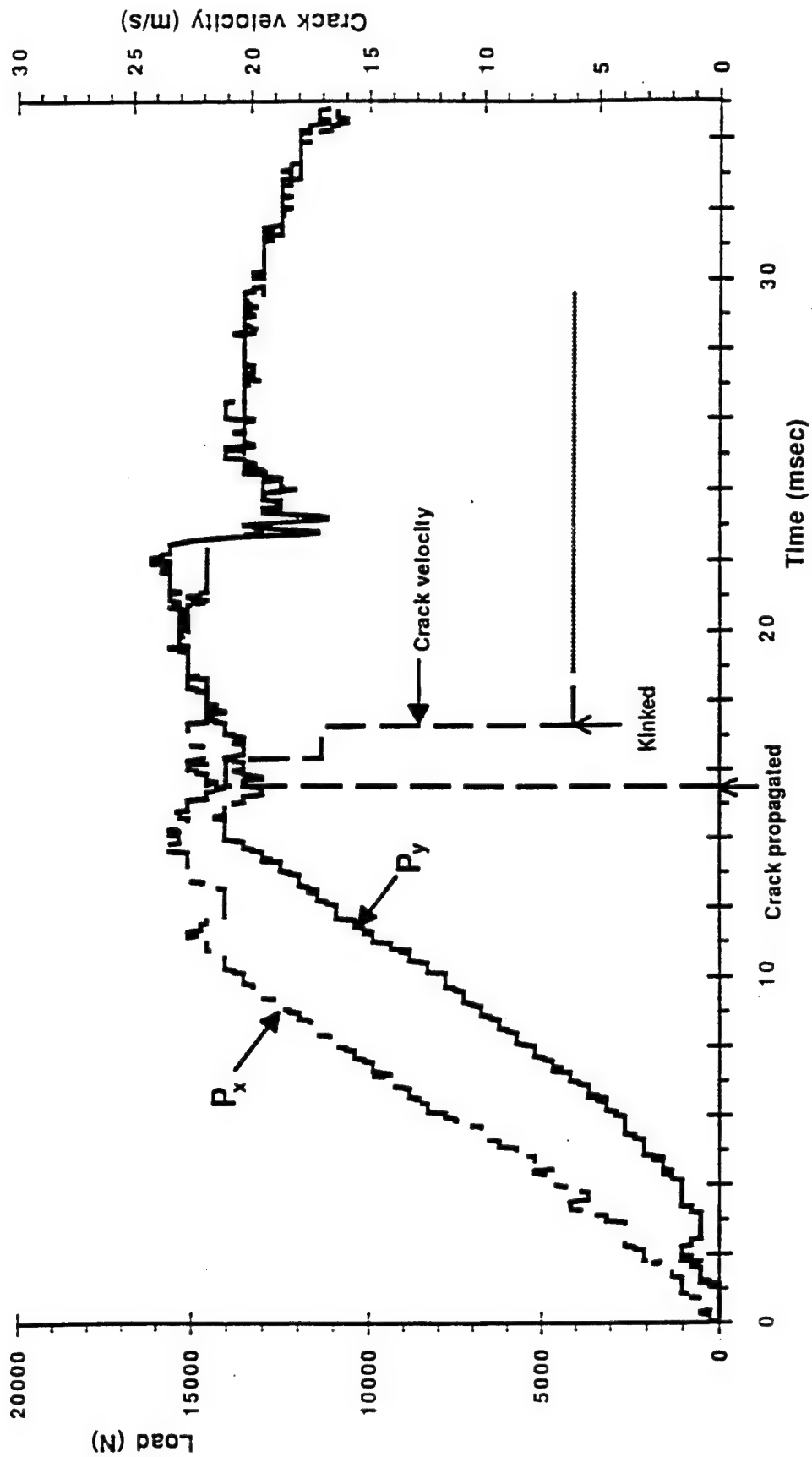


FIGURE 54. VARIATIONS IN P_x AND P_y . SPECIMEN MC-2.

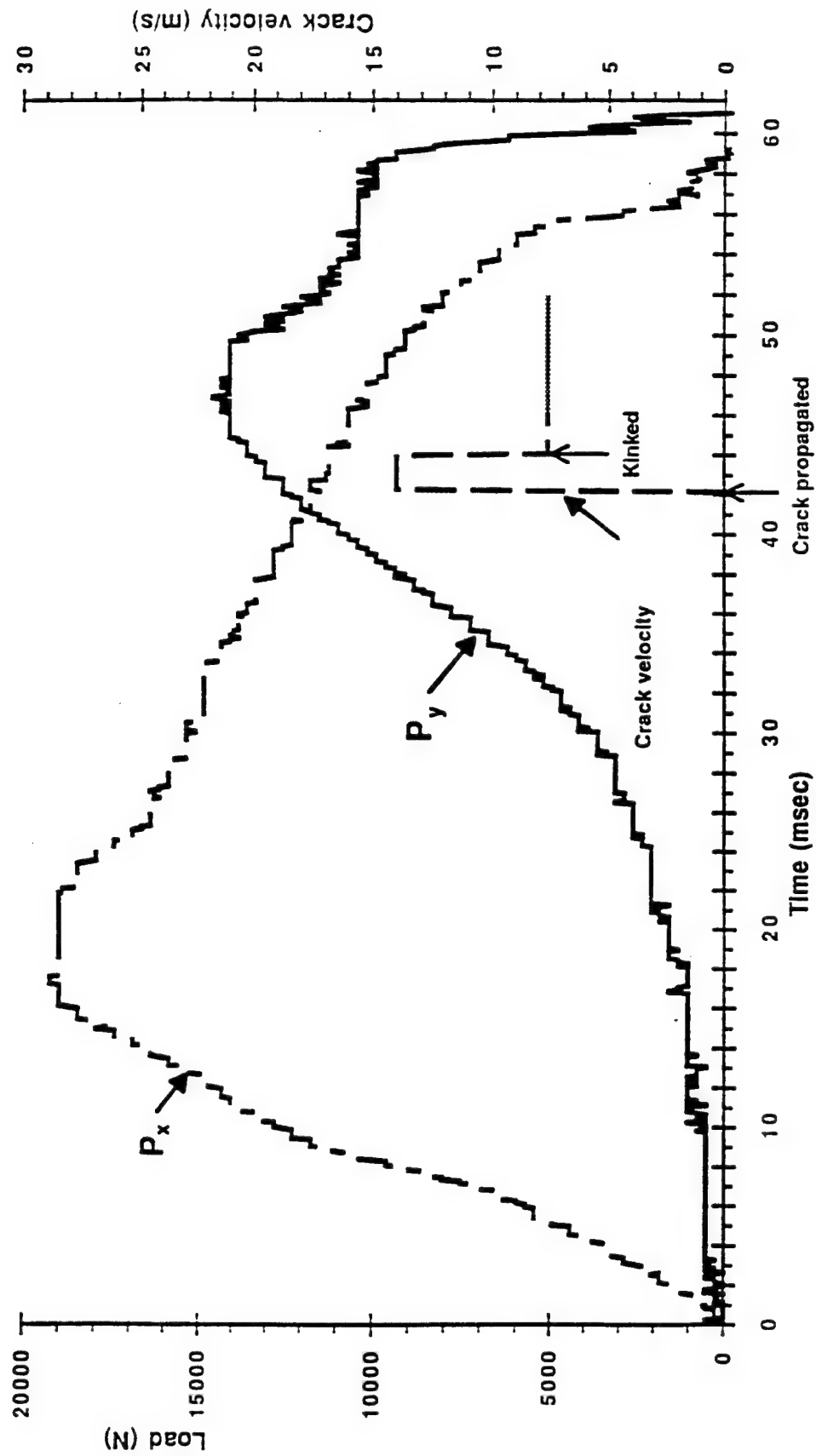


FIGURE 55. VARIATIONS IN P_x AND P_y . SPECIMEN MC-6.

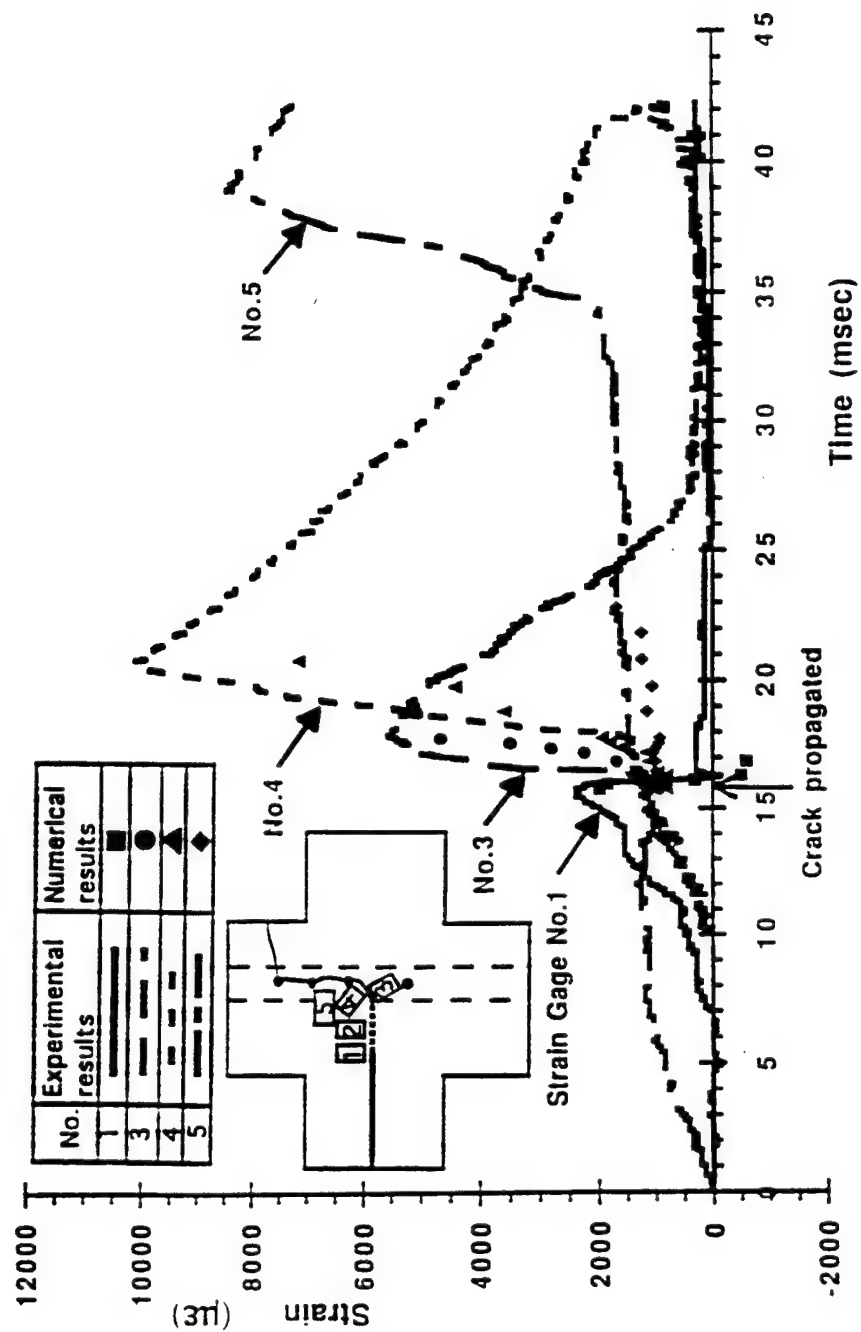


FIGURE 56. STRAIN GAGE RESPONSES, SPECIMEN MB-3.

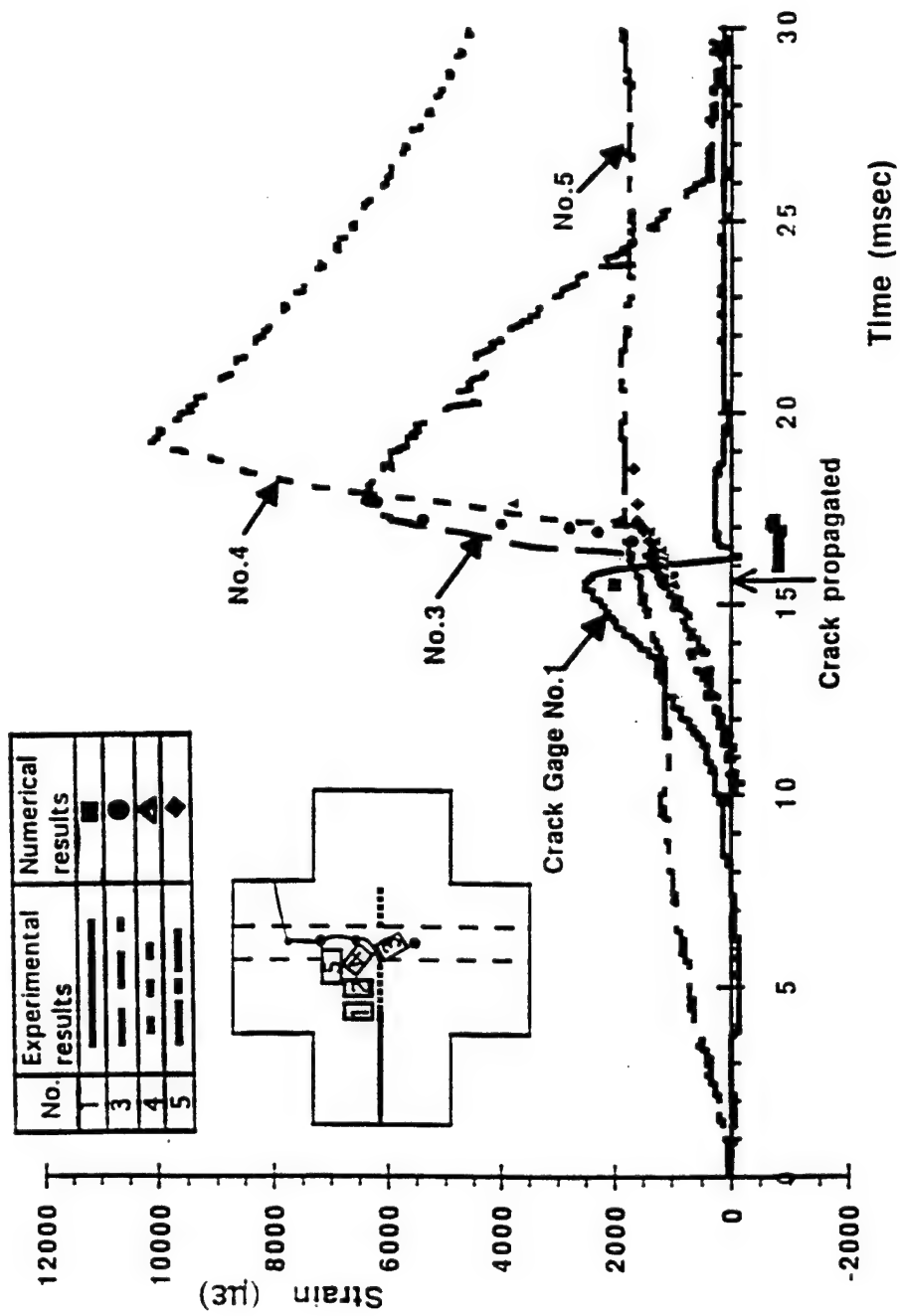


FIGURE 57. STRAIN GAGE RESPONSES. SPECIMEN MC-2.

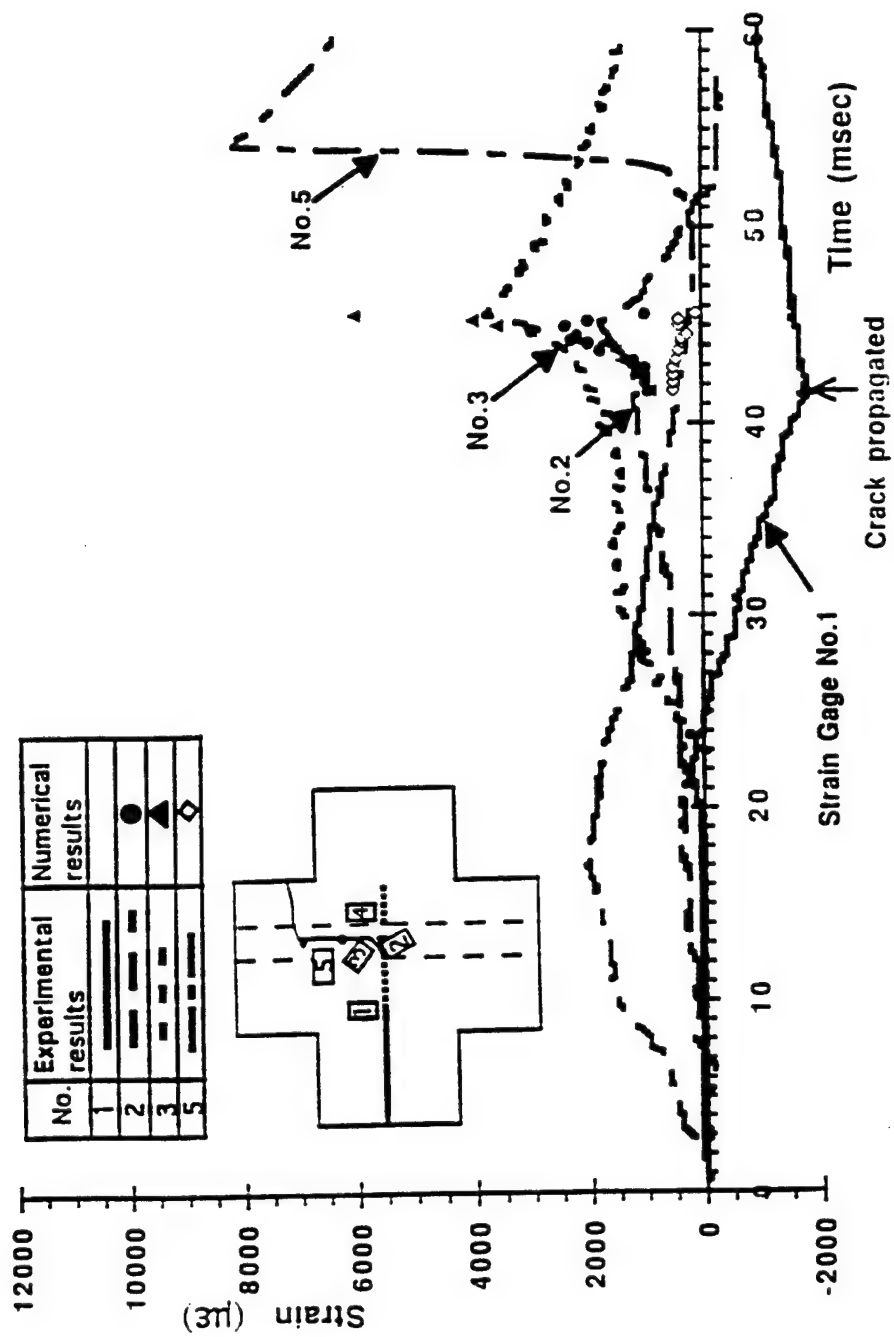


FIGURE 58. STRAIN GAGE RESPONSES. SPECIMEN MC-6.

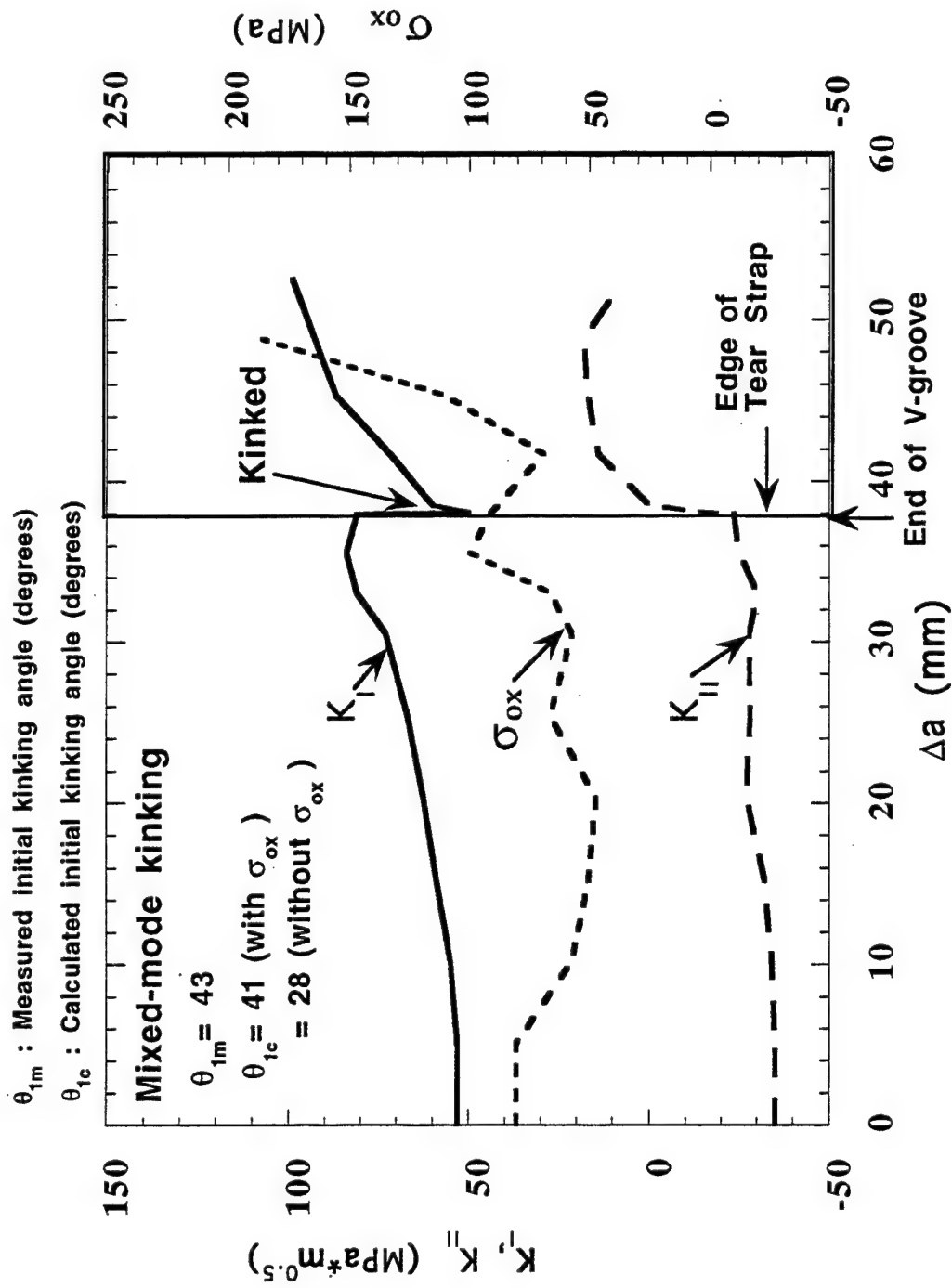


FIGURE 59. VARIATIONS IN K_I , K_{II} , AND σ_{ox} . SPECIMEN MB-3.

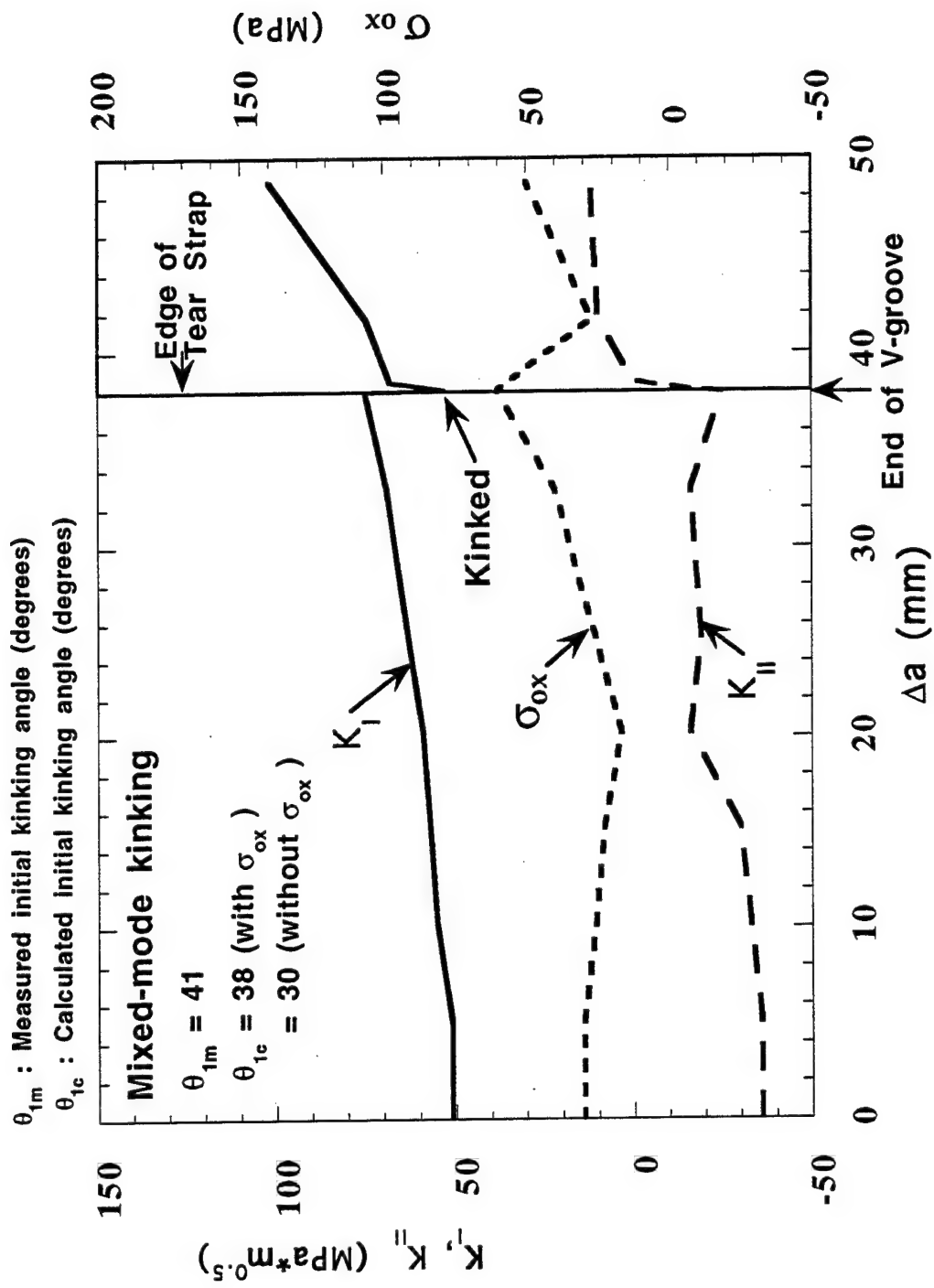


FIGURE 60. VARIATIONS IN K_I , K_{II} , AND σ_{ox} . SPECIMEN MC-2.

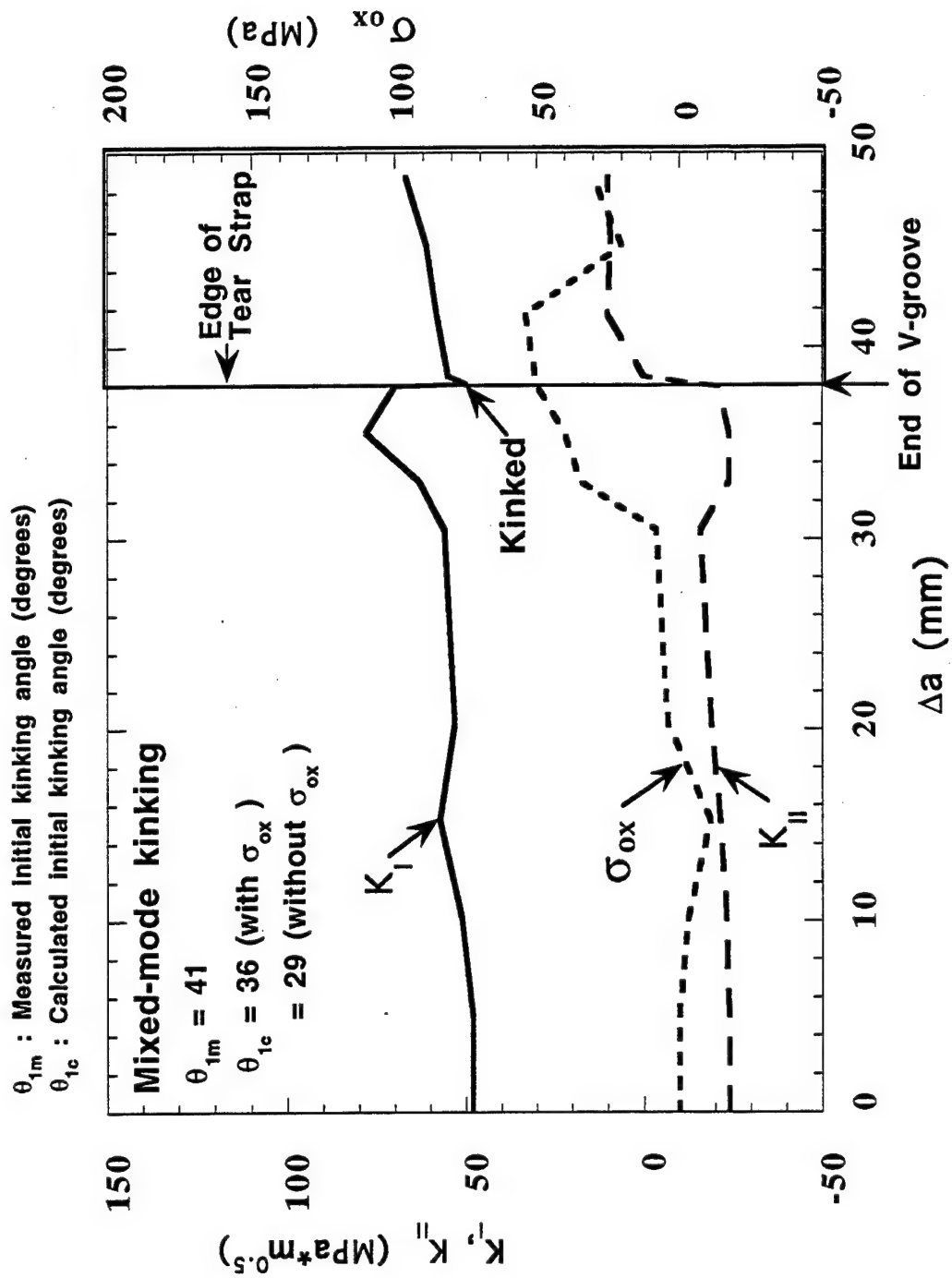


FIGURE 61. VARIATIONS IN K_I , K_{II} , AND σ_{ox} . SPECIMEN MC-6.

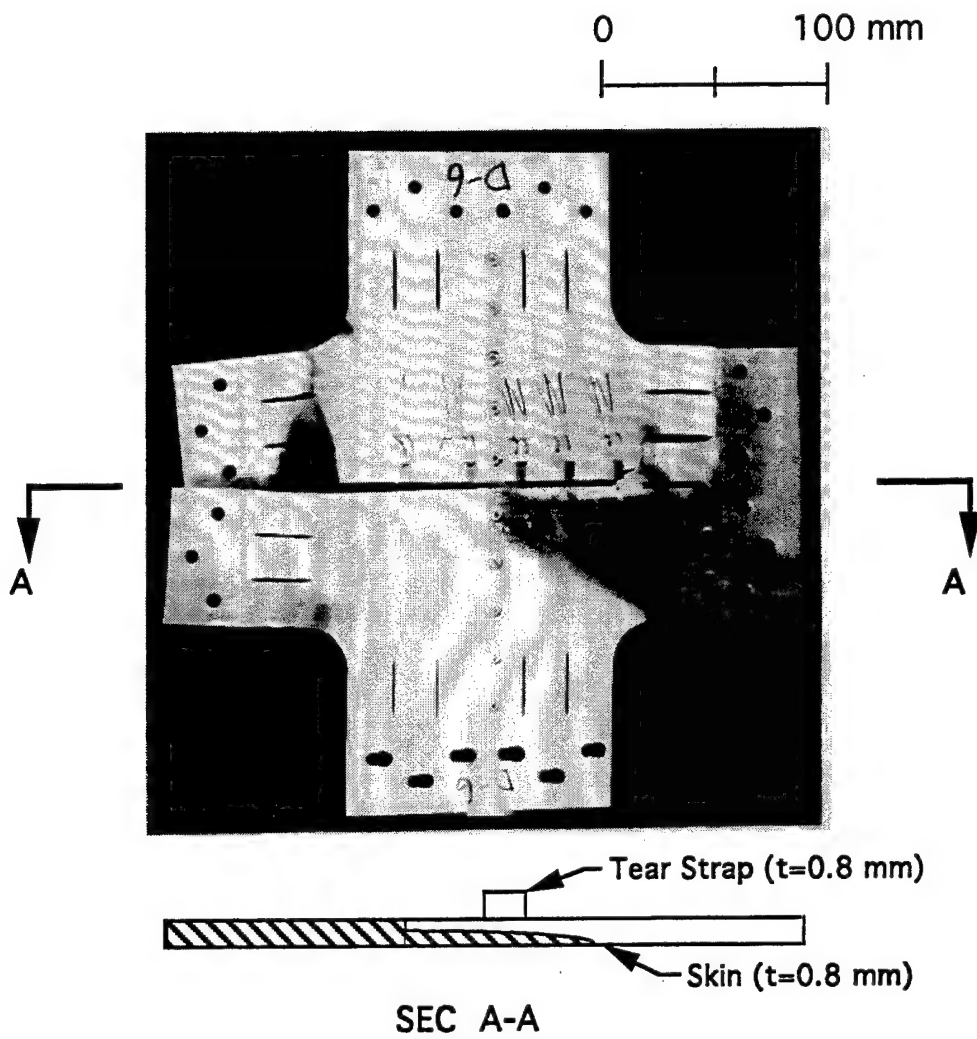


FIGURE 62. PHOTOGRAPH OF SPECIMEN MD-6

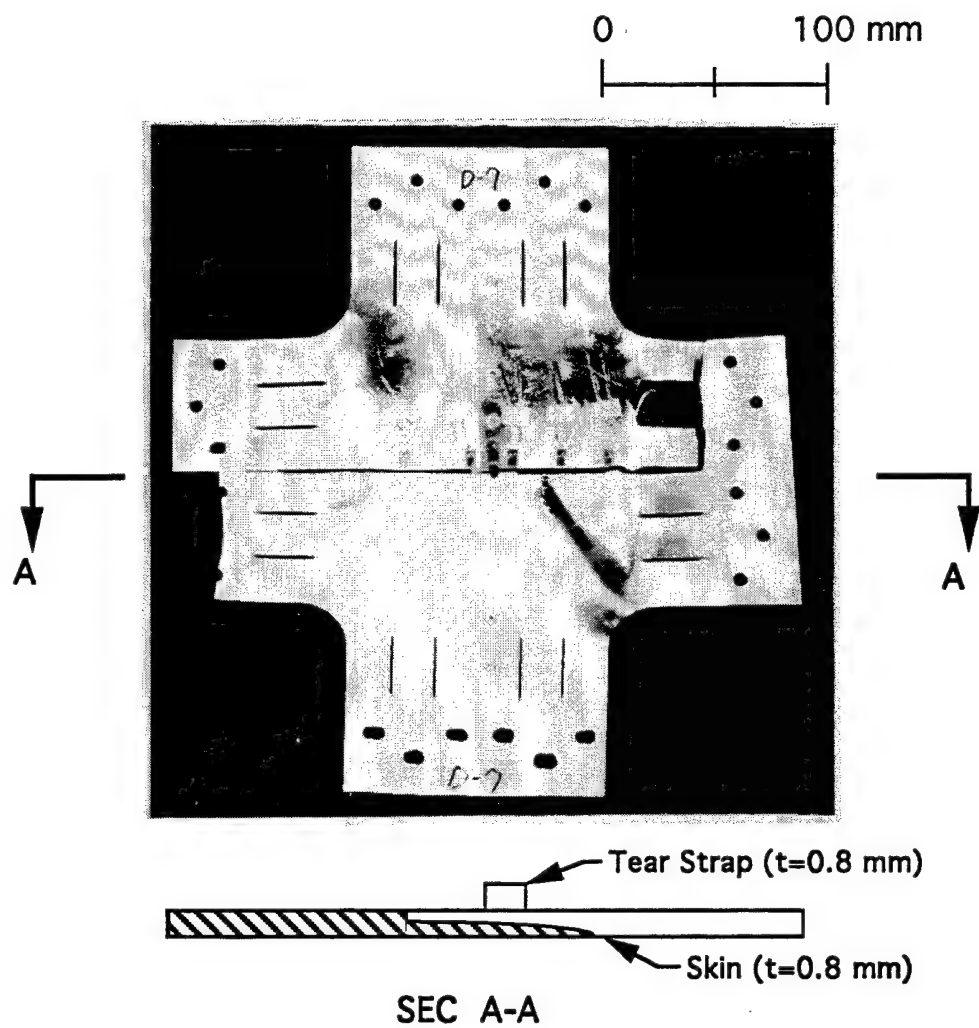


FIGURE 63. PHOTOGRAPH OF SPECIMEN MD-7

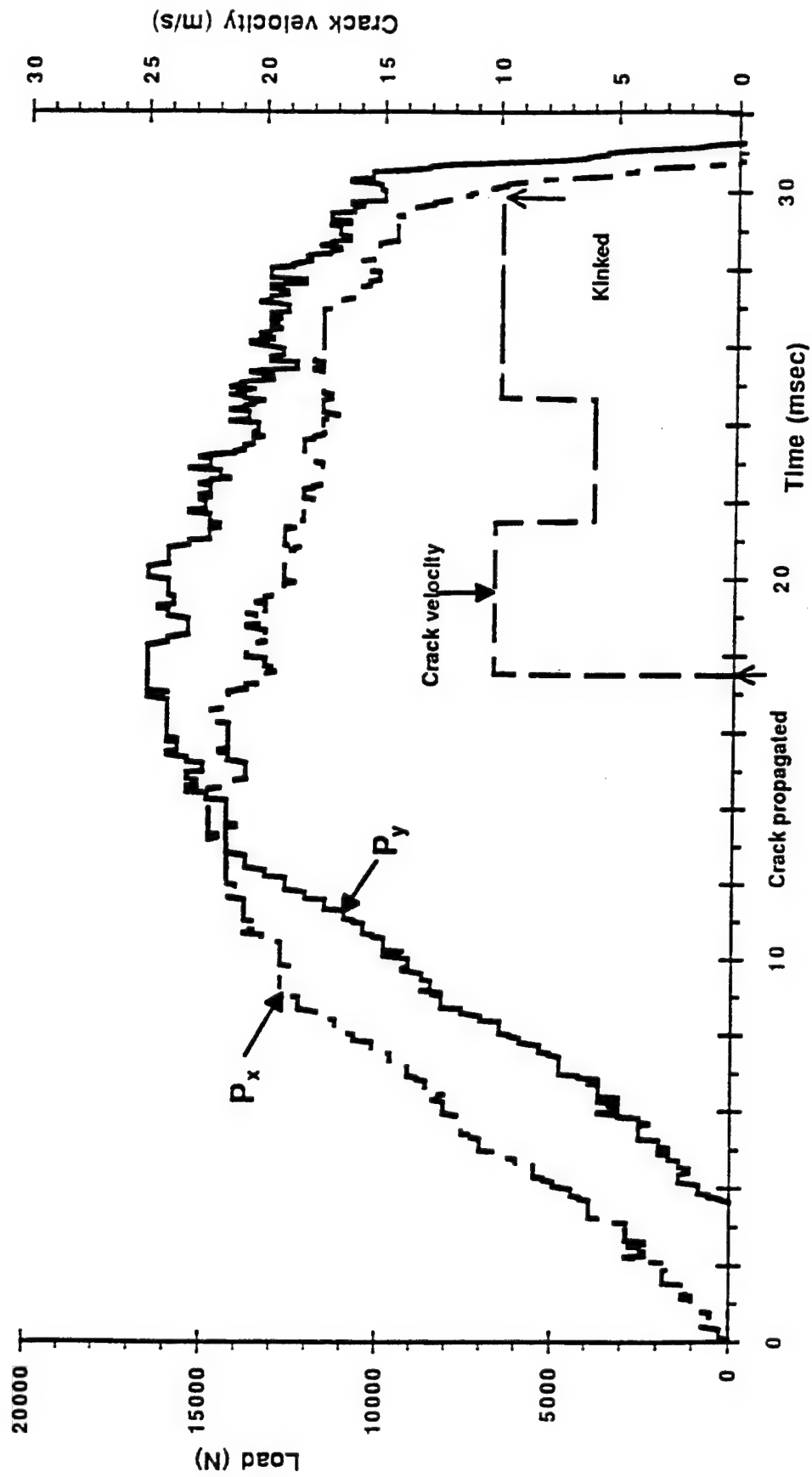


FIGURE 64. VARIATIONS IN P_x AND P_y . SPECIMEN MD-6.

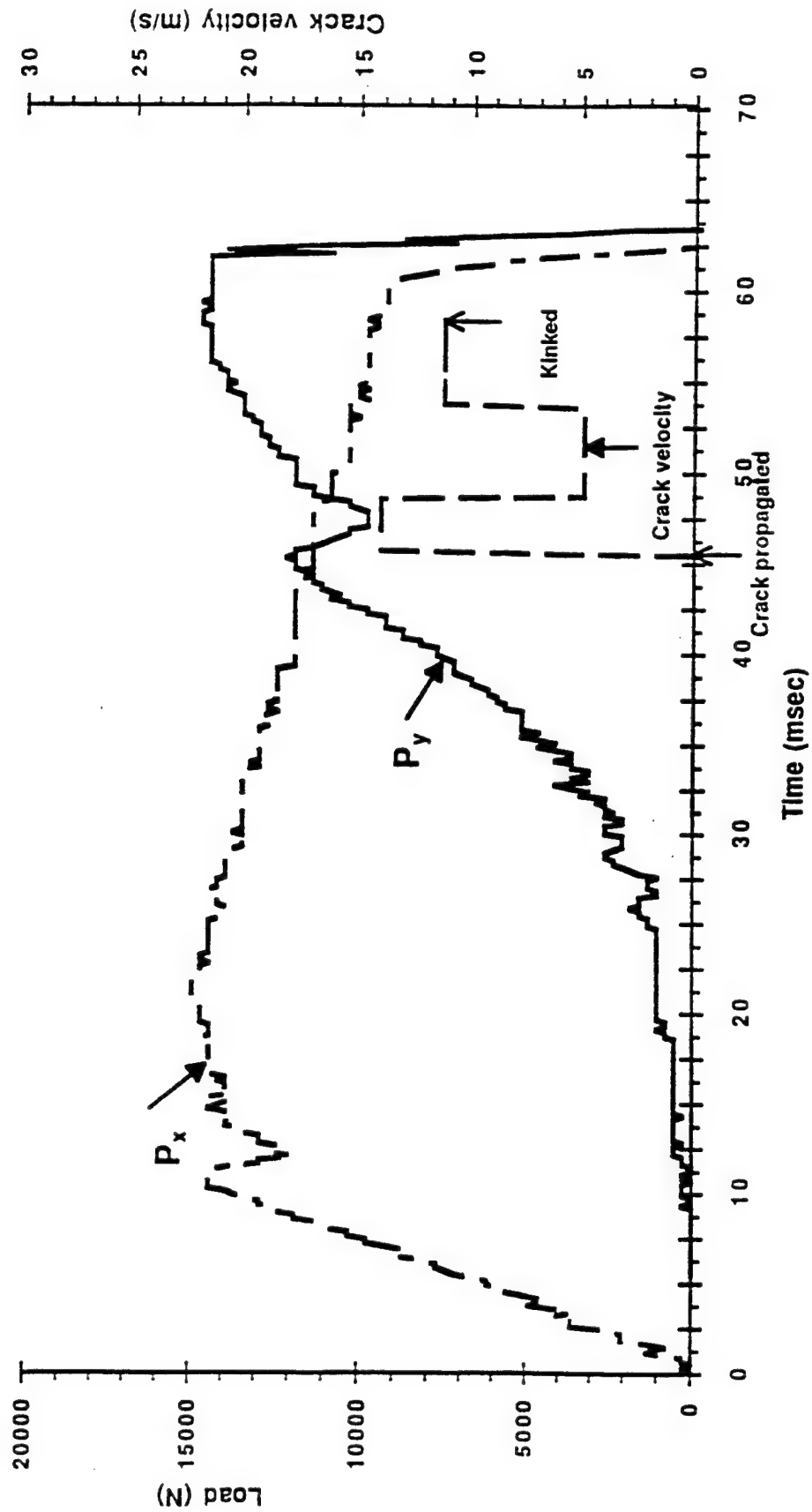


FIGURE 65. VARIATIONS IN P_x AND P_y . SPECIMEN MD-7.

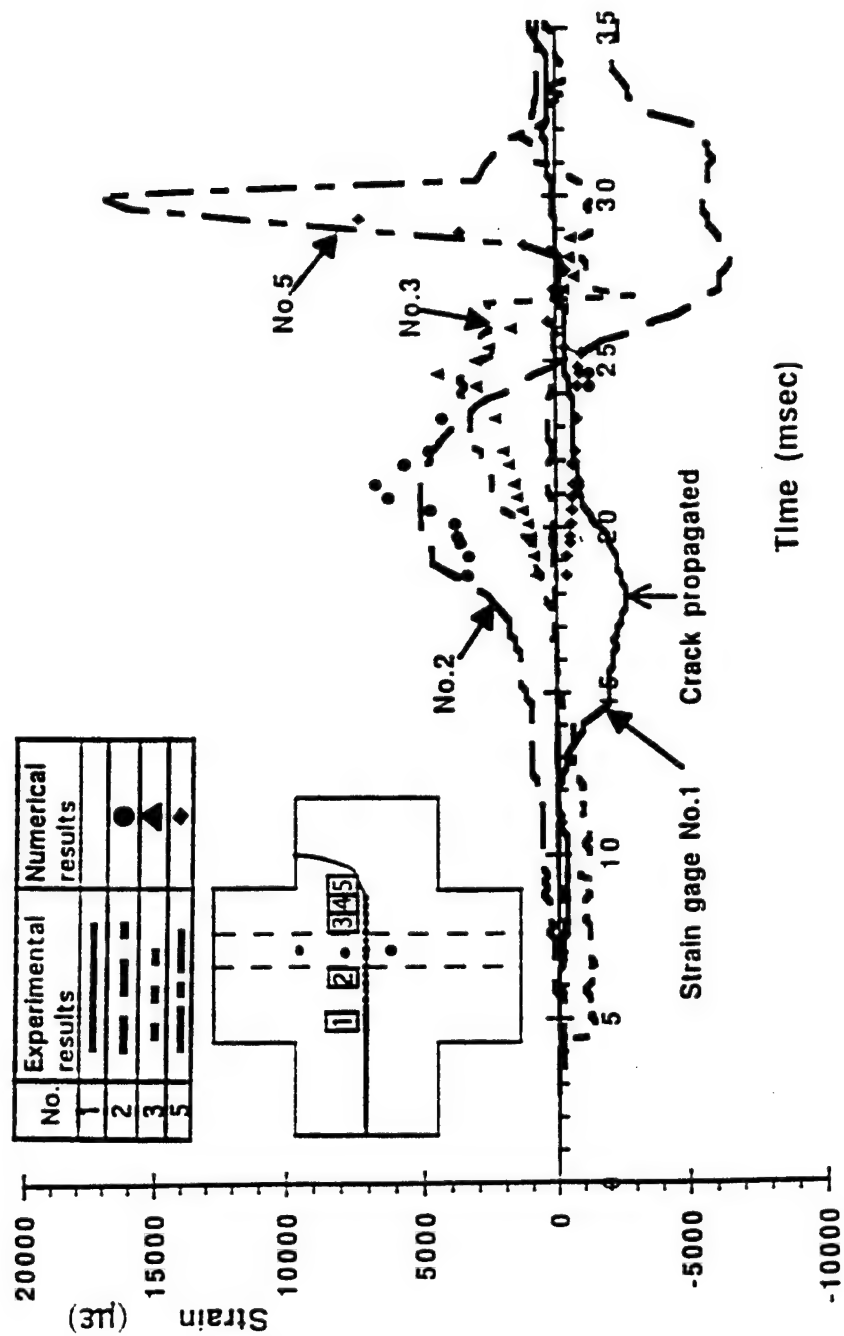


FIGURE 66. STRAIN GAGE RESPONSES. SPECIMEN MD-6.

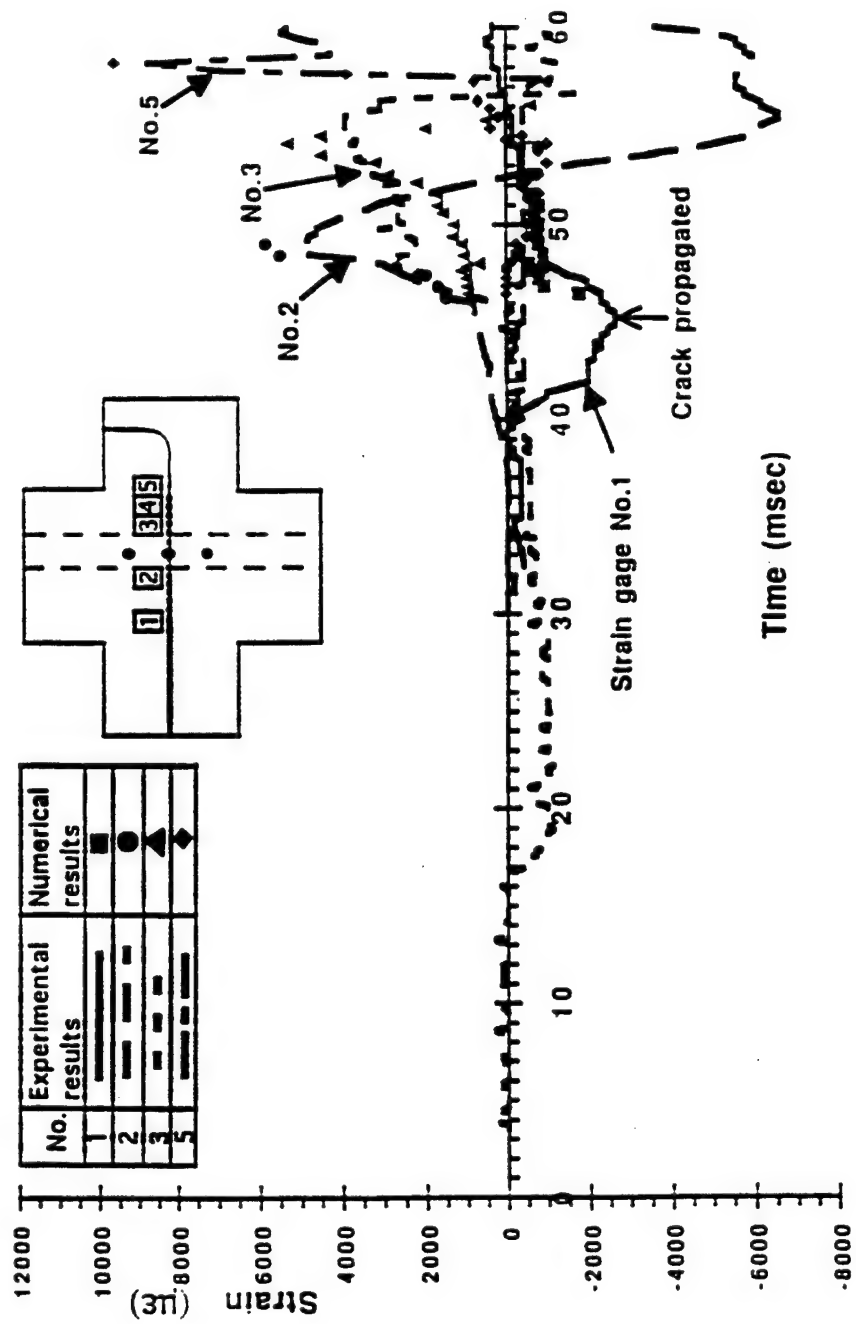


FIGURE 67. STRAIN GAGE RESPONSES. SPECIMEN MD-7.

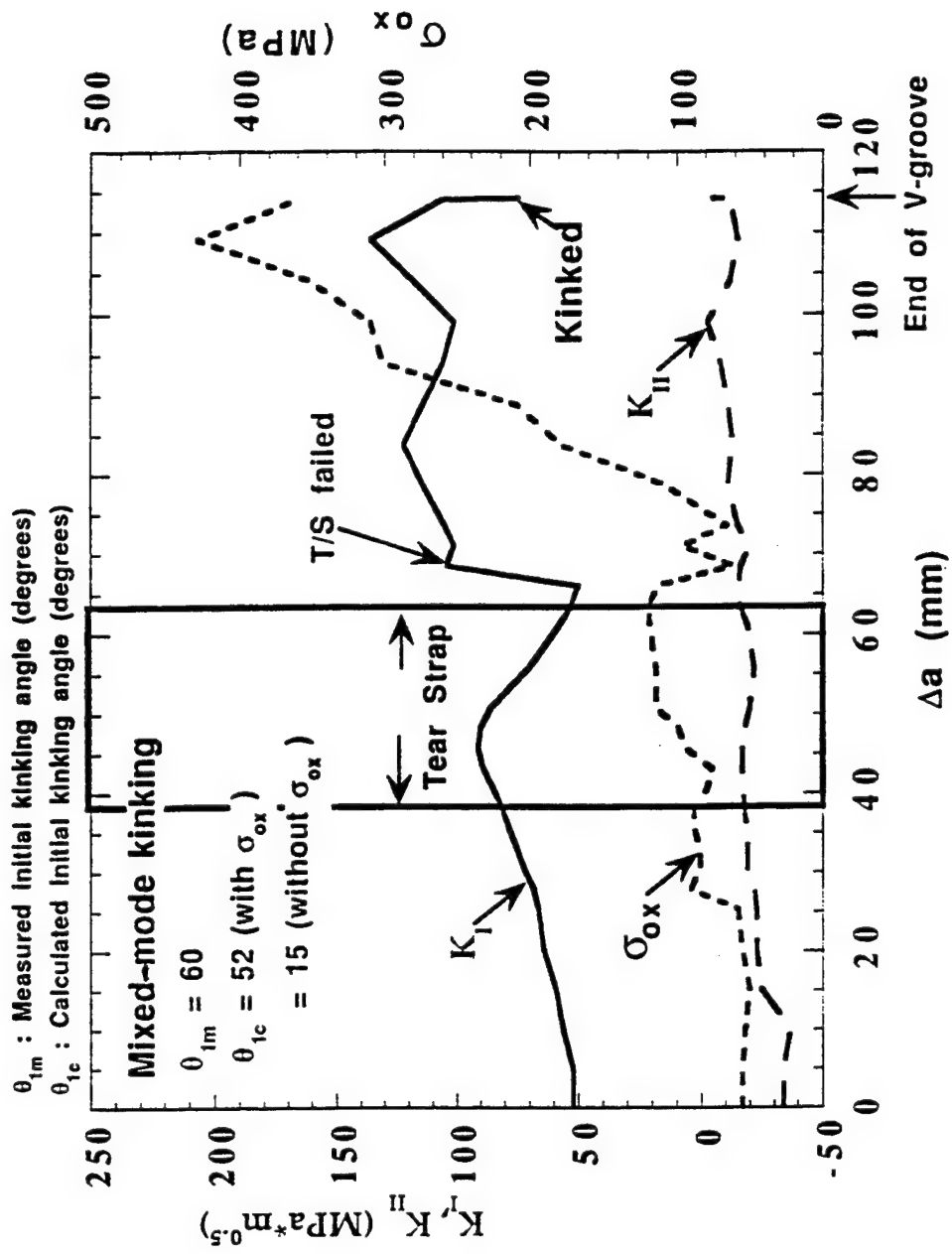


FIGURE 68. VARIATIONS IN K_I , K_{II} , AND σ_{ox} , SPECIMEN MD-6.

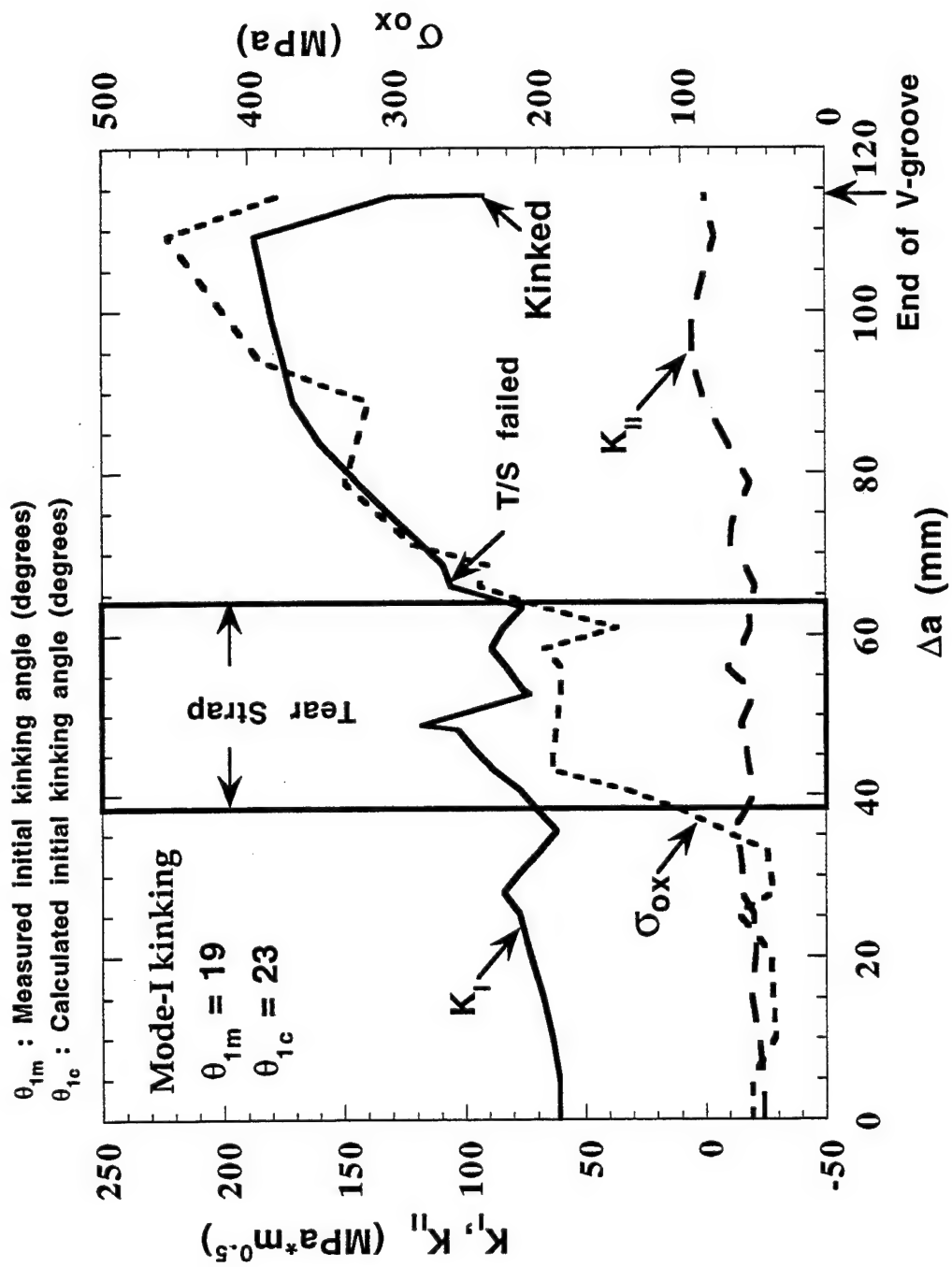


FIGURE 69. VARIATIONS IN K_I , K_{II} , AND σ_{ox} , SPECIMEN MD-7.

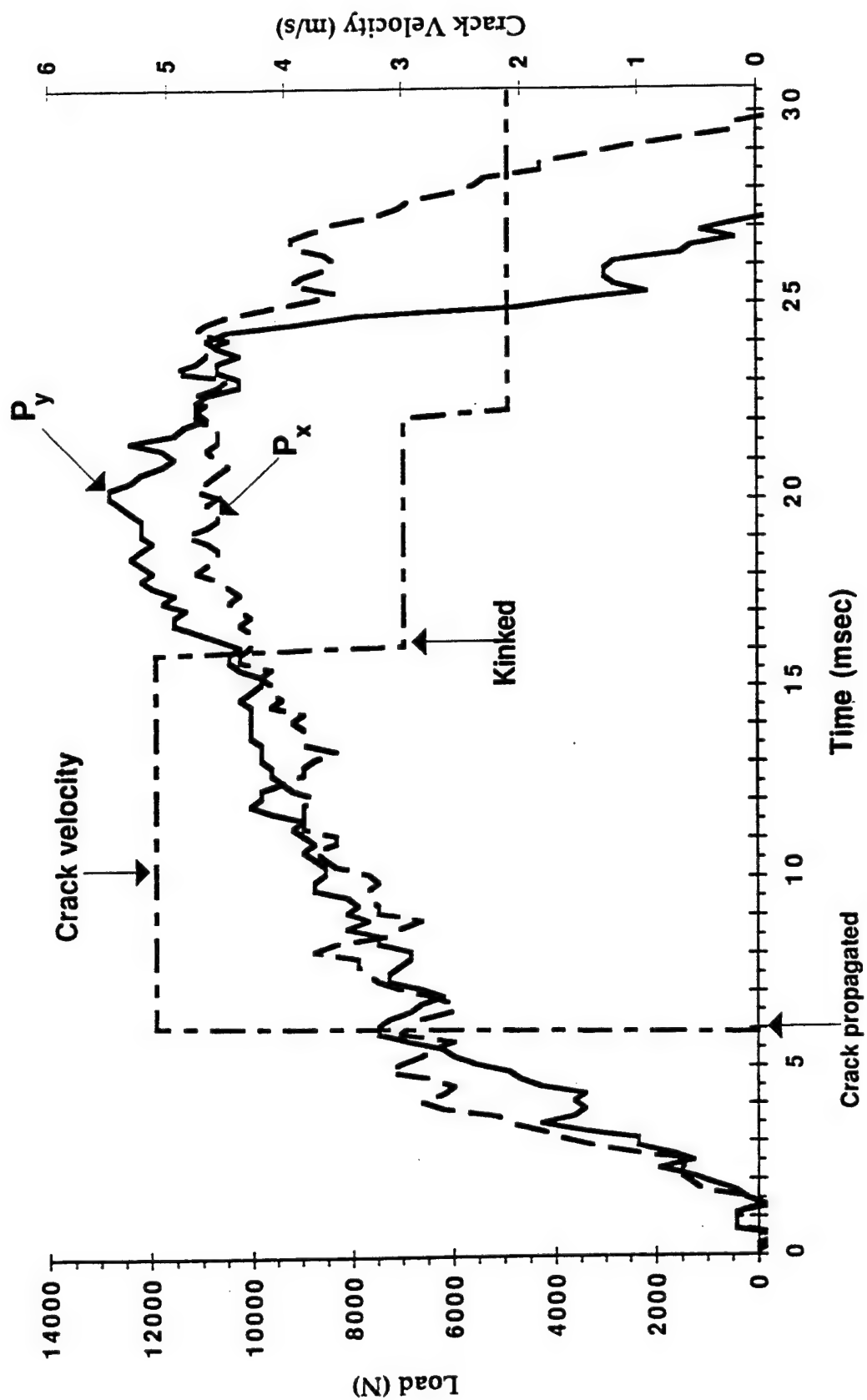


FIGURE 70. VARIATIONS IN P_x AND P_y . SPECIMEN MG-6.

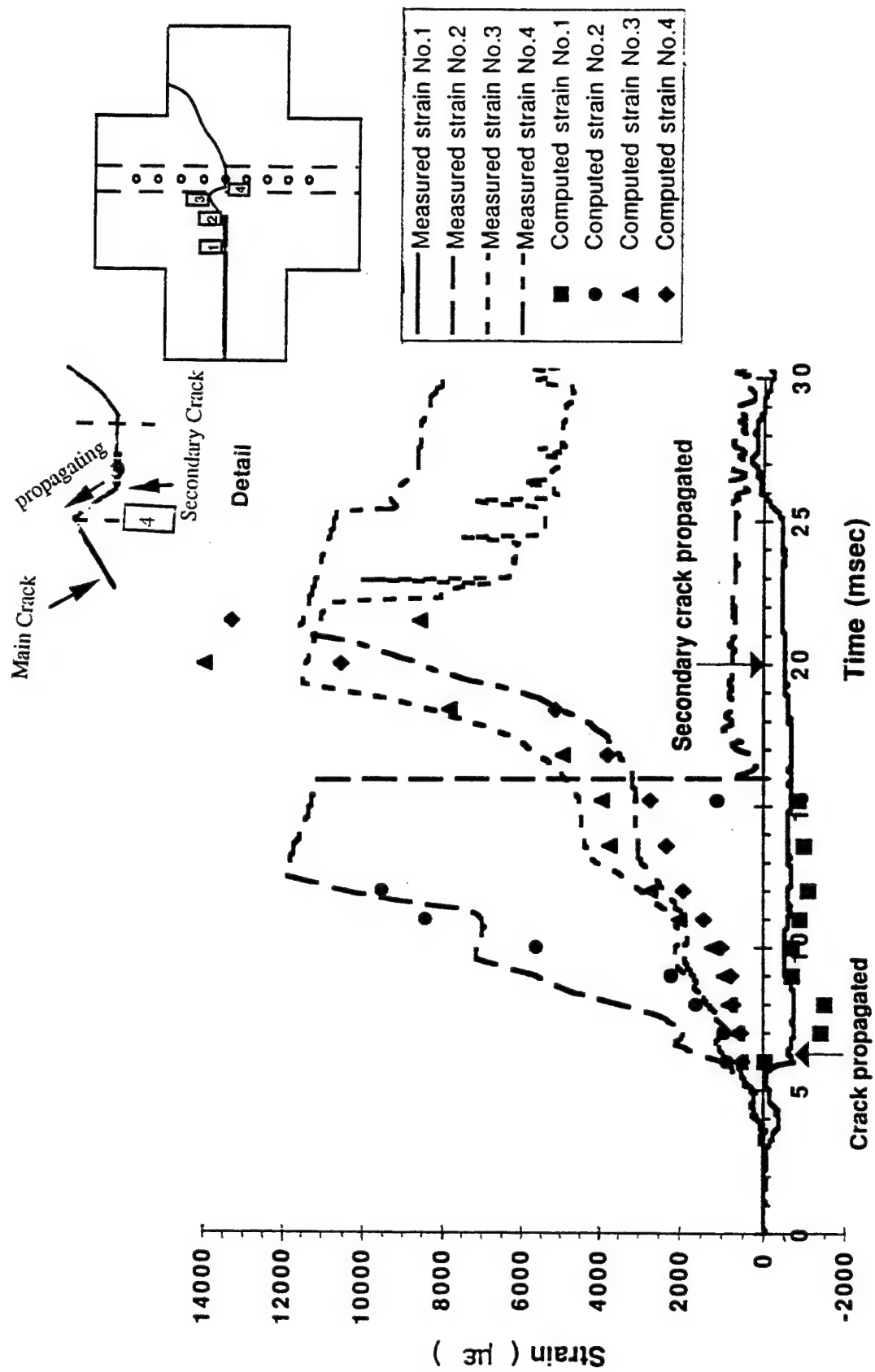


FIGURE 71. STRAIN GAGE RESPONSES. SPECIMEN MG-6.

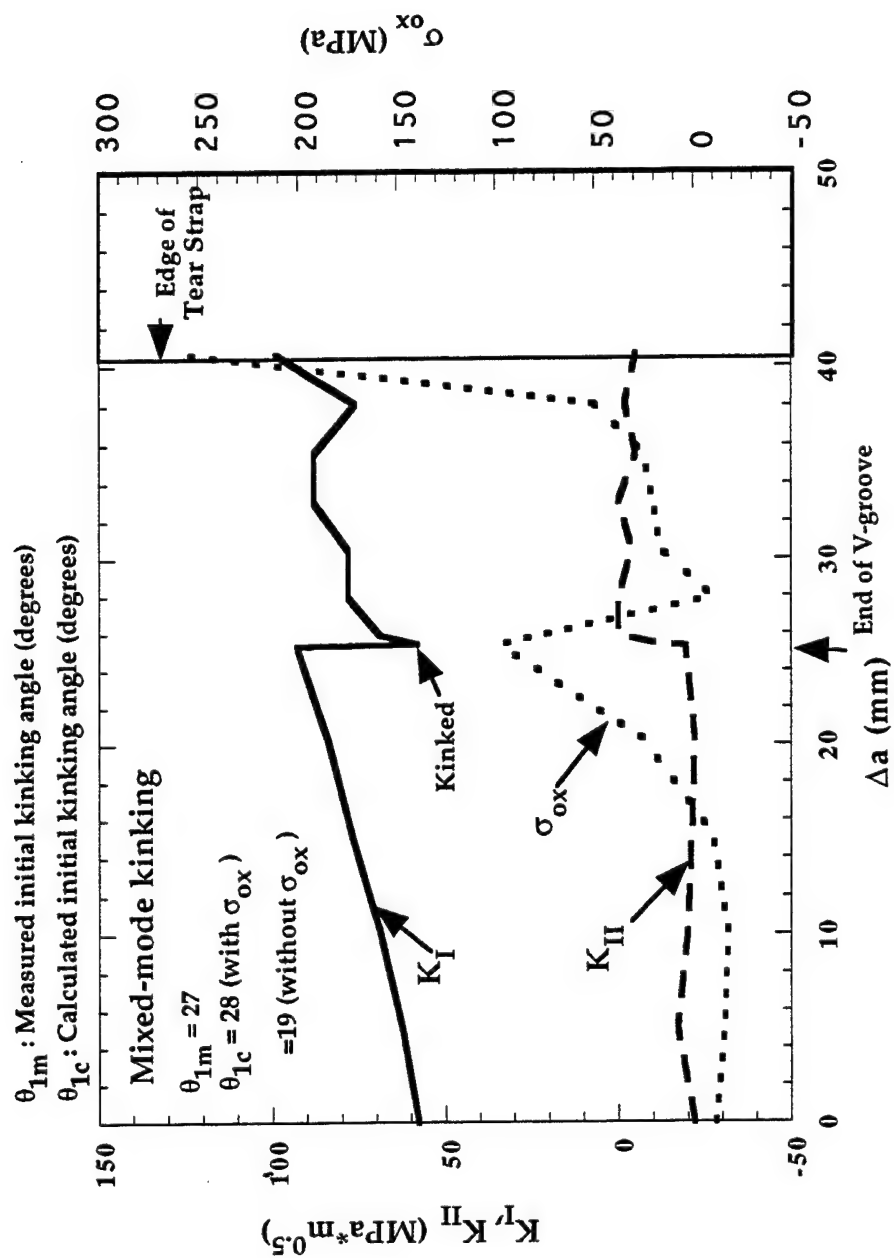


FIGURE 72. VARIATIONS IN K_I , K_{II} , AND σ_{ox} . SPECIMEN MG-6.

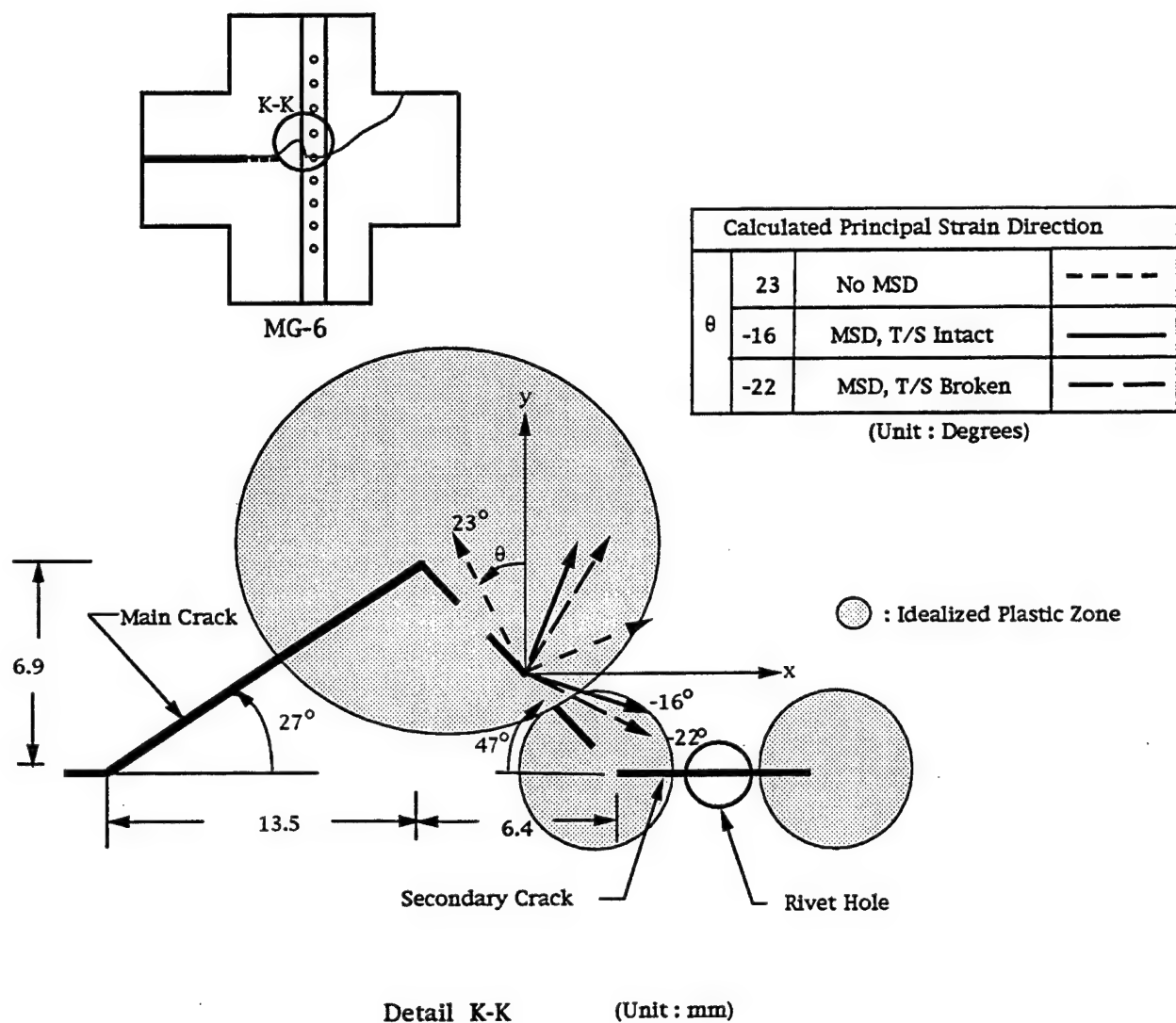


FIGURE 73. DIRECTION OF PRINCIPAL STRAINS. SPECIMEN MG-6.



FIGURE 74. PHOTOGRAPH OF SPECIMEN 1 (TYPE a-1) AFTER RUPTURE.

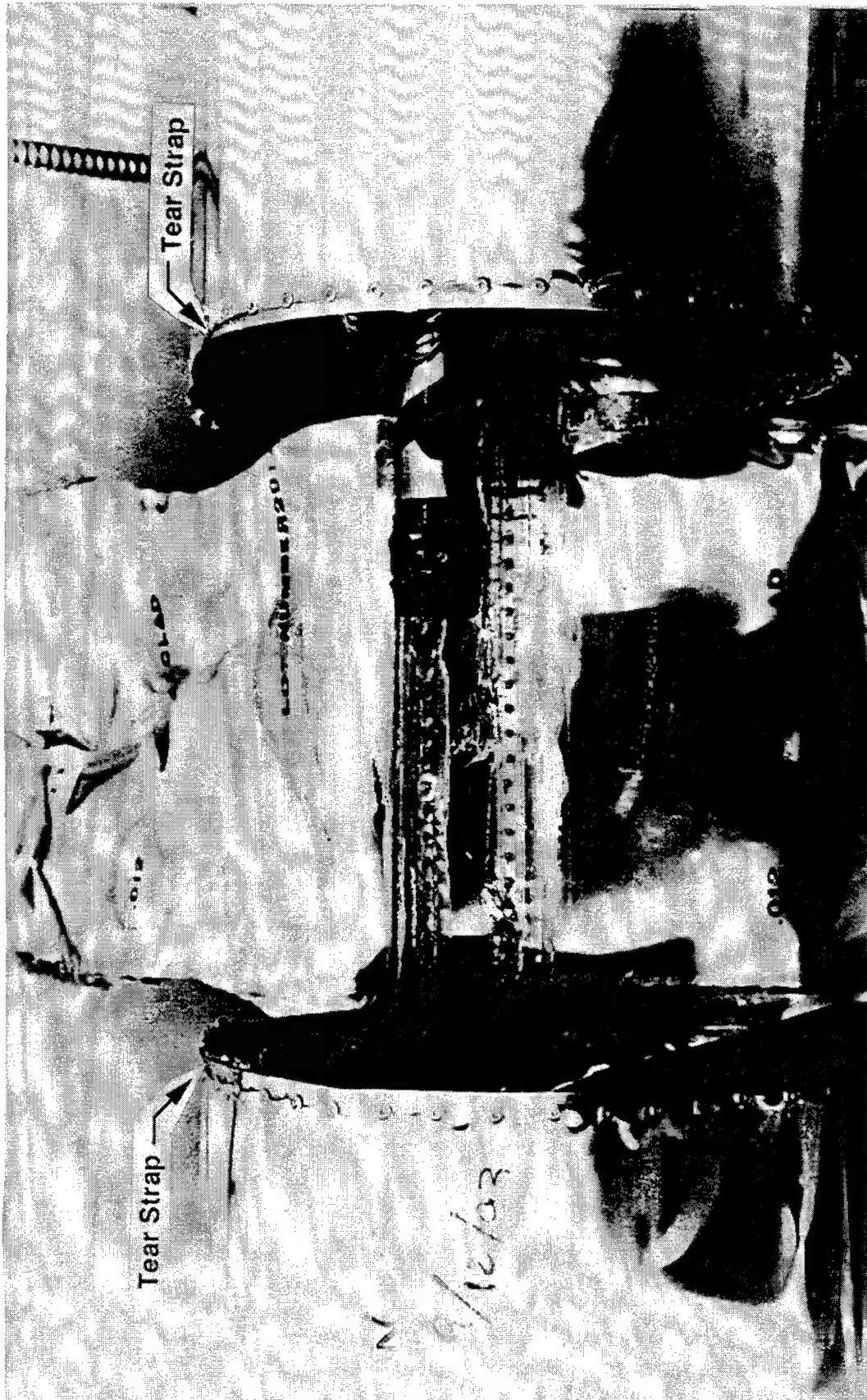


FIGURE 75. PHOTOGRAPH OF SPECIMEN 13 (TYPE c-1) AFTER RUPTURE

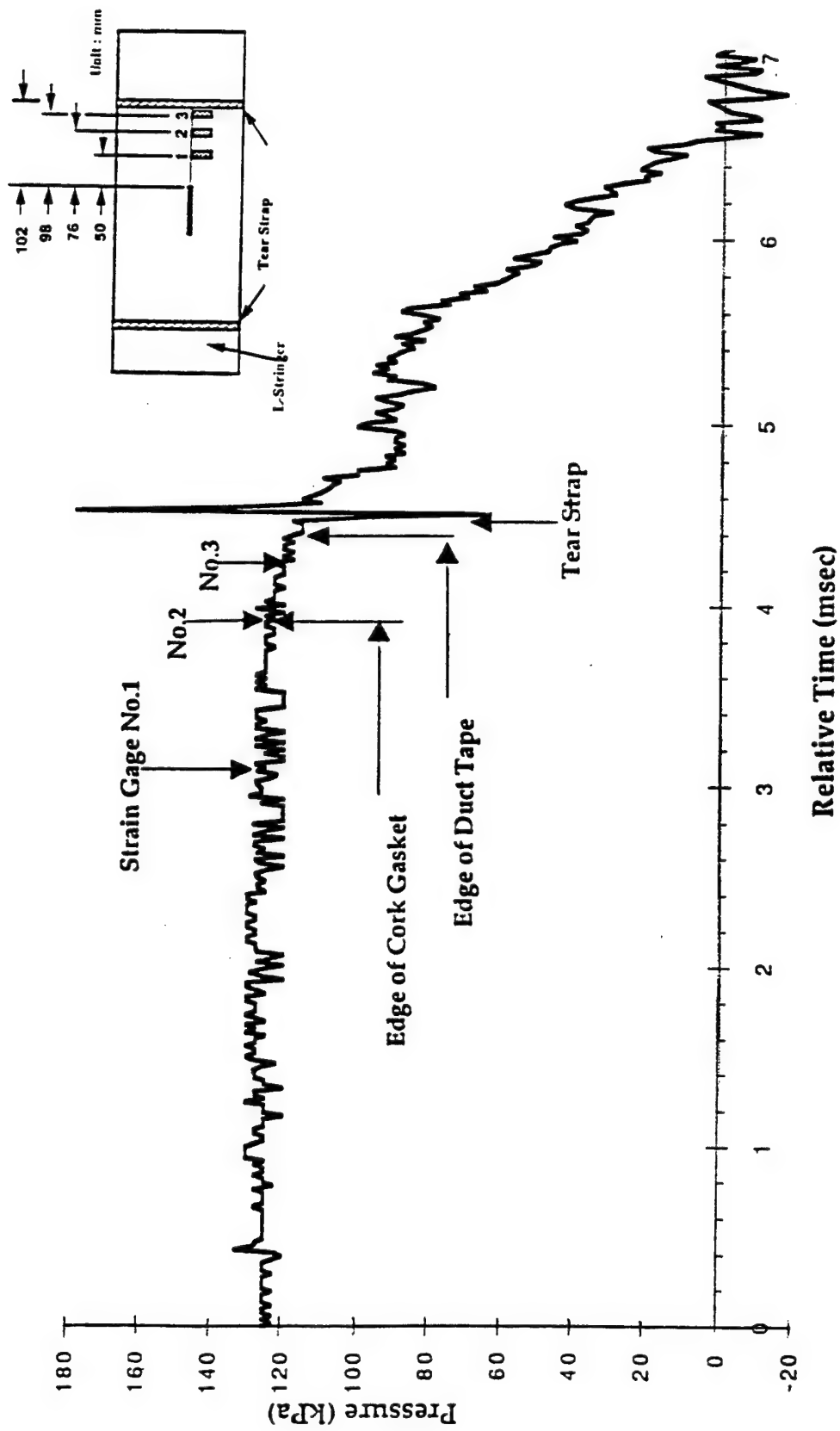


FIGURE 76. PRESSURE-TIME RELATION IN SPECIMEN 13 (TYPE e-1)

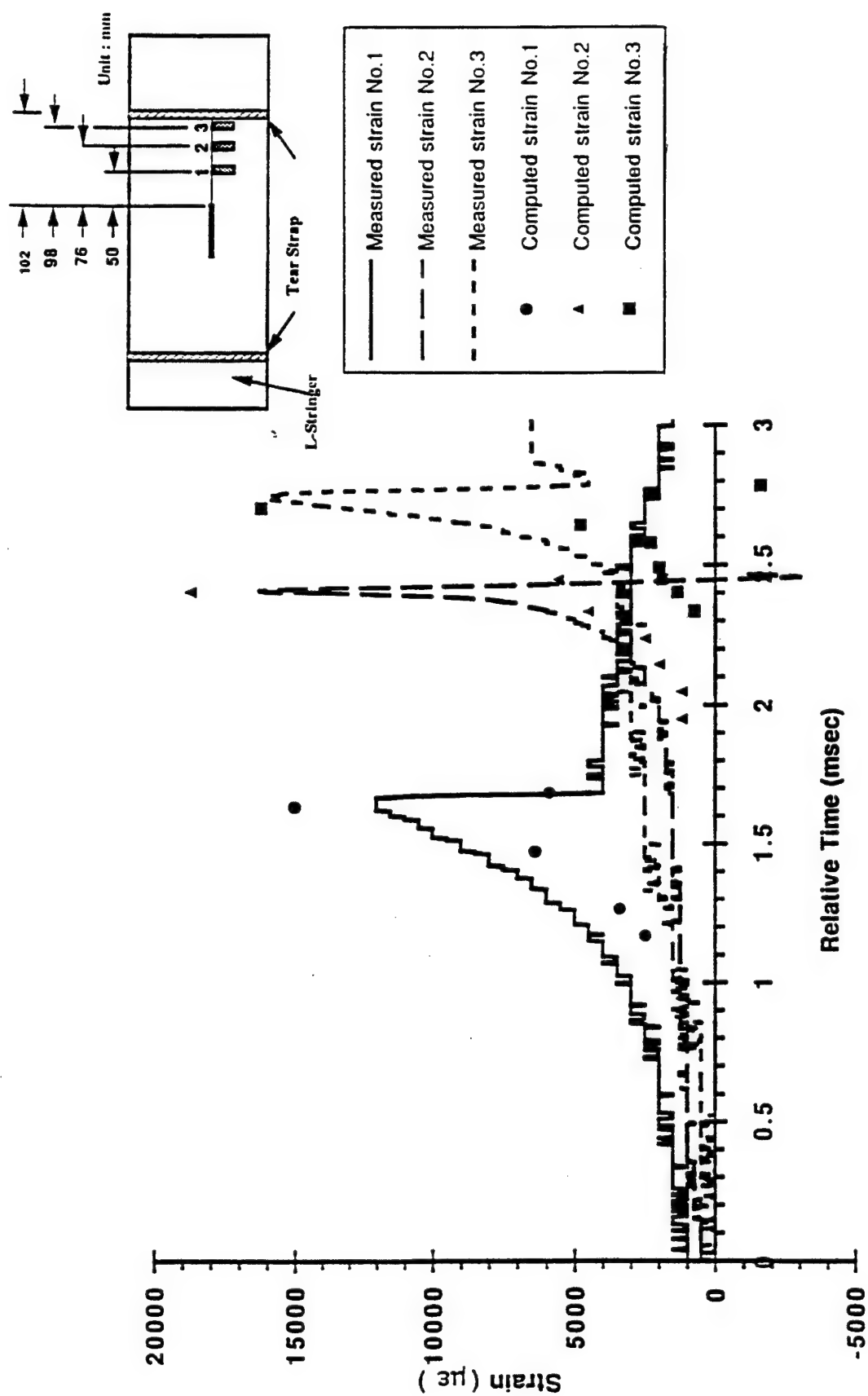


FIGURE 77. STRAIN GAGE RESPONSE IN SPECIMEN 13 (TYPE e-1)

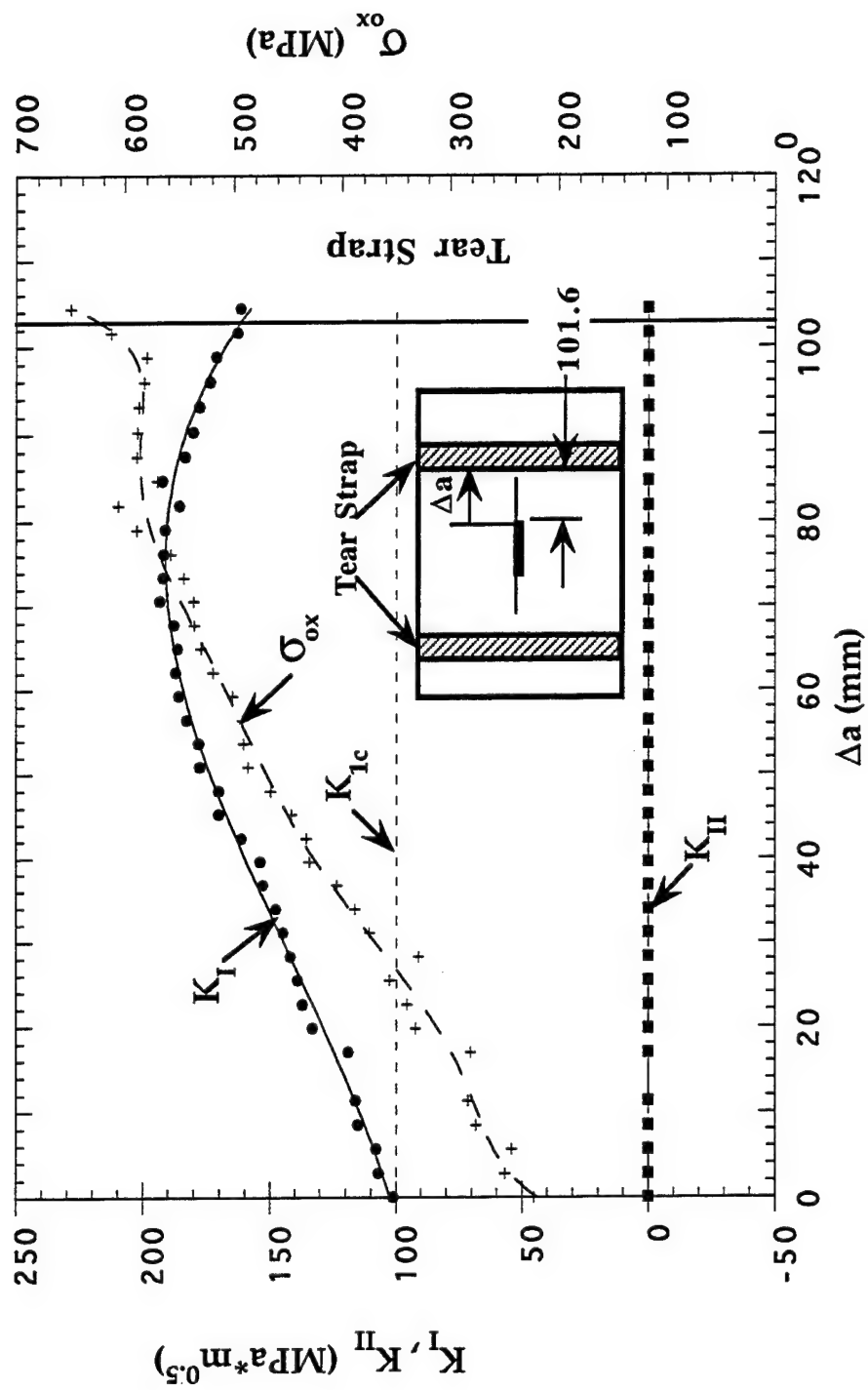


FIGURE 78. VARIATIONS IN K_I , K_{II} , AND σ_{ox} WITH CRACK EXTENSION. SPECIMEN 13 (TYPE e-1).

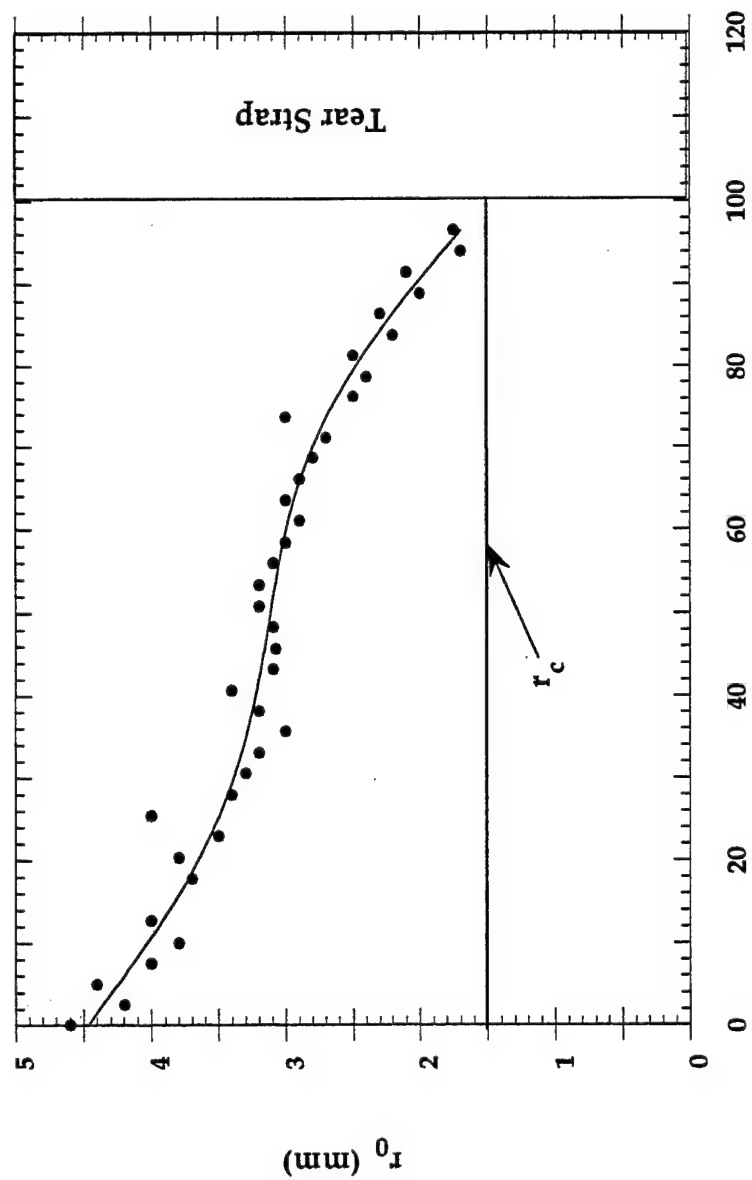


FIGURE 79. VARIATIONS IN r_0 WITH CRACK EXTENSION.
SPECIMEN 13 (TYPE e-1).

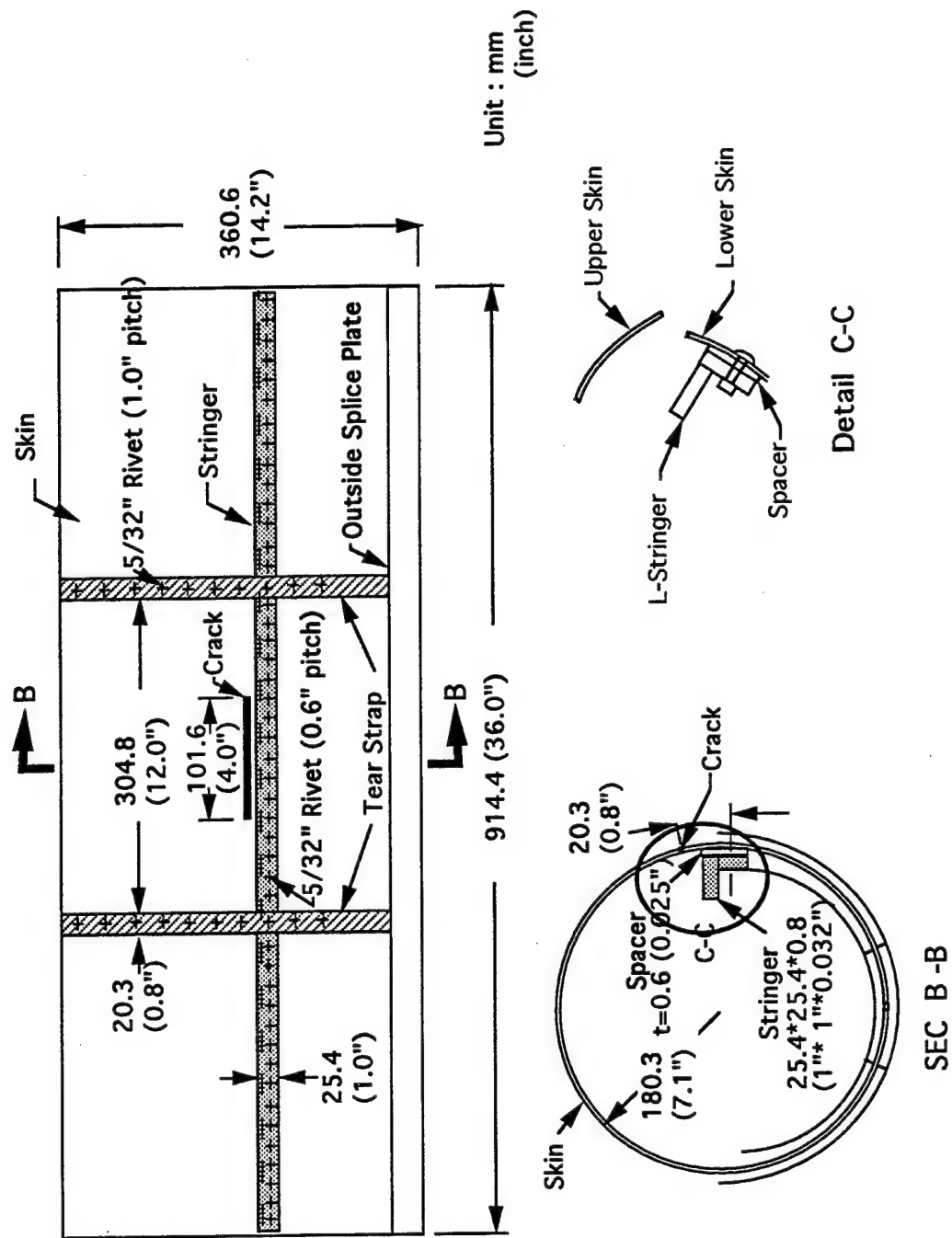


FIGURE 80. SCHEMATIC DRAWING OF ONE-SIDED CRACK OPENING

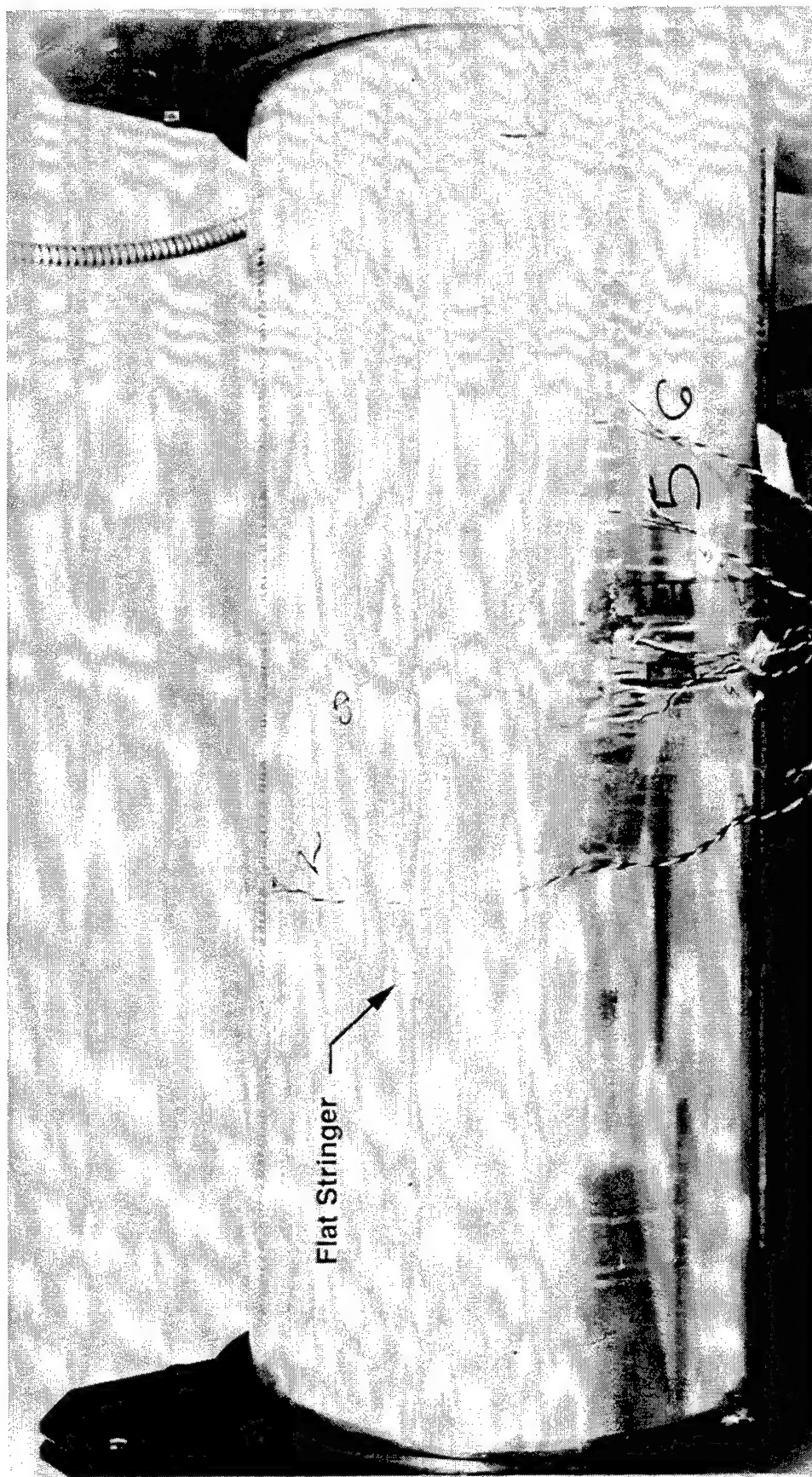


FIGURE 81. PHOTOGRAPH OF SPECIMEN 4 (TYPE b-1) BEFORE RUPTURE

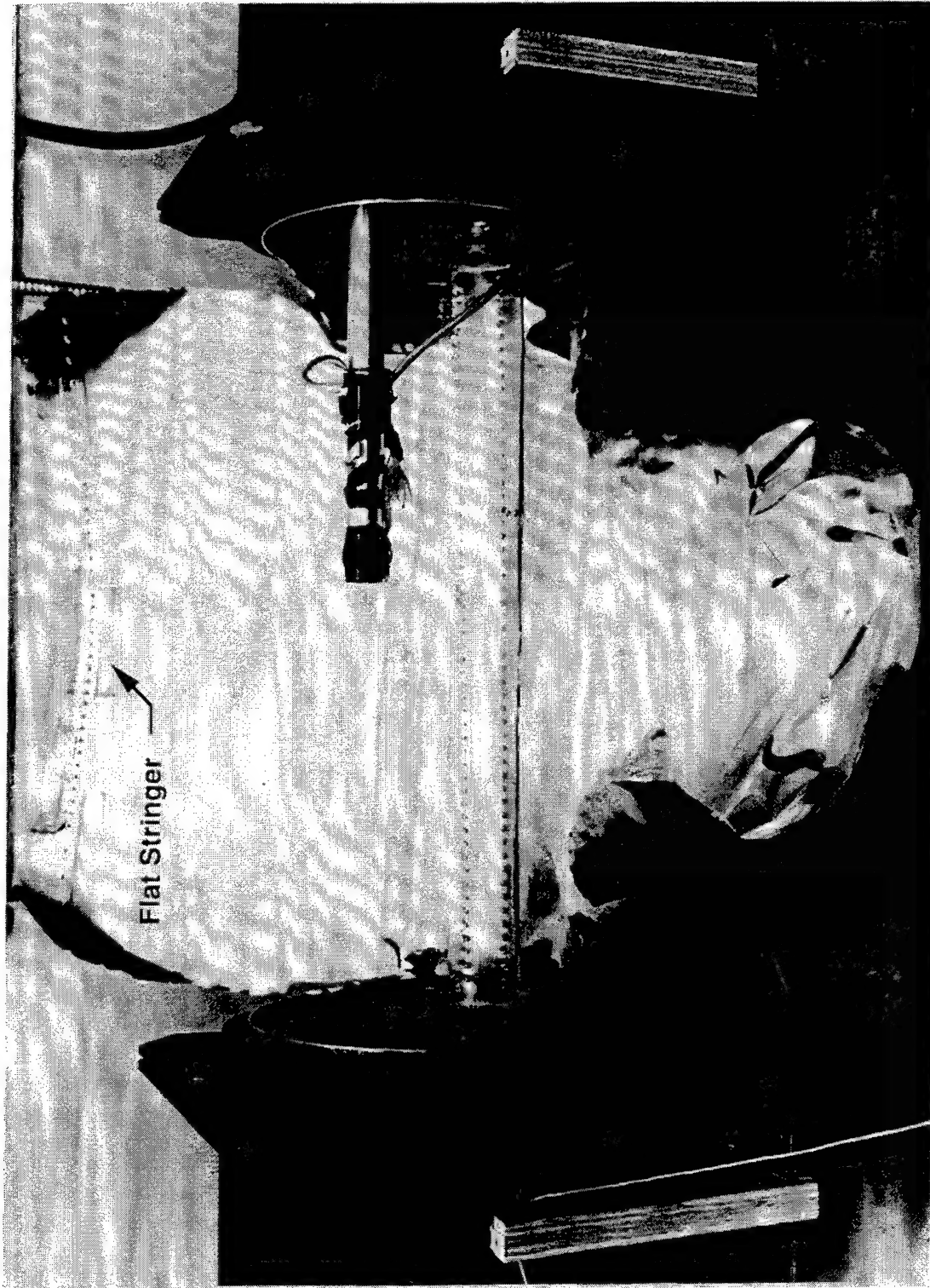


FIGURE 82. PHOTOGRAPH OF SPECIMEN 4 (TYPE b-1) AFTER RUPTURE

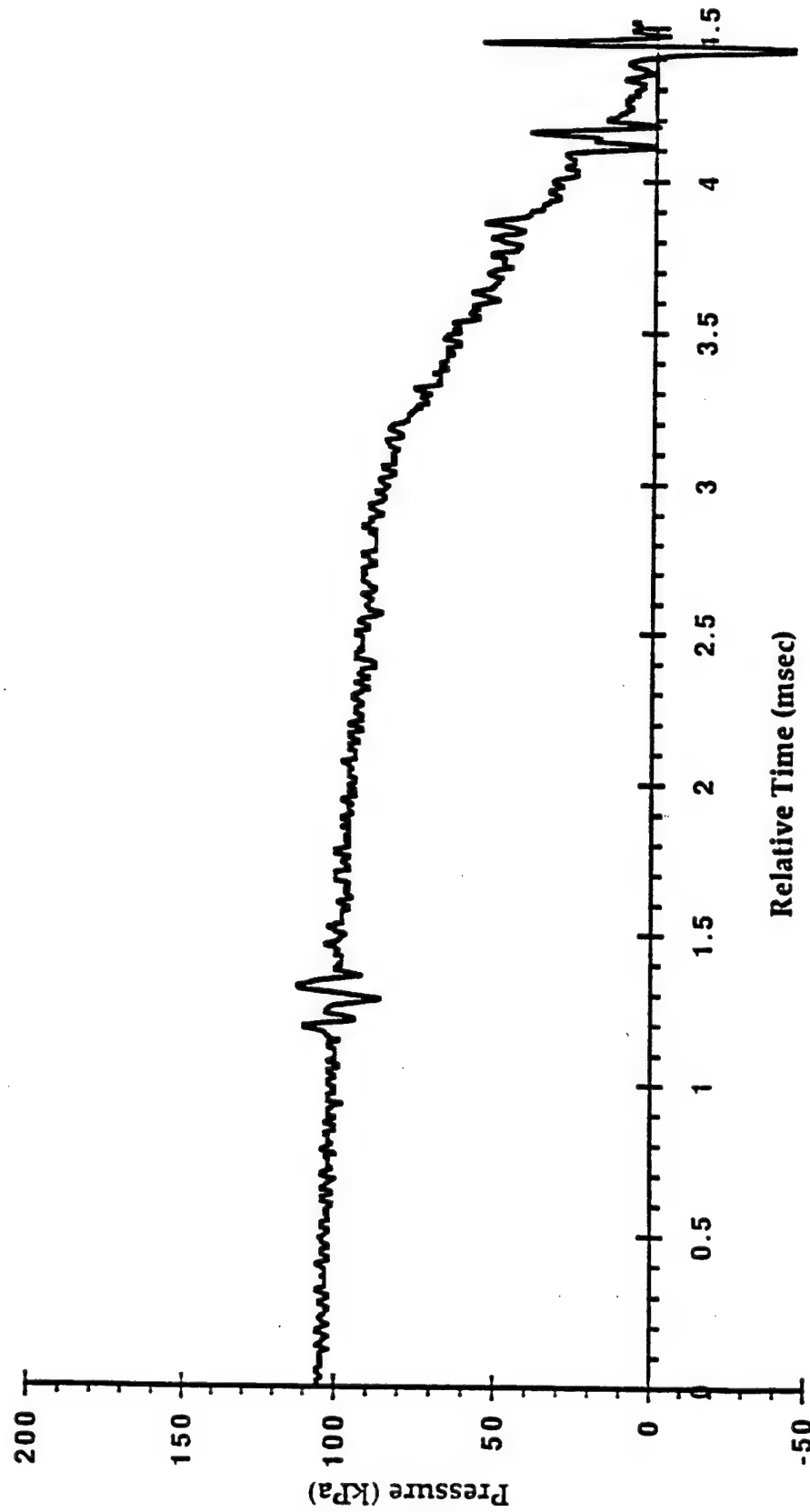


FIGURE 83. PRESSURE-TIME RELATION IN SPECIMEN 4 (TYPE b-1)

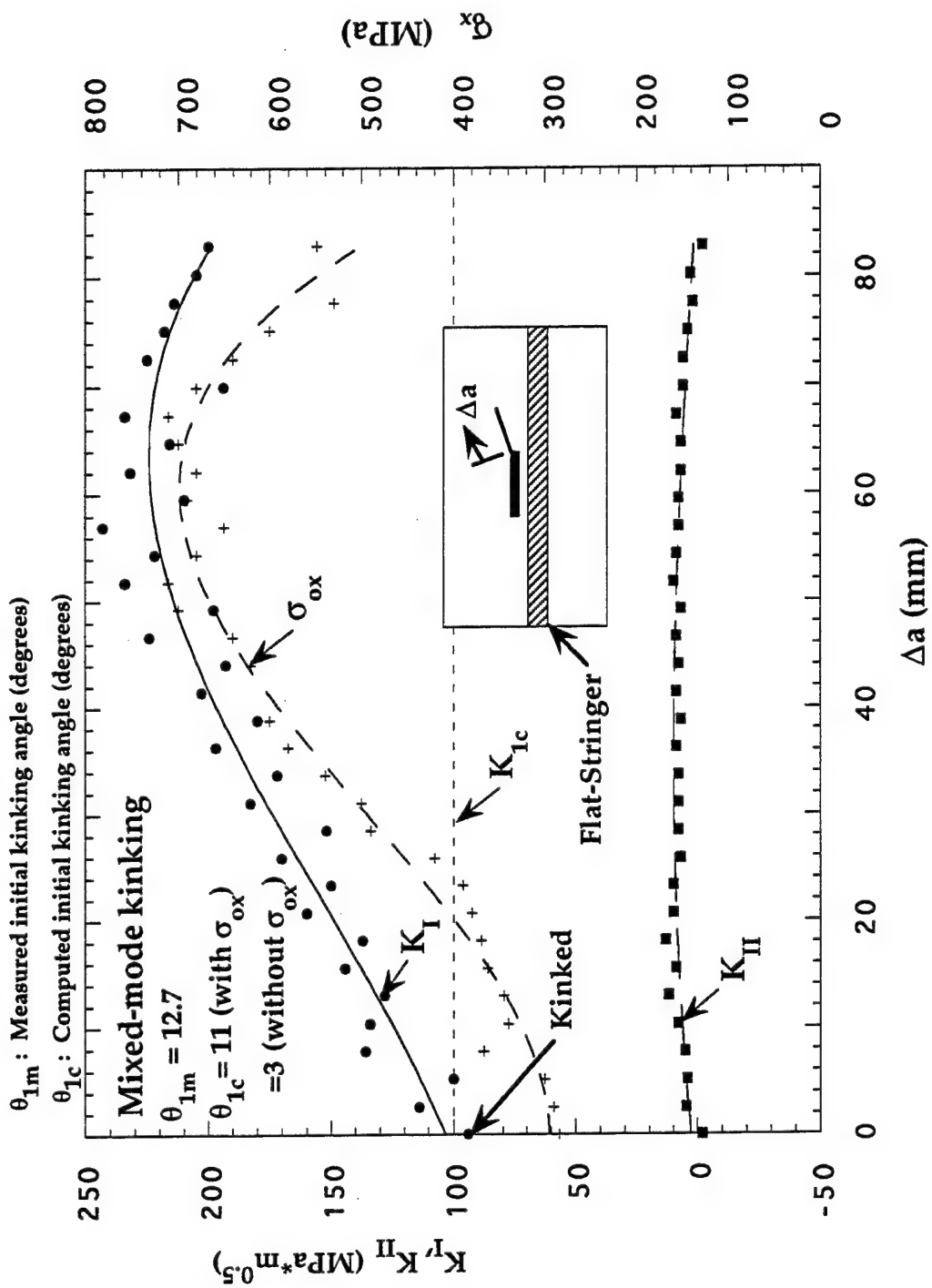


FIGURE 84. VARIATIONS IN K_I , K_{II} , AND σ_{ox} WITH CRACK EXTENSION. SPECIMEN 4 (TYPE b-1).

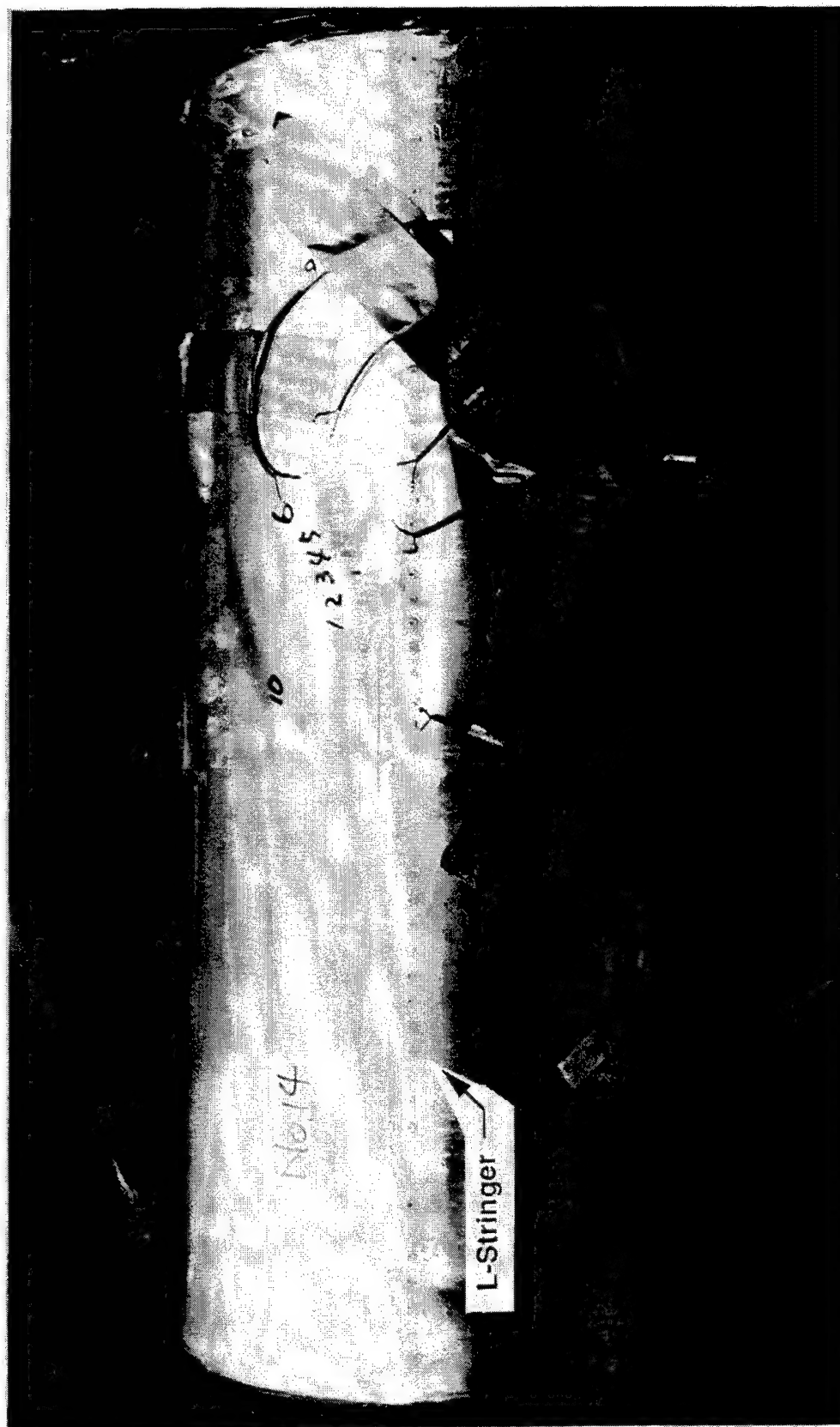


FIGURE 85. PHOTOGRAPH OF SPECIMEN 14 (TYPE b-2) BEFORE RUPTURE .

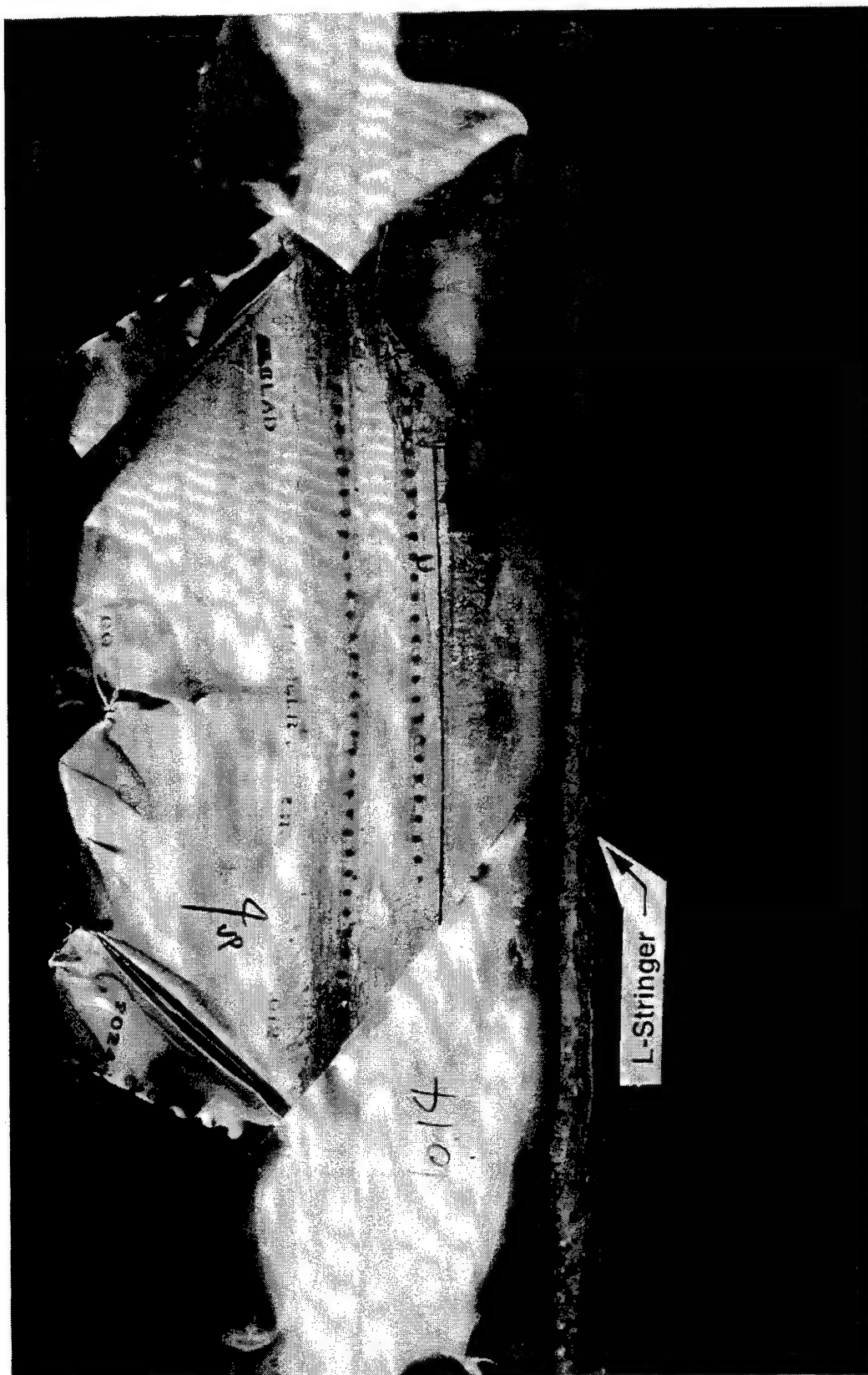


FIGURE 86. PHOTOGRAPH OF SPECIMEN 14 (TYPE b-2) AFTER RUPTURE

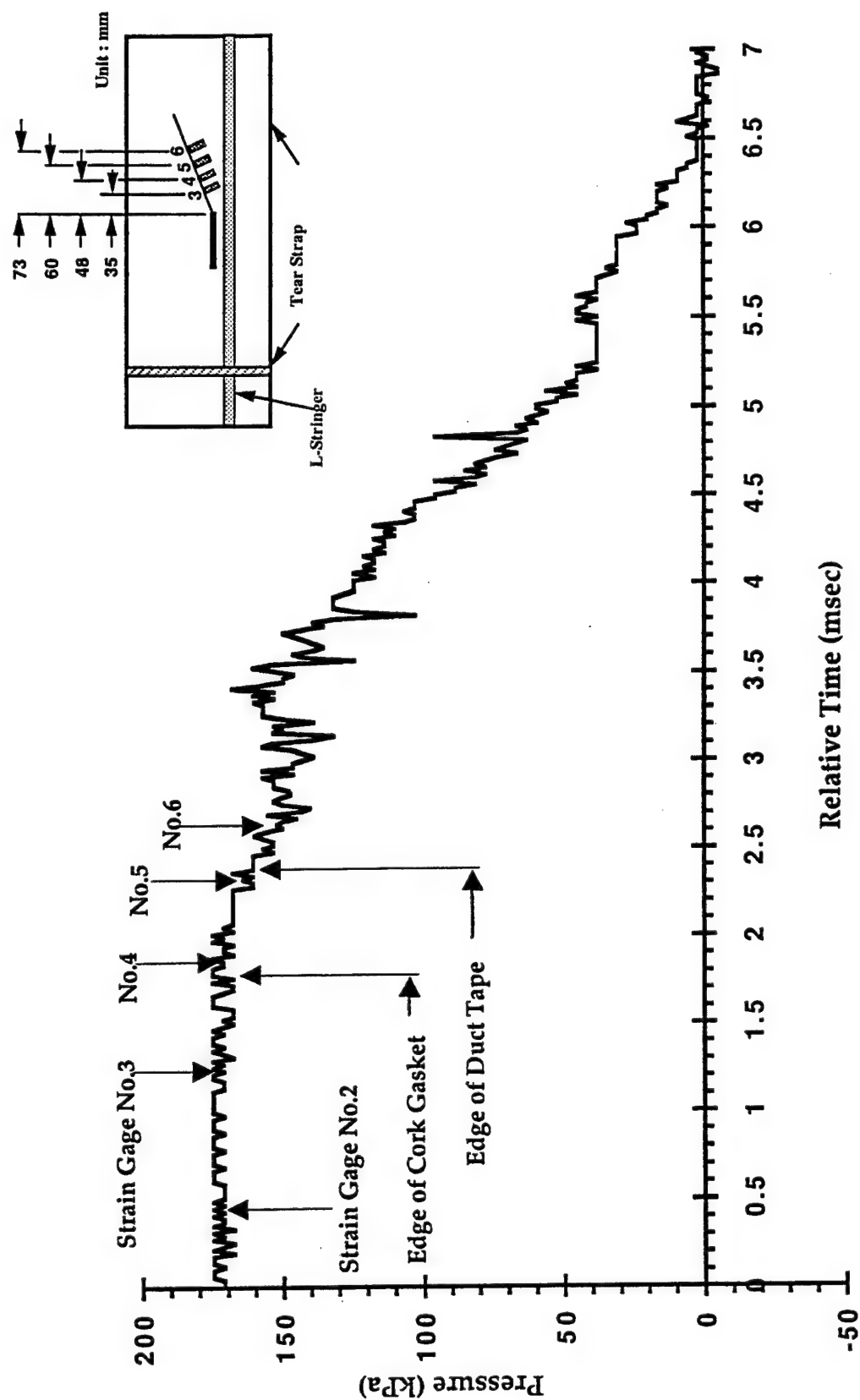


FIGURE 87. PRESSURE-TIME RELATION IN SPECIMEN 14 (TYPE b-2)

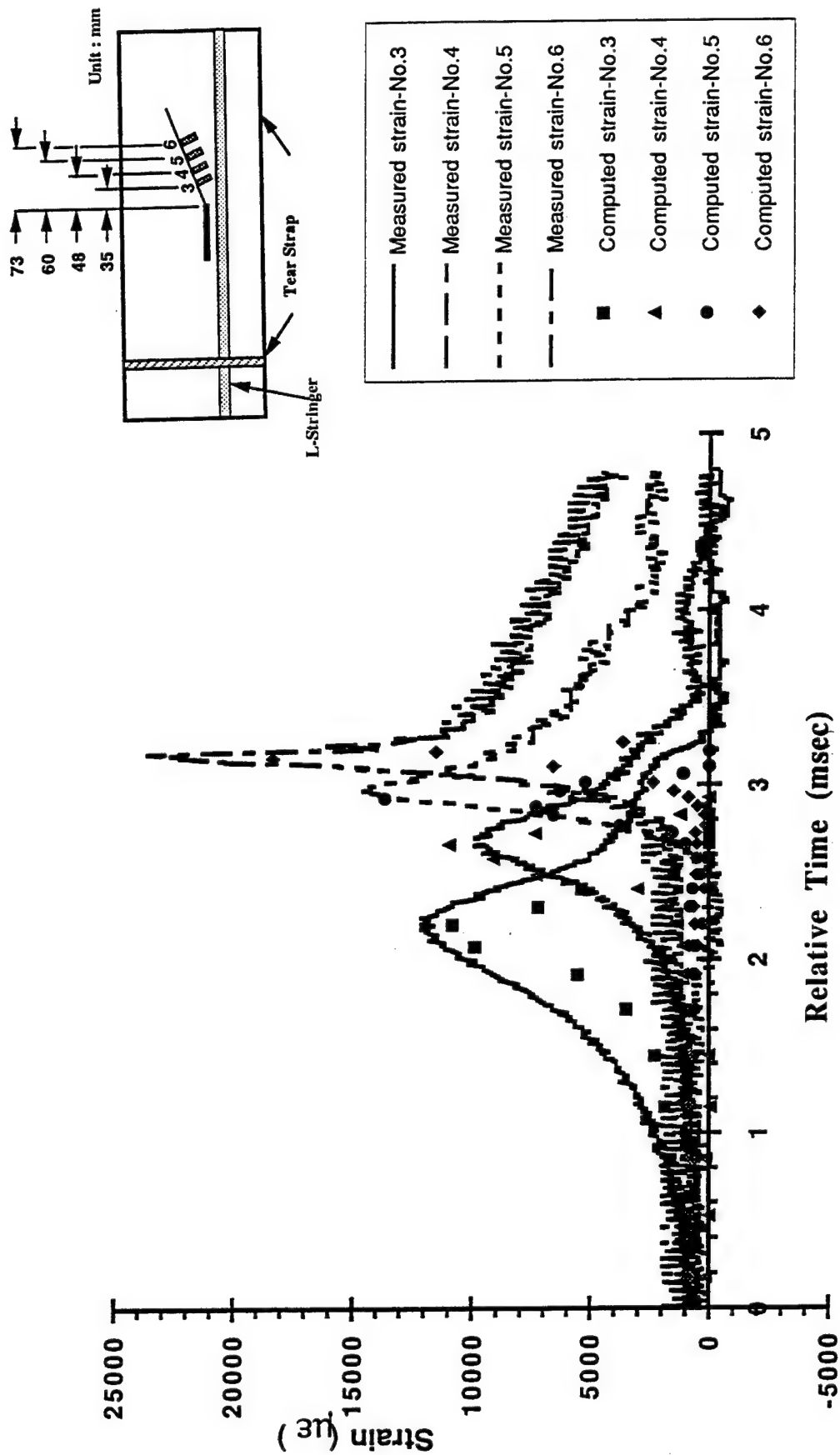


FIGURE 88. STRAIN GAGE RESPONSE IN SPECIMEN 14 (TYPE b-2)

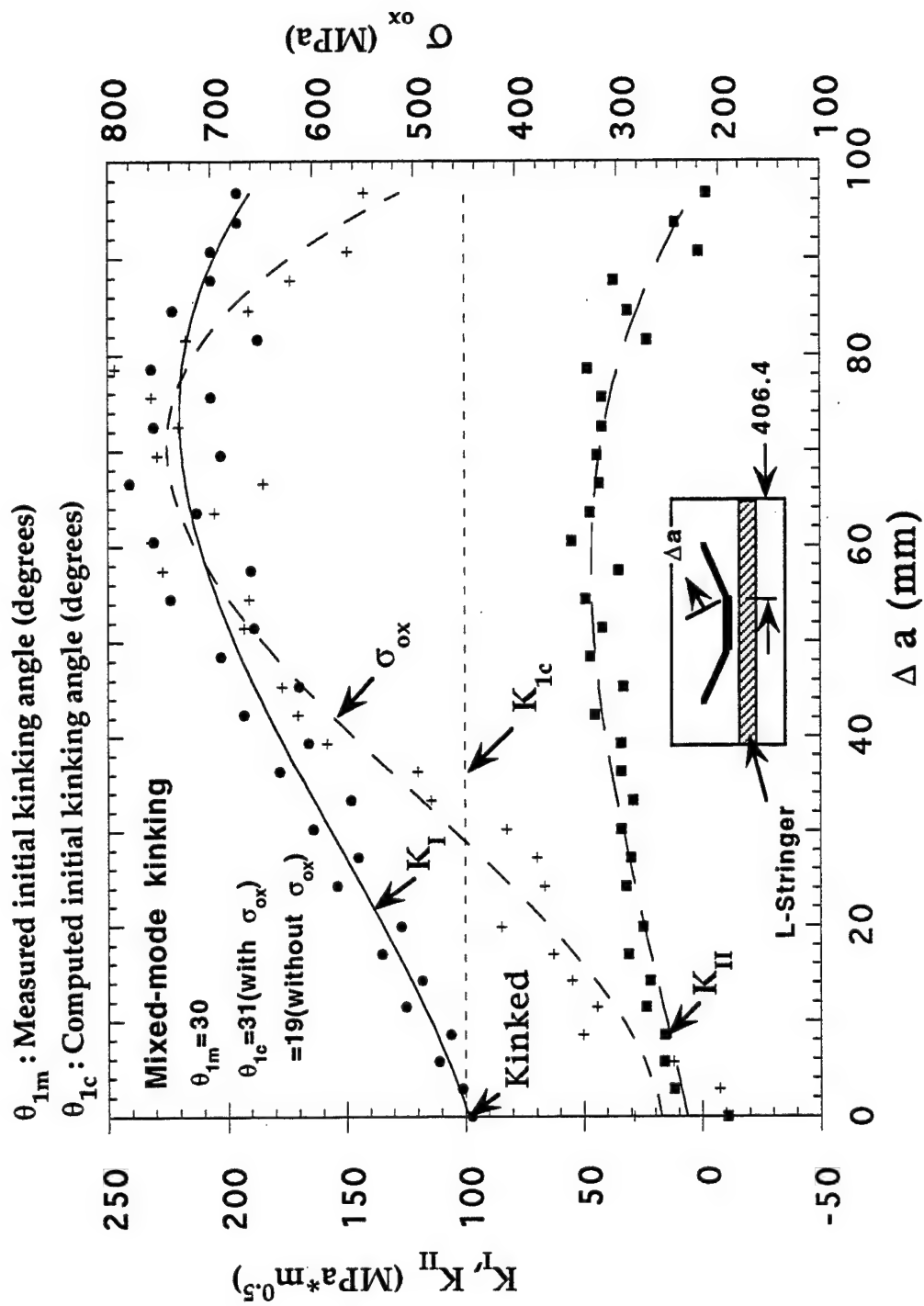


FIGURE 89. VARIATIONS IN K_I , K_{II} , AND σ_{ox} WITH CRACK EXTENSION. SPECIMEN 14 (TYPE b-2).

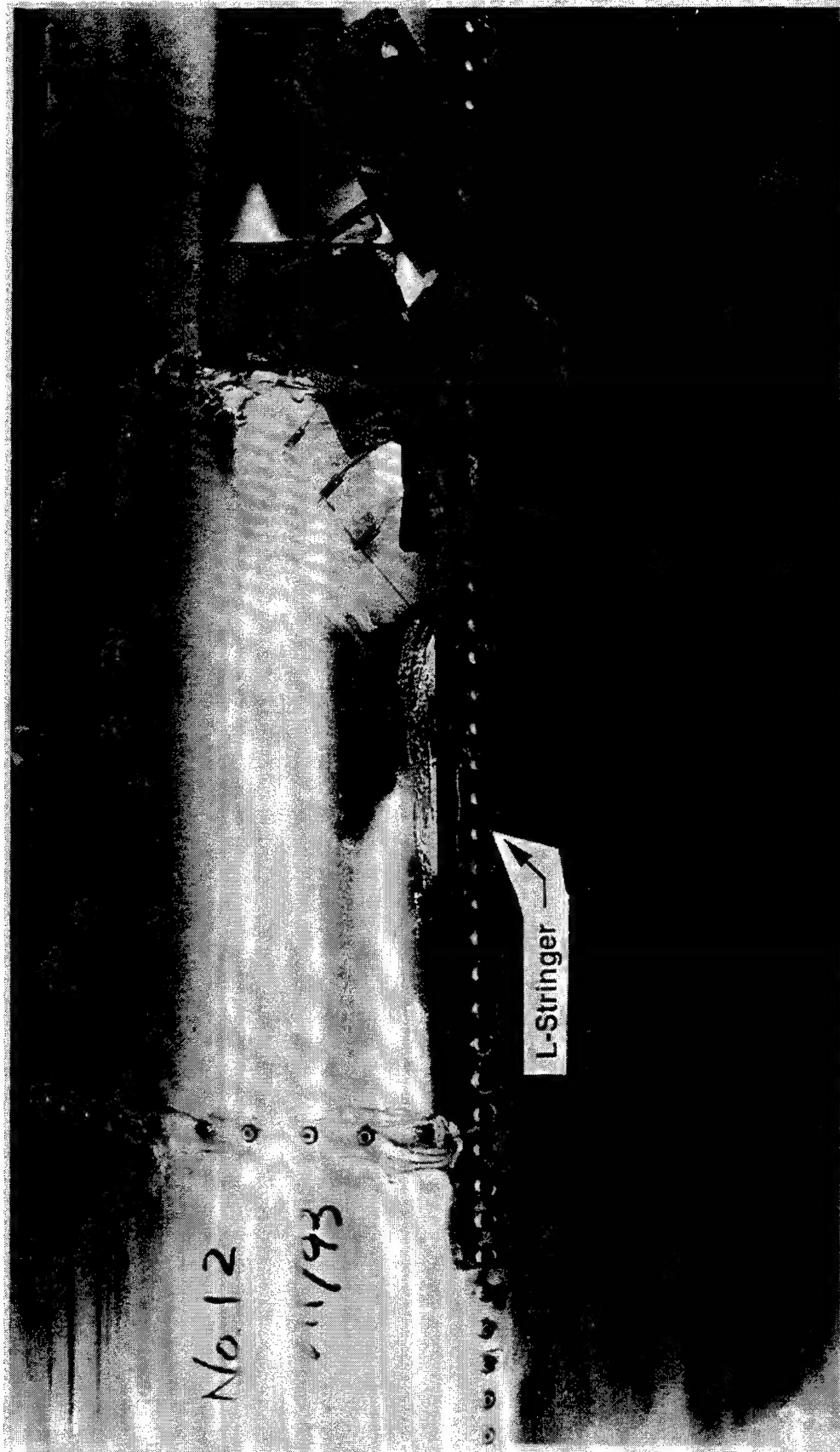


FIGURE 90. PHOTOGRAPH OF SPECIMEN 12 (TYPE d-1) BEFORE RUPTURE

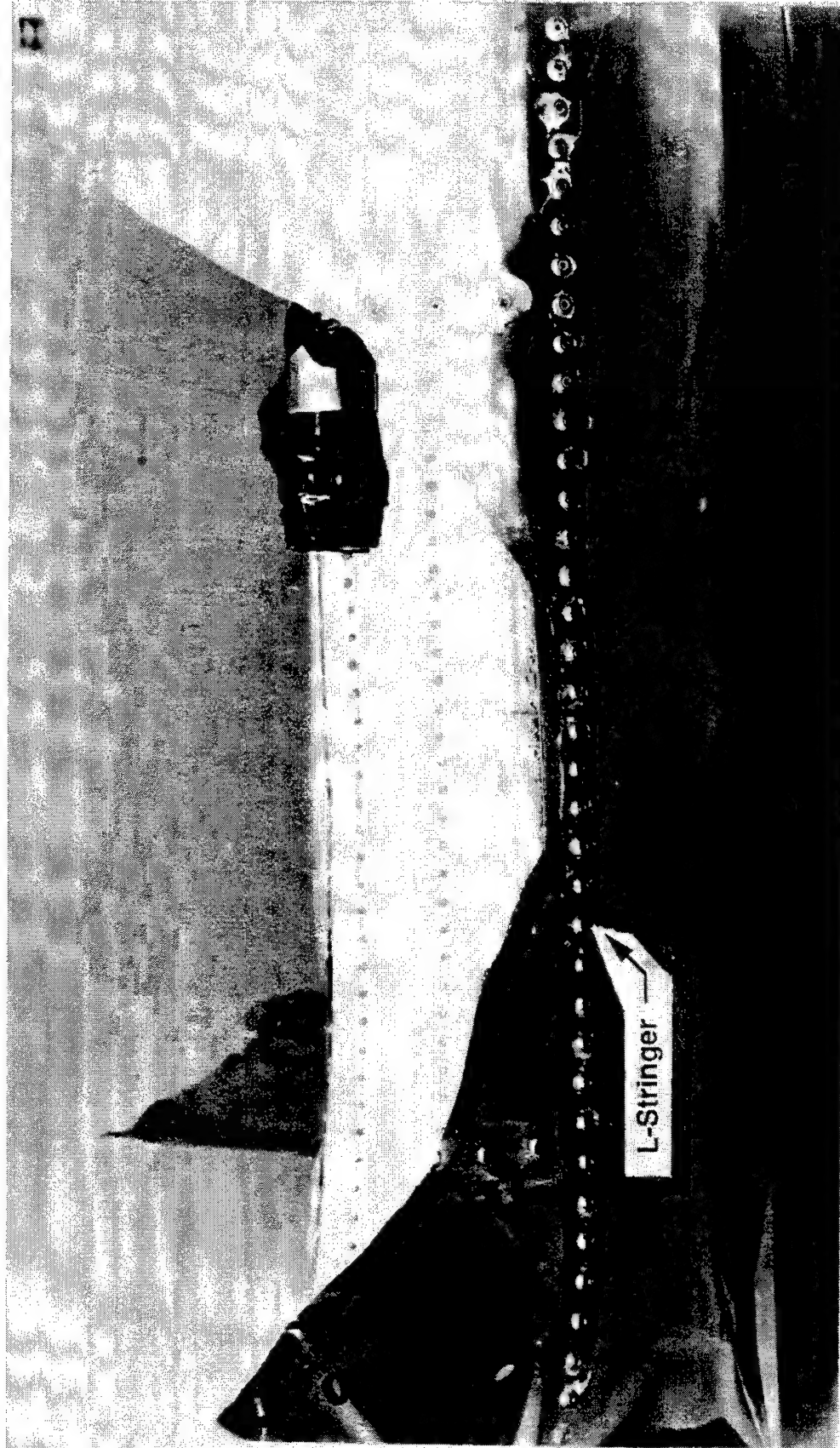


FIGURE 91. PHOTOGRAPH OF SPECIMEN 12 (TYPE d-1) AFTER RUPTURE

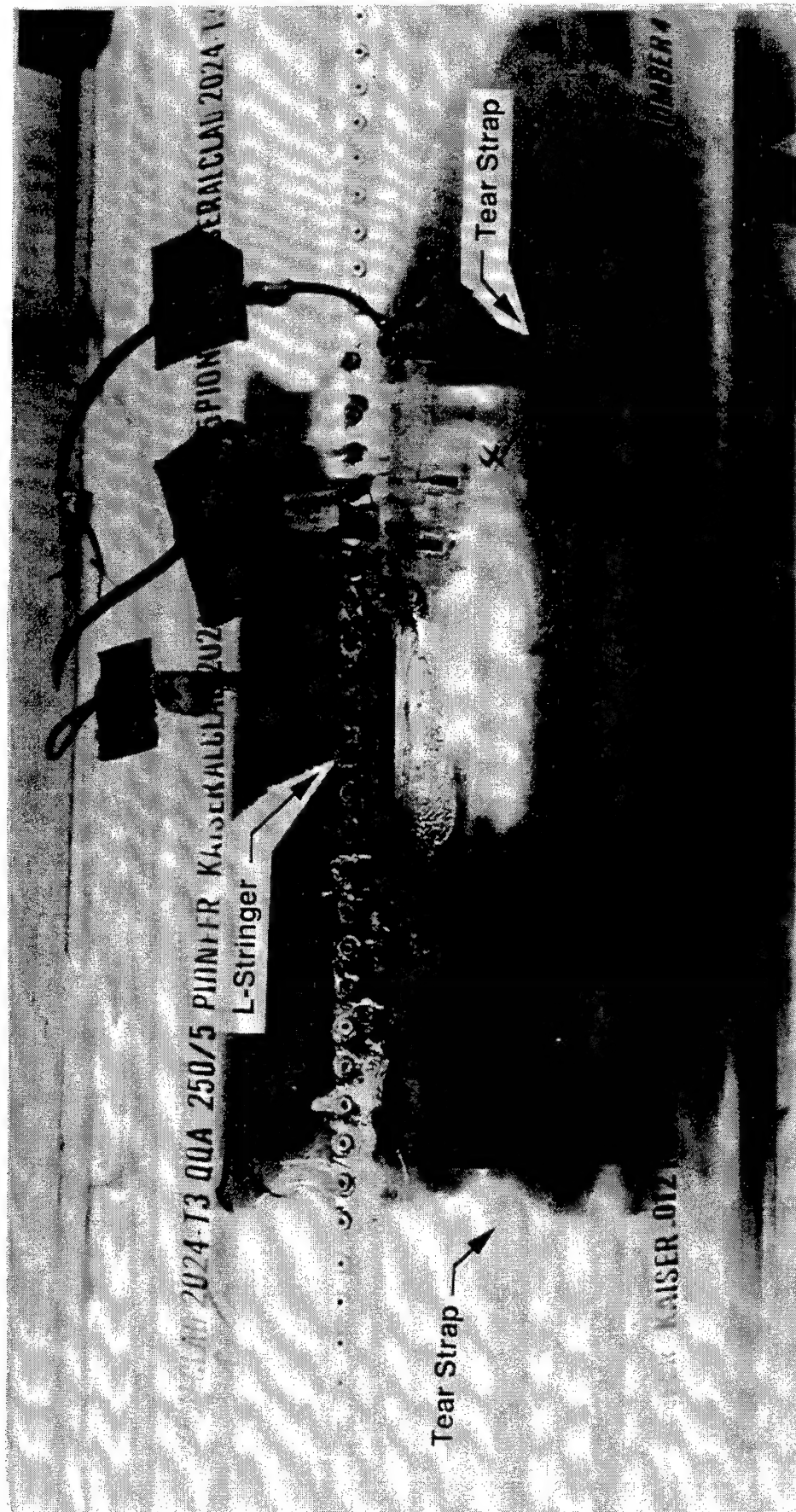


FIGURE 92. PHOTOGRAPH OF SPECIMEN 7 (TYPE c-1) BEFORE RUPTURE



FIGURE 93. PHOTOGRAPH OF SPECIMEN 7 (TYPE c-1) AFTER RUPTURE

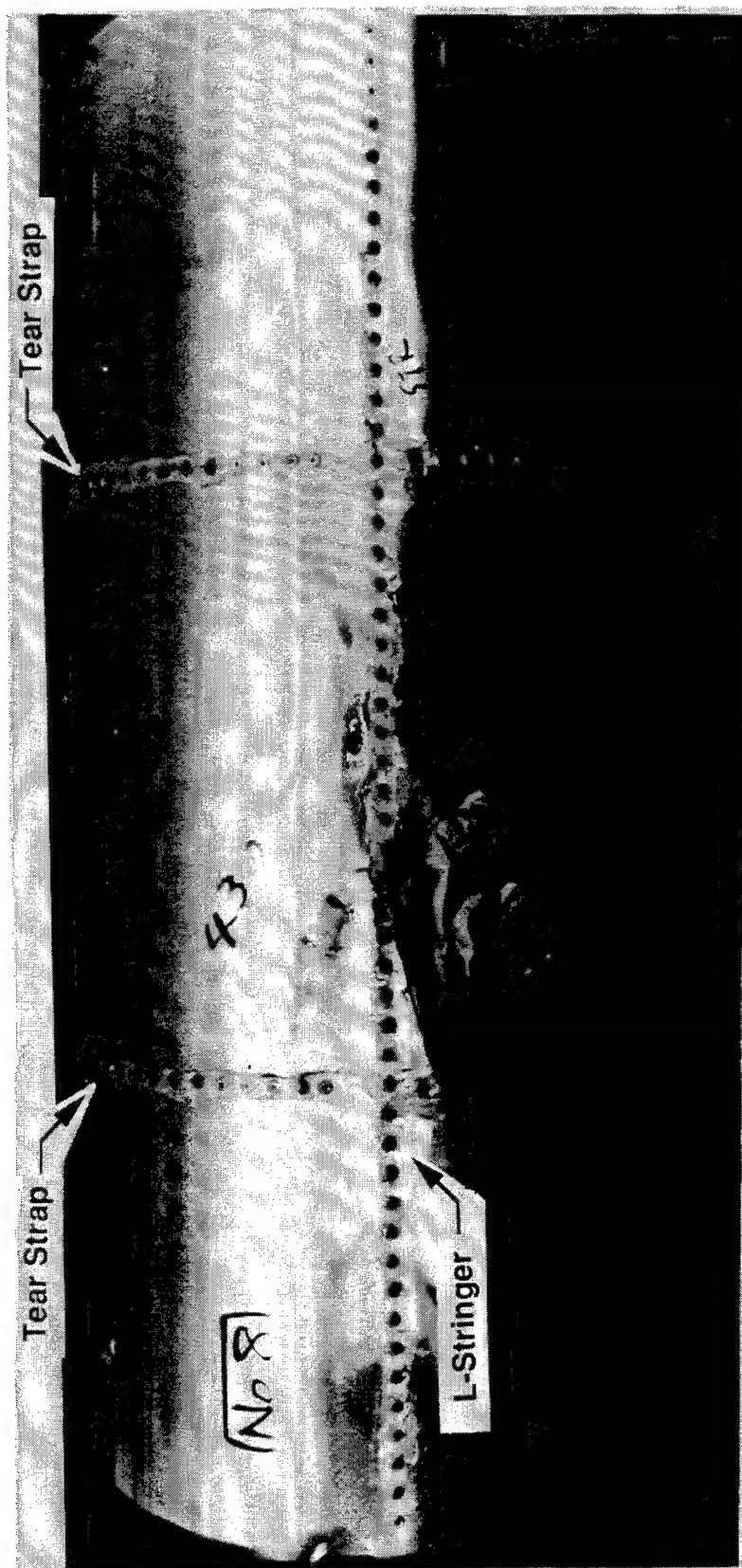


FIGURE 94. PHOTOGRAPH OF SPECIMEN 8 (TYPE c-2) BEFORE RUPTURE

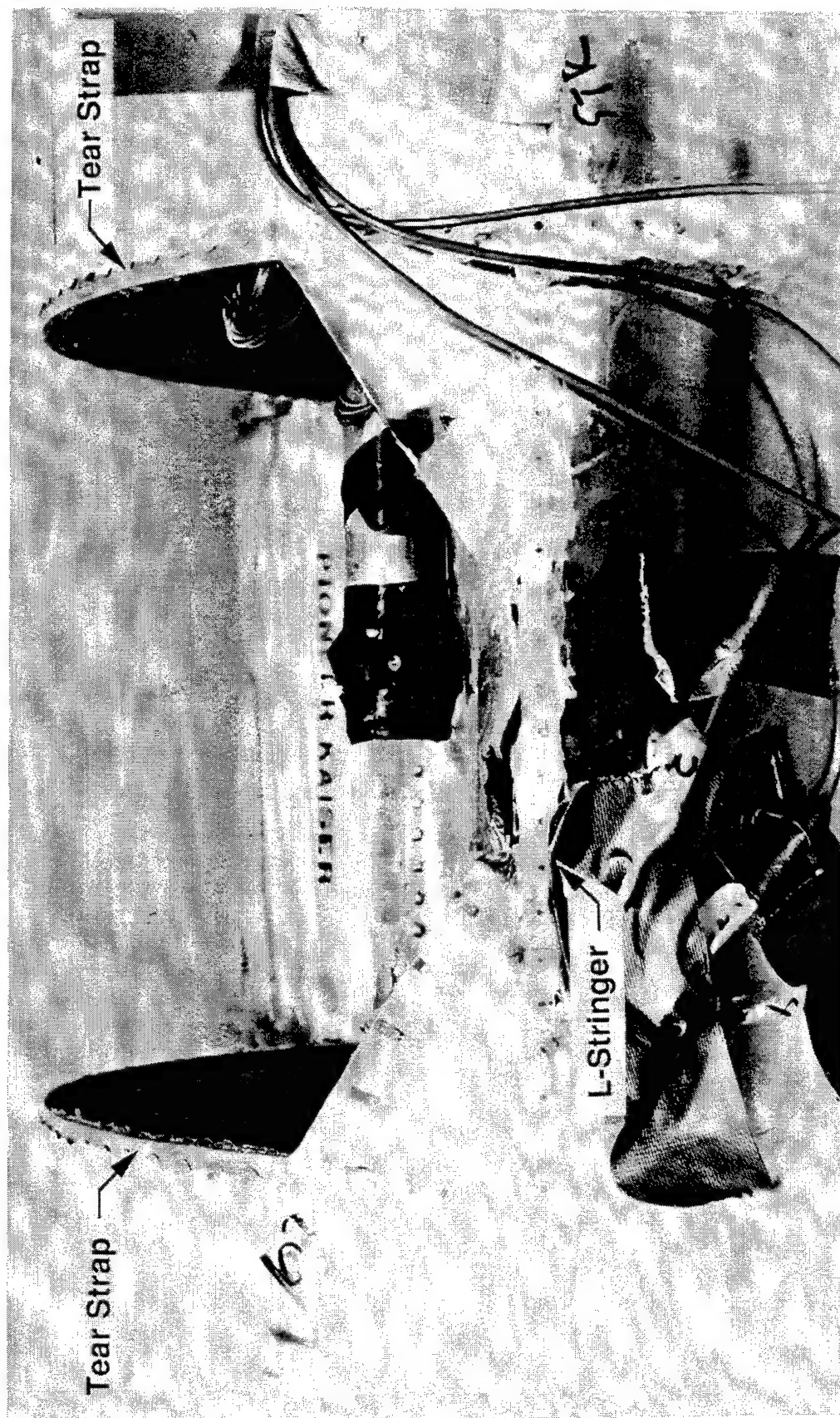


FIGURE 95. PHOTOGRAPH OF SPECIMEN 8 (TYPE c-2) AFTER RUPTURE

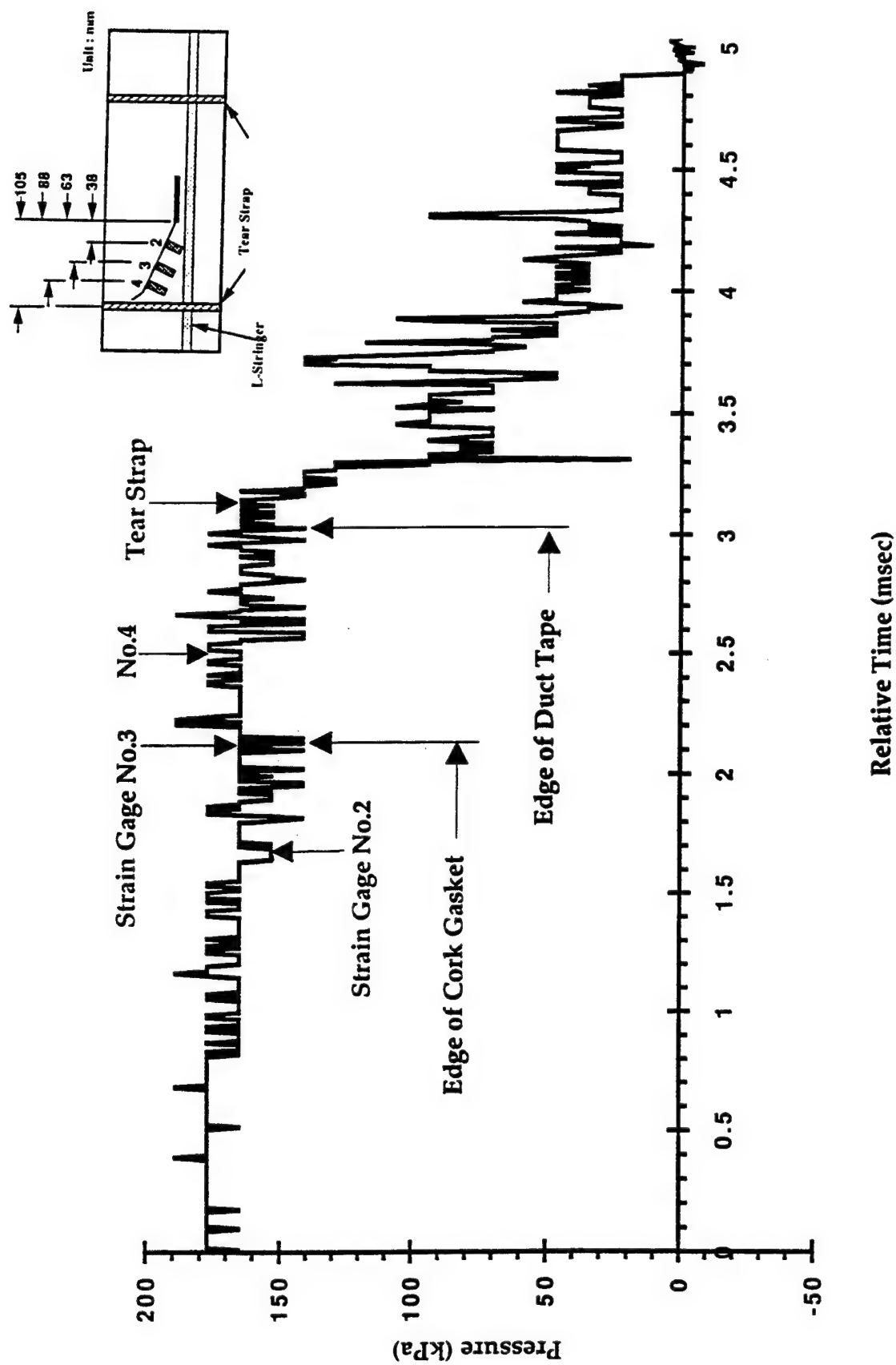


FIGURE 96. PRESSURE-TIME RELATION IN SPECIMEN 8 (TYPE c-2)

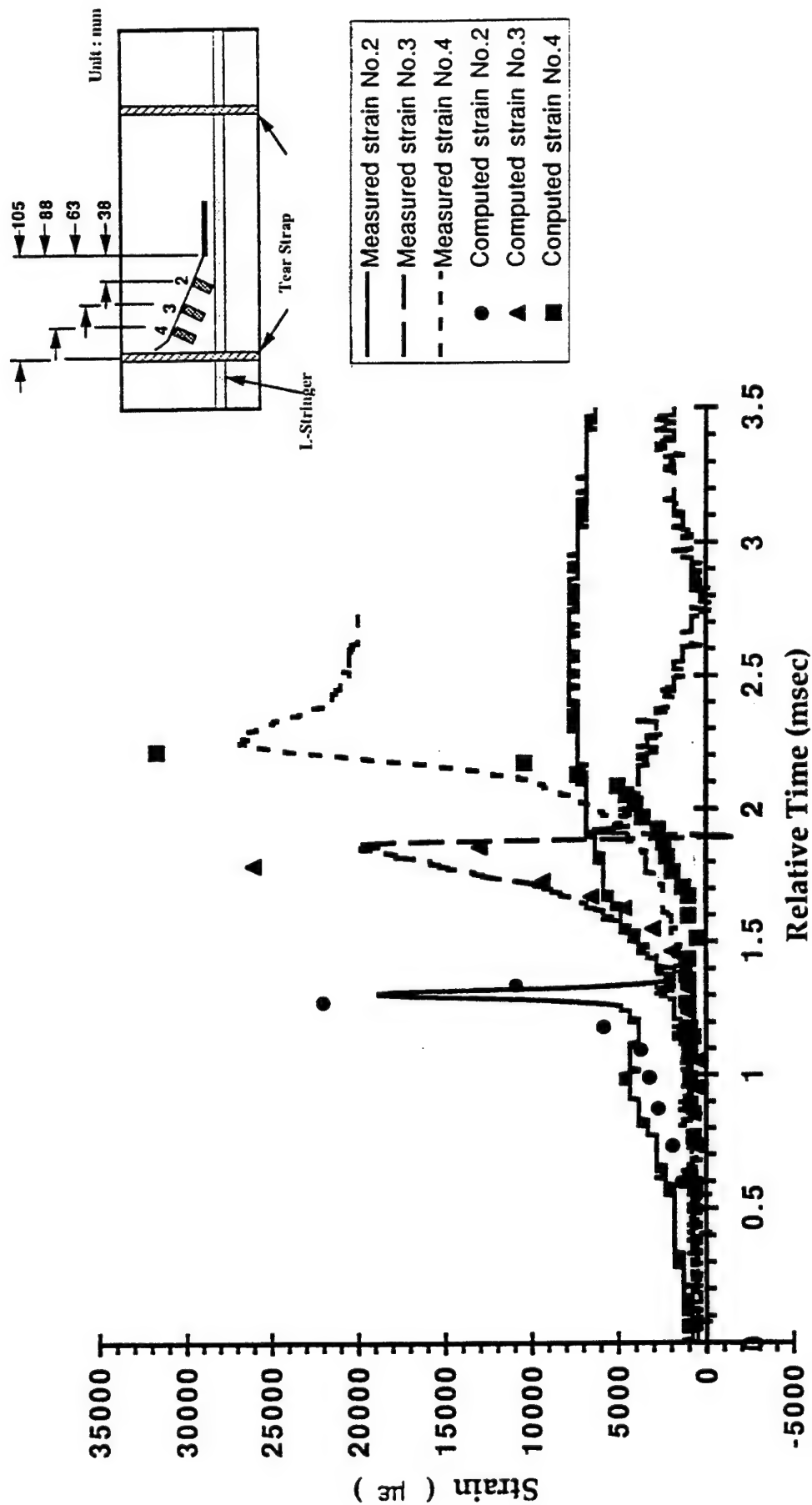


FIGURE 97. STRAIN GAGE RESPONSE IN SPECIMEN 8 (TYPE c-2)

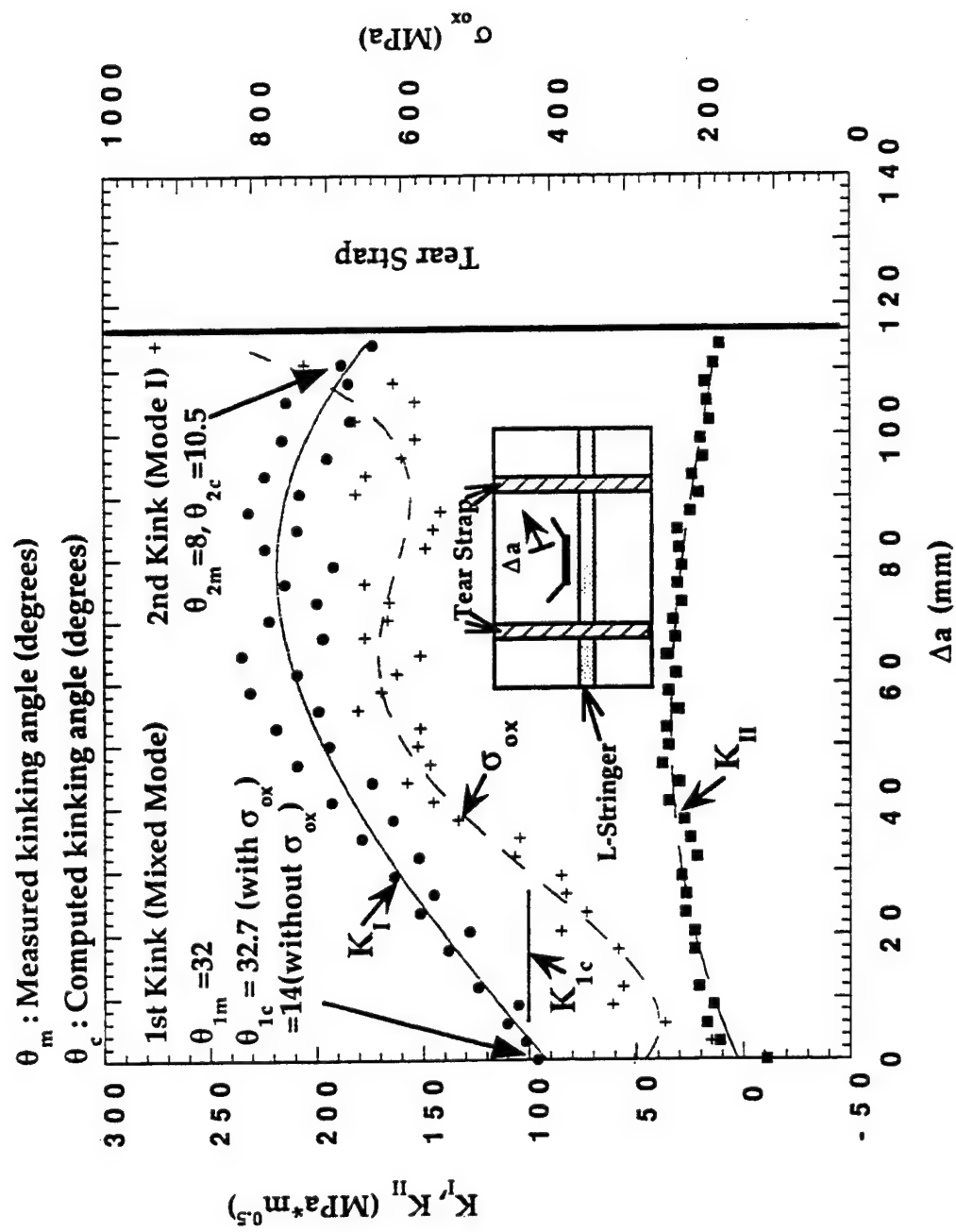


FIGURE 98. VARIATIONS IN K_I , K_{II} , AND σ_{ox} WITH CRACK EXTENSION. SPECIMEN 8 (TYPE c-2).

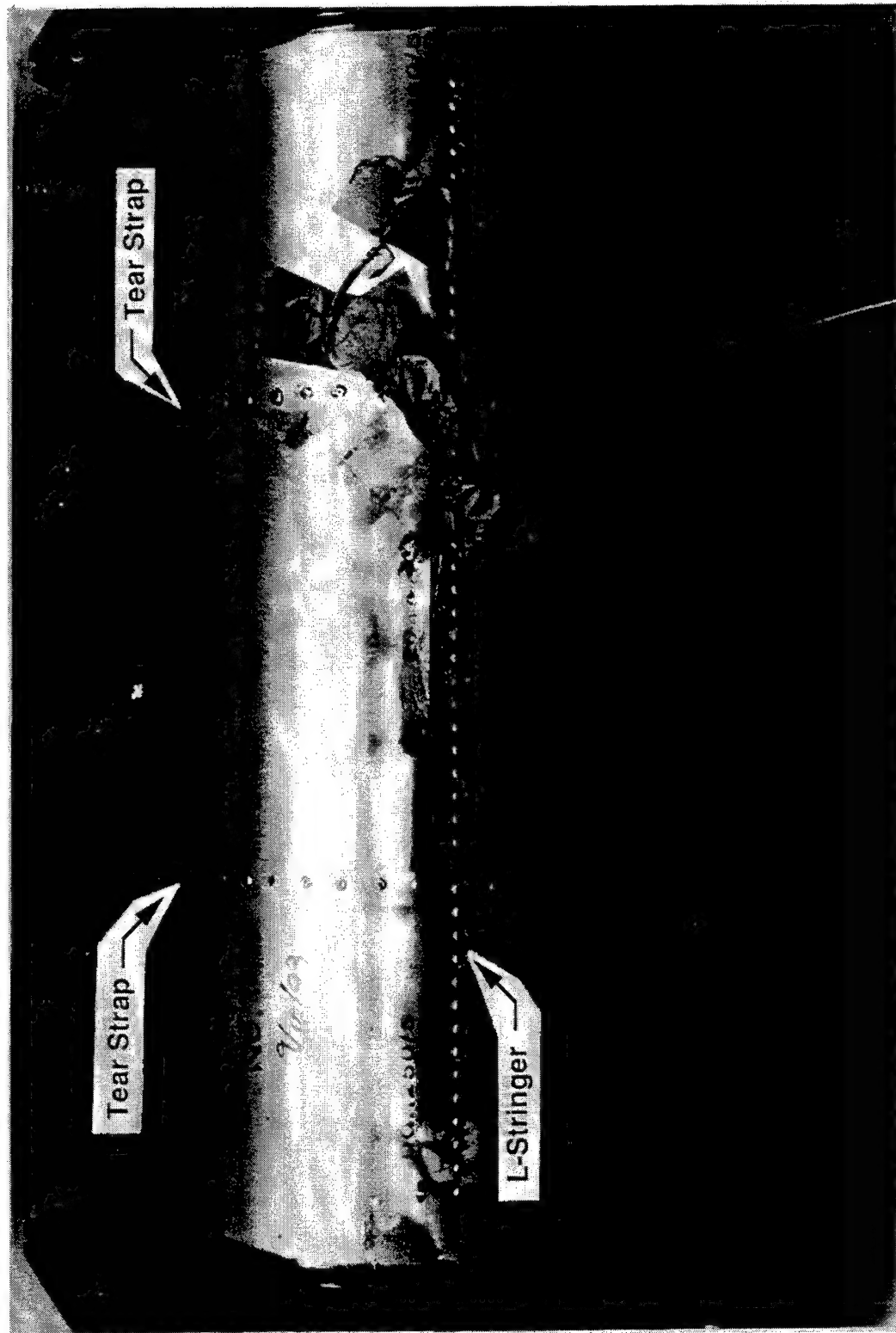


FIGURE 99. PHOTOGRAPH OF SPECIMEN 11 (TYPE c-3) BEFORE RUPTURE

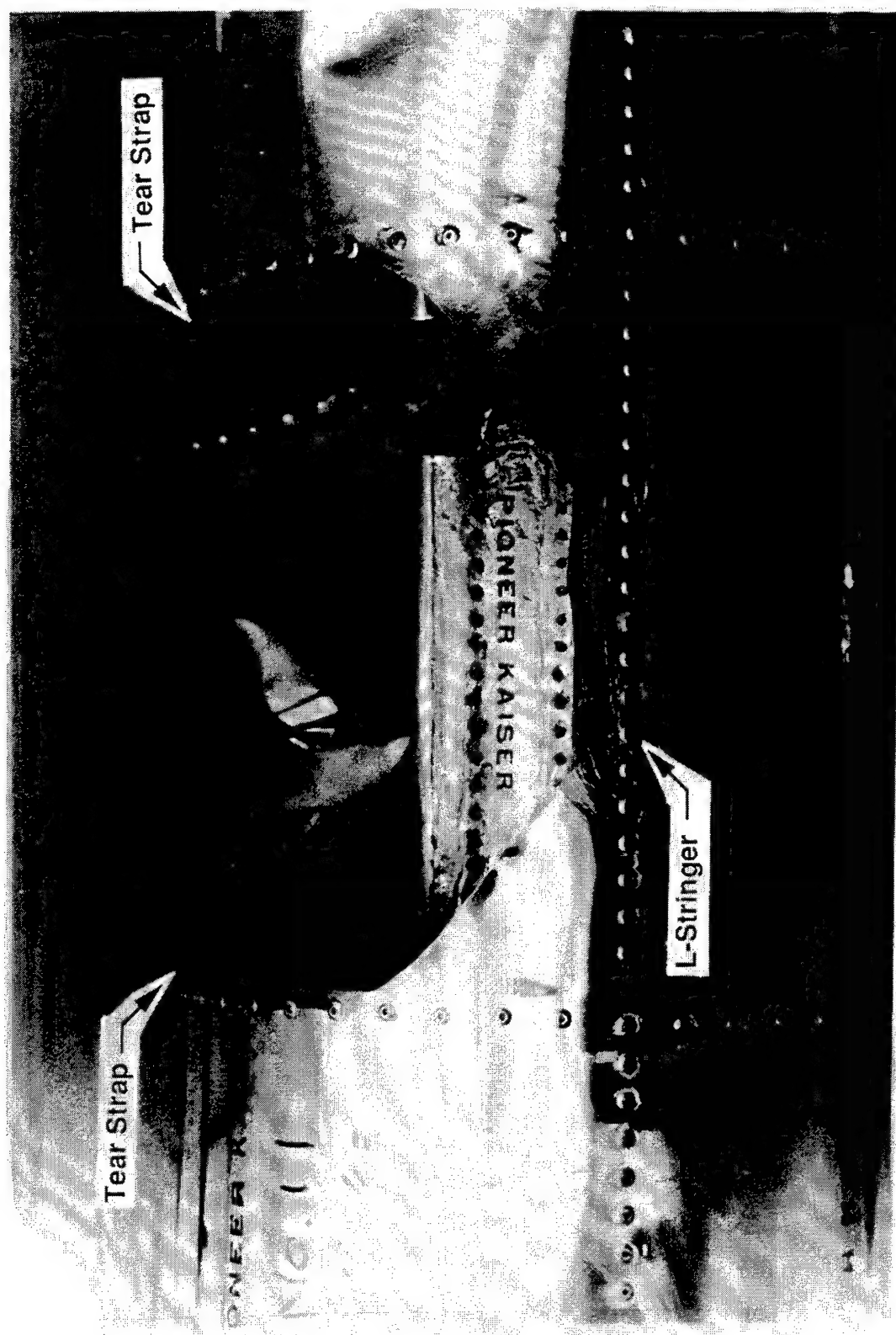


FIGURE 100. PHOTOGRAPH OF SPECIMEN 11 (TYPE c-3) AFTER RUPTURE

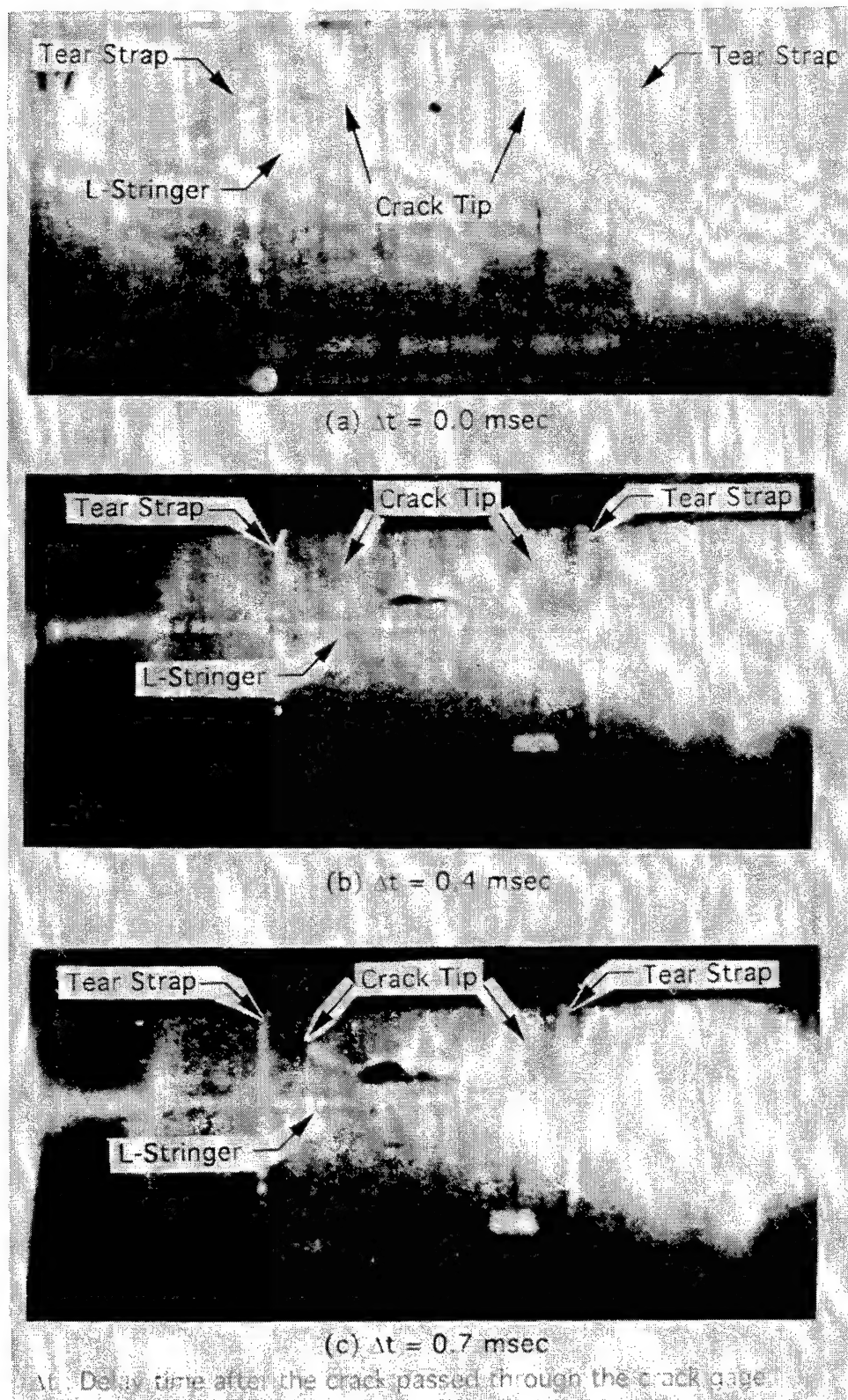


FIGURE 101. HIGH-SPEED PHOTOGRAPHS OF A RUPTURING SMALL-SCALE FUSELAGE (TYPE c-3)

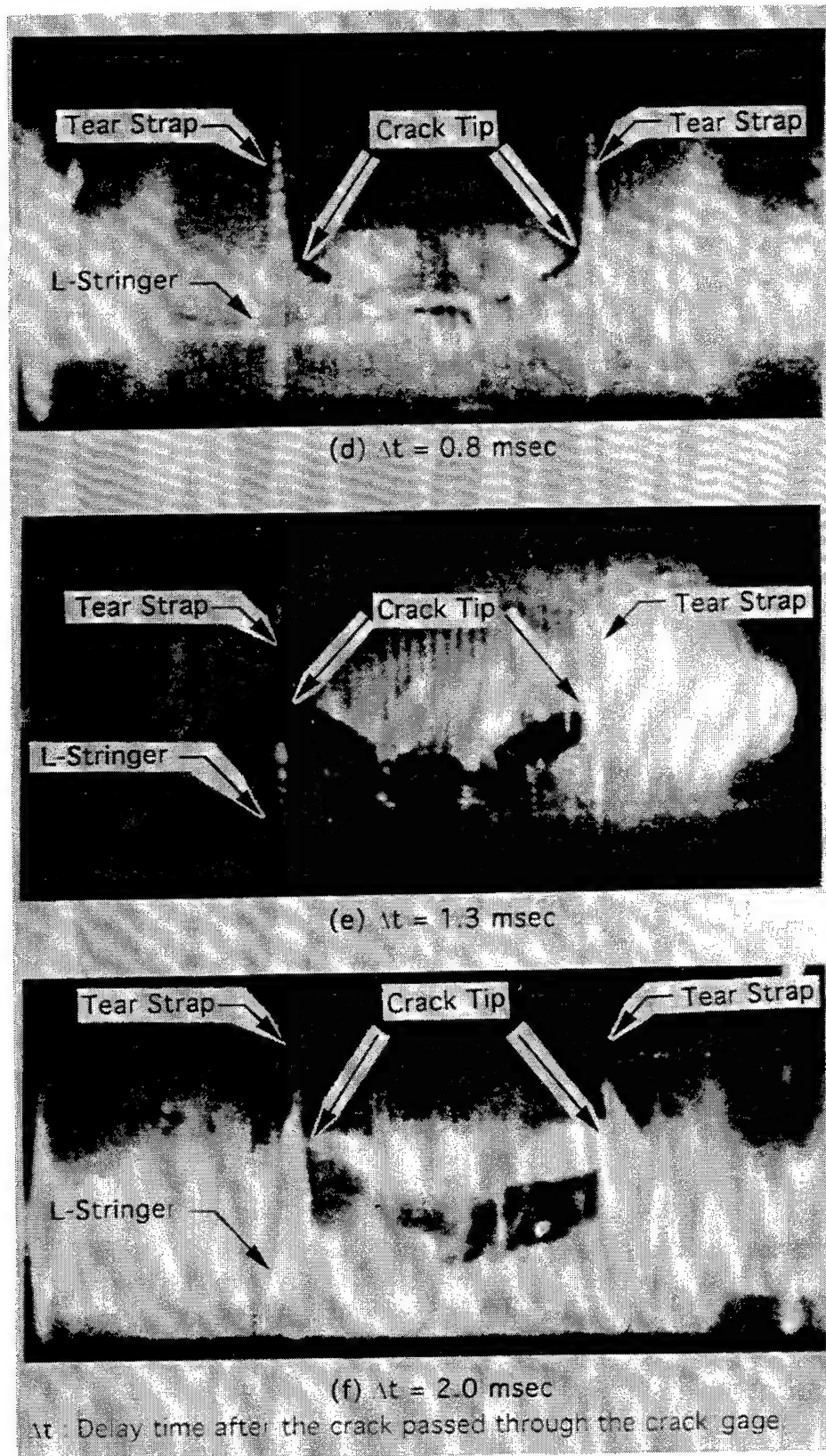


FIGURE 102. HIGH-SPEED PHOTOGRAPHS OF A RUPTURING SMALL-SCALE FUSELAGE (TYPE c-3)

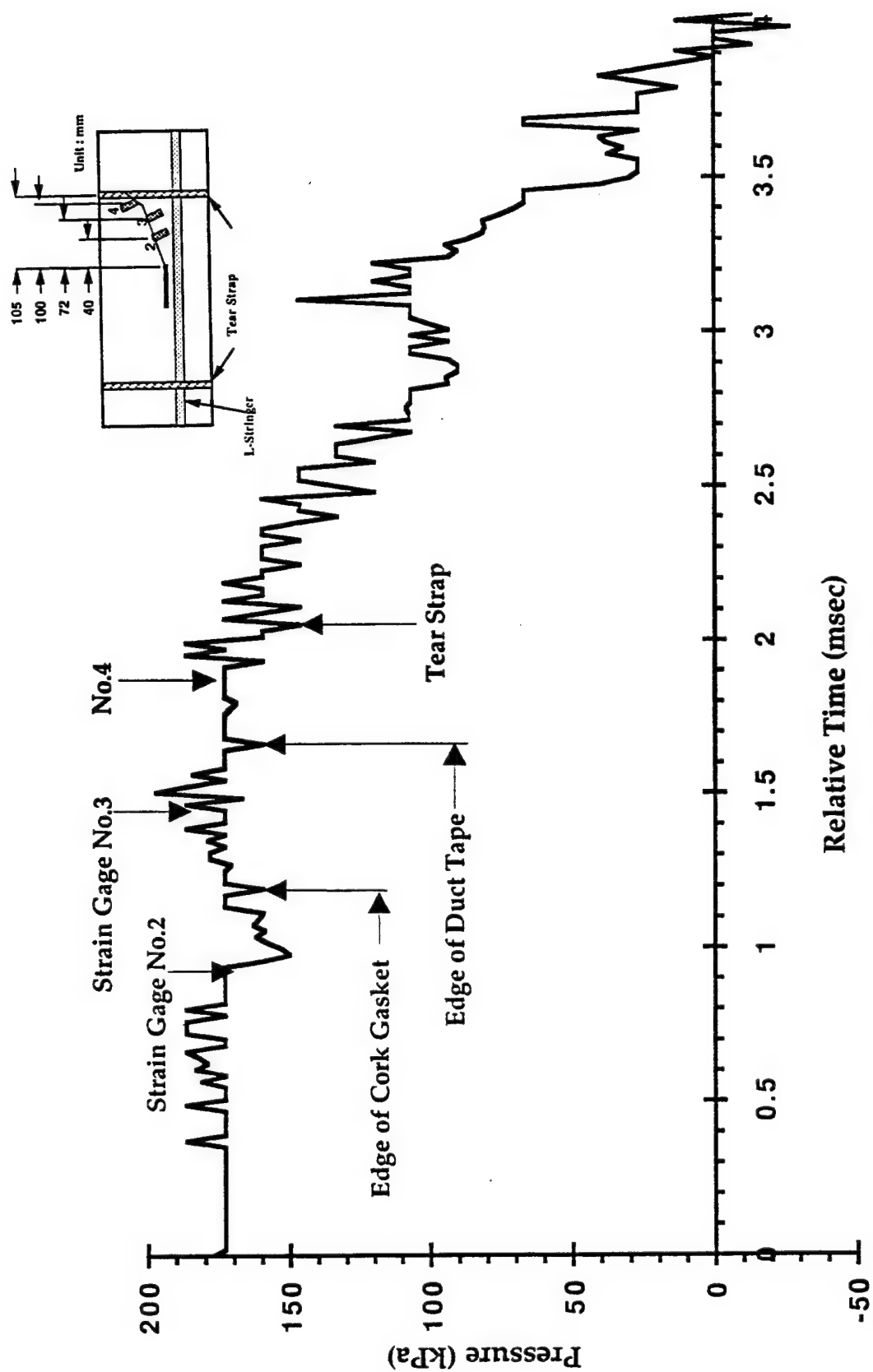


FIGURE 103. PRESSURE-TIME RELATION IN SPECIMEN 11 (TYPE c-3)

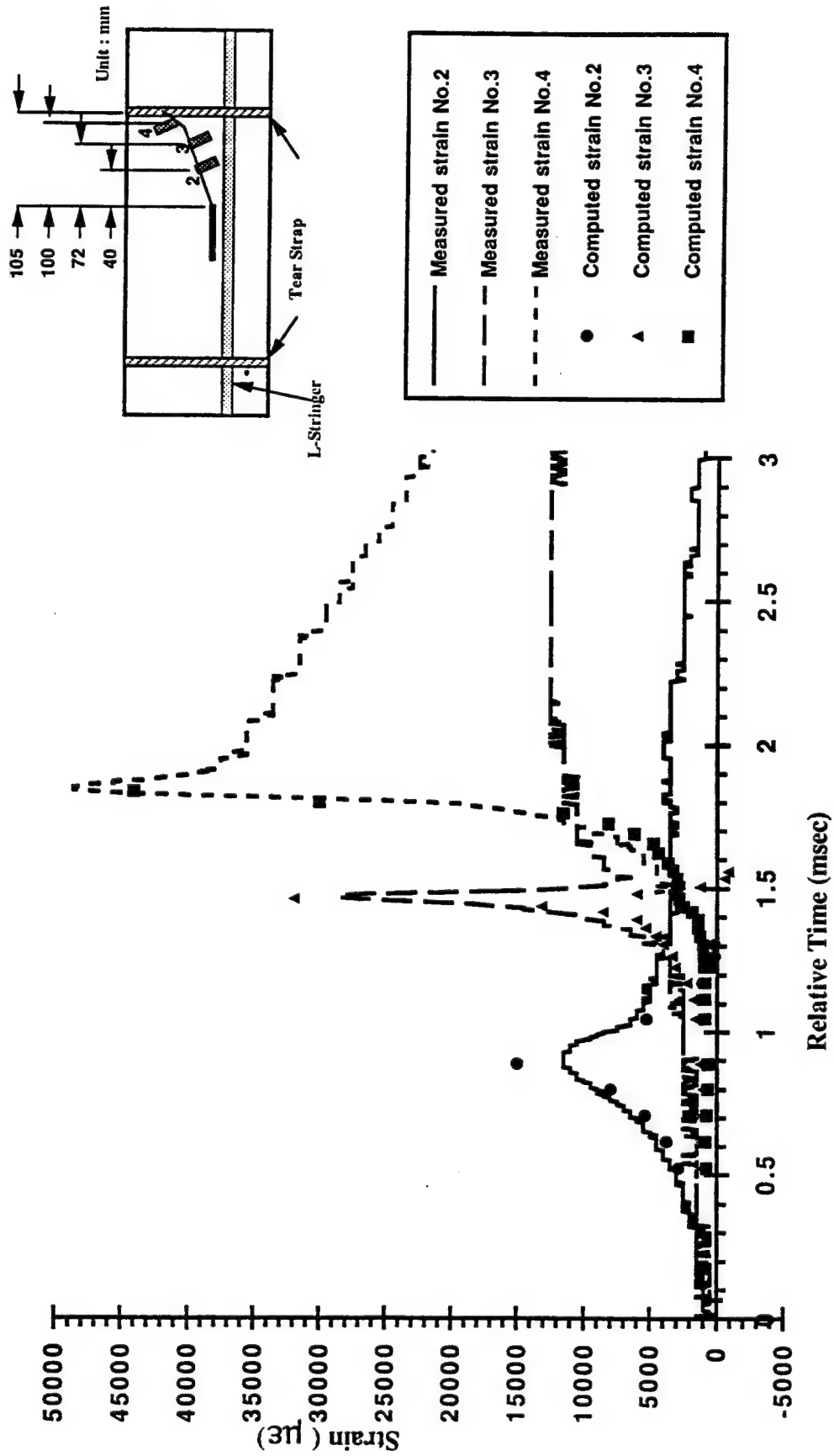


FIGURE 104. STRAIN GAGE RESPONSE IN SPECIMEN 11 (TYPE c-3)

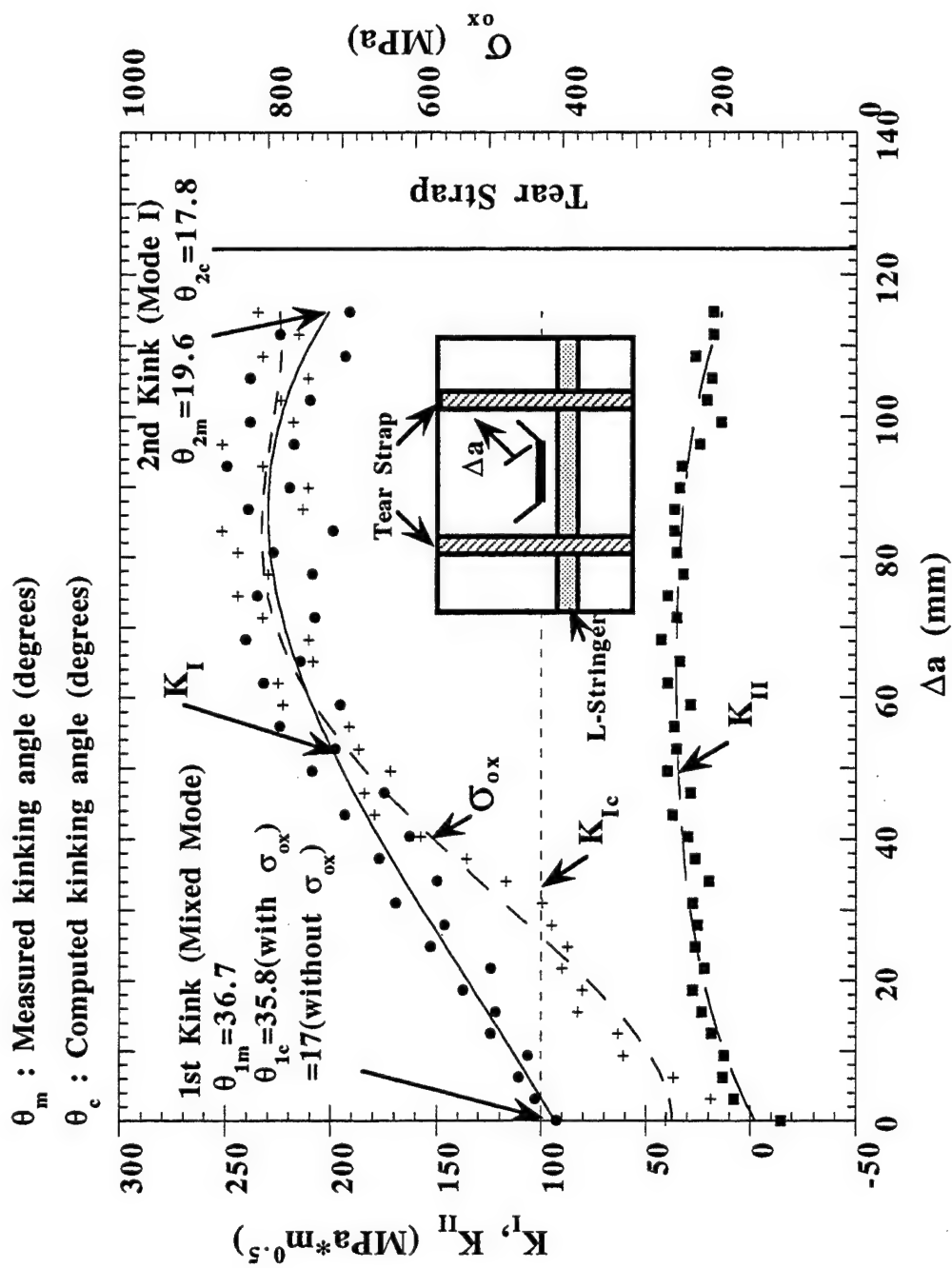


FIGURE 105. VARIATIONS IN K_I , K_{II} , AND σ_{ox} WITH CRACK EXTENSION. SPECIMEN 11 (TYPE c-3).

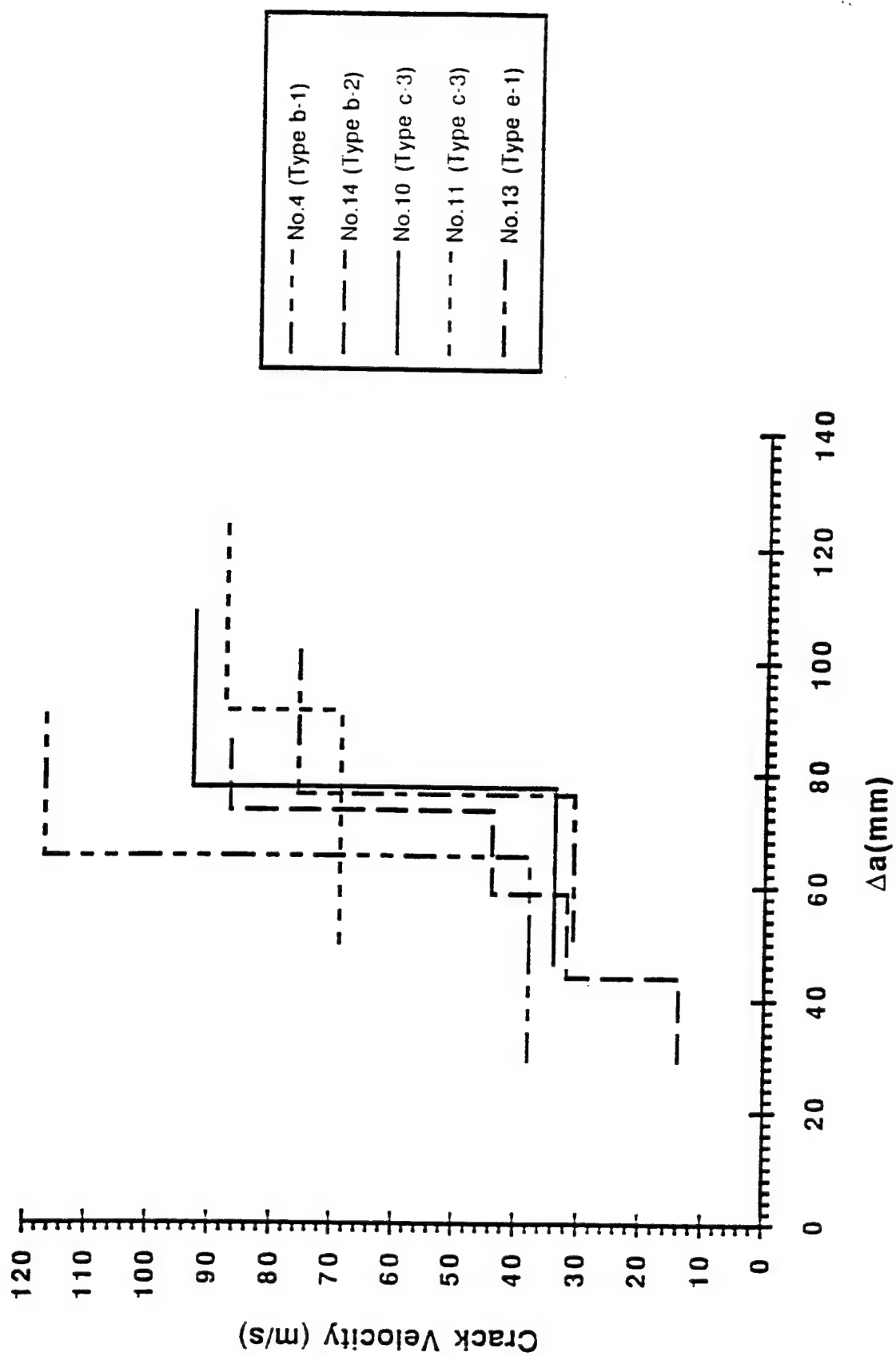


FIGURE 106. VARIATION IN CRACK VELOCITY WITH CRACK EXTENSION

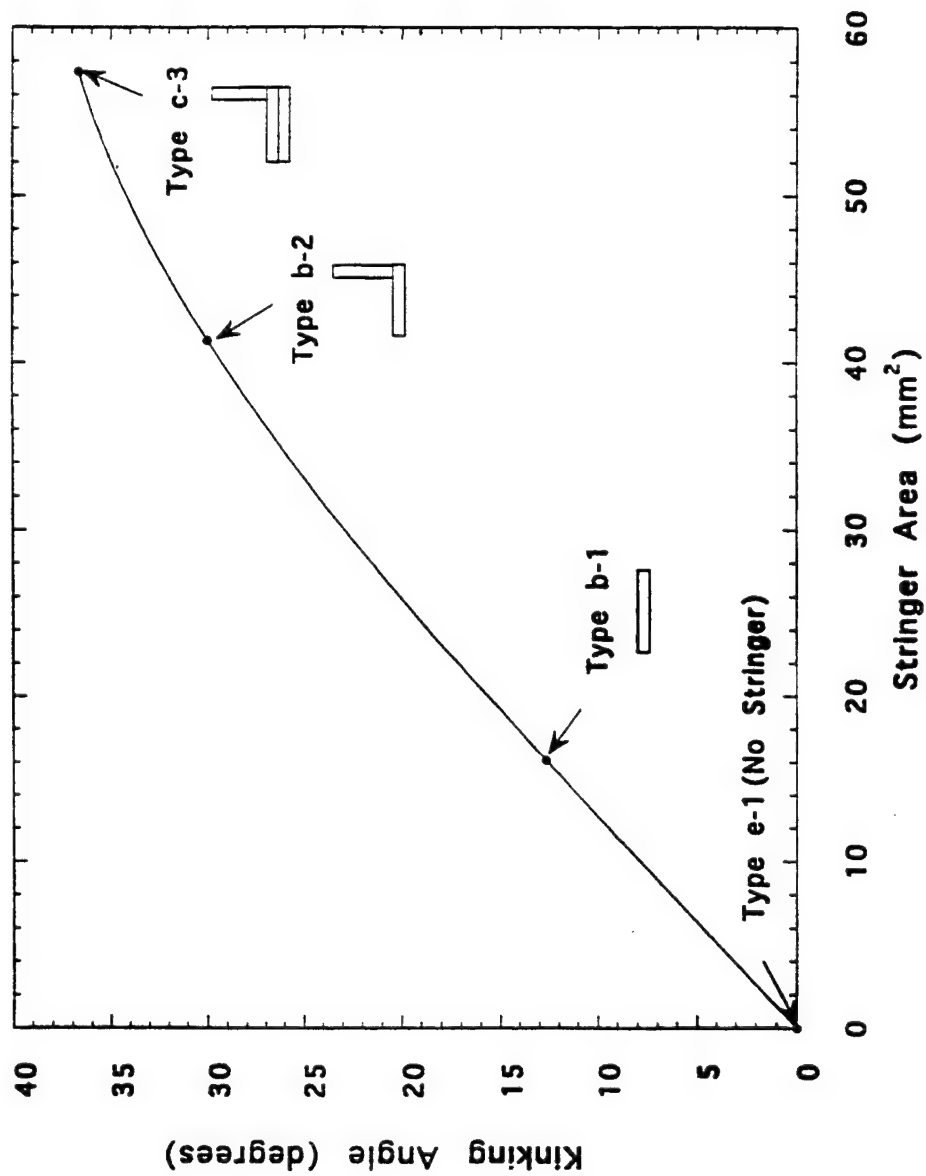


FIGURE 107. VARIATION IN CRACK KINKING ANGLE WITH STRINGER AREA



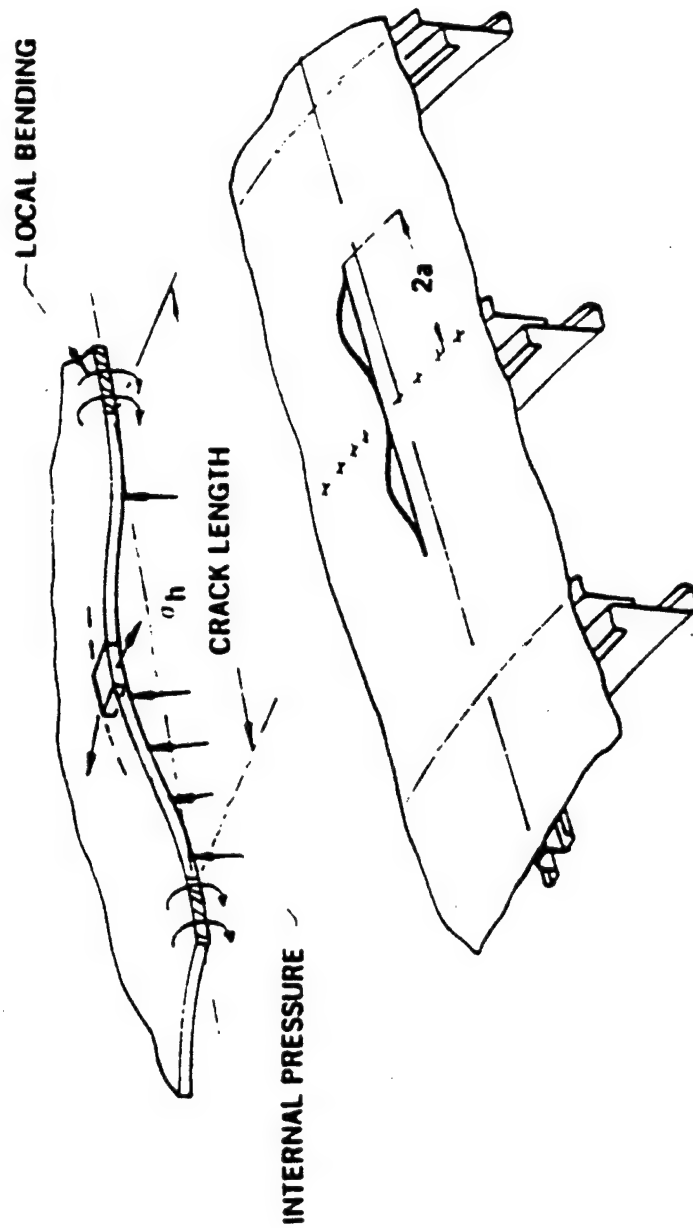


FIGURE 109. EFFECT OF BULGING DUE TO PRESSURE AND CURVATURE [9]

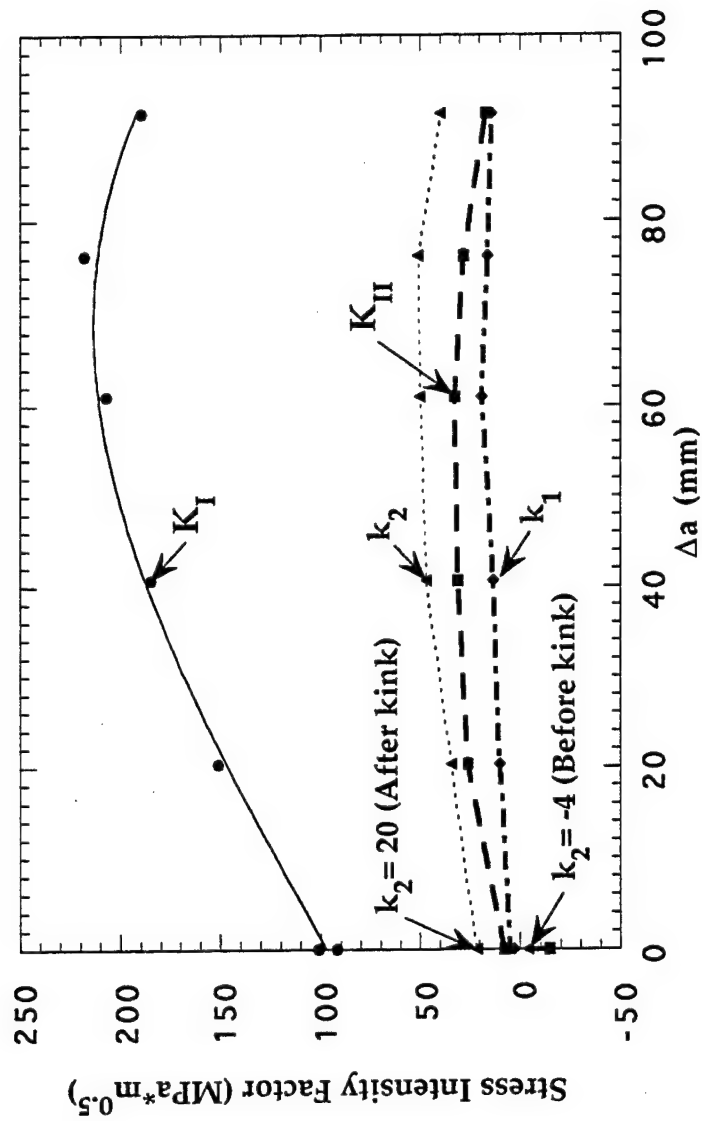


FIGURE 110. VARIATIONS IN K_I , K_{II} , k_1 , AND k_2 WITH CRACK EXTENSION. SPECIMEN 11 (TYPE c-3).

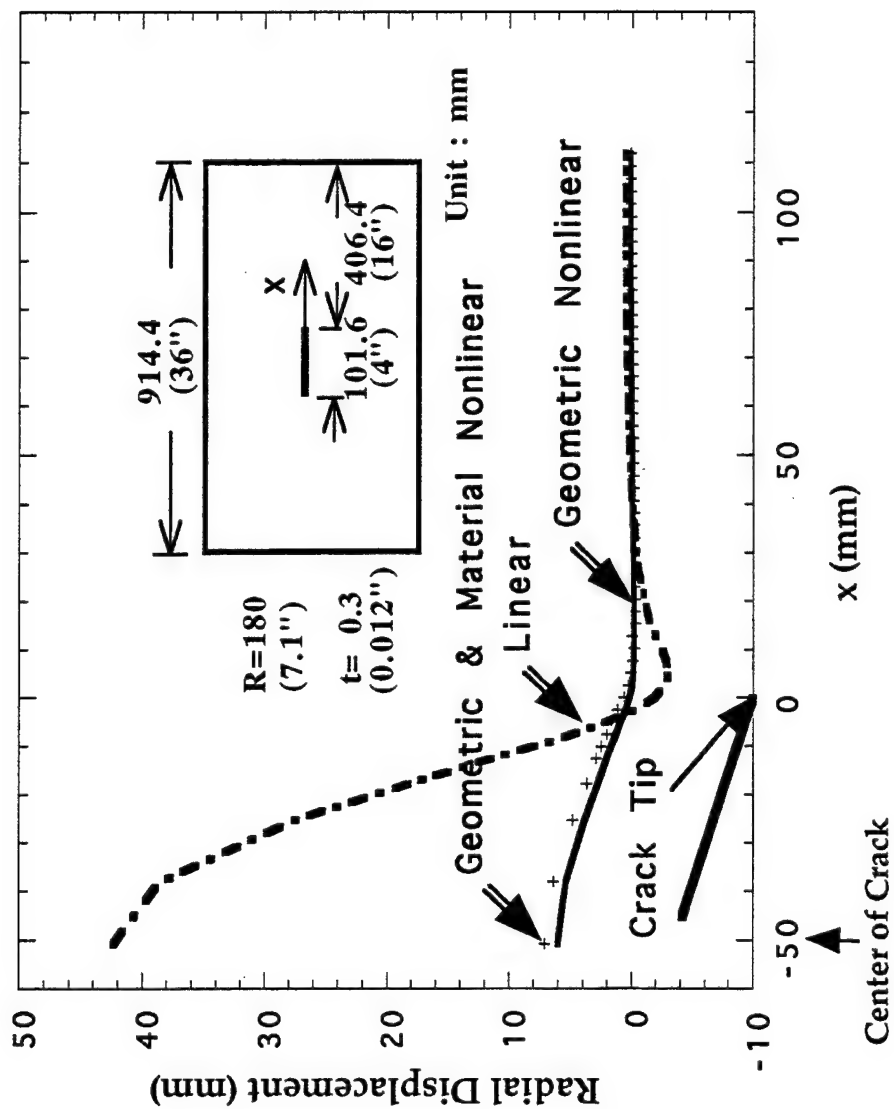


FIGURE 111. RADIAL DISPLACEMENT ALONG THE CRACK PATH.
SMALL-SCALE FUSELAGE MODEL.

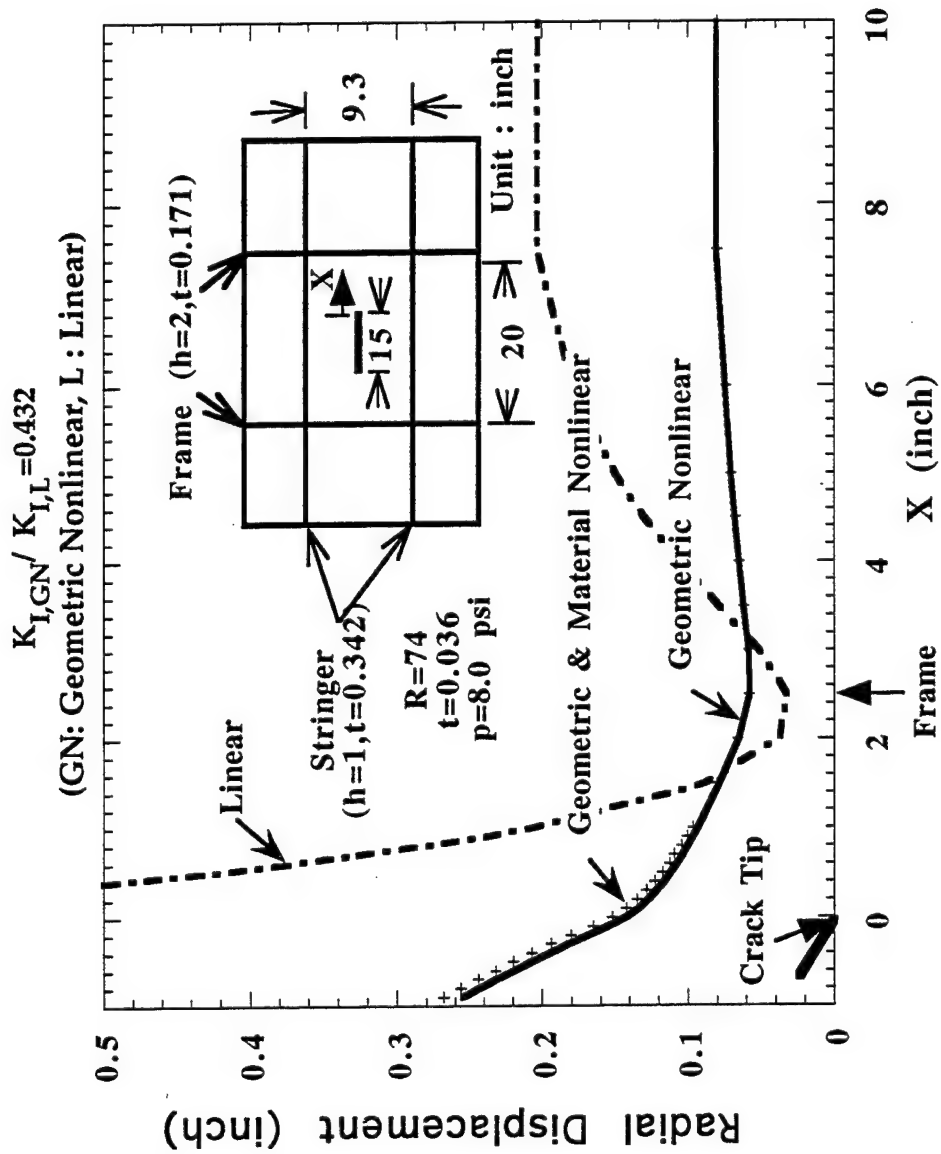


FIGURE 112. RADIAL DISPLACEMENT ALONG THE CRACK PATH.
IDEALIZED FUSELAGE MODEL [90].

TABLE 1. COMPARISON OF THE OLD AND NEW FAR REQUIREMENTS [4, 8]



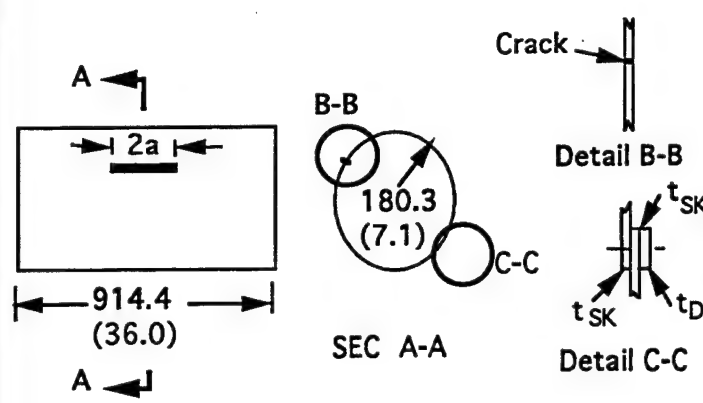
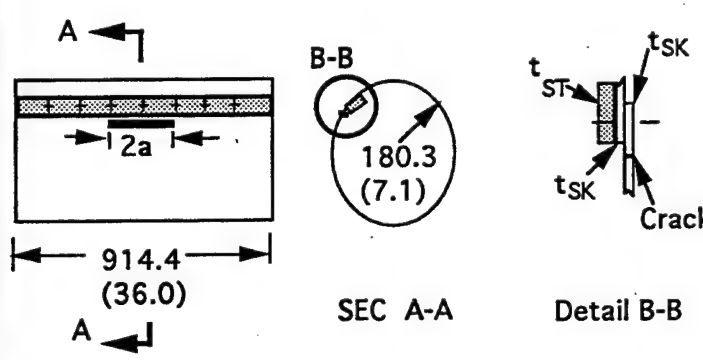
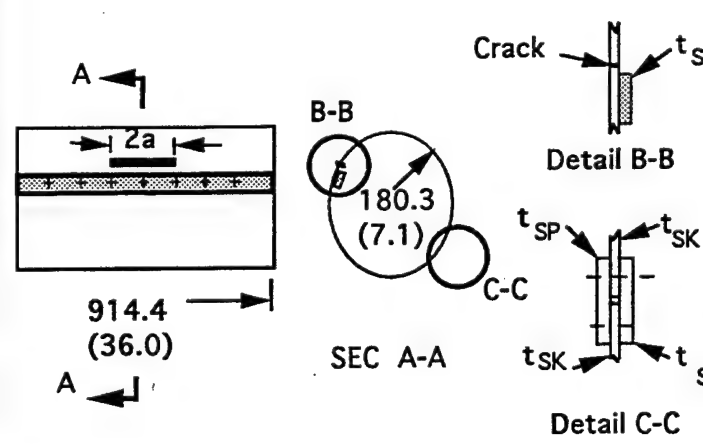
ACTIONS TO BE TAKEN	PHILOSOPHIES	
	FAIL-SAFE OLD FAR 25.571 (PRE-1978)	DAMAGE TOLERANT NEW FAR 25.571 (POST-1978)
RESIDUAL STRENGTH ANALYSIS	 <ul style="list-style-type: none"> • Single element or obvious partial failure. • Residual strength level equal to 80% limit load with an additional 15% dynamic factor. 	 <ul style="list-style-type: none"> • Multiple active cracks one of which is readily detectable. • Residual strength level equal to 100% limit load. No dynamic effects accounted for.
CRACK GROWTH ANALYSIS	<ul style="list-style-type: none"> • No analysis required. 	<ul style="list-style-type: none"> • Extensive analysis required for typical loading and environmental spectra expected in service.
ESTABLISHMENT OF INSPECTION AND MAINTENANCE PROGRAMME	<ul style="list-style-type: none"> • Based on past service history. • Not taken into account for type certificate. 	<ul style="list-style-type: none"> • Related to structural damage characteristics and past service history. • Taken into account for type certificate.

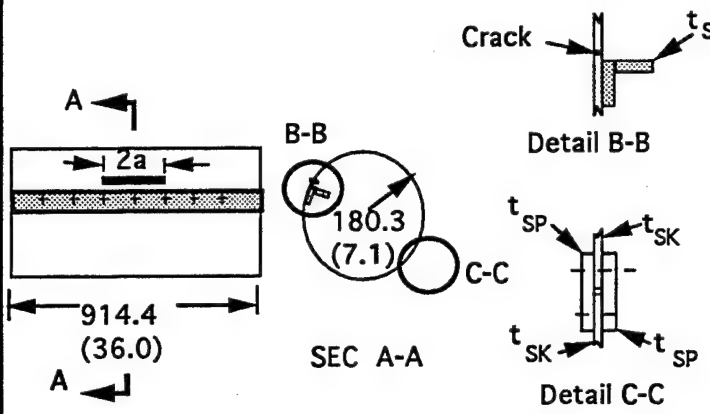
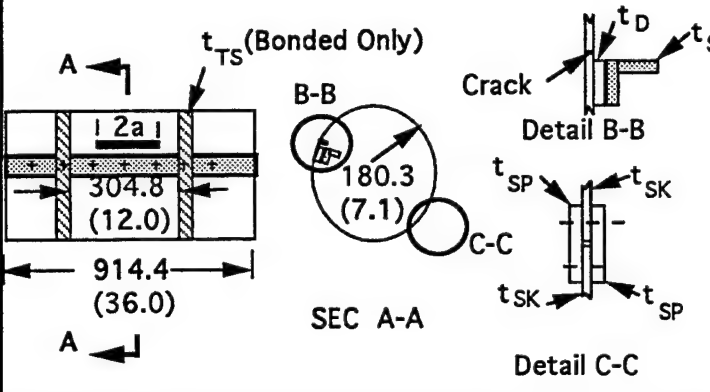
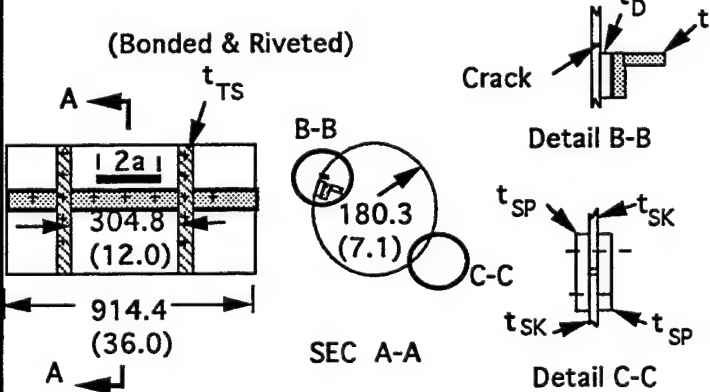
TABLE 2. SMALL-SCALE FUSELAGE SPECIMENS

Type	Configuration	Spec. No.
a-1	 <p> $2a = 127.0$ (5.0) $t_{SK} = 0.3$ (0.012) $t_D = 0.6$ (0.025) Lap Splice </p>	1
a-2	 <p> $2a = 101.6$ (4.0) $t_{SK} = 0.3$ (0.012) $t_{ST} = 0.6$ (0.025) Lap Splice 1" Width Flat Stringer </p>	2
b-1	 <p> $2a = 101.6$ (4.0) $t_{SK} = 0.3$ (0.012) $t_{ST} = 0.6$ (0.025) $t_{SP} = 0.6$ (0.025) Butt Splice 1" Width Flat Stringer </p>	3 4

SK: Skin ST: Stringer SP: Splice Plate D: Doubler

Unit: mm
(Inch)

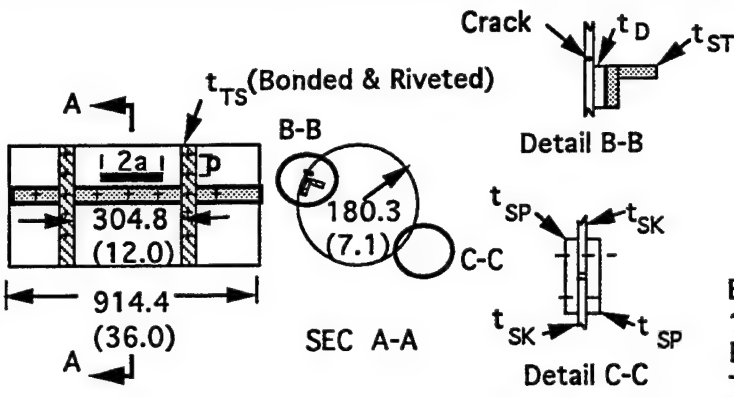
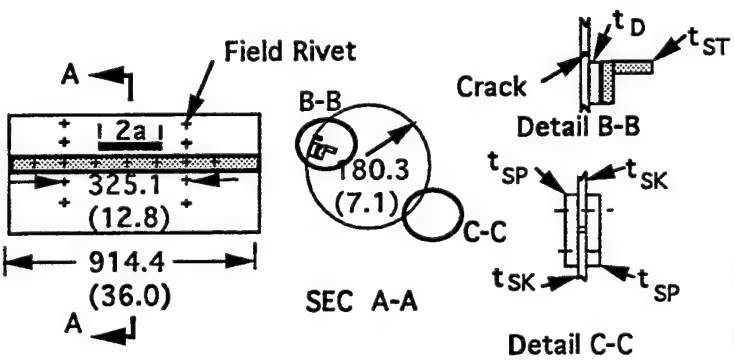
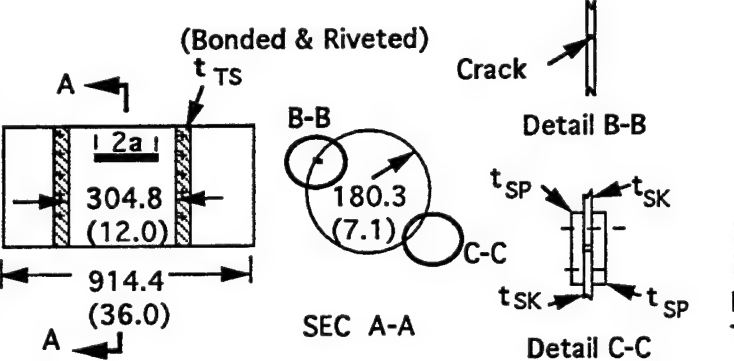
TABLE 3. SMALL-SCALE FUSELAGE SPECIMENS

Type	Configuration	Spec. No.
b-2		5
		6
		14*
		15*
		16*
c-1		7
c-2		8
		9

SK: Skin ST: Stringer TS: Tear Strap SP: Splice Plate D: Doubler
 * : Driven by the pneumatic riveter.

Unit: mm
 (Inch)

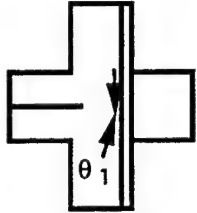
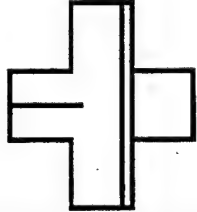
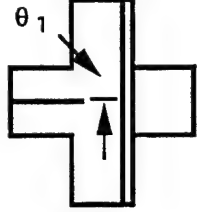
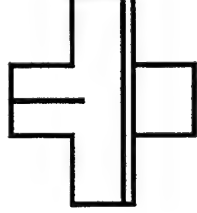
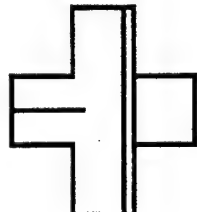
TABLE 4. SMALL-SCALE FUSELAGE SPECIMENS

Type	Configuration	Spec. No.
c-3	 <p>2a = 101.6 (4.0) $t_{SK} = 0.3$ (0.012) $t_{ST} = 0.8$ (0.032) $t_{TS} = t_{SP} = t_D = 0.6$ (0.025) Butt Splice 1"*1" L-Stringer Bonded & Riveted Tear Strap (w=0.8")</p>	10 11 17* 18* 19* 20* 21*
d-1	 <p>2a = 101.6 (4.0) $t_{SK} = 0.3$ (0.012) $t_{ST} = 0.8$ (0.032) $t_{SP} = t_D = 0.6$ (0.025) Butt Splice 1"*1" L-Stringer No Tear Strap</p>	12
e-1	 <p>2a = 101.6 (4.0) $t_{SK} = 0.3$ (0.012) $t_{TS} = t_{SP} = 0.6$ (0.025) Butt Splice No Stringer Bonded & Riveted Tear Strap (w=0.8")</p>	13

SK: Skin ST: Stringer TS: Tear Strap SP: Splice Plate D: Doubler Unit: mm (Inch)
 * : Driven by the pneumatic riveter.

TABLE 5. TEST RESULTS.

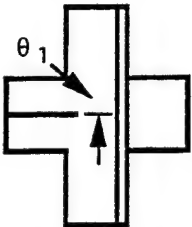
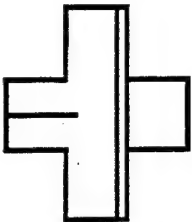
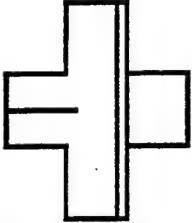
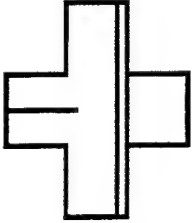
MATERIAL: 2024-T3, THICKNESS = 0.81 MM (0.032 IN.)

Specimen No.	Maximum Load (N)	Crack Path	Remarks
MV-1	$P_x = 0$ $P_y = 16,700$	$\Delta a = 88.9$ $\theta_1 = -6.5$ (Arrested) 	Crack propagated straight and arrested.
MV-2	$P_x = 0$ $P_y = 17,300$	$\Delta a = 114.3$ (Penetrated tear strap) 	
MV-3	$P_x = 17,000$ $P_y = 15,500$	$\Delta a = 58$ $\theta_1 = 31$ 	Crack kinked and arrested.
MV-4	$P_x = 16,500$ $P_y = 14,500$	$\Delta a = 21$ $\theta_1 = 25$ 	
MV-5	$P_x = 17,100$ $P_y = 16,000$	$\Delta a = 72$ $\theta_1 = 15$ 	

 Δa : Total crack extension (mm). θ_1 : Initial kinking angle (degrees). $K_{Ic} = 60 \text{ MPa}\cdot\text{m}^{0.5}$

TABLE 6. TEST RESULTS.

MATERIAL: 2024-T3, THICKNESS = 0.81 MM (0.032 IN.)

Specimen No.	Maximum Load (N)	Crack Path	Remarks
MV-6	P _x = 17,800 P _y = 17,300	$\Delta a = 120$ $\theta_1 = 30$ 	*
MV-7	P _x = 17,300 P _y = 19,600	$\Delta a = 154.8$ $\theta_1 = 30.8$ 	#
MV-8	P _x = 17,200 P _y = 19,200	$\Delta a = 151.4$ $\theta_1 = 23$ 	Crack penetrated through tear strap which broken.
MV-9	P _x = 18,100 P _y = 19,400	$\Delta a = 167.4$ $\theta_1 = 30$ 	

 Δa : Total crack extension (mm). θ_1 : Initial kinking angle (degrees).

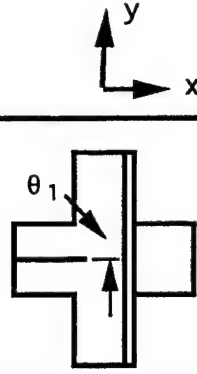
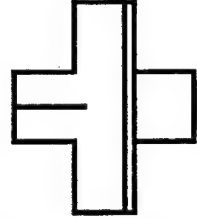
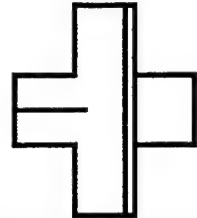
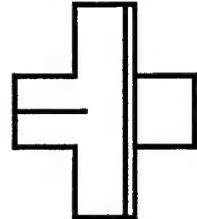
* : Crack penetrated through tear strap and arrested.

: Crack penetrated through tear strap which remained intact.

$$K_{Ic} = 69.7 \text{ MPa}\cdot\text{m}^{0.5}$$

TABLE 7. TEST RESULTS.

MATERIAL: 7075-T6, THICKNESS = 0.81 MM (0.032 IN.)

Specimen No.	Maximum Load (N)	Crack Path	Remarks
7MV-1	Px= 12,300 Py= 16,000	$\Delta a = 160.4$ $\theta_1 = 38$ 	*
7MV-2	Px= 12,000 Py= 18,200	$\Delta a = 166.6$ $\theta_1 = 35$ 	#
7MV-3	Px= 12,700 Py= 17,100	$\Delta a = 172.1$ $\theta_1 = 38$ 	Crack penetrated through tear strap which broken.
7MV-4	Px= 17,100 Py= 20,000	$\Delta a = 181.4$ $\theta_1 = 31$ 	

 Δa : Total crack extension (mm). θ_1 : Initial kinking angle (degrees).

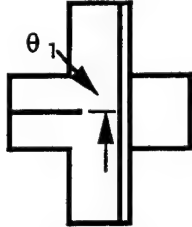
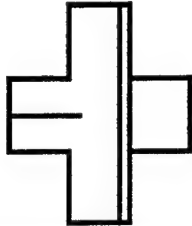
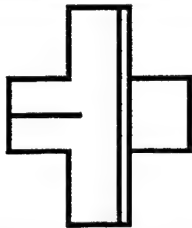
* : Crack kinked and arrested.

: Crack penetrated through tear strap which remained intact.

 $K_{1c} = 50 \text{ MPa} \cdot \text{m}^{0.5}$

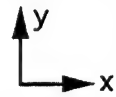
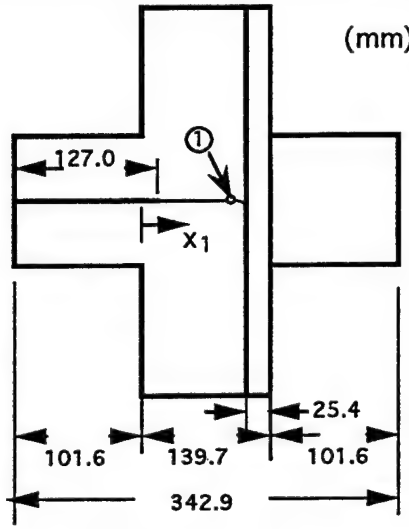
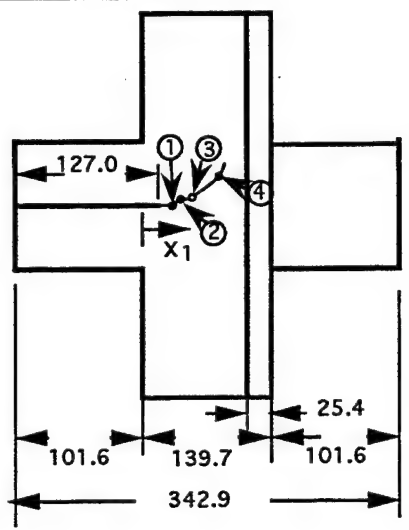
TABLE 8. TEST RESULTS.

MATERIAL: 7075-T6, THICKNESS = 0.81 MM (0.032 IN.)

Specimen No.	Maximum Load (N)	Crack Path	Remarks
7MV-5	P _x = 16,100 P _y = 16,700	$\Delta a = 173.9$ $\theta_1 = 24$ 	Crack penetrated through tear strap and arrested.
7MV-6	P _x = 11,300 P _y = 19,100	$\Delta a = 165.4$ $\theta_1 = 35$ 	
7MV-7	P _x = 12,100 P _y = 17,200	$\Delta a = 186.3$ $\theta_1 = 37$ 	

 Δa : Total crack extension (mm). θ_1 : Initial kinking angle (degrees). $K_{1c} = 60.5 \text{ MPa} \cdot \text{m}^{0.5}$

TABLE 9. COMPARISON OF EXPERIMENTAL AND FEM ANALYSIS.
MATERIAL: 2024-T3 CRUCIFORM SPECIMEN

Specimen No. Max. load	Kinking Point & Angle			Crack Path 
	Pt.	Measured	Calculated	
MV- 1 $P_x = 0$ $P_y = 16,700 \text{ N}$	1*	$x_{1m} = 111.3$ $\theta_m = 6.5$	$x_{1c} = 109.2$ $\theta_c = 5.9$ $r_o = 1.49$	
MV-3 $P_x = 17,000 \text{ N}$ $P_y = 15,500 \text{ N}$	+a 1	$x_{1m} = 50.8$ $\theta_m = 32$	$x_{1c} = 50.8$ $\theta_c = 33.1$	
	+b 2	$x_{1m} = 55.9$ $\theta_m = -32$	$x_{1c} = 55.9$ $\theta_c = -29.3$	
	* 3	$x_{1m} = 63.2$ $\theta_m = 27.8$	$x_{1c} = 63.5$ $\theta_c = 34.4$ $r_o = 1.12$	
	+c 4	$x_{1m} = 86.8$ $\theta_m = 16$	$x_{1c} = 94$ $\theta_c = 16.8$	

x_m : Measured length (mm).

x_c : Calculated length (mm).

θ_m : Measured angle (degrees).

θ_c : Calculated angle (degrees).

r_o : Characteristic radial distance (mm) equation 12.

* : Crack kinking under mode I.

When $r_o < r_c = 1.5 \text{ mm}$, θ_c is predicted by equation 13.

+ : Crack kinking under mixed mode.

When $K_I < K_{Ic}$, θ_c is predicted by equation 11.

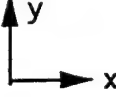
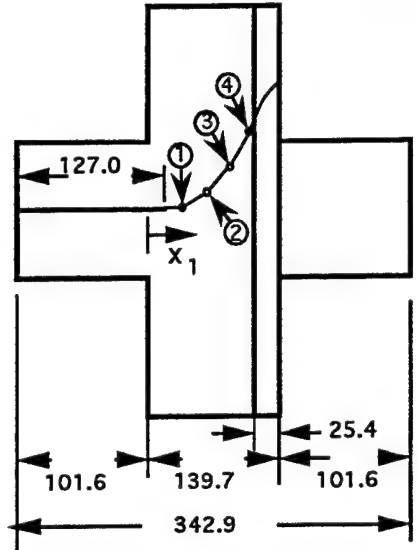
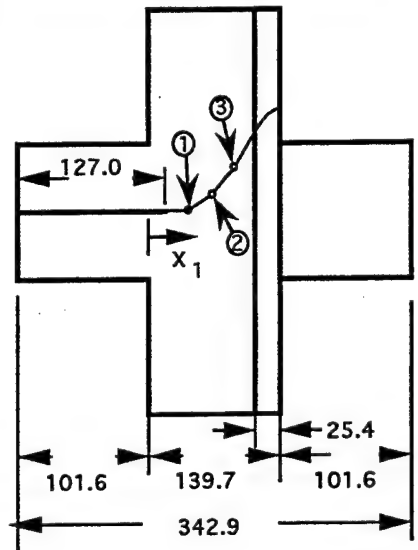
a : $K_{II} < 0$, $\sigma_{ox} > 0$ c : $K_{II} < 0$, $\sigma_{ox} < 0$

b : $K_{II} > 0$, $\sigma_{ox} > 0$

$K_I > K_{Ic}$ Actual K_I is probably 20~30% smaller than

the computed K_I due to unloading (see figure 35 strain gage 3 data).

TABLE 10. COMPARISON OF EXPERIMENTAL AND FEM ANALYSIS.
MATERIAL: 2024-T3 CRUCIFORM SPECIMEN

Specimen No.	Kinking Point & Angle			Crack Path 
	Pt.	Measured	Calculated	
MV-7 $P_x = 17,300 \text{ N}$ $P_y = 19,600 \text{ N}$	+a 1	$x_{1m} = 50.8$ $\theta_m = 30.8$	$x_{1c} = 50.8$ $\theta_c = 30.1$	
	2*	$x_{1m} = 70.4$ $\theta_m = 16.7$	$x_{1c} = 66.0$ $\theta_c = 15.6$ $r_o = 1.41$	
	* 3	$x_{1m} = 90.8$ $\theta_m = 15.0$	$x_{1c} = 86.4$ $\theta_c = 16.4$ $r_o = 1.41$	
	+c 4	$x_{1m} = 113.0$ $\theta_m = 12.2$	$x_{1c} = 114.3$ $\theta_c = 13.7$	
MV-9 $P_x = 18,100 \text{ N}$ $P_y = 19,400 \text{ N}$	+a 1	$x_{1m} = 50.8$ $\theta_m = 31$	$x_{1c} = 50.8$ $\theta_c = 31.7$	
	* 2	$x_{1m} = 68.6$ $\theta_m = 11.9$	$x_{1c} = 66.0$ $\theta_c = 11.0$ $r_o = 1.46$	
	* 3	$x_{1m} = 86.6$ $\theta_m = 13.4$	$x_{1c} = 81.3$ $\theta_c = 11.8$ $r_o = 1.45$	

x_{1m} : Measured length (mm)

x_{1c} : Calculated length (mm)

θ_m : Measured angle (degrees)

θ_c : Calculated angle (degrees)

r_o : Characteristic radial distance (mm) equation 12.

* : Crack kinking under mode I

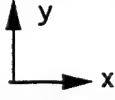
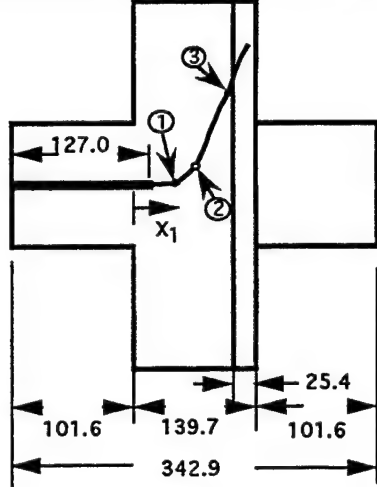
When $r_o < r_c = 1.5 \text{ mm}$, θ_c is predicted by equation 13.

+ : Crack kinking under mixed mode

When $K_I < K_{Ic}$, θ_c is predicted by equation 11.

a: $K_{II} < 0$, $\sigma_{ox} > 0$ c: $K_{II} < 0$, $\sigma_{ox} < 0$

TABLE 11. COMPARISON OF EXPERIMENTAL AND FEM ANALYSIS.
MATERIAL: 7075-T6 CRUCIFORM SPECIMEN

Specimen No.	Kinking Point & Angle			Crack Path 
	Pt.	Measured	Calculated	
7MV-7	+a 1	$x_{1m} = 50.8$ $\theta_m = 37$	$x_{1c} = 50.8$ $\theta_c = 38$	
	2*	$x_{1m} = 65.8$ $\theta_m = 11.8$	$x_{1c} = 66.0$ $\theta_c = 13.7$ $r_o = 1.24$	
	+c 3	$x_{1m} = 110.8$ $\theta_m = 17.5$	$x_{1c} = 113.0$ $\theta_c = 16.2$	

x_{1m} : Measured length (mm)

x_{1c} : Calculated length (mm)

θ_m : Measured angle (degrees)

θ_c : Calculated angle (degrees)

r_o : Characteristic radial distance (mm) equation 12.

* : Crack kinking under mode I


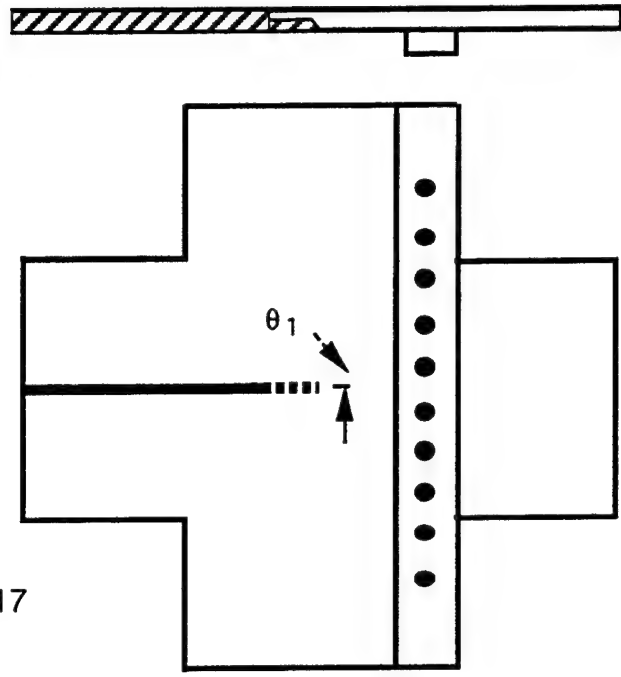
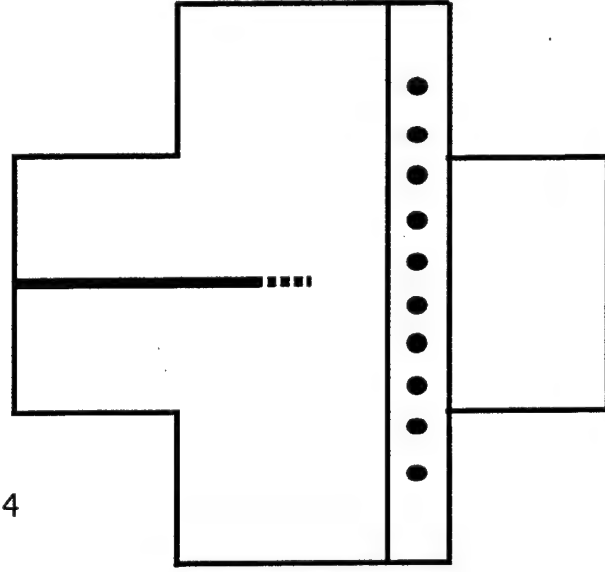
When $r_o < r_c = 1.3$ mm, θ_c is predicted by equation 13.

+ : Crack kinking under mixed mode

When $K_I < K_{Ic}$, θ_c is predicted by equation 11.

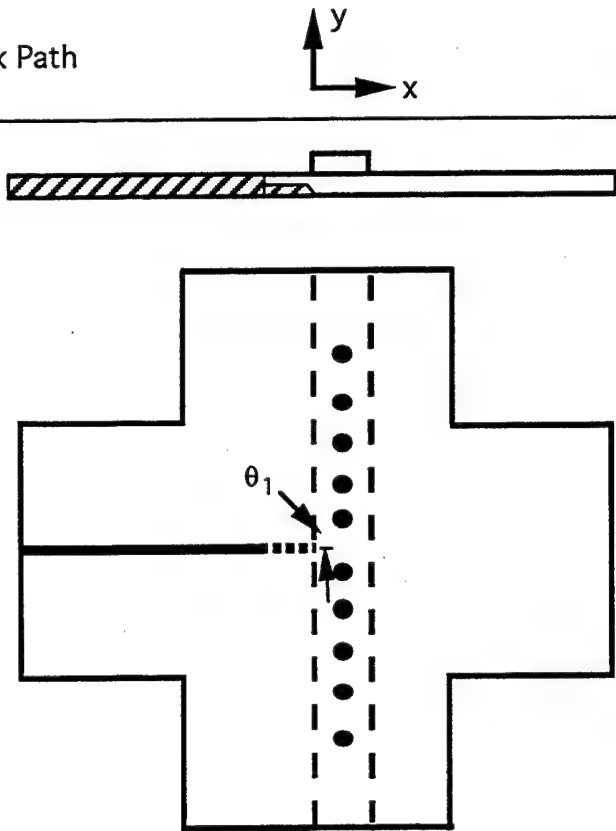
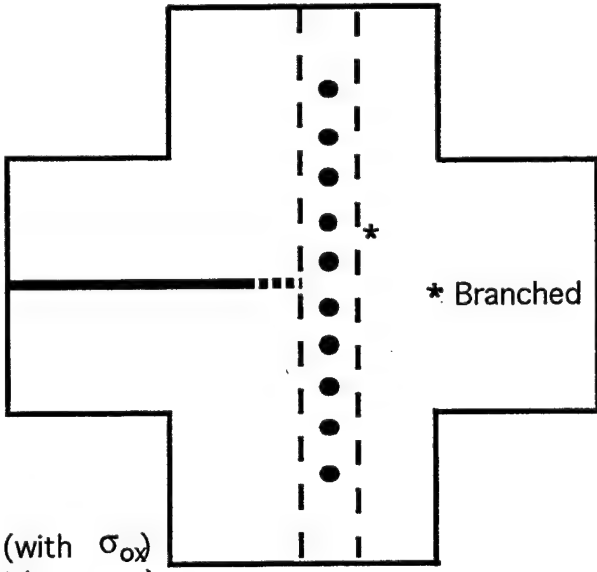
a : $K_{II} < 0$, $\sigma_{ox} > 0$ b : $K_{II} < 0$, $\sigma_{ox} < 0$

TABLE 12. TEST RESULTS (TYPE MA)

Specimen No.	Maximum Load (N)	Crack Path 
MA-1	$P_x = 14,200$ $P_y = 15,400$	 <p>$\theta_{1m} = 17$</p>
MA-2	$P_x = 15,600$ $P_y = 15,100$	 <p>$\theta_{1m} = 24$</p>

θ_{1m} : Measured initial kinking angle (degrees)

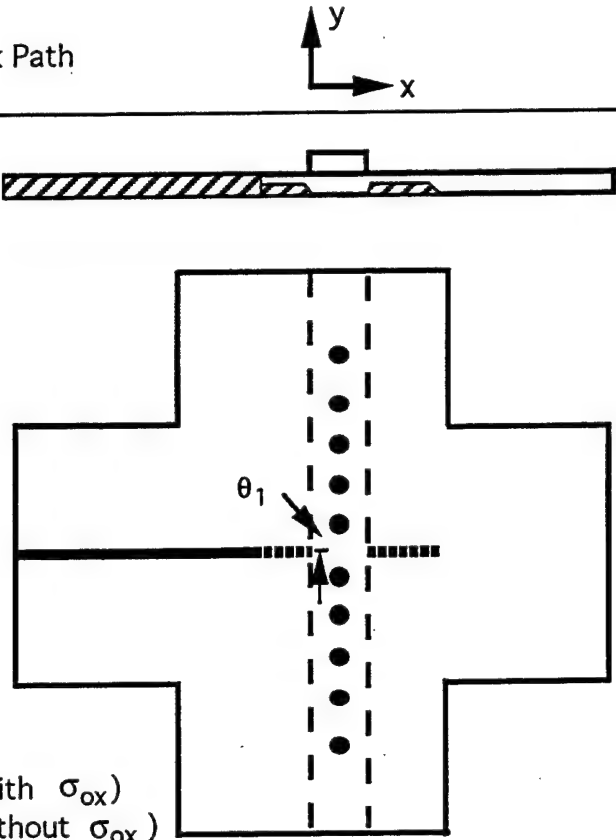
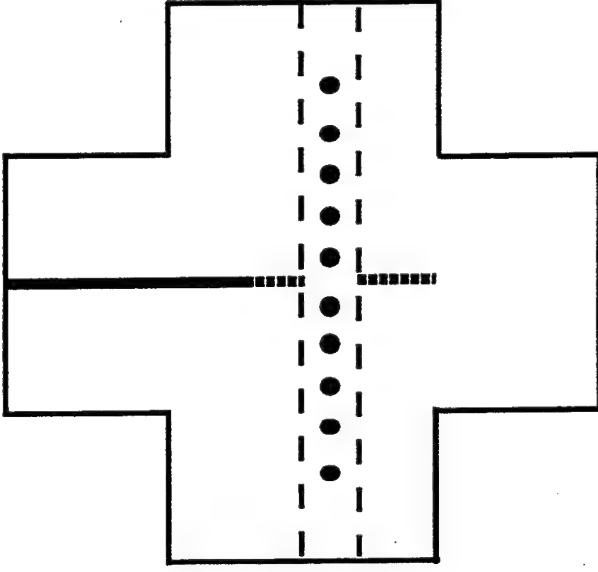
TABLE 13. TEST RESULTS (TYPE MB)

Specimen No.	Maximum Load (N)	Crack Path
MB-2	$P_x = 14,800$ $P_y = 17,500$	 <p>$\theta_{1m} = 40$</p>
MB-3	$P_x = 15,500$ $P_y = 16,300$	 <p>$\theta_{1m} = 43$ $\theta_{1c} = 40.8$ (with σ_{ox}) $= 28$ (without σ_{ox})</p> <p>* Branched</p>

θ_{1m} : Measured initial kinking angle (degrees)


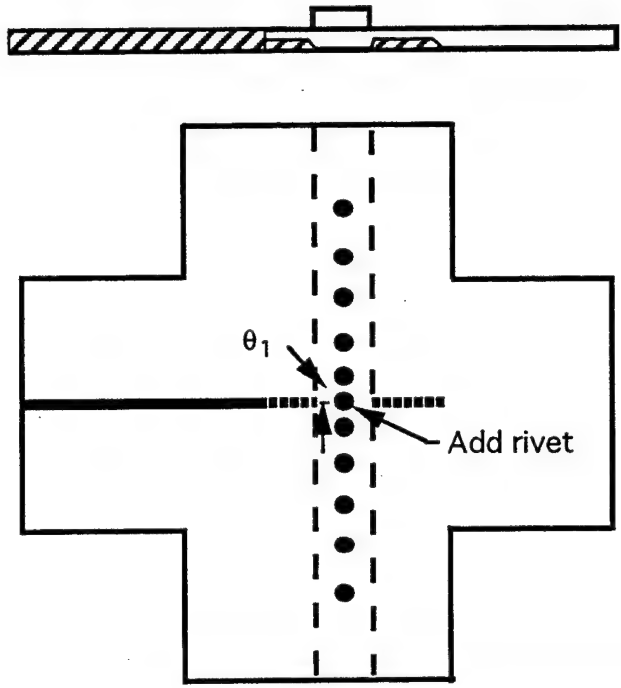
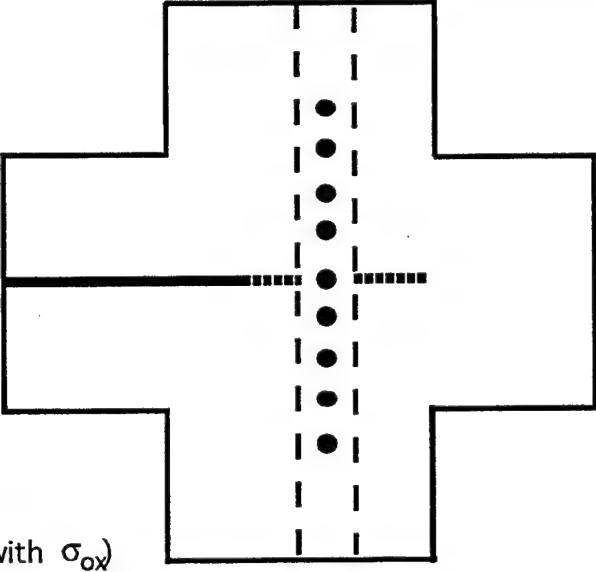
θ_{1c} : Calculated initial kinking angle (degrees)

TABLE 14. TEST RESULTS (TYPE MC)

Specimen No.	Maximum Load (N)	Crack Path
MC-2	$P_x = 15,200$ $P_y = 14,800$	 <p> $\theta_{1m} = 41$ $\theta_{1c} = 38$ (with σ_{ox}) $= 30$ (without σ_{ox}) </p>
MC-4	$P_x = 14,100$ $P_y = 15,500$	 <p> $\theta_{1m} = 36$ </p>

θ_{1m} : Measured initial kinking angle (degrees)
 θ_{1c} : Calculated initial kinking angle (degrees)


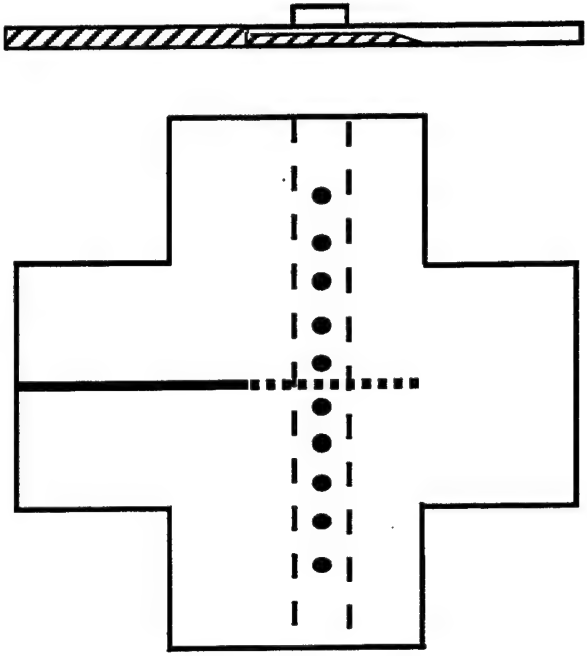
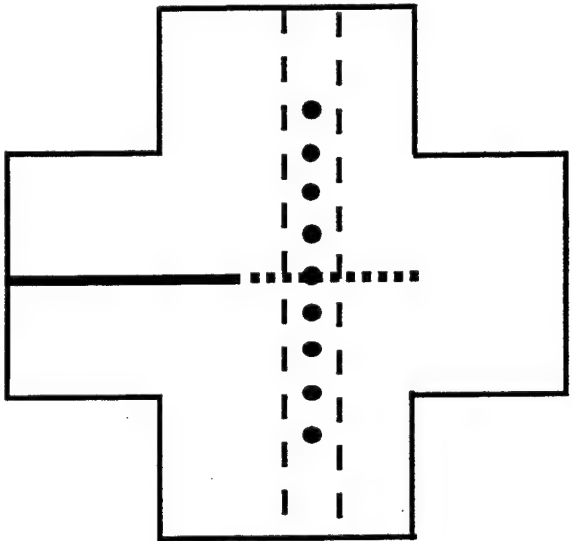
TABLE 15. TEST RESULTS (TYPE MC)

Specimen No.	Maximum Load (N)	Crack Path 
MC-5	$P_x = 20,100$ $P_y = 14,000$	 $\theta_{1m} = 45$
MC-6	$P_x = 19,300$ $P_y = 14,600$	 $\theta_{1m} = 41$ $\theta_{1c} = 36$ (with σ_{ox}) $= 29$ (without σ_{ox})

θ_{1m} : Measured initial kinking angle (degrees)

θ_{1c} : Calculated initial kinking angle (degrees)

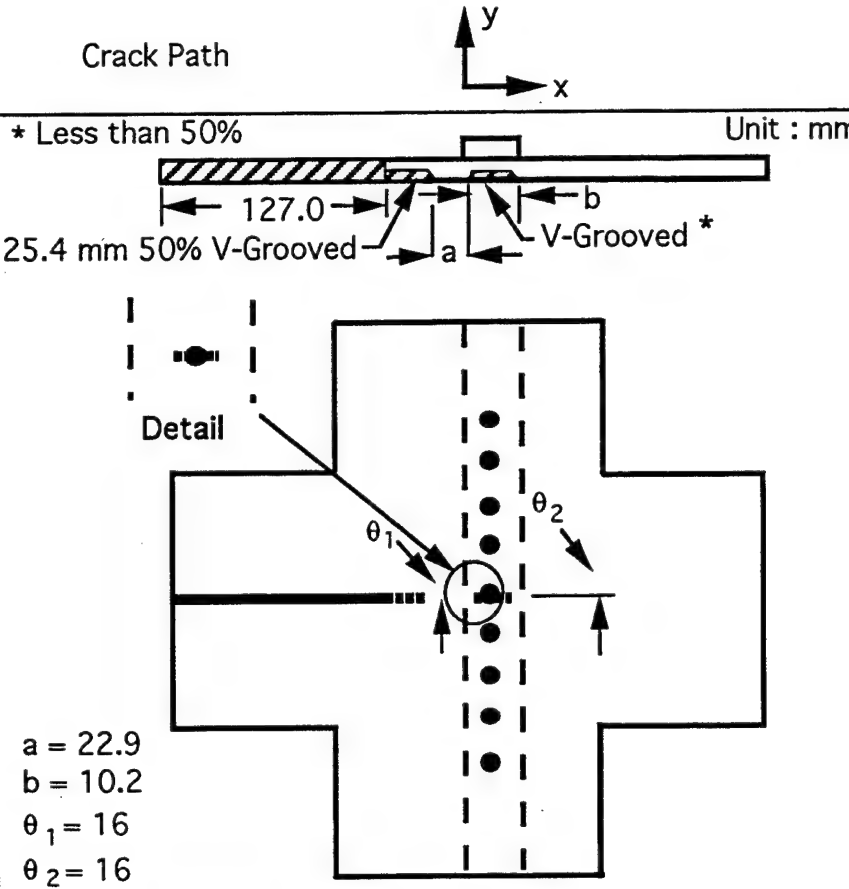
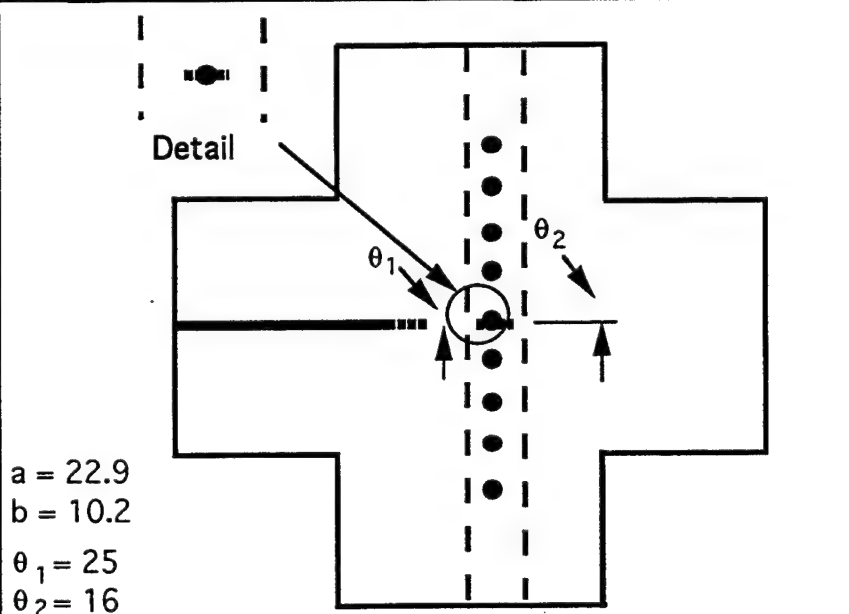
TABLE 16. TEST RESULTS (TYPE MD)

Specimen No.	Maximum Load (N)	Crack Path 
MD-6	$P_x = 14,300$ $P_y = 12,200$	 $\theta_{1m} = 0$ $\theta_{1c} = 0$
MD-7	$P_x = 14,900$ $P_y = 14,600$	 $\theta_{1m} = 0$ $\theta_{1c} = 0$

θ_{1m} : Measured initial kinking angle (degrees)

θ_{1c} : Calculated initial kinking angle (degrees)

TABLE 17. TEST RESULTS (TYPE MG)

Specimen No.	Maximum Load (N)	Crack Path
MG-5	$P_x = 10,900$ $P_y = 13,300$	<p>* Less than 50%</p> <p>Unit : mm</p>  <p>$a = 22.9$ $b = 10.2$ $\theta_1 = 16$ $\theta_2 = 16$</p>
MG-6	$P_x = 11,100$ $P_y = 12,800$	 <p>$a = 22.9$ $b = 10.2$ $\theta_1 = 25$ $\theta_2 = 16$</p>

θ_1 : Initial kinking angle (degrees)

TABLE 18. SUMMARY OF BURSTING PRESSURE

Specimen Number	Type	Configuration		Bursting Pressure		Initial Kinking Angle (degrees)
		Stringer	Tear Strap	(kPa)	(psi)	
1	a-1	No	No	82 **	11.9	0
2	a-2	Flat	No	130	18.6	12
3	b-1	Flat	No	110	16.0	9
4	b-1	Flat	No	100	14.5	12
5	b-2	L	No	NA		30
6	b-2	L	No	NA		30
7	c-1	L	Bonded	170	24.7	33
8	c-2	L	B & R*	177	25.7	32
9	c-2	L	B & R*	150	21.8	34
10	c-3	L	B & R*	160	23.2	35
11	c-3	L	B & R*	163	23.6	35
12	d-1	L	No ⁺	150	21.8	33
13	e-1	No	B & R*	126	18.3	0
14	b-2	L	No	170	24.7	30
15	b-2	L	No	150	21.8	31
16	b-2	L	No	155	22.5	35
17	c-3	L	B & R*	170	24.7	36
18	c-3	L	B & R*	170	24.7	37
19	c-3	L	B & R*	163	23.6	35
20	c-3	L	B & R*	177	25.7	37
21	c-3	L	B & R*	173	25.1	35

* : Bonded and Riveted

** : Initial Crack Length a =127 mm (5 in.), a =102 mm (4 in.) except specimen 1.

TABLE 19. SUMMARY OF K_I , K_{II} , AND APPARENT K_{III} AT THE ONSET OF THE RUPTURE

Unit : $\text{MPa} \cdot \text{m}^{0.5}$

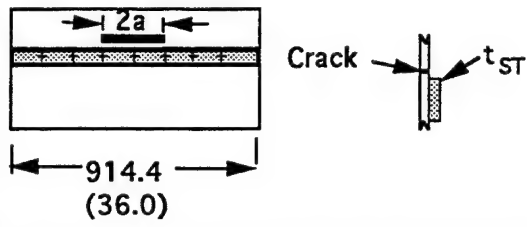
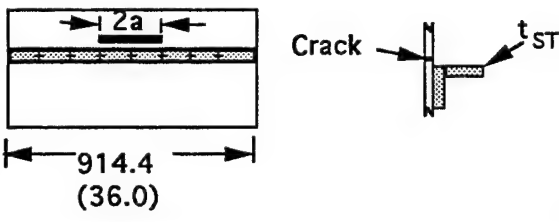
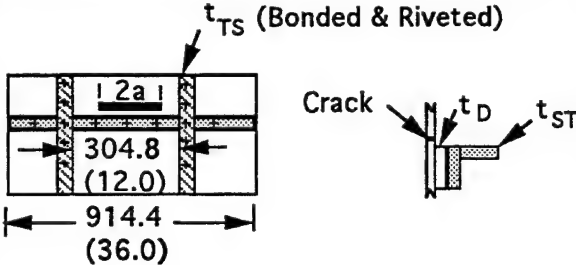
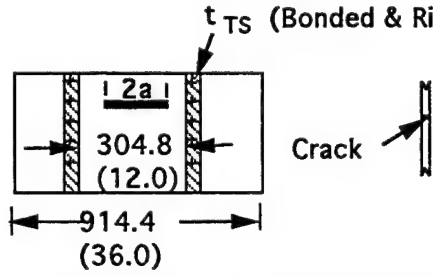
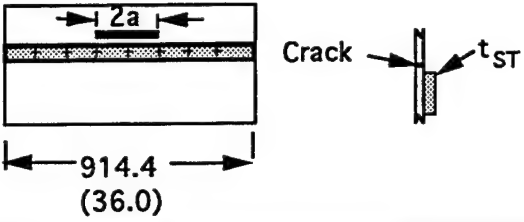
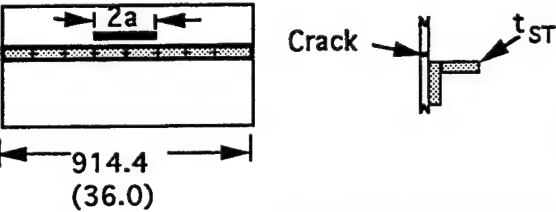
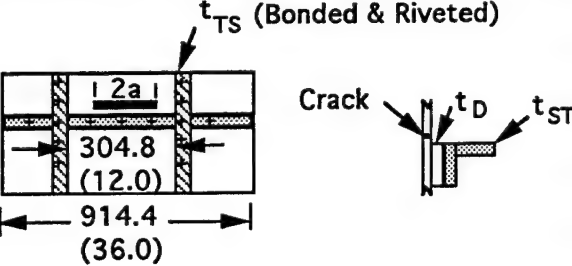
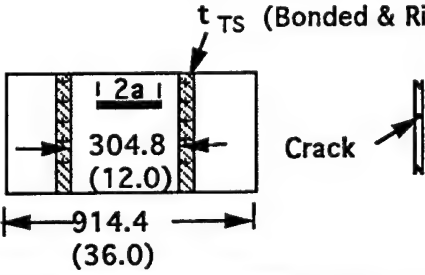
Type	Configuration	K_I	K_{II}	Apparent K_{III}
b-1		94	-2	0.7
b-2		97	-12	0.8
c-3		93	-15	0.8
e-1		101	0	0

TABLE 20. SUMMARY OF MEASURED AND COMPUTED CRACK KINKING ANGLE

Type	Configuration	Kinking Angle (Degrees)
b-1		<p>Mixed-Mode Kinking</p> <p>$\theta_{1m} = 12.7$</p> <p>$\theta_{1c} = 11$ (with σ_{ox})</p> <p>$= 3$ (without σ_{ox})</p>
b-2		<p>Mixed-Mode Kinking</p> <p>$\theta_{1m} = 30$</p> <p>$\theta_{1c} = 31$ (with σ_{ox})</p> <p>$= 14$ (without σ_{ox})</p>
c-3		<p>Mixed-Mode Kinking</p> <p>$\theta_{1m} = 36.7$</p> <p>$\theta_{1c} = 35.8$ (with σ_{ox})</p> <p>$= 17$ (without σ_{ox})</p> <p>Mode-I Kinking</p> <p>$\theta_{2m} = 19.6$</p> <p>$\theta_{2c} = 17.8$</p>
e-1		<p>$\theta_{1m} = 0$</p> <p>$\theta_{1c} = 0$</p>

θ_m : Measured kinking angle (degrees)

θ_c : Computed kinking angle (degrees)

APPENDIX A MIXED-MODE CRACK KINKING CRITERION

The static circumferential stress, $\sigma_{\theta\theta}$, derived by setting the crack velocity to 0 in the mixed-mode elasto-dynamic equation of Ramulu (84) is

$$\begin{aligned}\sigma_{\theta\theta} &= \frac{\cos \frac{\theta}{2}}{\sqrt{2\pi r}} \left[K_I \cos^2 \frac{\theta}{2} - \frac{3}{2} K_{II} \sin \theta \right] + \frac{\sigma_{ox}}{2} (1 - \cos 2\theta) \\ &= \frac{1}{\sqrt{2\pi r}} \left[K_I \cos^3 \frac{\theta}{2} - \frac{3}{2} K_{II} \sin \theta \cos \frac{\theta}{2} \right] + \frac{\sigma_{ox}}{2} (1 - \cos 2\theta)\end{aligned}\tag{A.1}$$

The crack kinking angle can be obtained by maximizing the circumferential stress:

$$\begin{aligned}\frac{\partial \sigma_{\theta\theta}}{\partial \theta} &= \frac{1}{\sqrt{2\pi r}} \left[-\frac{3}{2} K_I \cos^2 \frac{\theta}{2} \sin \frac{\theta}{2} - \frac{3}{2} K_{II} \cos \frac{\theta}{2} \cos \theta + \frac{3}{2} \left(\frac{K_{II}}{2} \right) \sin \theta \sin \frac{\theta}{2} \right] + \sigma_{ox} \sin 2\theta \\ &= -\frac{1}{\sqrt{2\pi r}} \frac{3}{2} \cos \frac{\theta}{2} \left[K_I \cos \frac{\theta}{2} \sin \frac{\theta}{2} + K_{II} \cos \theta - K_{II} \sin^2 \frac{\theta}{2} \right] + \sigma_{ox} \sin 2\theta \\ &= -\frac{1}{\sqrt{2\pi r}} \frac{3}{2} \cos \frac{\theta}{2} \left[\frac{K_I \sin \theta}{2} + K_{II} \left\{ \cos \theta - \frac{(1 - \cos \theta)}{2} \right\} \right] + \sigma_{ox} \sin 2\theta \\ &= -\frac{1}{\sqrt{2\pi r}} \frac{3}{4} \cos \frac{\theta}{2} [K_I \sin \theta + K_{II} (3 \cos \theta - 1)] + \sigma_{ox} \sin 2\theta\end{aligned}\tag{A.2}$$

For the condition of $\sigma_{\theta\theta}$ a maximum stress with respect to θ , $\partial\sigma_{\theta\theta}/\partial\theta$ must vanish.

$$\begin{aligned}
\frac{1}{\sqrt{2\pi r}} \frac{3}{4} \cos \frac{\theta}{2} [K_I \sin \theta + K_{II} (3 \cos \theta - 1)] &= \sigma_{ox} \sin 2\theta \\
\frac{1}{\sqrt{2\pi r}} \frac{3}{4} \cos \frac{\theta}{2} \left[K_I + \frac{K_{II} (3 \cos \theta - 1)}{\sin \theta} \right] &= \frac{2\sigma_{ox} \sin \theta \cos \theta}{\sin \theta} \\
1 + \frac{K_{II}}{K_I} \left(\frac{3 \cos \theta - 1}{\sin \theta} \right) &= \frac{16}{3} \sqrt{2\pi r} \sigma_{ox} \frac{\sin \frac{\theta}{2} \cos \theta}{\sin \theta} \\
\frac{K_{II}}{K_I} \left(\frac{3 \cos \theta - 1}{\sin \theta} \right) &= \frac{16}{3} \sqrt{2\pi r} \left(\frac{\sigma_{ox}}{K_I} \right) \frac{\sin \frac{\theta}{2} \cos \theta}{\sin \theta} - 1 \\
\frac{K_{II}}{K_I} &= \frac{1}{(3 \cos \theta - 1)} \left[\frac{16}{3} \sqrt{2\pi} \frac{\sqrt{r} \sigma_{ox}}{K_I} \sin \frac{\theta}{2} \cos \theta - \sin \theta \right] \\
\frac{K_{II}}{K_I} &= \frac{-\sin \frac{\theta}{2}}{(3 \cos \theta - 1)} \left[2 \cos \frac{\theta}{2} - \frac{16}{3} \sqrt{2\pi} \frac{\sqrt{r} \sigma_{ox}}{K_I} \cos \theta \right]
\end{aligned} \tag{A.3}$$

The final result can be given the following transcendental equation:

$$\begin{aligned}
\frac{K_{II}}{K_I} &= \frac{-\sin \frac{\theta}{2}}{(3 \cos \theta - 1)} \left[2 \cos \frac{\theta}{2} - \frac{16\sqrt{2\pi}}{3} A \cos \theta \right] \\
A &= \sqrt{r} \frac{\sigma_{ox}}{K_I}
\end{aligned} \tag{A.4}$$

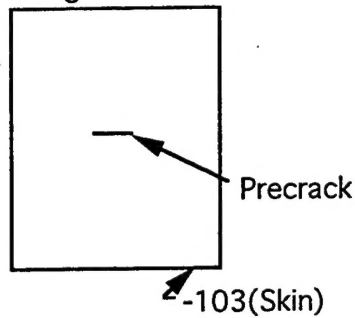
APPENDIX B

SMALL-SCALE FUSELAGE SPECIMEN PREPARATION

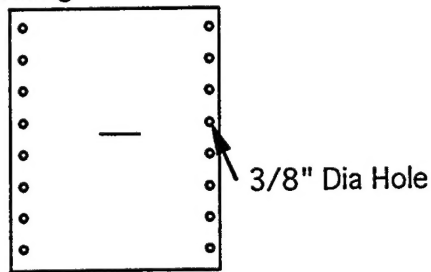
A schematic outlining the specimen preparation sequence is shown in figure B.1. This particular sequence is for type c-3 specimen.

- Step 1. Cut the 102 mm (4 inches) through-crack in the middle of the flat sheet (-103), which is 1168 mm (46 inches) by 914 mm (36 inches). The direction of the crack must be consistent with the rolling direction, which is equivalent to an axial crack in the real fuselage.
- Step 2. Drill twenty-five 9.5 mm (3/8 inch) holes along both sides of the sheet, which are perpendicular to the crack.
- Step 3. Bond two tear straps (-109) and spacers (-105, -107) on the sheet using epoxy bonding for type-c specimen. The bonding process is done at room temperature. Tear straps are riveted to the skin with 4 mm (5/32 in.) diameter pop-up rivets.
- Step 4. Use 4 mm (5/32 in.) diameter aluminum pop-up rivets to attach the stringer (-111) adjacent to the starter crack.
- Step 5. Roll and insert the sheet into the end cap with a 4.8 mm (3/16 in.) rubber gasket (-113). The end caps are made of steel and provide an interface between the fixtures and the specimen. Then put the inner ring inside the rolled specimen.
- Step 6. Tighten the specimen to the end cap using 6.4 mm (1/4 in.) diameter bolts.
- Step 7. Butt both ends of the sheet and make a butt joint with inside and outside splice plates using 4 mm (5/32 in.) diameter pop-up rivets.
- Step 8. Seal the starter crack with a cork gasket and a thicker layer of silicon rubber sealant to the inside of the specimen.
- Step 9. Seal all interface area with silicon rubber sealant.
- Step 10. Allow about 12 hours for the silicon rubber sealant to dry.

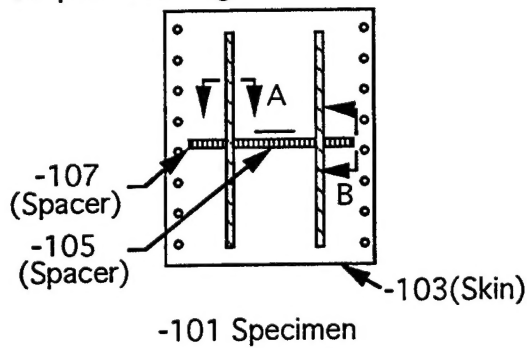
Step 1 Cutting



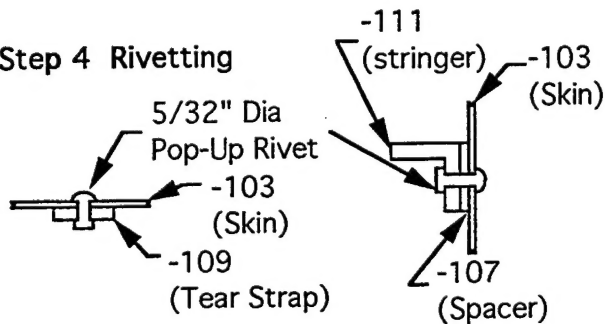
Step 2 Drilling



Step 3 Bonding



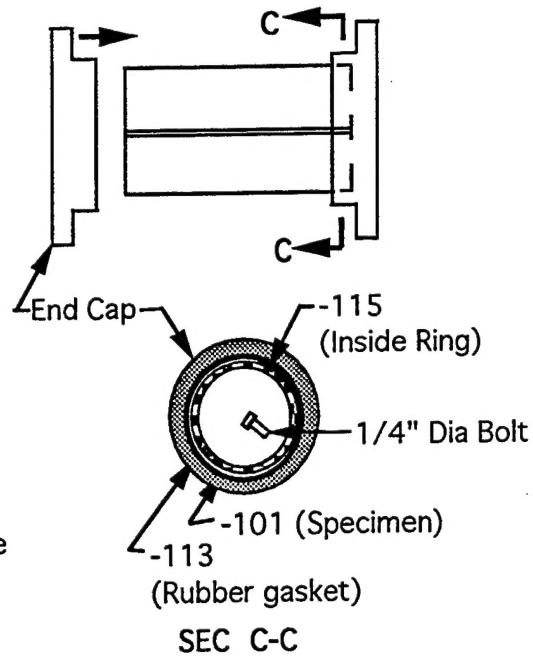
Step 4 Rivetting



SEC A-A

SEC B-B

Steps 5 and 6 Setting



Step 7 Assembling

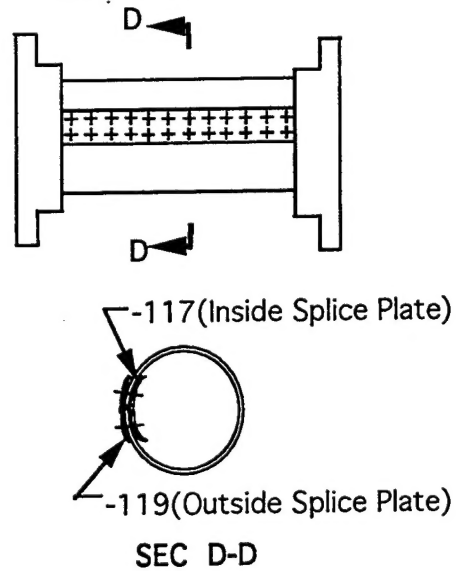


FIGURE B-1. SMALL-SCALE FUSELAGE SPECIMEN PREPARATION

APPENDIX C
MATERIAL PROPERTIES OF 2024-T3 AND 7075-T6 ALLOYS

Table C-1 shows material properties of 2024-T3 and 7075-T6 alloys.

TABLE C-1. MATERIAL PROPERTIES OF 2024-T3 AND 7075-T6 ALLOYS

Aluminum Alloy	Thickness	Ultimate Strength	Yield Strength	Young Modulus	Plane Stress Fracture Toughness*
2024-T3 Clad Sheet	0.3 mm (0.012")	427 MPa (62 ksi)	324 MPa (47 ksi)	72 GPa (10.5x10 ³ ksi)	96 MPa*m ^{0.5} (87 ksi*in ^{0.5})
	0.8 mm (0.032")				60 MPa*m ^{0.5} (54 ksi*in ^{0.5})
7075-T6 Clad Sheet	0.8 mm (0.032")	537MPa (78 ksi)	496 MPa (72 ksi)	71 GPa (10.3x10 ³ ksi)	50 MPa*m ^{0.5} (46 ksi*in ^{0.5})

* Ref : MCIC-HB-01R, " Damage Tolerant Design Handbook"